Sedimentology and Paleogeographic Reconstruction of the Strata in and Adjacent to the Sudbury Impact Layer in the Northern Paleoproterozoic Animikie Basin

by

Monica M. McCullough

Submitted in conformity with the requirements
for the degree of Masters of Science in Geology (M.Sc. Geol.)

Department of Geology
Lakehead University

Sedimentology and Paleogeographic Reconstruction of the Strata in and Adjacent to the Sudbury Impact Layer in the Northern Paleoproterozoic Animikie Basin

Monica M. McCullough

Masters of Science in Geology (M.Sc. in Geology)

Department of Geology
Lakehead University

2016

Abstract

The Sudbury Impact Layer (S.I.L.) is dated at 1850 Ma and is located between the underlying Gunflint Formation, with an age of 1878±1 Ma that was obtained from zircons in a tuffaceous zone approximately 105 meters below the S.I.L., and the overlying Rove Formation that has an U-Pb zircon age of 1832 Ma which was obtained from tuffs 5-6 meters above the S.I.L.   There is an 18 Ma hiatus between the Sudbury Impact Layer and from where the zircon was extracted from the overlying Rove Formation, and a 46 Ma hiatus between the Sudbury Impact Layer and the underlying Gunflint Formation. These large age anomalies associated with the hiatuses, along with little sedimentation between the tuffs that supplied the ages, suggest that periods of non-deposition and sub-aerial exposure eroded the land, resulting in a lack of sedimentation in the allotted age gaps.

This time interval was investigated in a number of outcrops and cored drill-holes in the northern portion of the basin. Sedimentological aspects of the rocks were noted and samples collected for geochemical studies. The upper portion of the Gunflint Formation contains grainstones that were deposited in shallow water along with chemical sediments precipitated

from Paleoproterozoic seawater. Positive Ce anomalies indicate oxygen production by stromatolites in the inter-tidal to very shallow sub-tidal lead to some oxygenation of the shallow nearshore. The chemical sediments in the limestone that overlies the Gunflint ankerite and chert had their calcite cement formed in meteoric phreatic conditions, with extremely elevated contents of vanadium and large negative cerium anomalies indicating these waters were significantly oxic. The overlying Sudbury Impact Layer shares these characteristic, though in the southeast it was probably deposited in a very wet, likely marine, setting. Ankeritic grainstones overlying the Sudbury Impact Layer refute the idea that the impact caused an end to iron formation deposition and show a transition from flooding and sub-tidal deposition to extensive sabkha development. The common occurrence of gypsum is indicated by the presence of its pseudomorphs forming bladed crystals, desert roses and vein systems. The Rove sea flooded over this surface after lithification.

Table of Contents

Acknowledgments

List of Figures

List of Tables

1 Introduction

1.1 Purpose

The Sudbury Impact Layer (S.I.L) is dated at 1850±1 m.y. by Krogh et al. (1984) and is located between two distinct lithologies: 1) The underlying Gunflint iron formation, with an age of 1878±1 m.y. that was obtained from zircons in a tuffaceous zone approximately 105 meters below the Sudbury Impact Layer (Fralick et al., 2002) and 2) The overlying Rove Formation that has an U-Pb zircon age of 1832±3 m.y. (Addison et al., 2005) that was obtained from tuffs 5-6 meters above the Sudbury Impact Layer. There is an 18 m.y. hiatus between the Sudbury Impact Layer and the layer where the zircon was extracted from the overlying Rove Formation, and a 46 m.y. hiatus between the Sudbury Impact Layer and the underlying Gunflint Formation. The purpose of this study is to gain an understanding of the depositional environments prior to, during, and after the deposition of the Sudbury Impact Layer in the Animikie Basin, taking into account that there are large age anomalies between each lithology, but little sedimentation within the periods of hiatus. Due to the long hiatuses, it is inferred that periods of subaerial exposure eroded the land, resulting in a lack of sedimentation in the allotted age gaps.

1.2   Geologic Setting

The Sudbury impact event occurred during a time of tectonic activity along the southern margin of the Animikie Shelf, Superior craton. The Sudbury Impact Layer (S.I.L.) overlies the Gunflint Formation and underlies the Rove Formation. One explanation by Kissin and Fralick (1994), Hemming et al. (1995), Van Wyck and Johnson (1997), and Pufahl and Fralick (2000) states that prior to the Sudbury impact event, a backarc basin was formed on the southern margin as a result of extension, which possibly was caused by subduction roll-back, that caused an area of continental crust to subside and become flooded. Another explanation involves successive island-arc collisions and the development of a foreland basin that then subsided to receive the Gunflint Formation sediments on its northern margin (Schneider et al., 2002; Schulz and Cannon, 2007). A shallow marine tide and wave-dominated shelf (Ojakangas, 1983; Fralick, 1988; Pufahl and Fralick, 2000; Pufahl and Fralick, 2004) developed in the basin, and on the Archaean basement was deposited, organized, and sorted volcaniclastic material and chemical sediments consisting of cherts, iron carbonates, iron oxides and carbonaceous shales (Gill, 1926; Tanton, 1931; Moorhouse and Goodwin, 1960). The upper two-thirds of the Gunflint Formation is composed of coarsening- and thickening-upward successions representing shoaling-upwards cycles (Fralick and Barrett, 1995). The end of Gunflint deposition is marked by stromatolites in a thin limestone unit present at the top of the formation in the Thunder Bay area, which Shegelski (1982) believed was indicative of a lagoon environment. The hiatus of 46 Ma between the top of the 1878±1 m.y. (Fralick et al., 2002) Gunflint Formation and the overlying 1832±3 m.y. (Addison et al., 2005) basal Rove Formation was very probably formed due to the Penokean orogeny to the south, which resulted in a crustal up-warping and regression of the sea (Johnston et al., 2006). Because the land became sub-aerially exposed, Gunflint Formation surfaces are

altered. Alteration includes silicification below the limestone unit, shattering of silicified units and formation of white blocky calcite cements by meteoric water infiltration (Tanton, 1931; Burton and Fralick, 2007; Fralick and Burton, 2008; Addison et al., 2010). The Sudbury Impact Layer overlies the stromatolitic limestone and underlying silicified carbonate upper portion of the Gunflint Formation. The Rove Formation, which consists of carbonaceous silts and black shales overlies the Sudbury Impact Layer. The deposition of the Rove Formation is an indicator of the end of the Penokean orogeny and the start of crustal relaxation and flooding. Maric and Fralick (2005) and Johnston et al. (2006) state that the Rove sediments were very likely to have been eroded from the Trans-Hudson orogen to the northwest.

Today, the Gunflint Formation and Rove Formation are situated on a homocline that is dipping southeast toward Lake Superior at an average of 5° (Gill, 1926). The Gunflint Formation is the eastern extension of the Biwabik Iron Formation that is exposed along the Mesabi Iron Range. This was bisected by a large area of Mesoproterozoic intrusions of the Duluth Complex (~1100 Ma). Both the Gunflint and Biwabik Iron Formations lie unconformably on a deformed Archaean terrain of the Wawa subprovince of the Superior Province, and the Paleoproterozoic diabase dikes that cut the Archaean rocks locally (Jirsa et al., 2011). The deposits at Gunflint Lake in Minnesota were affected by contact metamorphism of the Duluth Complex, evidence being in the amphibole and pyroxene-rich hornfels present in the rock (Floran and Papike, 1978). The Gunflint Formation and Rove Formations to the north remained unmetamorphosed except for localized zones and areas that are adjacent to diabase sills and dikes (Tanton, 1931).

1.3 Location
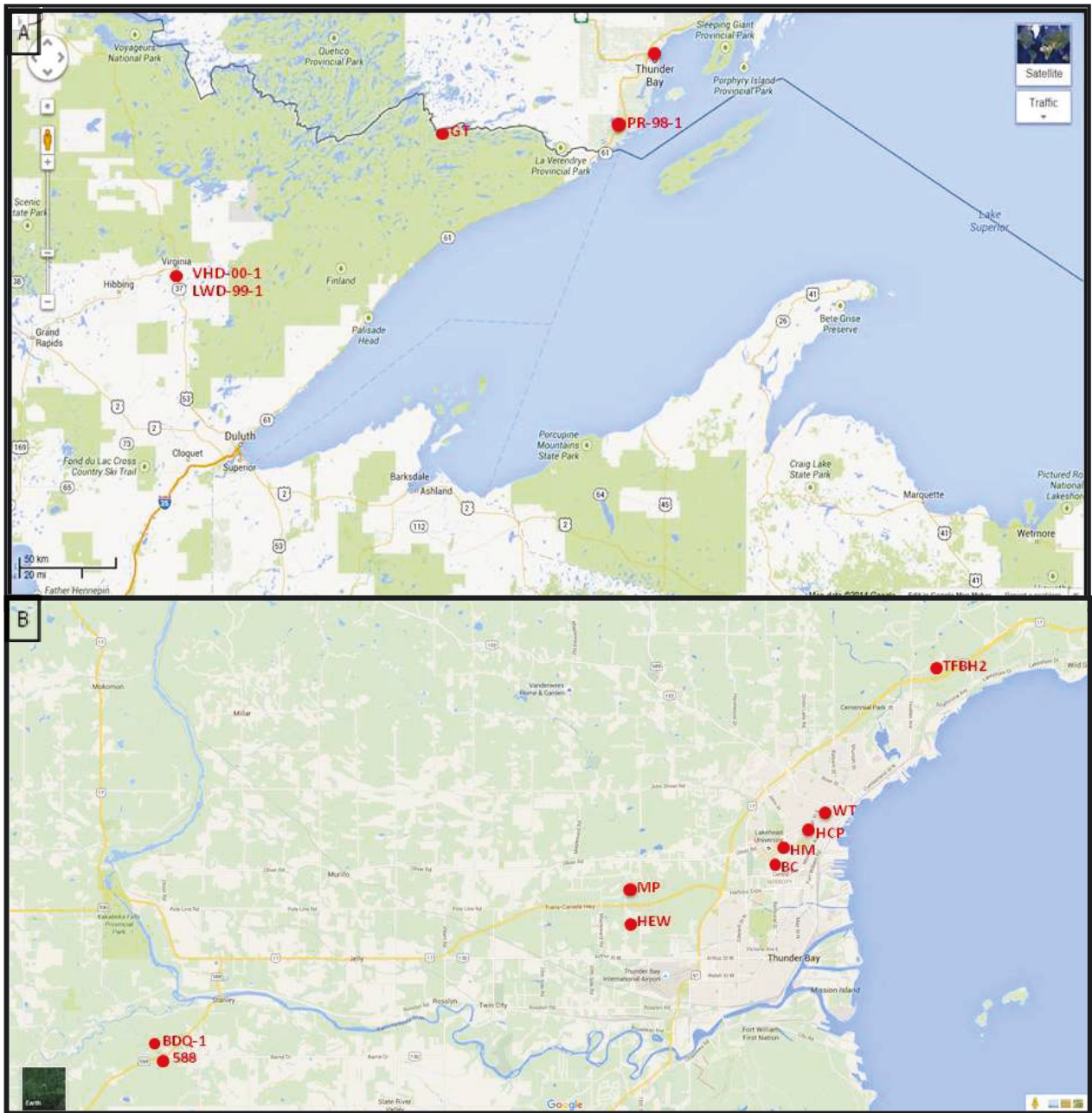
Figure 1. Map of Site Locations. Figure 1A. Overview map of Canada, and United States locations. Drillcore PR-98-1 and fieldsite GT are located in Canada near the Canada-U.S. border while drillcore VHD-00-1 and LWD-99-1 are located in the U.S. Figure 1B. Overview detailed map of Thunder Bay site locations, which include fieldsites Highway 588, Harbour Expressway, Mapleward, Baseball Central, Hill and Markland, Hillcrest Park, Waverly Towers, Terry Fox, and drillcore BDQ-1 and Terry Fox Borehole 2. Map source: Google Earth, modified with site symbols labeled for each locality.

1.4   Detailed Geological Framework

1.4.1   Lithofacies

When viewing and describing both fieldsites and drillcore, a consistent definition was used in classifying the rock types throughout this study. The classification of carbonate rocks was based on Dunham's classification of carbonate rocks according to depositional texture (Dunham, 1962). The Gunflint Formation is the main unit studied and it includes iron carbonate grainstone and micrite. Carbonate grainstone is classified as "original components not bound together during deposition, lacks mud, and is grain-supported". Micrite is classified as "original components not bound together during deposition, contains mud (particles of clay and fine silt-sized material), is mud supported, and contains less than 10% grains". The Sudbury Impact Layer was classified according to what was observed in each and every fieldsite and drillcore. As variability was observed in every fieldsite, there are a few different descriptors of the actual impact layer. The Sudbury Impact Layer ranges in particle size from fine to medium to coarse-grained sand, to pebble, to cobble, and boulder-size for the large boulders ripped up in the shear basal flow. The overlying Rove Formation was classified as siltstones and mudstones (Maric and Fralick, 2005)

1.4.1.1   Gunflint Formation

The Gunflint Formation consists of two sequences, and each of those two sequences consists of two members. Figure 2, after Jirsa et al. (2011), displays the lower and upper sequences of the Gunflint Formation, in Minnesota. The lower cherty and lower slaty members, and a part of the upper cherty member represents deposition during a single marine transgression and regression. This is defined as the lower sequence (Goodwin, 1956). The lower sequence grades from conglomerate and sandstone at the base (Kakabeka conglomerate), which was deposited in paleo depressions unconformably overlying the Neoachaean bedrock, to locally stromatolitic chert and microbial structures. These are overlain by ankeritic and siliceous grainstone, at the base of a thinning and fining-upward sequence that grades0 to a predominantly iron-rich mudstone with thin grainstone layers. Fralick and Barret (1995) state that this sequence then coarsens and thickens upwards to a regressive surface, where it was then capped by strata that were cemented sub-aerially. The next transgression then took place and during its beginning stages, microbial structures formed on the silicified surface and then were overlain by coarse siliceous grainstone. At this point, an influx of fine-grained volcanic ash occurred, which was possibly related to basaltic volcanism located approximately 10 km north of the Canadian-United States border (Jirsa et al., 2011). These ash layers consist of iron-rich chlorite with some beds of volcanic accretionary lapilli, not to be confused with impact lapilli. Near the Thunder Bay area, in the north, the grainstone layers are interlayered with black shale creating lenticular bedding, which progressively becomes more abundant travelling up the stratigraphic column, until the grainstone facies dominate the column. In the Gunflint Lake area, to the south, the volcanic ash is mixed in with chemical sediments, thus forming the upper slaty member. The siliceous grainstone units are made of coarsening- and thickening-upwards cycles. These cycles form parasequences in the transgressive environment (Jirsa et al., 2011).

Taking a closer look at the Thunder Bay area as compared with the Gunflint Lake area, both exhibit different characteristics pertaining to the upper parts of the Gunflint Formation. The top of the Gunflint Formation in the Thunder Bay area shows evidence for additional volcanism that adds ash that is reworked into sand and interlayered with stromatolites. Both lithologies developed a white, blocky, calcite cement (Fralick and Burton; 2008). Burton and Fralick (2007) and Fralick and Burton (2008) also noticed that this unit is underlain by a regressive surface with intense silicification, and is overlain by breccia of the Sudbury Impact Layer. The Gunflint Lake area, on the other hand, has in the uppermost meters of the iron formation a brecciated and/or extremely folded unit covered by the Sudbury Impact Layer. The deformation and folding of the topmost layers in the Gunflint Lake area signify that the sediments were water saturated, shocked and liquefied (Jirsa et al., 2011).

The upper layers in the Thunder Bay area contain a different lithology. Moorhouse and Goodwin (1960) noted that the uppermost layers of the Gunflint Formation are comprised of a thin calcite-rich unit, which has been labeled the Limestone Member. The calcite-rich unit is approximately 1-2 meters thick and separates the silicified and sub-aerially exposed regression surface from the overlying Sudbury Impact Layer. Fralick and Burton (2008) state that the calcite cements were present prior to the impact and that they were formed from meteoric waters, not seawater.
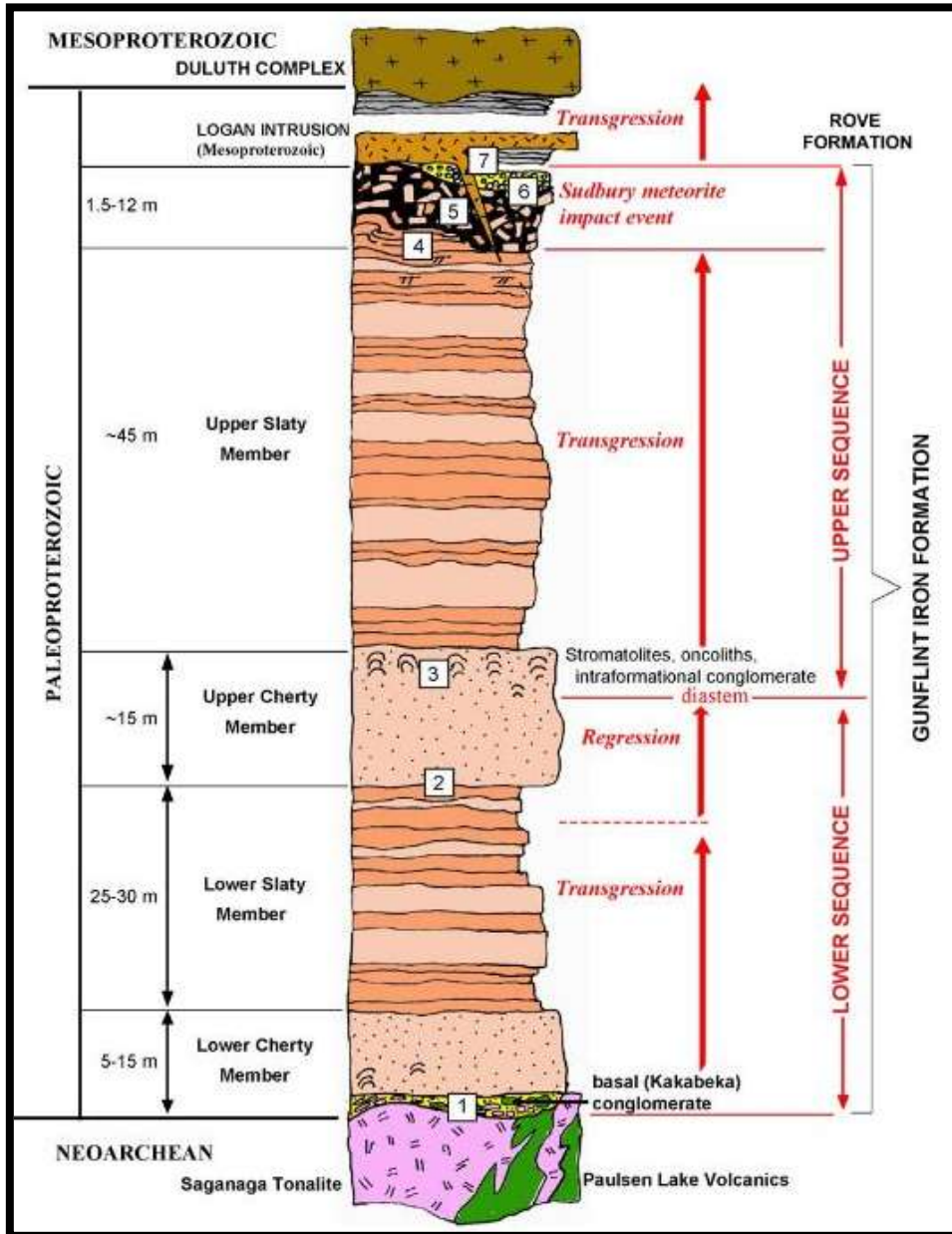
Figure 2. Sedimentological model after Jirsa and Fralick (2011). Stratigraphic representation of the Gunflint Formation and underlying and overlying rock in Northern Minnesota.

1.4.1.2   Sudbury Impact Layer (S.I.L.)

1850±1 million years ago (Krogh et al., 1984), a bolide struck what is now Sudbury, Ontario in Canada, creating a catastrophic chain of events. The bolide nearly 10 kilometres in diameter, formed a crater with a radius of ~130 km, making the Sudbury Impact Event the third largest impact known in history (Earth Impact Database, 2015). The collision created impact-induced earthquakes likely around magnitude 10 on the Richter scale in the vicinity and managed to fracture bedrock hundreds of kilometres away (Addison et al., 2010).

Material ejected from the impact event has been discovered as far as 600-800 kilometres, or ~5-7 crater radii (Spray et al., 2004) from the Sudbury crater. This distal ejecta layer is found between the 1878±1 Ma (Fralick et al., 2002) underlying Gunflint Formation and the overlying 1832±3 Ma (Addison et al., 2005) Rove Formation in the Lake Superior Basin.

Gault et al. (1968) state that at the moment of impact, the energy and momentum carried by the projectile acted to melt and vaporize both projectile and target material as well as generate an immense shock wave through the target material. Experimental evidence and observation from lunar and smaller terrestrial impacts inspired Collins et al. (2005) to create a dramatic recreation of an impact event, like the Sudbury impact as listed below:

1. Fireball: ~13 seconds (modern equivalent to 3rd degree burns)

2. Earthquake: ~2-3 minutes (10.9-13 at epicenter)

3. Ejecta ground surge: ~5-10 minutes (predicts ejecta 1-3 meters thick, grain sizes ~1cm)

4. Air blast: ~40 minutes (sonic boom)

Although stratigraphic and sedimentological characteristic of the ejecta vary from site to site and outcrop to outcrop, due to local and uneven paleo-topography, generally the impact related deposits in the western Lake Superior region include material interpreted to be seismically folded and/or brecciated iron formation, commonly carbonate facies, that are overlain by ejecta material that appear to be mixtures of locally and distally derived materials (Jirsa et al., 2011).

The Sudbury Impact Layer (S.I.L.) is composed of two constituents: The first portion is a chaotic debrisite that was formed from the initial shock from impact which generated ground-hugging base surges that picked up and transported loose and fractured bedrock from the Gunflint. This is the primary component of the Sudbury Impact Layer. The second portion consists of the ejecta material from the impact that is a mixture of local and distal material and includes devitrified glass, spherules, planar features in quartz grains, and lapilli (Addison et al., 2010). The two constituents of the Sudbury Impact Layer are detailed below.

The first constituent and primary component of the Sudbury Impact Layer consists of chaotic shattered and ripped-up underlying bedrock of the Gunflint Formation that include ripped-up carbonate grainstones, chert, and stromatolites. These pieces range in size from granular- to boulder-sized material. The second constituent of the Sudbury Impact Layer consists of macro- to micro-scaled material such as lapilli; devitrified glass, which are sub-categorized as a) vesicular impact glass (DVIG), and b) the rarer tektites and microtektites; planar deformation features (PFDs) in shocked quartz grains; and glass spherules.

Accretionary lapilli and armoured lapilli have a spherical to slightly elongated shape, and in some cases are abraded and irregular. The lapilli range from fairly uniformly grey accreted grains to ones with alternating dark-gray thick bands with thinner bands of very fine black amorphous material (Addison et al., 2010). Some of the accretionary lapilli are cracked in half and display concentric banding of layers that vary in width, all of which surround the primary core. The accretionary lapilli found in this study range in size from 1.0mm to 25mm in diameter. Figures 3-7 all display various lapilli.

Figure 3. (Upper) Lapilli embedded in ejecta matrix in the field.
Figure 4. (Lower) Various sizes of lapilli.
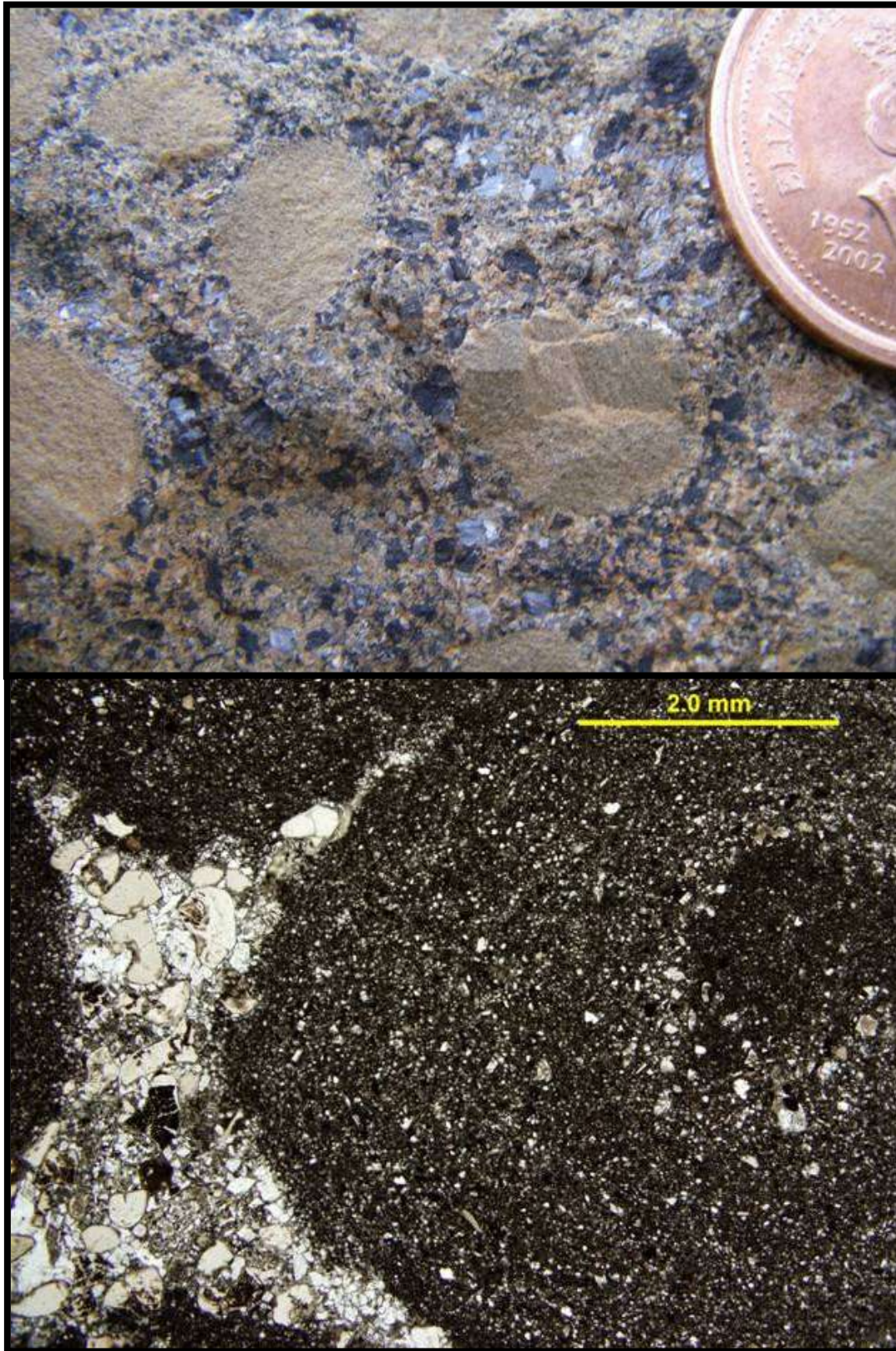
Figure 5. (Upper) Fine-grained dark lapilli in the field, surrounded by ejecta material and cement.
Figure 6. (Lower) Photomicrograph of banded accretionary lapilli with defined core.

Devitrified vesicular impact glass (DVIG) is usually irregularly shaped and ranges in size from 1-2mm and can be up to 5cm. Vesicles in DVIG that were once void space are now usually infilled with carbonate, mostly calcite. Vesicles are commonly round to ovoid, and vary in size (Addison et al., 2005). Microtektites and tektites are difficult to identify because their internal composition has been compromised with replacement by carbonate, therefore the only factor for identification is searching visually for the splash-form shape, which is difficult to observe without any more evidence (Addison et al., 2010). Figures 7 and 8 display devitrified glass in the field, figures 9 and 10 in thin section.

Figure 7. (Upper) Devitrified glass in blocky calcite cement in fieldsite.
Figure 8. (Lower) Devitrified glass in blocky calcite cement in fieldsite.
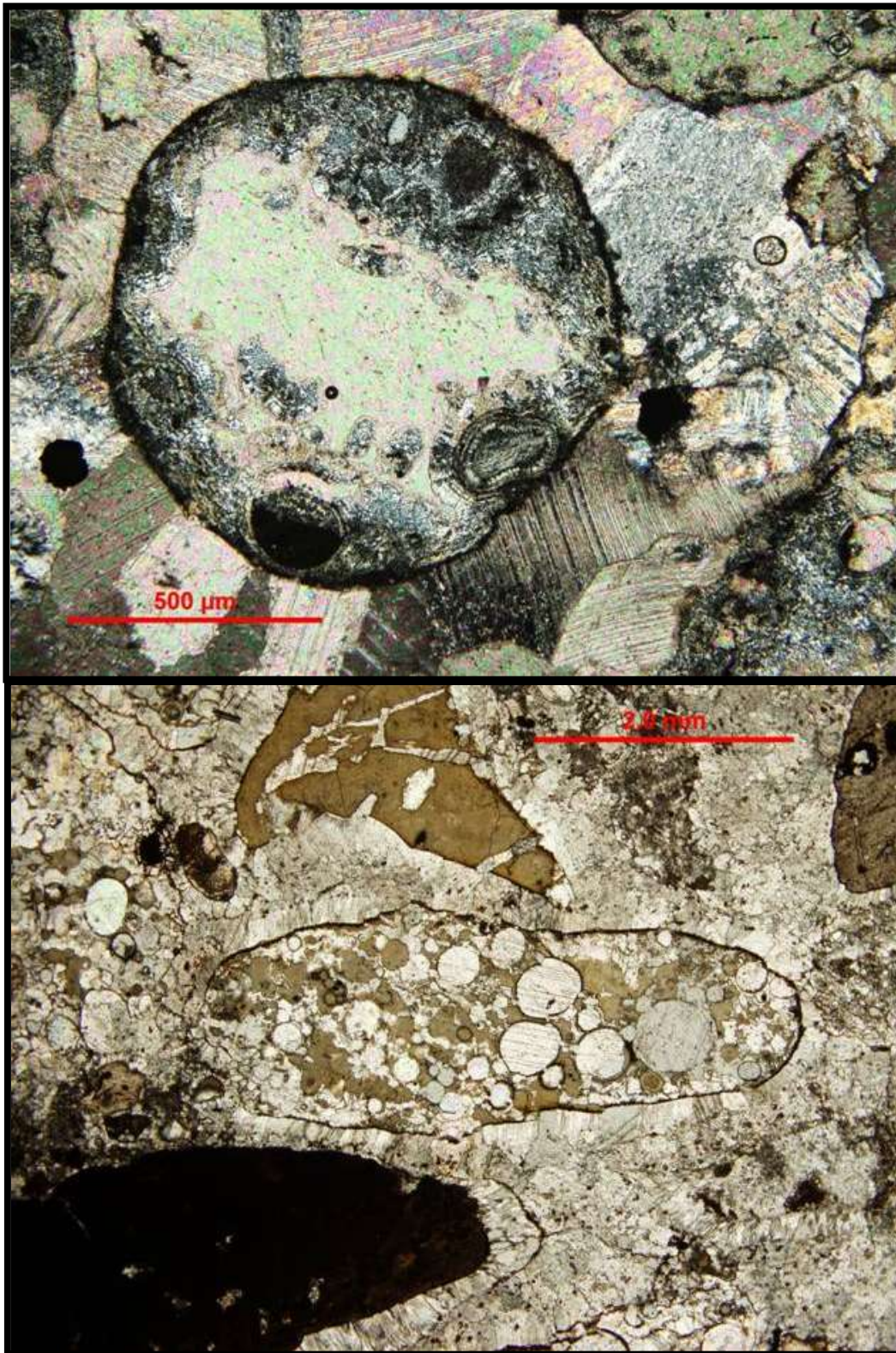
Figure 9. (Upper) Photomicrograph of devitrified vesicular impact glass with vesicles (cross polarized light).
Figure 10. (Lower) Photomicrograph of vesicular glass of tektite-shape (plane polarized light).

Planar Deformation Features (PDFs) as defined by French (1998) are formed when a high velocity impact occurs and "ladders" a mineral such as quartz along a plane(s) of weakness. So far, up to three "ladder" sets have been observed in quartz crystals. Figure 11-12 displays PDFs in a shocked quartz crystal.
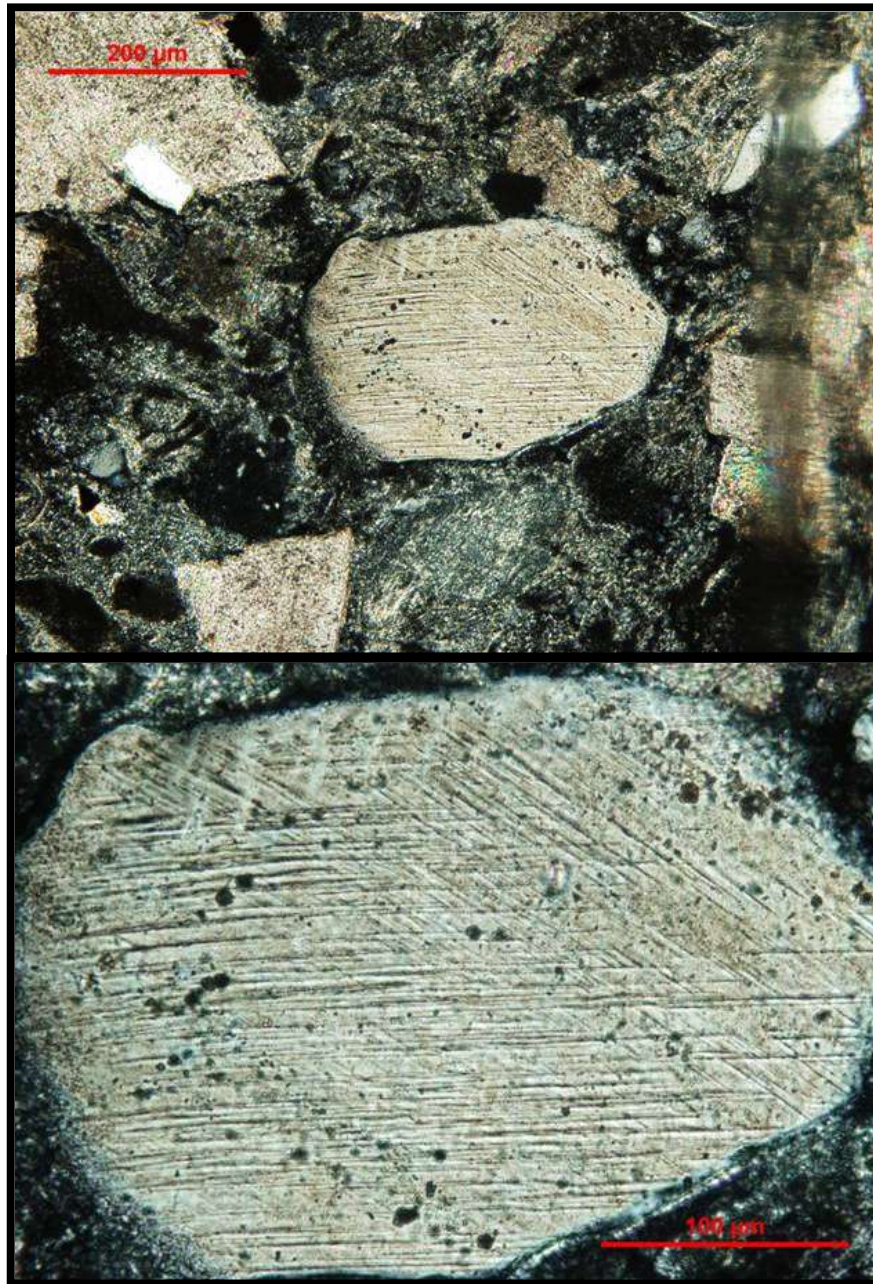
Figure 11. (Upper) Photomicrograph of shocked quartz crystal in cross polarized light with two sets of PDFs (sample supplied from JN set, core BP99-2 from Steve Kissin).
Figure 12. (Lower) Photomicrograph of close up of same shocked quartz crystal in cross polarized light (sample supplied from JN set, core BP99-2 from Steve Kissin).

Features known as spherules have been found in the Sudbury Impact Layer. These spherules range in size from the macro-scale to granular-sized material of about 100μm to 1mm in width. Some spherules have a single-walled silica rim, while others have a double-walled silica rim (Figure 13-15). While some spherules are hollow like a bubble, some are infilled with carbonate (Figure 14), while other spherules are composed entirely of silica (Figure 16). Some solid spherules display an 'LP record' look to them (Figure 17). Spherules can be free-floating, individually present alongside cements such as dolomite (Figure 18), or more commonly spherules are fused together in clusters (Figure 19). There is another complex spherule feature named the sphere-in-sphere feature (Figure 20) where a large spherule has many smaller spherules in one unit.

In many spherulic structures, the glass that originally occupied the structure has been devitrified or replaced by another mineral, due to the unstable nature of glass. It is important to note that many of the silica glass droplets have since been replaced by other minerals, but a large number still contain the silica rims, but rarely the centers (Figure 21).
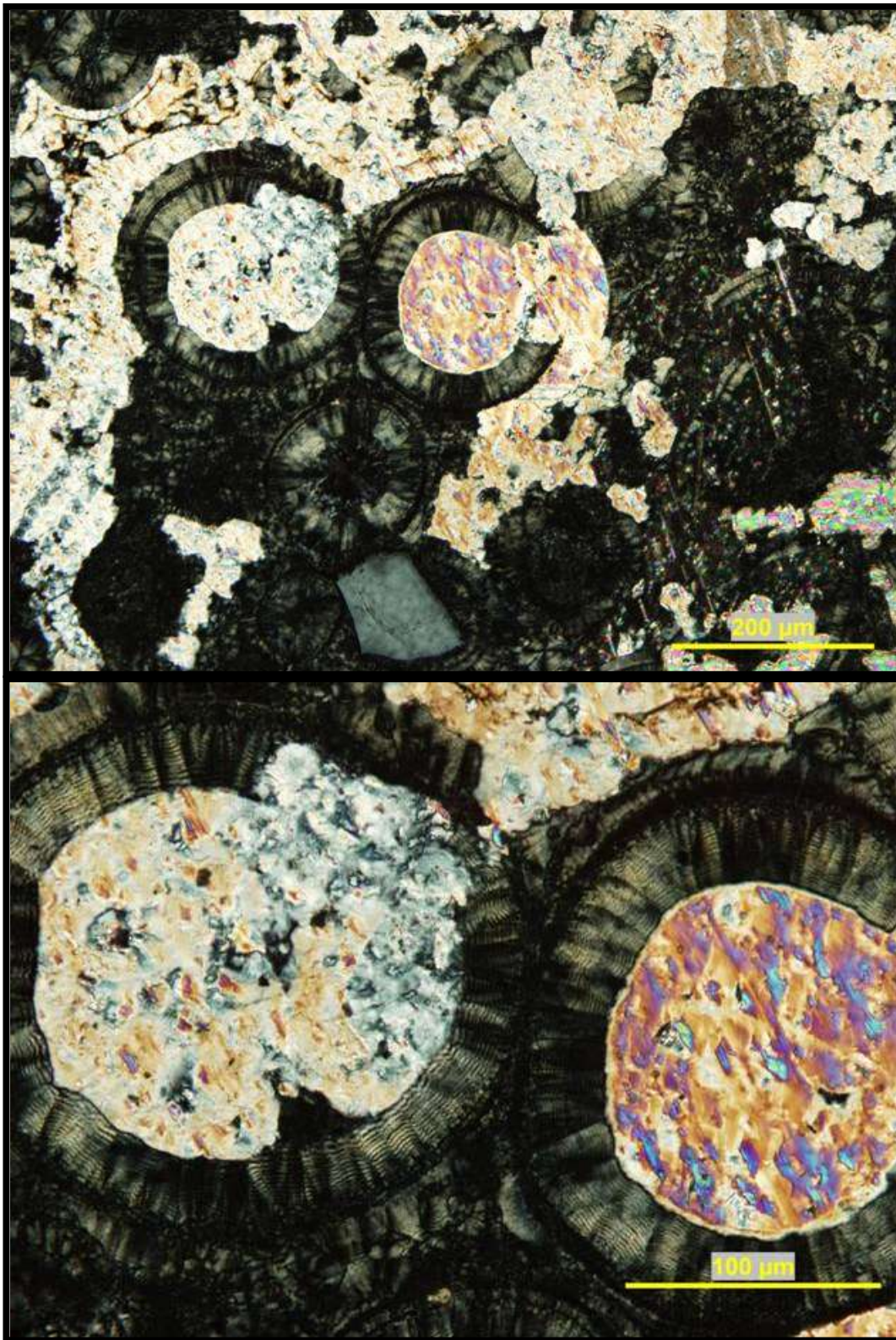
Figure 13. (Upper) Spherules with double-walled silica rims with hollow centers that have been infilled with carbonate (cross polarized light).
Figure 14. (Lower) Spherules with finely banded, double-walled silica rims (cross polarized light).
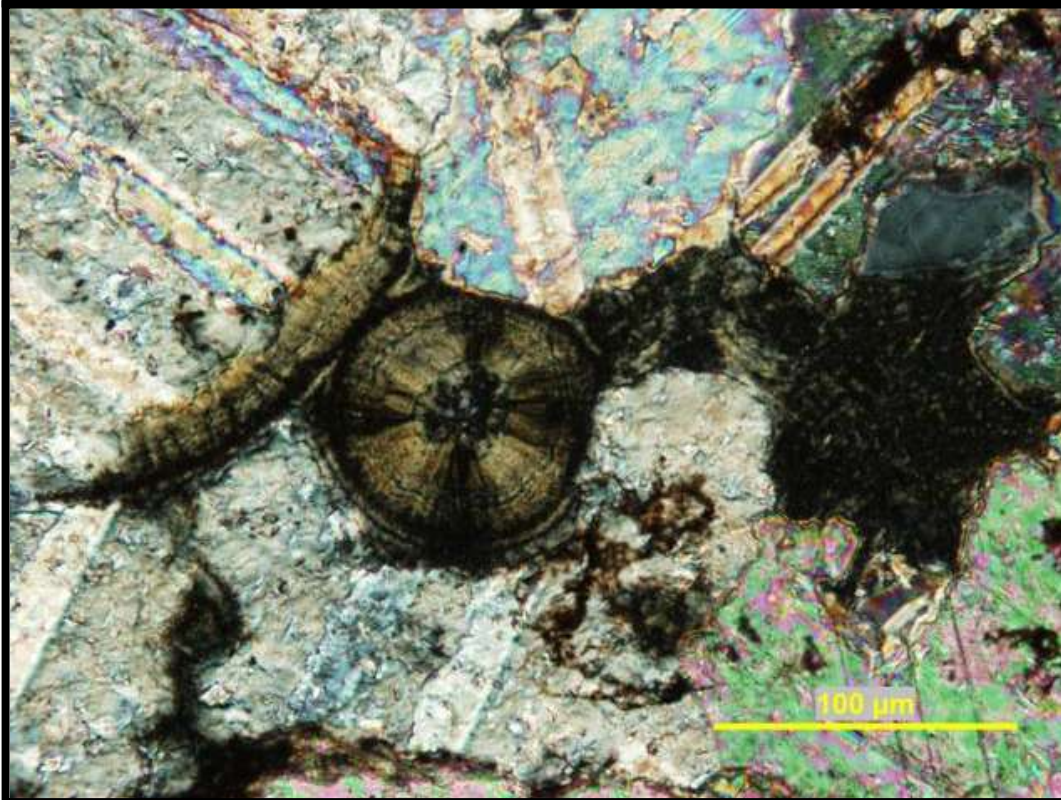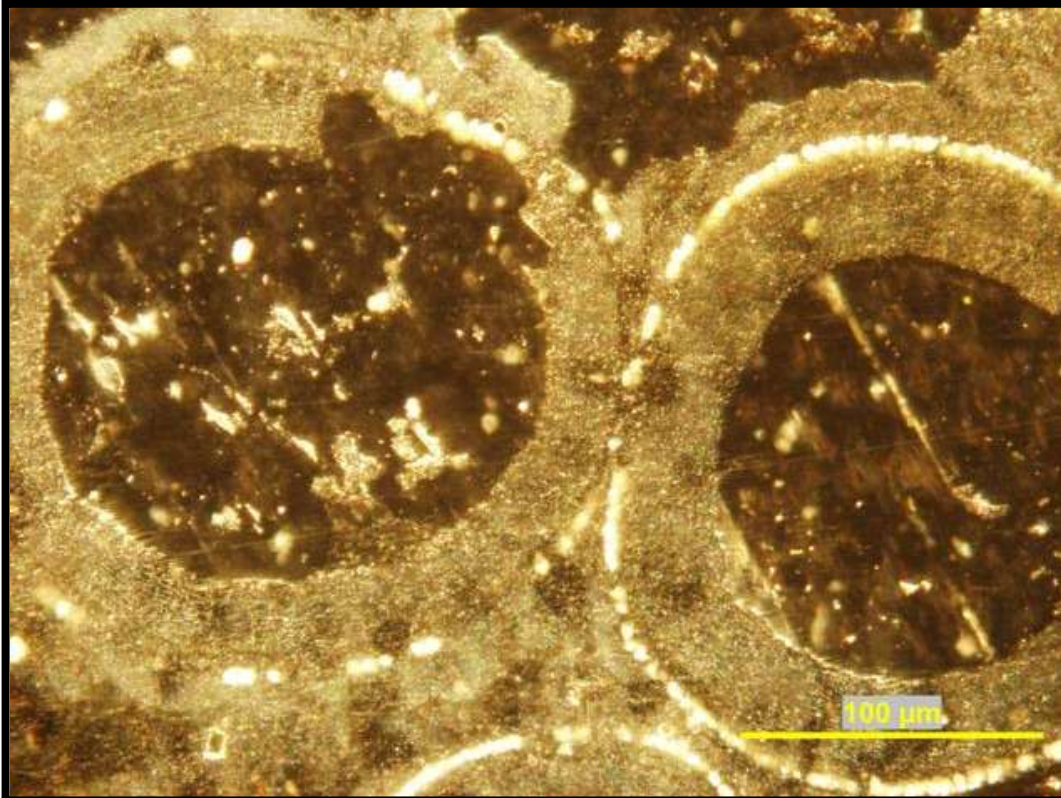
Figure 15. (Upper) Double-walled spherule in reflected light with metalloid substance surrounding the outer rims of the spherules (rl).
Figure 16. (Lower) Solid banded spherule (xpl).
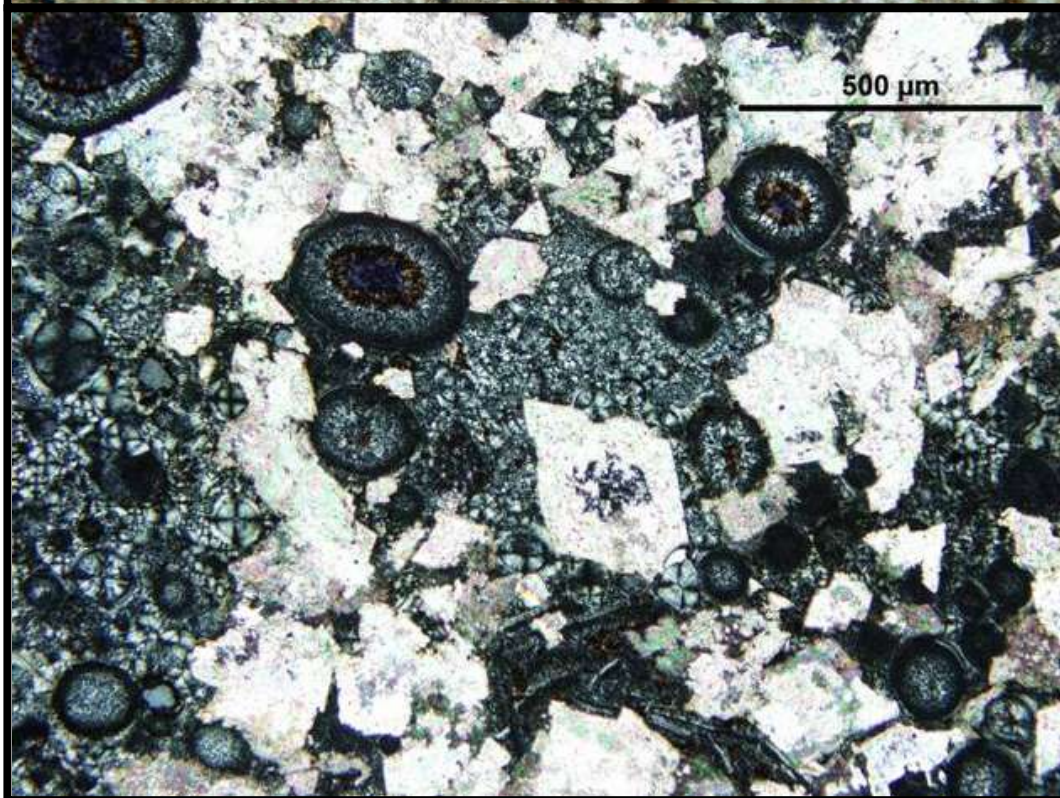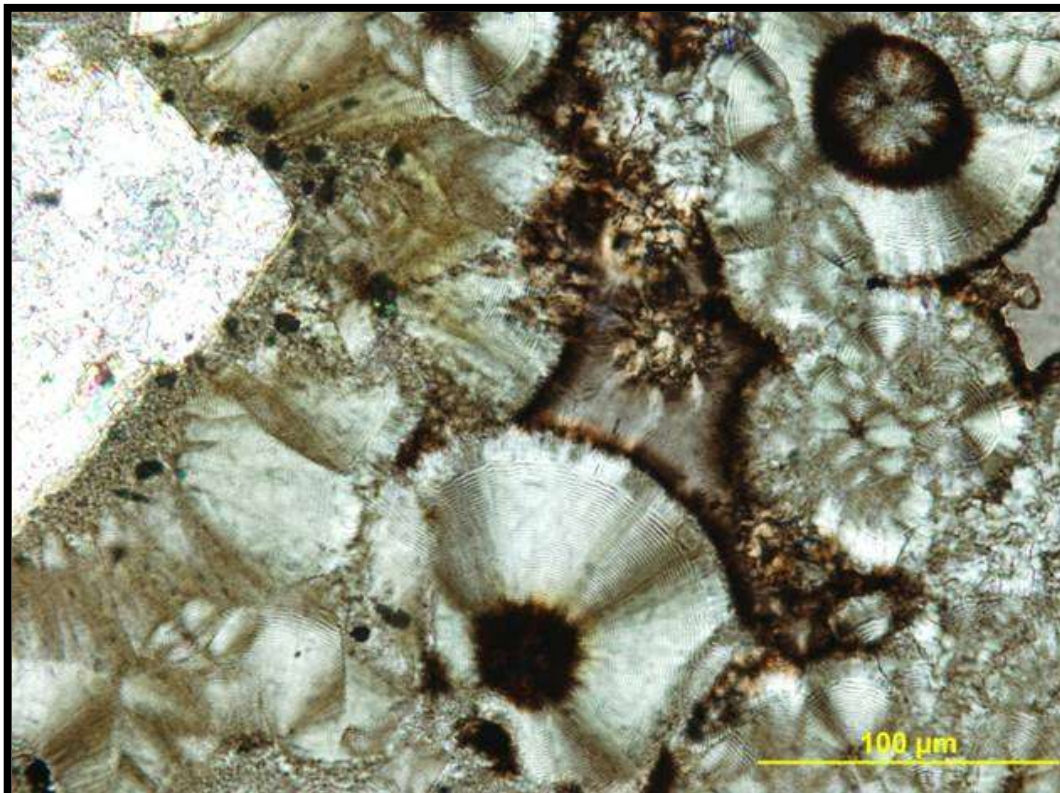
Figure 17. (Upper) Photomicrograph of 'LP record' solid silica spherules (ppl).
Figure 18. (Lower) Photomicrograph of individual spherules with thick rim. Rhomboid dolomite overgrowth present (xpl).
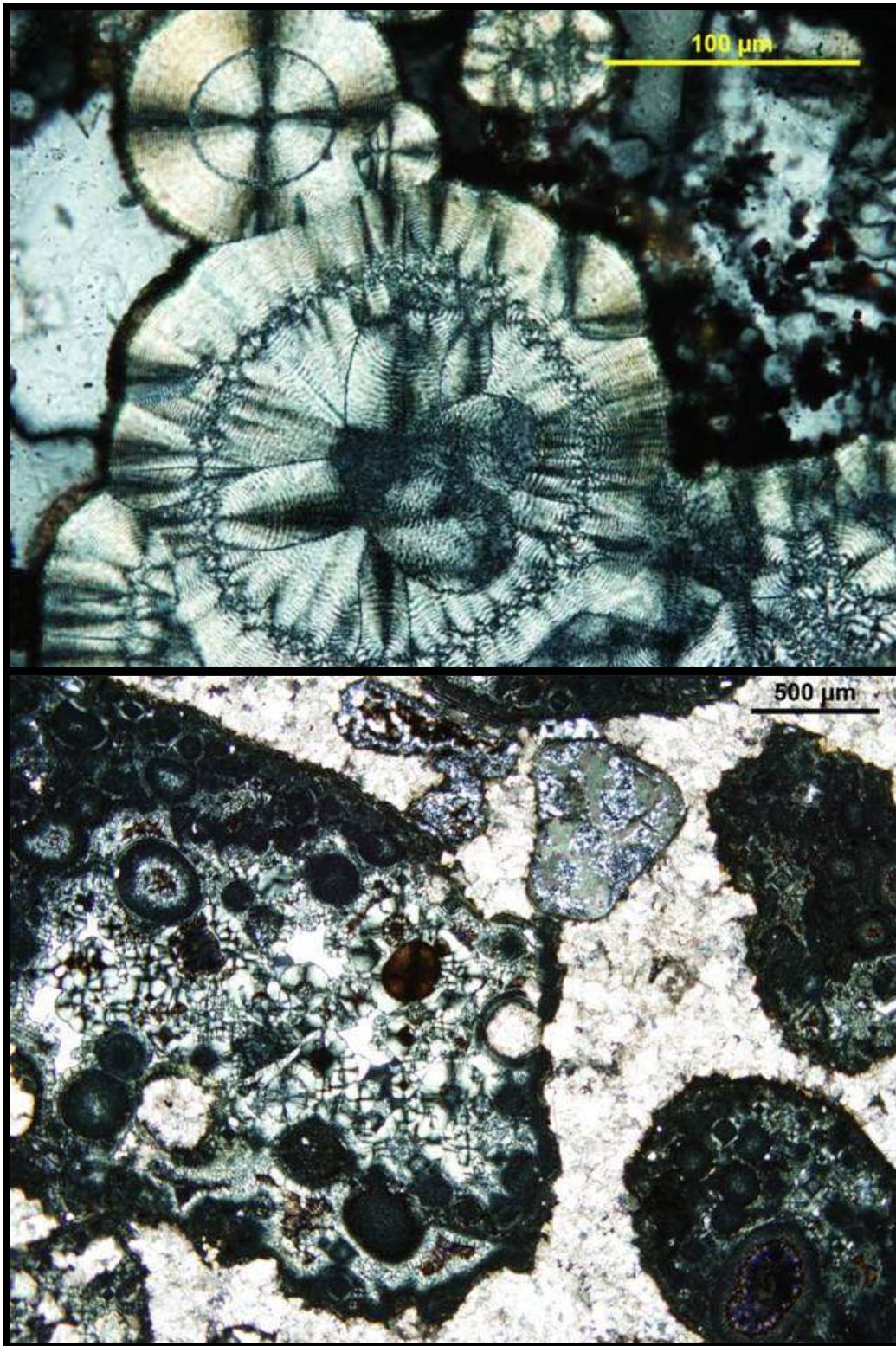
Figure 19. (Upper) Photomicrograph of closeup of sphere-in-sphere features. Note intricate silica design comprising spherules (ppl).
Figure 20. (Lower) Photomicrograph of sphere-in-sphere feature in (ppl).
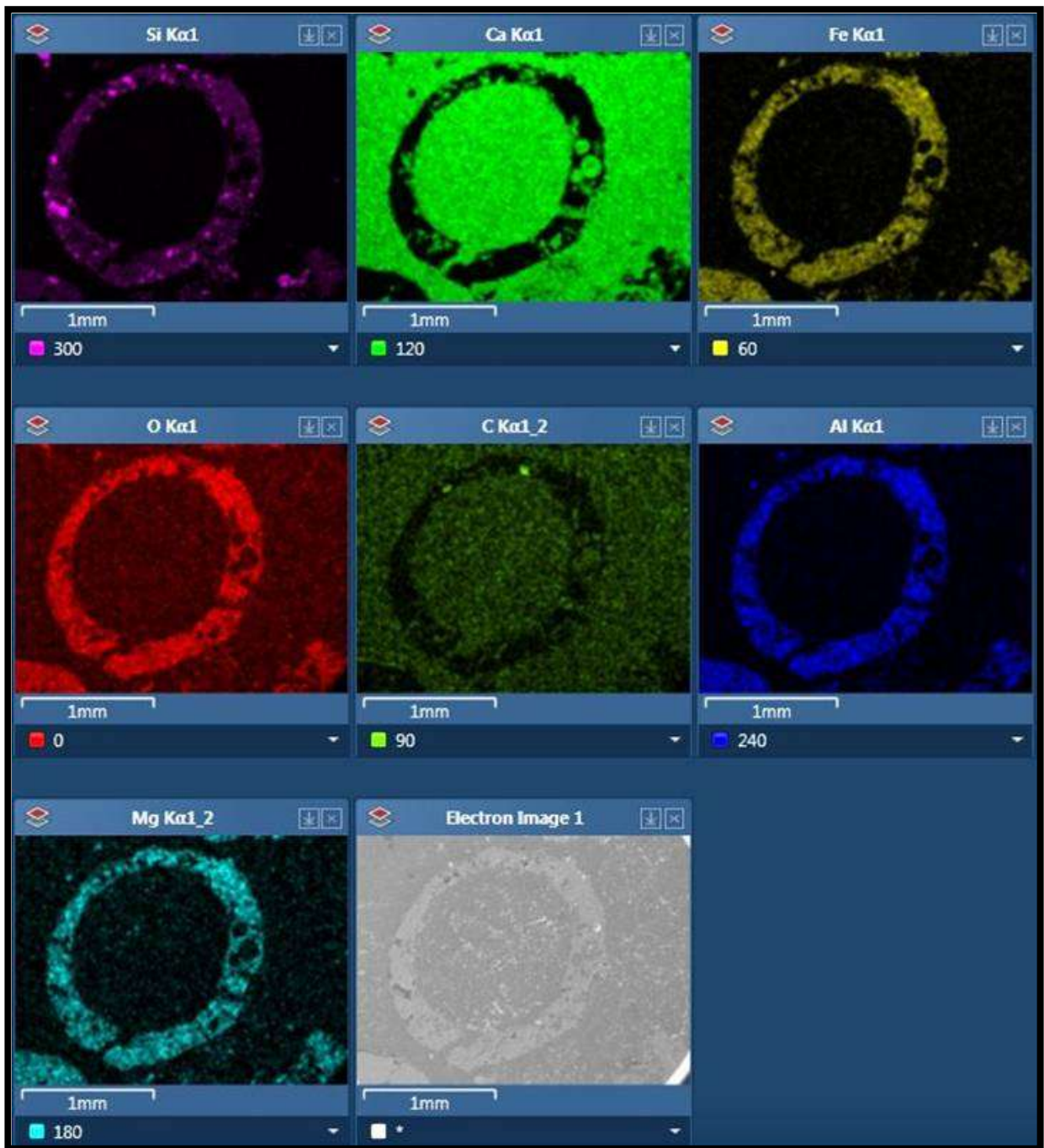
Figure 21. SEM EDS backscatter false colour maps showing major element composition of a spherule.

1.4.1.3   Rove Formation

The Rove Formation that overlies the Sudbury Impact Layer consists of gray siltstone to carbonaceous and pyritic shales and graded medium- to fine-grained, clay-rich sandstone beds, dated at approximately 1832 Ma (Kissin et al., 2003; Addison et al., 2005; Jirsa et al., 2011). The Rove Formation dominates the stratigraphic column above the Gunflint Formation for about 1000 meters, with the carbonaceous shales grading upwards into outbuilding prodelataic, turbidite lobes (Maric and Fralick, 2005).

1.4.2   Geochemistry

Trace element geochemistry was examined in this study to determine if the water that the sediments precipitated from was meteoric (fresh) or marine. Trace element geochemistry was also used to specify the type of environment the sediments were deposited in by determining if and how any available oxygen was utilized in the environment at the time of deposition.

The element enrichments examined in this study include the rare earth elements (REEs), in particular europium (Eu), cerium (Ce), gadolinium (Gd), and yttrium holmium ratios, and other redox sensitive elements, ie. molybdenum and vanadium, which provide a fuller understanding of the depositional environment of sediments at the time, or shortly thereafter during early diagenesis. From the rare earth elements, cerium will supply the most information about oxygen levels in a system.

Redox (reduction-oxidation) sensitive elements, ie. cerium, vanadium, and molybdenum, behave differently when they encounter oxygen. By using these elements, one can pinpoint

where the oxygen is in a depositional system. Apart from cerium where it is soluble when reduced, these redox sensitive elements are virtually insoluble when reduced, and soluble when oxidized. When oxygenated water is enriched with redox-sensitive elements, and this water travels throughout a system, these elements will precipitate when they encounter an area of low Eh. After the reduction reaction, the sediment will then become enriched with the precipitated element making the groundwater depleted of that specific element, causing a negative anomaly.

Europium

Under near surface conditions, the REEs normally have a constant valence of 3+ in their geochemistry (Henderson, 1984). However, europium is one exception which sometimes does not conform to generalized REE behaviour, creating the Eu anomaly (Danielson et al., 1992). Eu anomalies occur when Eu^{3+} is partly reduced to Eu^{2+}. The change in the state of valence determines the behaviour of Eu species because Eu^{2+} differs in size, complex formation, sorption on mineral surfaces, and the incorporation in crystals compared to the other REEs (Danielson, 1992). Reduced europium is roughly the same atomic size as calcium in the +2 state and europium can easily substitute for calcium in a system because of the similarity in size and charge of the two ions. Europium can substitute in calcium-rich plagioclase feldspar very easily because of this. Basaltic oceanic crust contains a large amount of calcium-rich plagioclase feldspar which means that there is an abundance of Eu in the rock because of substitution, making the ocean crust enriched with europium (Danielson et al., 1992). Hydrothermal solutions can provide the reduction potentials necessary for maintaining Eu reduction. Mathematical calculations achieved by Sverjensky (1984), as well as experimental data of Bilal (1992), have shown that the Eu redox potential is very strongly temperature dependent. Therefore,

hydrothermal solutions in excess of 250°C are capable of leaching reduced Eu from the basaltic ocean crust (Danielson et al., 1992).

When magma chambers in the oceanic crust heat downward percolating seawater, the hot fluid will rise up through the crust, to the ocean floor and form hydrothermal vents. In the Precambrian, this type of hydrothermal circulation controlled the chemistry of the ocean (Veizer et al., 1982); therefore, the oceans would have been enriched in europium. Indeed, Precambrian ocean water appears to have had a positive Eu anomaly, whereas Precambrian freshwater had no Eu anomaly (Bolhar and van Kranendonk, 2007).

As shown by Jacobsen and Pimentel-Klose (1988a, b) and Derry and Jacobsen (1990), hydrothermal solutions were the primary source for REE, and the profuse amounts of Eu in Archaean seawater. During the Archaean era, deep ocean water was very oxygen-deficient relative to hydrothermal Fe^{2+} input, which is different than modern ocean water where most of the Fe^{2+} and Mn^{2+} hydrothermally discharged to the deep oceans accumulates proximal to vent sources (Danielson et al., 1992). In the modern system the amount of REEs released into the oceans through hydrothermal alteration does not significantly influence the REE budget of seawater, because the infused REEs are scavenged by precipitating hydroxides near the location of the hydrothermal vents (Ruhlin and Owen, 1986; Olivarez and Owen, 1989). The disappearance of the positive Eu anomaly in the early Proterozoic indicates a decrease in the contribution of high temperature alteration fluids to the marine environment (Danielson et al., 1992) and the growing importance of riverine input in controlling ocean chemistry.

Cerium

The rare earth element cerium can have either a +3 or +4 charge. When cerium is in the +3 state, it is able to go into solution, whereas cerium in the +4 state is insoluble. Soils from various modern climatic zones typically exhibit Ce enrichment, which is commonly attributed to either oxidation of dissolved Ce^{3+} and formation of cerianite (CeO_2), commonly as globules adhering to minerals in Mn oxide-rich areas; or oxidation and scavenging of dissolved Ce^{3+} by Mn oxyhydroxides and possibly Fe oxyhydroxides (Rankin and Childs, 1976; Lei et al., 1986; Marsh, 1991; Koppi et al., 1996; Braun et al., 1998; Bau, 1999; Ohta and Kawabe, 2001; Ji et al., 2004). These types of precipitation processes lead to negative Ce anomalies in both surface water (Sholkovitz, 1995) and groundwater (Smedley, 1991; Braun et al., 1998; Dia et al., 2000; Compton et al., 2003). Because of the sensitivity of dissolved cerium to redox conditions, combined with the stability of REE signatures in calcite (Zhong and Mucci, 1995; Cherniak, 1998; Webb et al., 2009), the use of cerium anomalies as a proxy for Eh has been widespread (Wright et al., 1987; Liu et al., 1988; Murray et al., 1990; Holser, 1997; Bau et al., 1998; Yang et al., 1999; Kamber et al., 2004). Gruau et al. (2004) noted that though oxidized groundwater from upland areas had REE signatures with significant Ce depletion, groundwater from a nearby organic-rich wetland did not. The groundwater from the nearby wetland had a lower redox potential and a humped REE pattern. They concluded that Ce in the oxidized groundwater was fractionated, due to its oxidation to Ce^{4+} and removal either by direct precipitation or oxidative scavenging on the surfaces of Fe and Mn oxyhydroxides forming in the soil.

When a cerium-rich fluid encounters an oxygenated area, cerium will precipitate out as CeO_2 (cerianite), or adsorbs onto iron hydroxides or manganese oxides and creates a positive cerium anomaly. Because the cerium precipitates out of solution, the fluid is depleted in the

element, thus creating a negative cerium anomaly in any precipitates forming from the fluid. Modern groundwater is deficient in cerium because it has precipitated in the sediment during weathering. In the Archaean, the ocean and atmosphere was deficient in oxygen (Cloud, 1972) so Ce^{+3} was not oxidized, while in the Paleoproterozoic at approximately 2.4 Ga there *is* thought to have been approximately 0.5% oxygen in the atmosphere (Holland, 2006) so Ce^{+3} could have been oxidized. Therefore, there is the possibility of a negative cerium anomaly in Paleoproterozoic groundwater, and preliminary work has documented this (Burton and Fralick, 2007), as well as positive Ce anomalies in paleosols of this age (Pan and Stauffer, 2000).

Molybdenum

The redox-sensitive transition metal molybdenum is another element that can indicate an oxygenated or unoxygenated environment and is used as a tracer of oxygen availability in the atmosphere and marine environment (Voegelin et al., 2010). It is a valuable proxy in Precambrian oceanic studies because of its redox-sensitive characteristics which are excellent indicators of local and global redox conditions (Scott et. al., 2008). The use of molybdenum isotopic signatures for paleo-redox reconstruction have indicated increased Mo mobility due to partial oxidation of the atmosphere since around 2.7 Ga (Anbar et al., 2007; Wille et al., 2007; Frei et al., 2009; Duan et al., 2010; Kendall et al., 2010; Voegelin et al., 2010). Molybdenum in oxic seawater is dominantly present as the soluble and highly stable oxyanion, molybdate (MoO_4^{2-}). It has a low chemical reactivity that results in a relatively long residence time in ocean water of around 800 ka (Colodner et al., 1995; Emerson and Huested, 1991). Weathering under oxidized atmospheric conditions oxidizes molybdenum into its soluble oxyanion, molybdate. The low chemical reactivity of molybdate in solution leads to a homogeneous seawater

concentration for the metal (Emerson and Huested, 1991). Because of its long residence time,

molybdenum is one of the most abundant transition metals in today's oceans (Collier, 1985). The

input of dissolved molybdenum into the ocean via rivers is from chemically weathered

continental input. It has been shown that under highly reducing conditions, and in the presence

of H_2S, the molybdenum seawater signature can be amplified in euxinic sediments through

quantitative molybdenum removal from the water column into the sediment by Fe-Mo sulfides

(Siebert et al., 2003; Anbar, 2004; Helz et al., 2011). It is believed that molybdenum enrichment

in euxenic sediments is due to the transformation of the unreactive molybdate (MoO_4^{2-}) to highly

reactive thiomolybdate under elevated levels of dissolved sulphide (Erickson and Helz, 2000;

Helz et al., 1996). Molybdenum is highly enriched in euxinic sediments (Scott et al., 2008),

commonly two orders of magnitude above the average crustal abundance of 1-2 ppm (Taylor and

McLennan, 1995). The modern-day Black Sea serves as an example of Mo-enrichment in

euxinic sediments due to the presence of H_2S-rich waters, organic matter, and/or Fe colloids

(Spencer et al., 1972; Emerson et al., 1979; Eary and Rai, 1989; Pettine et al., 1994; Colodner et

al., 1995; Helz et al., 1996; Morford and Emerson, 1999; Kim et al., 2001; Algeo, 2004; Kim et

al., 2007; Frei et al., 2009; Dossing et al., 2011). Because of the efficient burial of molybdenum

in sulfide-rich environments, Proterozoic oceans with extensively developed sulfidic conditions

underwent a sustained period of time of Mo-associated stress that may have contributed to the

delayed diversification of eukaryotes (Anbar and Knoll, 2002). The existence of a Mo-depleted

Proterozoic ocean was confirmed, but it still remains a mystery if the Mo limitation was

biologically significant (Scott et al., 2008).

Vanadium

Vanadium is more soluble in oxygenated water, and less so in reduced water (Sugiyama, 1989; Shiller and Mao, 1999, 2000), and its solubility can be further increased under oxidizing conditions by its ability to form complexes with sulfate (Wanty and Goldhaber, 1992). This leads vanadium to be removed from solution from oxygenated soil profiles (Marsh, 1991) and to precipitate in a reduced environment. The precipitation of vanadium is enhanced due to a reduction reaction of the vanadate (V) or vanadyl (IV) ion to the plus III state from which it very likely precipitates in association with oxyhydroxides (Hostetller and Garrels, 1962; Northrop and Goldhaber, 1990; Wanty and Goldhaber, 1992). When vanadium is in solution and goes from an oxic environment to a reducing one, its redox chemistry results in a decrease in its solubility (Wehrli and Stumm, 1989; Shiller and Mao, 2000). Northrop and Goldhaber (1990) have shown that vanadium content is directly related to the organic carbon content of the rocks they examined. Using the Colorado Plateau sandstones as an example, organic matter and hydrogen sulfide, created reducing conditions from materials such as bitumen and organic-rich sedimentary rocks. The vanadium in solution spread into the sediments, where it was complexed by tetrapyrrole (Lewan and Maynard, 1982) or forms of vanadyl porphyrins (Premovic et al., 1986; Wanty and Goldhaber, 1992); both of these two compounds are directly derived from chlorophylls. When the vanadium present associated with an oxyhydroxide or complexed with an organic molecule underwent diagenesis, the V was assimilated into chlorite forming in the sediment (Wanty and Goldhaber, 1992).

It is interesting to note that coarse-grained limestone and the stromatolitic unit in the Limestone Member of the Gunflint Formation have high amounts of vanadium (Burton and Fralick, 2007). These authors found a direct correlation of vanadium to organic matter in the

sediment i.e. the microbial colonies of stromatolites. The coarse grainstone has more stromatolitic debris and an overall higher porosity leading to elevated vanadium levels due to more organic material from the microbial constituents. The fine grainstone has less stromatolitic debris and less porosity, leading to lower vanadium levels (Burton and Fralick, 2007). This suggests that vanadium was precipitated in the sediments from fluids that were originally well oxidized to allow the vanadium to become more soluble and go into solution. The vanadium precipitated in the presence of organic matter creating a redox boundary (Burton and Fralick, 2007).

Yttrium and Holmium

Yttrium and REEs are physicochemically very similar, all being trivalent and showing similar ionic radii and electronegativities. Close similarity exists between Y and Ho, which show identical valencies and very similar ionic radii. The geochemical twin Y and Ho remain tightly coupled in many geochemical processes, leading to the maintenance of the chondritic Y/Ho weight ratio of 28 or molar ratio of 52 in common igneous rocks and epiclastic sediments (Bau et al., 1995). In contrast, aqueous fluids and their precipitates are often characterized by non-chondritic Y/Ho ratios. Super-chondritic Y/Ho molar ratios above 90 have been found typical of modern seawater (Zhang et al., 1994). Oceanic distributions of Y most closely resemble those of Ho, as expected from the similarity in their ionic radii (Zhang et al., 1994), but it is important to take note that the differences in Y and Ho geochemical behaviour also results in strong fractionation between the two elements.

There is evidence from Paleoproterozoic iron formations that they precipitated from seawater that showed elevated, non-chondritic Y/Ho ratios (Bau and Dulski, 1996b; Bau et al., 1997b). However, REE elemental and Nd isotopic studies have shown that a significant fraction of the REEs in these waters were of mantle origin and supplied to seawater by black smoker-type, high temperature hydrothermal activity (Dymek and Klein, 1988; Jacobsen and Pimentel-Klose, 1988a, b; Derry and Jacobsen, 1990; Danielson et al., 1992; Alibert and McCulloch, 1993; Bau et al., 1997b). Bau and Dulski, (1998) state that since the removal of the REEs by precipitating Fe-oxyhydroxides was absent from Precambrian anoxic deep ocean basins, hydrothermal rare earth elements and yttrium could collect in the deeper areas of the layered Precambrian oceans. They state that the elevated Y/Ho ratios of the seawater from which the Precambrian iron formations were formed can only be provided by surface waters not affected by high-temperature hydrothermal input.

The nutrient-like distributions of Y and Ho throughout the ocean shows that their distributions are strongly governed by biogeochemical processes. The most important fractionation step of Y and Ho takes place during the removal from the surface of the ocean by scavenging particulate matter (Nozaki et al., 1997). There are several mechanisms of Y and Ho fractionation, including weathering, different solution complexation, and phosphate salt solubilities, which are possible causes of Y enrichment relative to Ho in seawater according to Bau et al. (1995). Bau et al. (1995) also suggest that the largest fractionation step may possibly occur outside the ocean, in rivers and estuaries, but is less sufficient compared to the oceanic Y/Ho abundancy. Also, the carbonate complexation stability constant of Y resembles that of Tb and is similar to that of Ho (Liu and Byrne, 1995). The complexation behaviour of Y with the soft organic surface of particulate matter is similar to that of LREEs (Lee and Byrne, 1993) therefore it is very likely that Y deviates markedly from Ho and other REEs due to the

aggressive reactions during scavenging by particulate matter. Thus, the Y/Ho ratio gives an indication of the amount of fractionation these two elements have undergone relative to one another from their chondritic ratio of approximately 28.

1.5 Methodology

1.5.1   Rationale

The general rationale behind this study was to collect and analyze samples taken from different lithologies in each outcrop and drillcore to determine the depositional environment and the types of fluid that precipitated the chemical sediments and cement.

1.5.2   Analytical Methods

All analyses of rock samples were conducted at Lakehead University in Thunder Bay, Ontario, Canada. These analyses included whole rock digestion procedures, which entailed treating 0.5g of sample in Teflon beakers with acids over five days. First the CO_2 was removed with a weak nitric acid solution, then, after heating to dryness three treatments with concentrated hydrofluoric and nitric acid were conducted. On the fifth day samples were dissolved in a 2% nitric acid solution and diluted 200x for the ICP-AES (Inductively Coupled Plasma Atomic Emission Spectrometry) for determination of major, minor, and trace elements using a Varian Vista Pro Radical ICP-AES for analyses. Solutions were also diluted 1000x for the ICP-MS (Inductively Coupled Plasma Mass Spectrometry) for determination of rare earth elements, Y and Mo using a Perkin-Elmer Elan DRC-e for analyses. The solutions were sent to the Lakehead University Instrumentation Laboratory (LUIL) for analysis. A blank was run for every three

samples. U.S.G.S. standard basalt and quartz latite, plus in house ankerite grainstone and limestone standards, were analyzed to measure accuracy. Duplicates were measured to gauge precision. Both accuracy and precision were within acceptable limits, i.e. less than 15% error for accuracy of ICP-AES measurements, less than 10% error for accuracy for ICP-MS data, and precision errors less than 5%. As the anomalous concentrations in this study are commonly an order of magnitude higher than expected values these errors are within acceptable limits. Lower detection limits were taken as three times the average blank concentration for an element.

X-Ray diffraction (XRD) was utilized for a few powdered rock samples to determine the crystal structure using a Panalytical Xpert Pro Diffractometer for analyses. Transmitted and reflected light optical microscopy was utilized for visual mapping, mineral identification, and photographing thin sections using an Olympus IX51 Microscope with digital camera. Scanning electron microscopy (SEM) was utilized to analyze carbon-coated polished thin sections and discs for mineral composition by using X-ray mapping and Backscatter Electron image using 20.0kV at 15.0mm x50, using a Hitachi Su-70 Schottky Field Emission SEM.

2   Lithofacies and Geochemistry of Outcrops

2.1   Harbour Expressway (HEW)

2.1.1   Lithofacies Description

The Harbour Expressway fieldsite is located directly south of the Trans-Canada Highway approximately 1.6km east of Mapleward Road. This fieldsite has previously been discovered prior to this study, but has been extensively cleaned, swept and looked at for the purpose of this thesis. The first outcrop examined (HEW Plaque) is located at UTM coordinates 27185E and 63242N 16 N NAD 83. This outcrop contains a 60cm by 40cm silica plaque (a localized abnormal patch on a surface)-like area of 2-3cm sized white and yellow-tinged circular crystal features, coined as "flowerettes" by the author, due to their radial flower-like shape (Figure 22). Figure 23 shows the flowerettes which consist of a brownish 2-4mm circular cryptocrystalline core around which are radiating white quartz crystals that appear to feather out towards the edges. The white quartz crystals are in turn surrounded by the same brown cryptocrystalline quartz banding, approximately 2-4mm thick, capping each flowerette. This capping can be seen both in plan view (Figure 24) and lateral view (Figure 25). In lateral view, each flowerette that is surrounded by the brown cryptocrystalline material is surrounded by more white quartz crystal growth, which sits upon a 2-3mm band of the same cryptocrystalline material as the cores are composed of. This sits directly above approximately 1cm of lath-like white quartz crystals. Directly below these white quartz lath-like crystals, is another 2-3mm layer of brown cryptocrystalline material at the base of this unit. The thickness of the flowerette plaque is variable between different areas, but it approximately measures 3-3.5cm thick. It is possible that the top of this layer was eroded through subaerial exposure. Figures 26 and 27 are photomicrographs of the silica flowerette plaque in lateral view. They show the various growth phases of the formation.

Directly beside the plaque, is what is described as a double-walled lath-like crystal growth (Samples HEW3A □) (Figures 28, 29). There, two distinct and separate crystal bands grew, either one right after the first, or right into each other from opposite walls. Each crystal growth band is approximately 0.7-9mm wide. It appears that these double-walled features prohibited the growth, or spreading, of the flowerette plaque because the edges of the plaque seem to contour the double-walled features.

Abruptly beneath the flowerette plaque, is a layer of intergrown botryoidal features (Figures 30, 31) that display intergrown lath-like crystals, the same in appearance to a rosette crystal habit. These botryoidal rosettes have been determined to be composed of calcite (Sample HEW2 ▲) from ICP-AES results (See Table 1). When exploring the area, strike and dip measurements were taken to deduce that the S.I.L. (Figure 32) is directly underneath the botryoidal rosette layer. The Sudbury Impact Layer consists of rip-up pieces of the underlying rocks. Figure 32 also shows a 1.5cm green-coloured pebble, similar to the green material found in the impact layer at many other locations. Throughout the rock underlying the botryoidal carbonate features, black chert veining is common (Sample HEW4 ■) (Figure 33). Moving further away from the flowerette plaque, a chalky material (Sample HEW5 ◇) and fine granular carbonate crystals that have a chicken-wire structure (Samples HEW6 ◆ and HEW7 ⬡) (Figure 34) are present in the outcrop. Another outcrop in the field where the previous ones are located contained siliceous radiating crystals in the ankerite groundmass. Some of these had the habit of twinned swallowtail gypsum crystals (Figure 35).

Figure 22. (Above) Plan view of HEW Plaque outcrop.
Figure 23. (Below) Close up of silica flowerettes consisting of brownish 2-4mm circular cryptocrystalline cores surrounded by radiating white quartz crystals that feather out towards the edges.

Figure 24. (Above) Close up and texture of silica flowerettes.
Figure 25. (Below) Side view of silica flowerette sample.
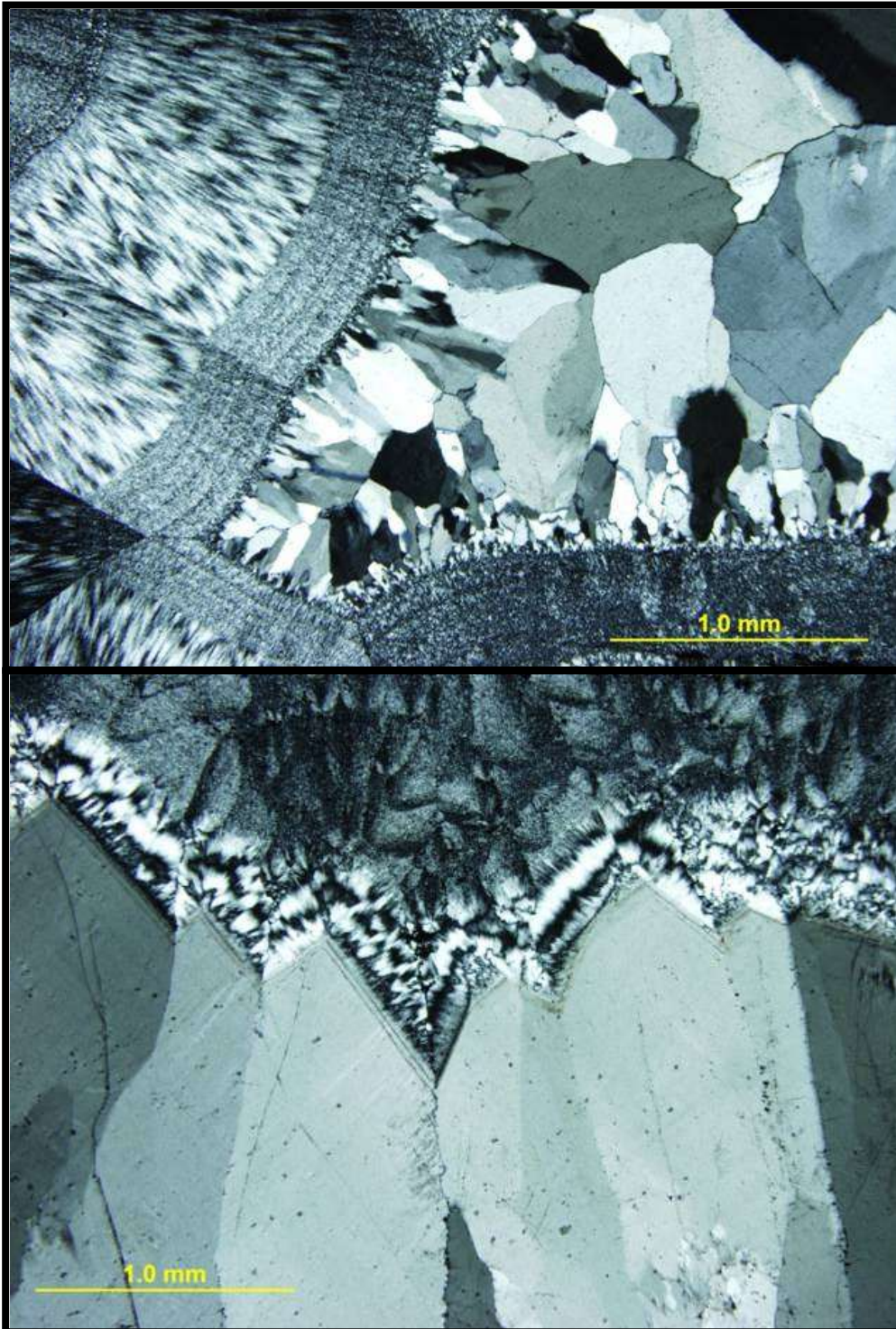
Figure 26. Photomicrograph of silica flowerettes in lateral view showing feathered-like crystals, with cryptocrystalline banding around crystal growth (xpl).
Figure 27. Photomicrograph of silica flowerette in lateral view showing lath-like crystals (xpl).

Figure 28. (Above) Double-walled lath-like crystals growing alongside the edges of the HEW Plaque outcrop.
Figure 29. (Below) Close up of double-walled veins.
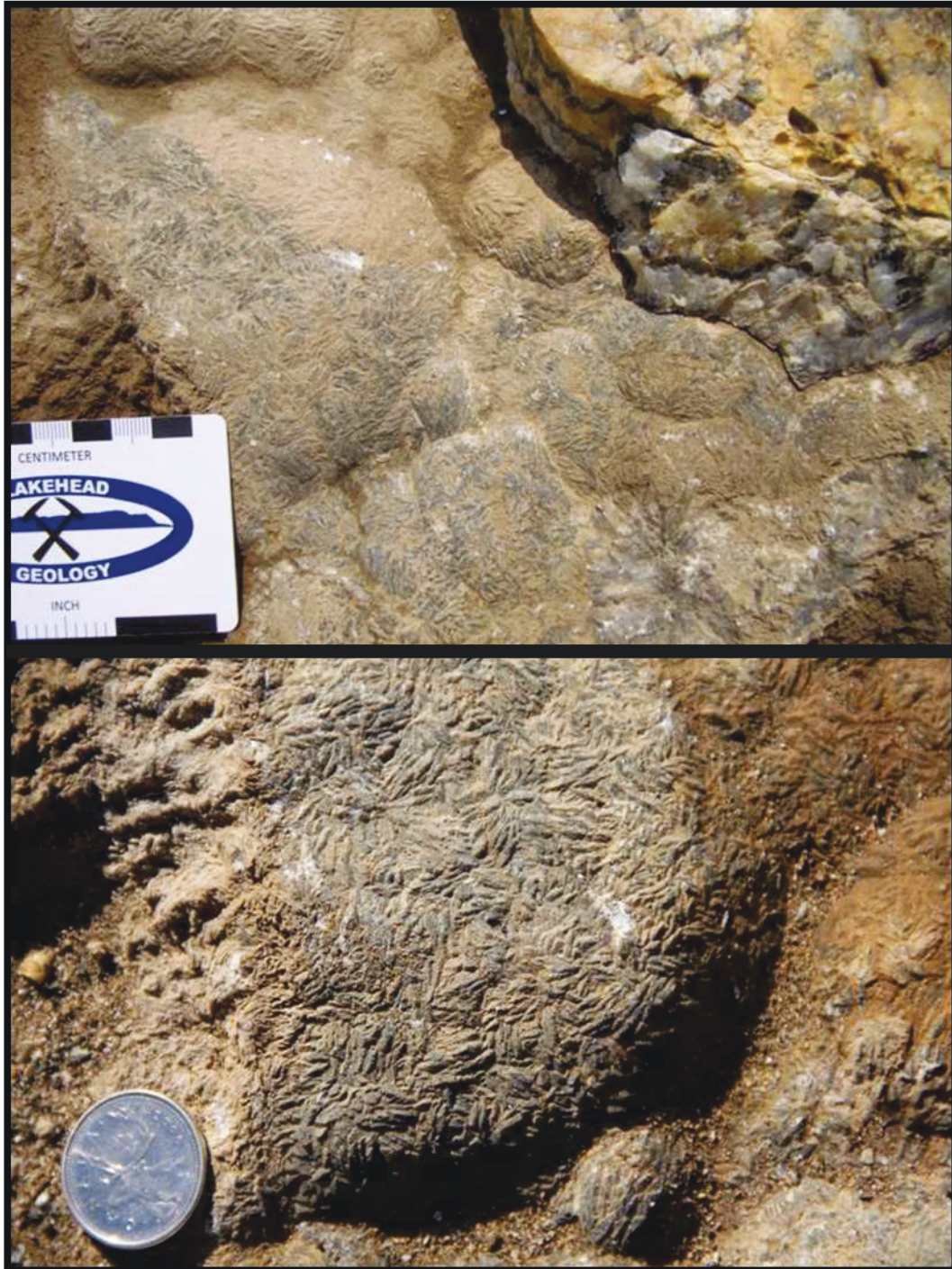
Figure 30. (Above) Intergrown botryoidal features resembling rosettes composed of calcite directly underlying the silica flowerette plaque.
Figure 31. (Below) Close up of botryoidal rosettes displaying lath-like crystals.

Figure 32. (Above) Sudbury Impact Layer that directly underlies the botryoidal layer. The S.I.L. consists of rip-up pieces of the underlying rocks. The S.I.L. also shows a 1.5cm green-coloured pebble, similar to the green material found in the impact layer at many other locations.
Figure 33. (Below) Black chert veining is present throughout the rock underlying the carbonate botryoidal features.

Figure 34. (Above) Fine granular crystal material featuring a chicken-wire texture underlies the botryoidal features. The fine granular material appears to be located farther away from the silica flowerette plaque.
Figure 35. (Below) Silica rosette with a large (3cm) crystal showing the typical shape of a twinned swallowtail gypsum crystal. Sample courtesy of Mr. Greg Brumpton.

The second outcrop logged at the HEW site is the cliff face (HEW Cliff Face) at the southwestern side of the fieldsite located at UTM coordinates 327003.71E and 5363189.13N 16 N NAD 83. Figure 36 is a stratigraphic representation of HEW Cliff Face and Figure 37 is the outcrop photo. Starting at the bottom of the cliff face is a 15cm unit of lenticular-bedded facies composed of thin layers of fine-grained hematitic chert grainstone with thin layers of shale between them (Figure 38). Following this, is a 6cm fine-grained hematitic grainstone lens. This is followed by another 12cm of cherty hematite lenticular-bedded material. Sitting on top is a 7cm fine-grained hematitic grainstone layer. Overlying the grainstone layer, is 51cm of the lenticular-bedded cherty hematite grainstone (HEW18 ◆ is taken from this unit), followed by a fine-grained hematitic grainstone lens approximately 6cm thick (Figure 39). Again, the lenticular-bedded material is present and measures approximately 26cm thick, followed by another 8cm thick fine-grained grainstone lens (HEW19 ▽) but this time rip-ups are present in the lens (Figure 40). Overlying this unit is approximately 440cm of the hematitic chert to cherty hematite lenticular-bedded material, with layers no thicker than 3cm (HEW20 ▼ and HEW21 ⬡ are taken from within this unit). Another 100cm of lenticular-bedded material rests on top, near the top of the cliff face, but this unit is badly silicified (HEW22 ⬡ is taken from within this unit). The Sudbury Impact Layer resides right on top of the silicified areas, and has an approximate thickness of 250cm. It consists of broken pieces of the underlying lenticular bedded facies, broken limestone stromatolites (Figure 41), and ejecta material that consists of devitrified glass, surrounded by white blocky calcite cement (Figure 42). Samples HEW11-17 are taken from the Sudbury Impact Layer on the top of the cliff face hill. HEW11 ☆ consists of a sample of a stromatolite, HEW12 ★ is a sample of ankeritic cement, HEW13 ✛ is a sample of calcite cement, HEW14 ✛ is another sample of blocky calcite cement for quality purpose testing,

HEW15 ⨯ another stromatolite from top of the hill, HEW16 ⨯ is a sample of the contact

between a stromatolite and the S.I.L., and HEW17 ◇ is a sample of ankeritic cement 7 meters

downhill from the top of the cliff.

Figure 36. Stratigraphic Representation of Harbour Expressway Cliff Face

46

6

HEW22 ⬡ Fine-grained silicified
grainstone

HEW21 ⬡ Fine-grained grainstone

5

4

3 — HEW20 ▽ Shale

2 —

HEW19 ▽ Fine-grained grainstone lense

1 —

HEW18 ◆ Fine-grained hematitic grainstone
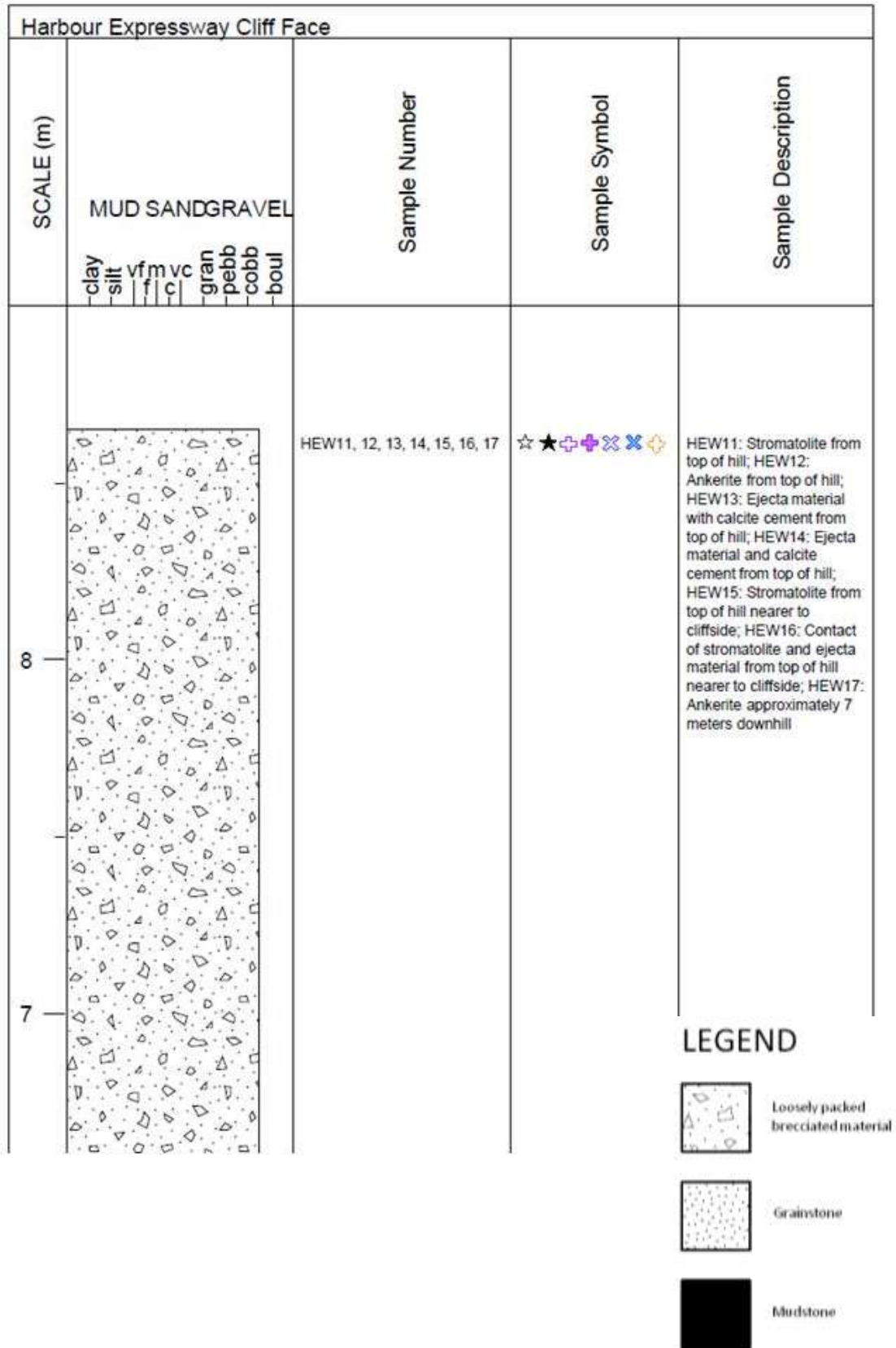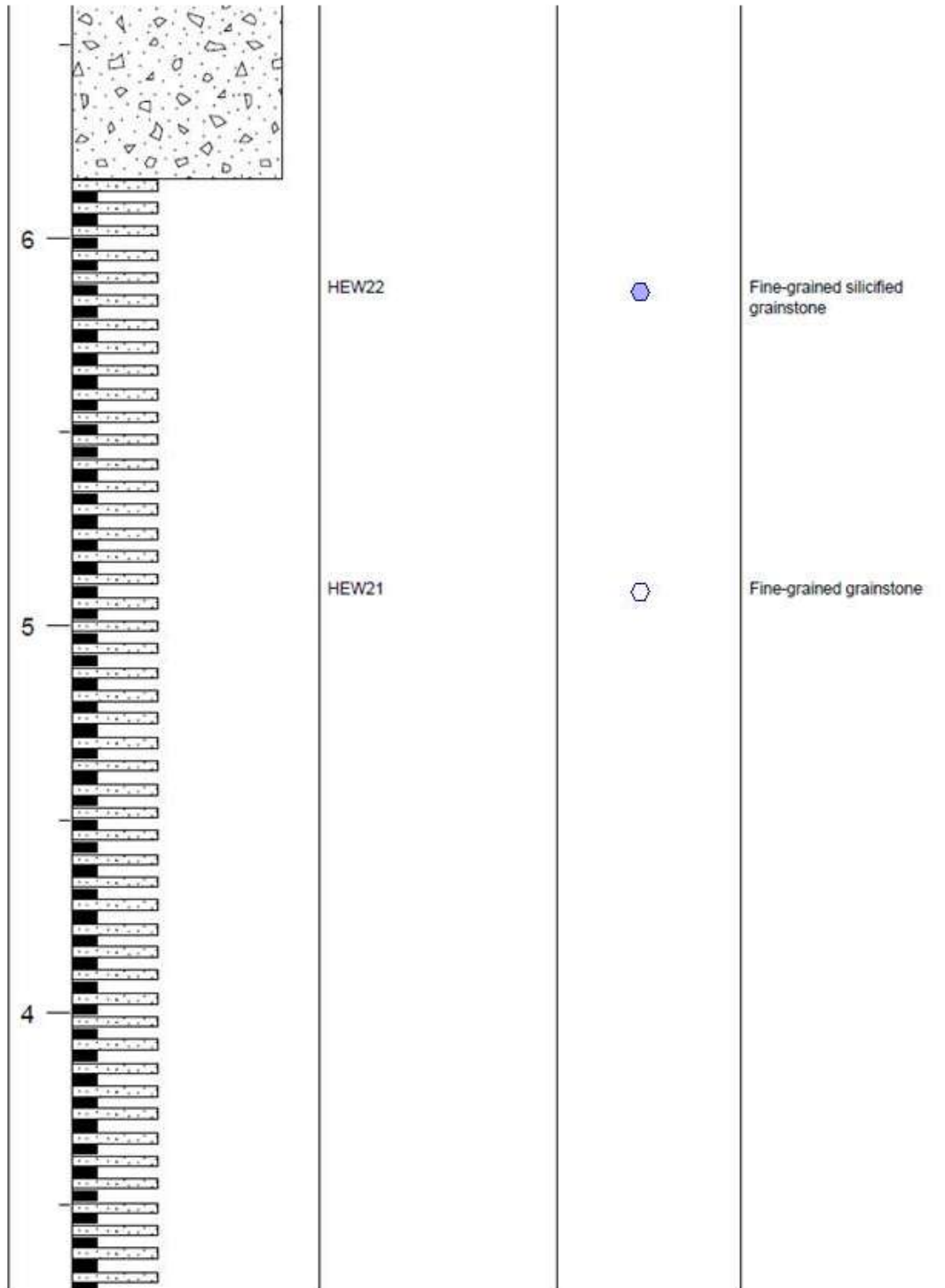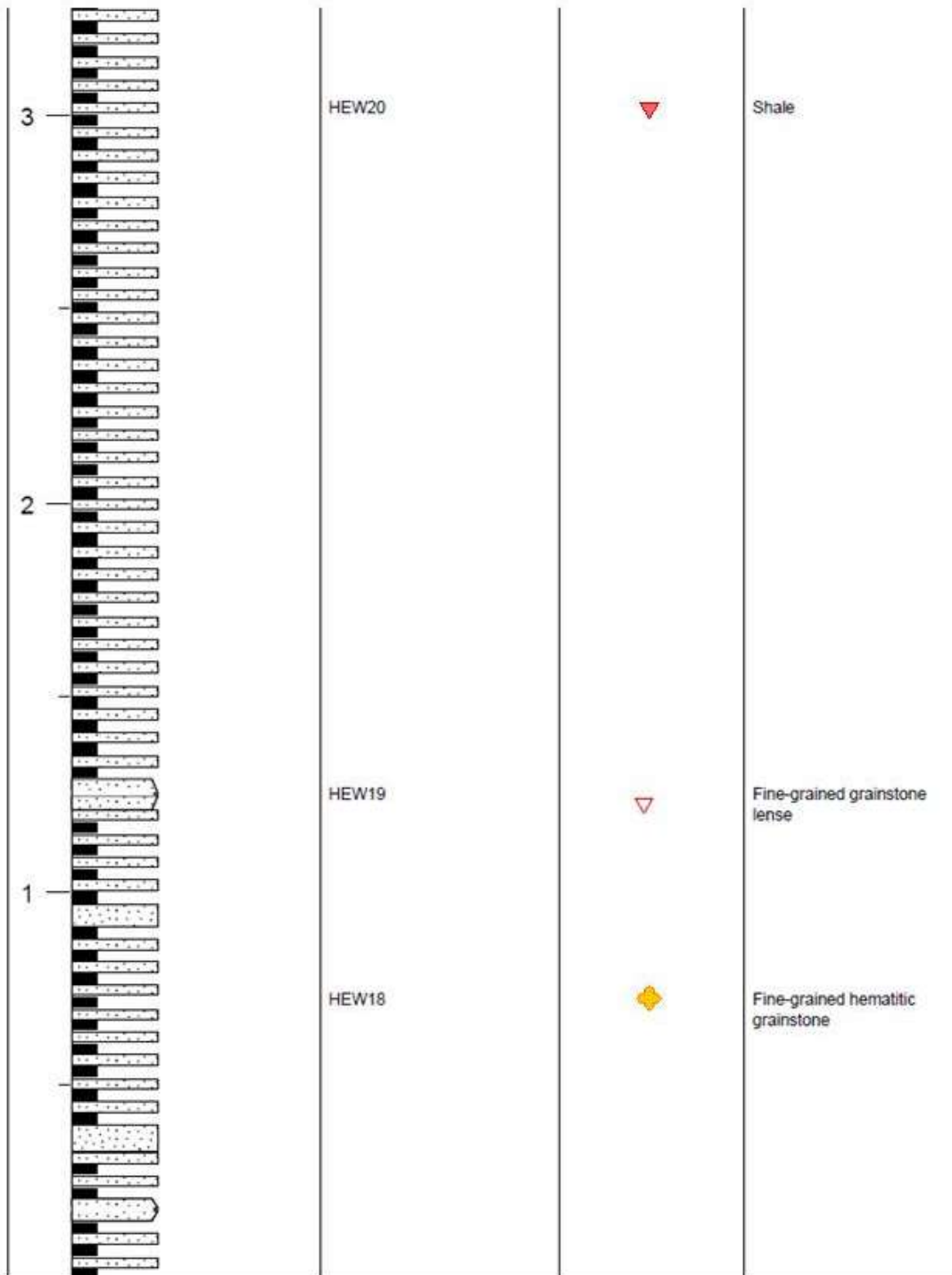
Figure 37. (Above) Outcrop of HEW Cliff Face.
Figure 38. (Below) Lenticular-bedded facies composed of thin layers of fine-grained grainstone with thin layers of shale.

Figure 39. (Above) Lenticular-bedded material. Fine-grained hematitic grainstone lens approximately 6cm thick is situated in between.
Figure 40. (Below) Lenticular-bedded material. Fine-grained grainstone lens approximately 8cm thick with rip-ups.

Figure 41. (Above) Broken stromatolites at top of cliff face outcrop.
Figure 42. (Below) Ejecta material; devitrified vesicular impact glass with white blocky calcite cement.

The third and final outcrop examined and logged at the HEW site is located in the ditch alongside the Harbour Expressway (Figure 43) at UTM coordinates 327245.50E and 5363407.36N 16 N NAD83. The bottom most facies of the outcrop consist of lenticular bedded shaley layers (Figure 44) (Sample HEW8 ⬤). This is overlain, and cut into, by a channel filled with the Sudbury Impact Layer debris (Figure 45) which consists of pebbly ejecta material, ripped up underlying units, devitrified vesicular impact glass and blocky calcite cement. Sample HEW9 ✚ is a sample of the blocky cement taken from the ejecta material in the lens itself (Figure 46).   Sample HEW10 ✳, is a sample of ejecta material sampled 100cm above the ejecta lens (Figure 47).

Figure 43. (Above) Photo of ditch outcrop in Harbour Expressway.
Figure 44. (Below) Lenticular-bedded shaley layers in Harbour Expressway.
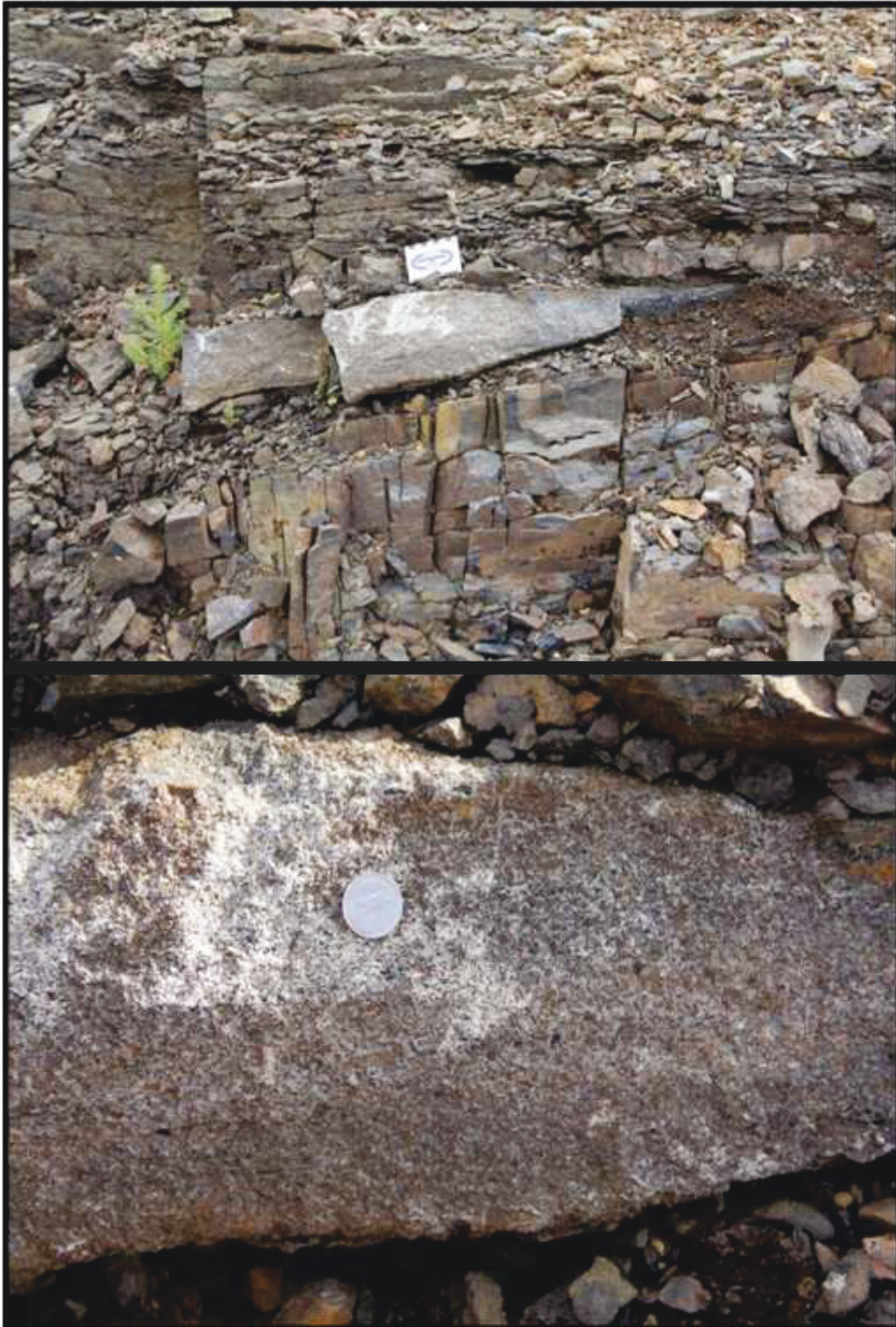
Figure 45. (Above) Channel filled with Sudbury Impact debris consisting of pebbly ejecta material, ripped up underlying units, devitrified vesicular impact glass and blocky calcite cement.
Figure 46. (Below) Lens of Sudbury Impact debris

Figure 47. Sudbury Impact material from top of ditch outcrop consisting of pebbly ejecta material, devitrified impact glass, and blocky calcite cement.

2.1.2   Geochemistry

View Table 1 for Harbour Expressway geochemistry. The samples in Harbour

Expressway have very low to minor amounts of siliciclastic material that is mixed in with the

chemical sediments (Figure 48A). A clustered, yet slightly positive correlation is seen between

Al_2O_3 vs REEs Total where most samples that increase in abundance in Al_2O_3 also increase in

abundance in REEs, hovering in the average range of 70-80ppm (Figure 48B). However, any

correlation that exists is very weak. HEW2 (botryoidal rosettes) has both low Al_2O_3 and REEs

Total levels as compared to the other samples, and are composed of calcite as found from ICP-

AES results. HEW21 (fine-grained grainstone) has the highest level of REEs Total measuring at

718ppm, outweighing the rest of the samples. There is a slight positive correlation in the cluster

of samples in Figure 48C between Al_2O_3 and vanadium, with the usual sample, HEW2, as an

exception, being of low range, and HEW11 (stromatolite from top of the cliff), HEW15

(stromatolite from top of the cliff nearer to cliff side) and HEW16 (contact of stromatolite and

ejecta material from top of cliff face) with the most vanadium enrichment. Figure 48D

demonstrates that half of the samples have extremely low molybdenum values (0-3ppm), except

for HEW15 and HEW16. There is a slight positive correlation between Mo and V (Figure 49A)

and strong correlations between Y/Ho and Ce anomaly (Figure 49B), Y/Ho and V (Figure 49C)

and cerium anomaly and V (Figure 49D). HEW4, 6, 10-19 and 22 all exhibit significant

europium anomalies with associated high levels of gadolinium (Figures 50 and 51). The

remaining samples simply have elevated levels of gadolinium but not enough to be called

anomalies. HEW11, 15, 16 (samples which have blocky calcite cement) all have extreme

negative cerium anomalies (Figures 50 and 51).   HEW21 (fine-grained grainstone) is the sample

that has the largest positive cerium anomaly, and most REEs Total at 718ppm, and the second

smallest amount of vanadium. There seems to be a moderate correlation between europium and

gadolinium anomalies for the majority of samples, where if europium is elevated, so is

gadolinium.
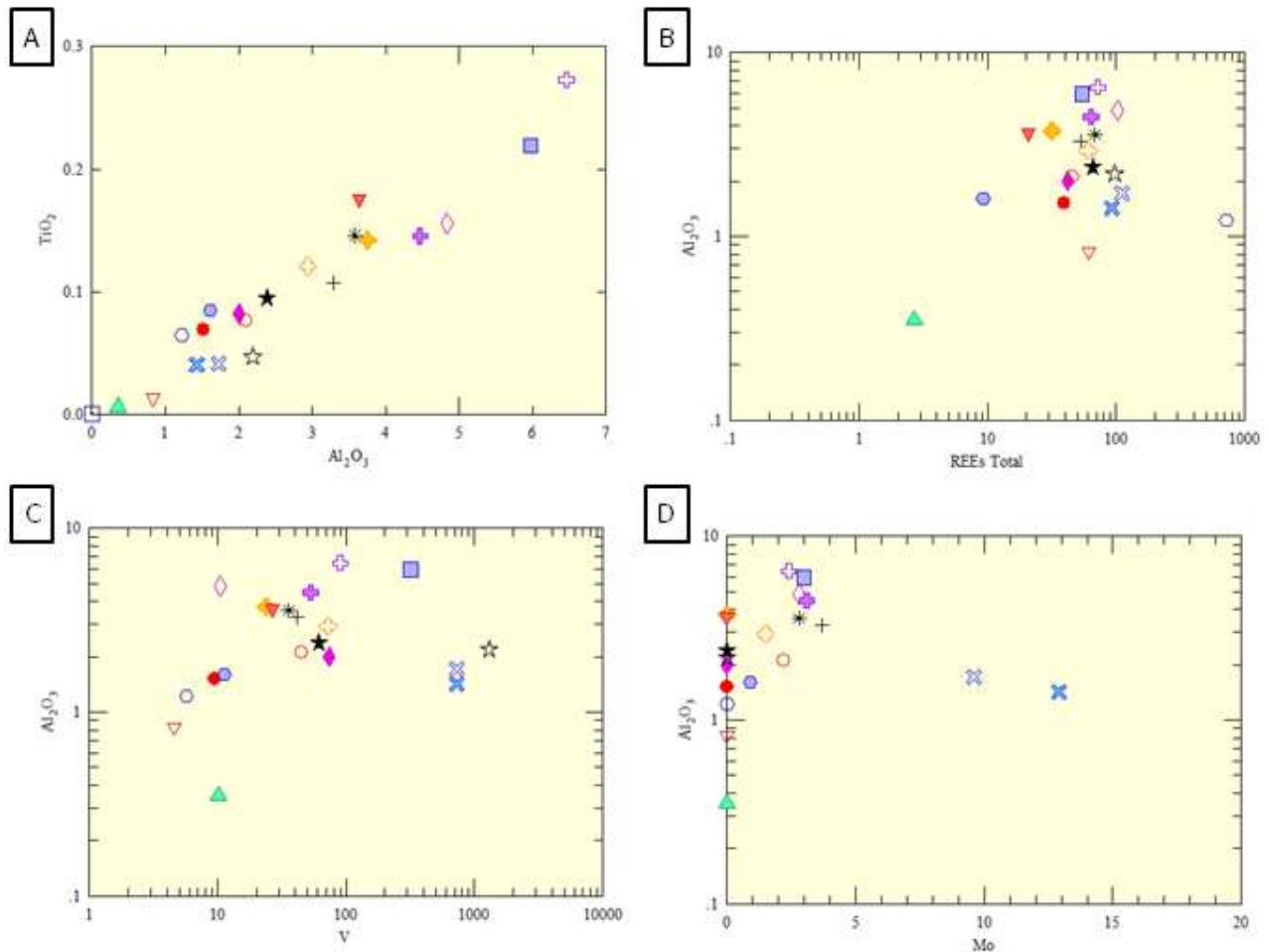
Figure 48. Bivariate plots of samples from Harbour Expressway. A) Tight positive linear correlation exists between TiO₂ vs Al₂O₃. B) Cluster of points situated in the high range of both Al₂O₃ and REE Total with the exception of Sample HEW2 (calcite botryoidal features) showing lower levels of both Al₂O₃ and REEs and HEW21(fine-grained grainstone from lenticular-bedded facies) showing average amount of Al₂O₃ but extreme enrichment in REEs. C) Cluster of points with a possible slight positive correlation. Sample HEW2 once again is depleted in Al₂O₃ but Samples HEW 11 (Stromatolite from top of cliff face), HEW15 (stromatolite from top of cliff face) and HEW16 (contact of stromatolite and ejecta material from top of cliff face) are highly enriched in V. D) Most samples have low levels of molybdenum but higher levels of Al₂O₃ with some samples increasing in a positive linear fashion. Once again, outlier samples HEW15 and HEW16 are enriched, this time with molybdenum.
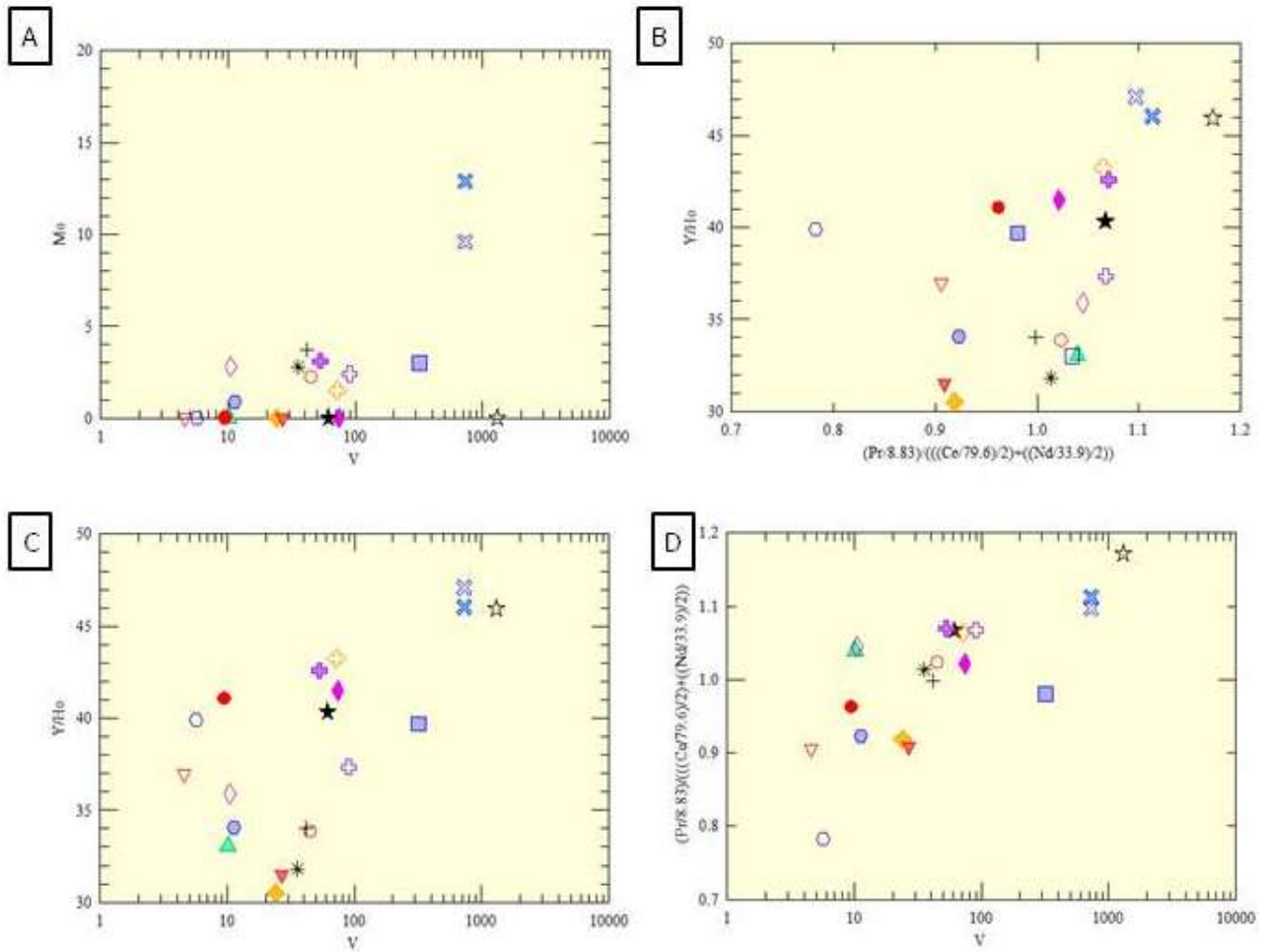
Figure 49. Bivariate plots of samples from Harbour Expressway. A) A slight positive correlation exists between Mo and V between samples. Nearly half of samples are below detection in Mo. Samples HEW4 (black chert veining) and HEW11 (stromatolite) contain high levels of vanadium while samples HEW15 (stromatolites) and HEW16 (contact between stromatolite and ejecta) display high enrichment in both vanadium and molybdenum, as compared to the rest of the samples. B) A loose cluster of samples correlated in a positive manner between the Y/Ho ratio and cerium anomaly. Outlier sample HEW21 has a slight cerium anomaly. C) Loose cluster of samples, but displaying a slight positive correlation between Y/Ho vs V with samples HEW11, 15 and 16 once again displaying extreme enrichment in both Y/Ho ratio and V. D) Positive correlation between cerium anomaly and vanadium.

58
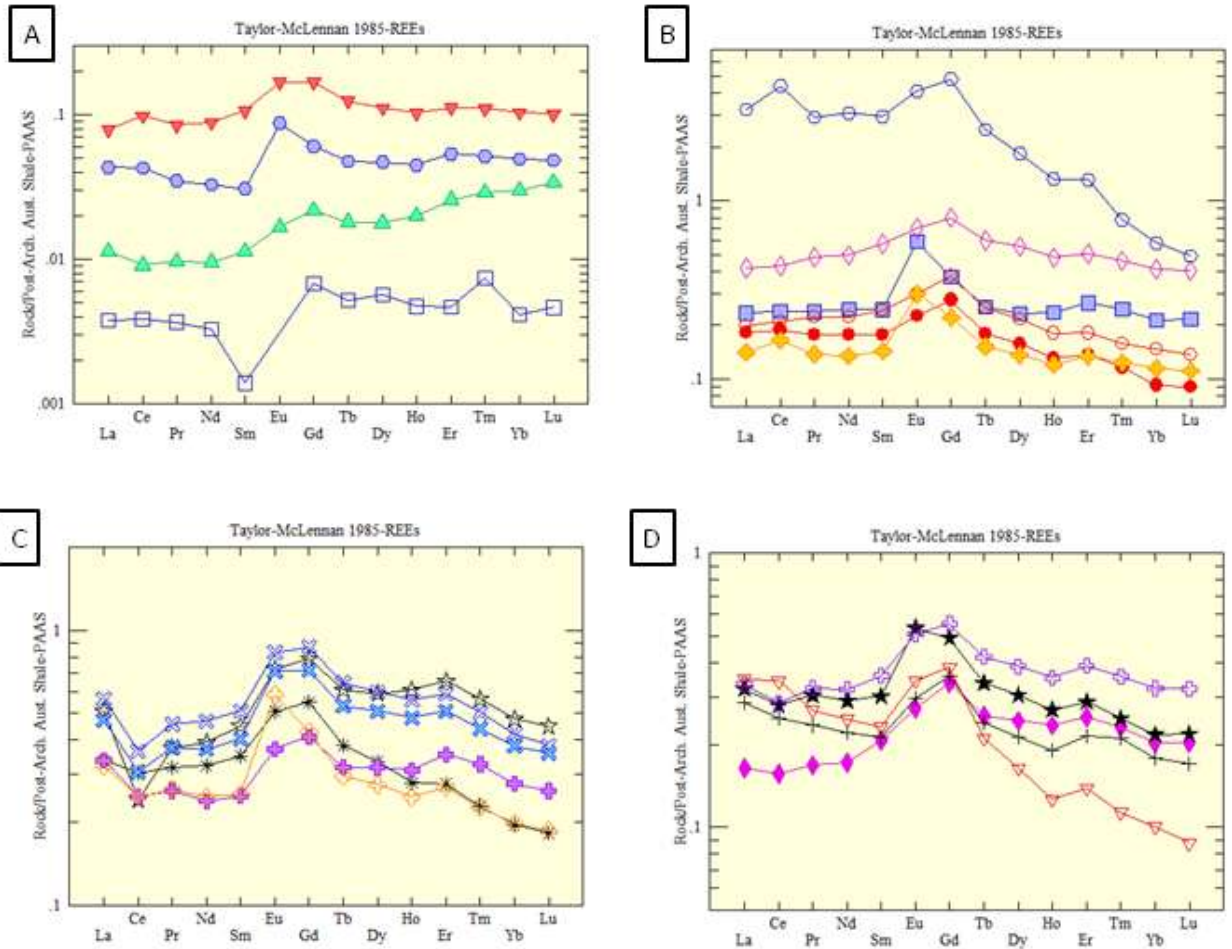
Figure 50. Rare Earth Element plots standardized to Taylor and McLennan (1985) PAAS. A) HEW3 and HEW22 both show decreasing levels in the LREEs; while HEW3 exhibits undetectable below detection levels of europium (hence point was unable to plot), europium peaks in HEW22. Both samples exhibit low levels of samarium. B) HEW5, HEW7, and HEW8 all peak at gadolinium. HEW4 and HEW18 both show similar peak patterns both with a distinct positive europium anomaly. HEW21 is enriched in cerium, europium and gadolinium tapering off at the HREEs. C) All samples in this plot show similar REE curves with negative cerium anomalies (with the exception of HEW10) and pronounced positive europium and gadolinium peaks, except for HEW17 which is missing the pronounced gadolinium peak. D) HEW6, HEW9 and HEW13 exhibit similar curves with pronounced gadolinium peaks and slight negative cerium values. HEW12 has a curve with an elevated europium level and a lesser gadolinium level as compared to the other samples. HEW19 displays a peaked curve at gadolinium, but less with europium, is enriched in LREEs and less so with the HREEs.
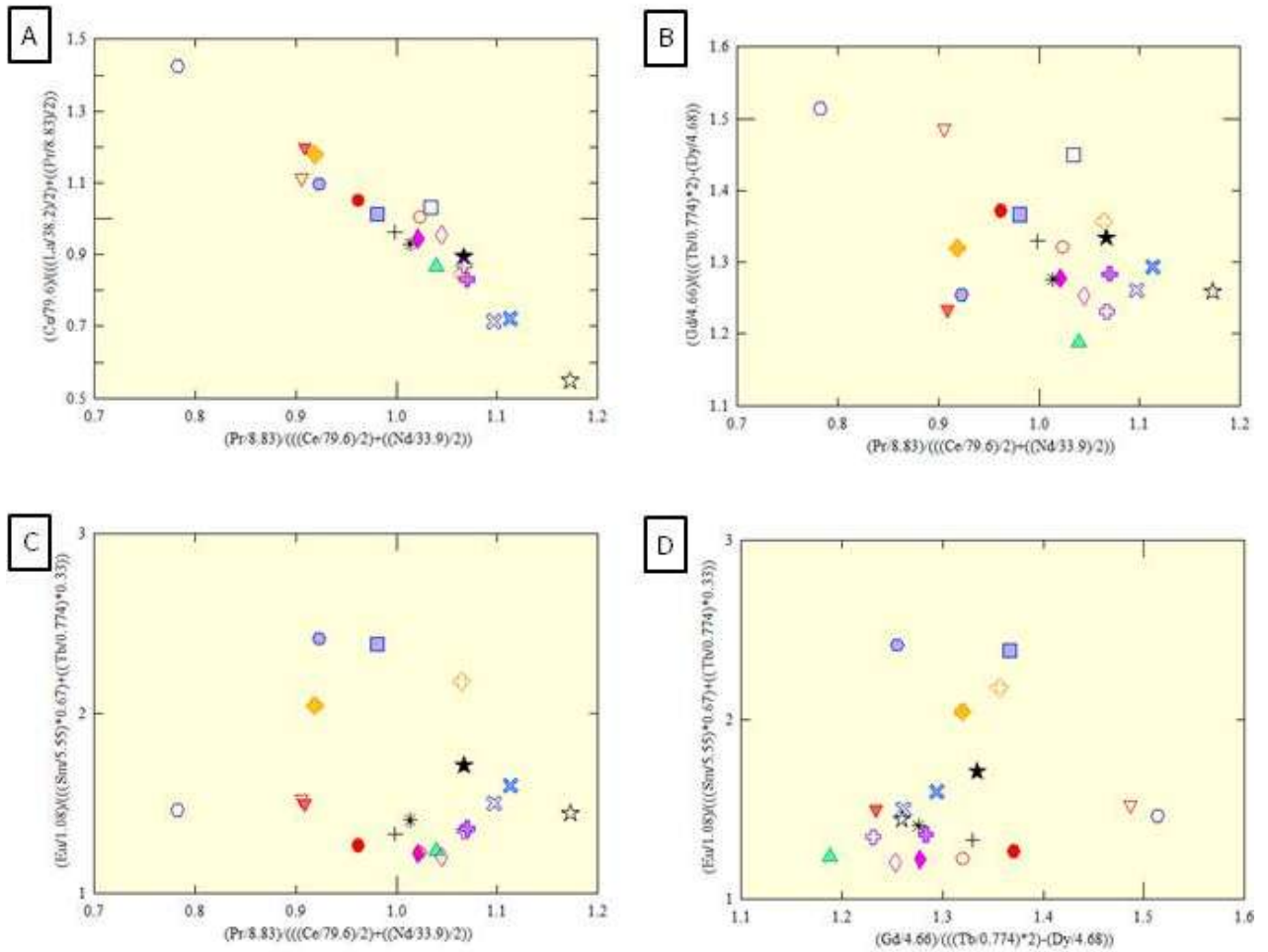
Figure 51. Bivariate plots displaying REE anomalies of the Harbour Expressway samples. All values were normalized to PAAS before anomaly calculations. A) Linear correlation exhibited between lanthanum anomalies (y-axis) and cerium anomalies (x-axis). This relationship is probably due to cerium being present in both equations. B) Possibly a very weak correlation between Gd vs Ce anomalies. HEW21 has the largest gadolinium anomaly and also a positive cerium anomaly. HEW11 has the most defined negative cerium anomaly. C) a diffuse cluster of points formed between europium and cerium. Many samples have elevated levels of europium. Once again HEW21 is an outlier sample with a positive cerium anomaly, and HEW11 has the negative cerium anomaly. D) Weak positive correlation between europium and gadolinium anomalies, with the exception of outlier samples such as HEW19, HEW21, and HEW22.

2.1.3   Interpretations

Lenticular bedded units in the Gunflint Formation, similar to those present in the cliff face, have previously been assigned to the foreshore and upper shoreface environment (Pufahl, 1996; Pufahl and Fralick, 2000). It is proposed that when the overlying Sudbury Impact material fell, it fell onto an already subaerially exposed surface (Addison et al., 2010; Fralick et al., 2012). The high degree of silicification of the upper meters of the Gunflint directly underlying this exposure surface is similar to silicification of the uppermost Gunflint reported at other locations (Poulton et al., 2004, Addison et al., 2010), and has been attributed to alteration during subaerial exposure (Burton and Fralick, 2007; Fralick and Burton, 2008). The ripped-up pieces of limestone stromatolites the ejecta contains come from a limestone unit overlying the silicified Gunflint at other locations, and noted and given member status by Moorhouse and Goodwin (1960). Whether it was deposited during a minor transgression after the regression that lead to the silification, or represents lacustrine or wet surface sub-aerial stromatolite growth is unknown (Burton and Fralick, 2007; Fralick and Burton, 2008). The Sudbury Impact Layer contains white blocky calcite cement which, by analogy with similar blocky calcite cements described and interpreted in the underlying limestone and other S.I.L. outcrops (Burton and Fralick, 2007; Fralick and Burton, 2008), indicates that meteoric water infiltrated the S.I.L. rather than oceanic water. ICP-AES and MS results show that samples of stromatolite fragments and cement taken from the S.I.L. have a negative cerium anomaly. This indicates that the meteoric water that deposited the calcite cements were deficient in Ce compared to the other REEs. This was likely caused by the water acquiring its REE load during weathering in a somewhat oxic environment or encountering an oxic environment and having the Ce (III) oxidize to Ce (IV) and leave solution (Refer back to Geochemistry section for discussion of this process). The correlation between the negative Ce anomalies and enrichment of V and Mo in the samples

also indicates that the meteoric waters the calcite cements formed from were somewhat oxic, as the mobility of these elements is greatly increased when they are in higher valance state.

It is difficult to understand excatly how the silica flowerette plaque was formed since it is a rare geologic formation, with no literature found on this type of occurrence. Underneath the plaque lies fine-grained, granular textured crystals that exhibit a chicken-wire structure, which has been replaced by carbonate. This is very similar in appearance to the chicken-wire anhydrite textures preserved in dolostone in Paleoproterozoic rocks of the Baltic Shield that were deposited on a coastal sabkha (Brasier et al., 2011) and mosaic chicken-wire anhydrite present in Devonian supratidal sabkhas of Bulgaria (Andreeva, 2015). Associated spheroidal clumps of platy carbonate crystals in the Harbour Expressway outcrop are identical in appearance to gypsum desert roses, which are described by Whitlock (1930) as: "groups of overlapping platelike crystals deposited by groundwater in desert sand that resemble the petals of a rose." Most modern examples of desert roses have grown in loose sediment near the surface of sabkhas (i.e., Almohandis, 2002) and are a strong indicator of an arid climate (Keyser, 1968). For an in depth discussion of their formation mechanism see Pettenati et al. (2008). The fibrous carbonate veins associated with the desert roses strikingly resemble gypsum veins (see papers by Machel, 1985; and Philipp, 2008). Gypsum veins are composed of satinspar, which grows from both sides of an open fracture forming a central parting where the crystals meet (Machel 1985). They are developed in desiccation cracks and associated with coarse-grained gypsum rosettes up to 2 to 3 cm in diameter on dry mudflats forming inland sabkhas in the Neogene of Turkey (Turkmen and Ozkul, 1999). This is a very similar association to what is seen at the Harbour Expressway outcrop.

When the siliceous radiating crystal forms (plaque) are put into this scenario they become more understandable. El Khorily (2005) describes siliceous nodules composed of a central cavity filled with megaquartz surrounded by radiating megaquartz crystals and bounded by a thin veneer of microquartz. They are 2 to 3 cm in diameter, botryoidal, nodules that are crystalline and rose-like. He believes that they were originally gypsum and were replaced by silica due to the groundwater fluctuating between relatively fresh water and brines in marginal sabkhas of the Western Desert, Egypt. These nodules are reasonably similar to the siliceous plaques present in the Harbour Expressway outcrop. All the evidence strongly supports the development of a dry sabkha setting directly above the ejecta layer.

Whether the water associated with the sabkha was of marine or meteoric origin is difficult to answer. Eu anomalies are developed in marine waters of this time period, but not meteoric waters, so the extent of the Eu anomalies in these sediments compared to the underlying Gunflint lower shoreface sediments may provide information on this. The desert roses, chickenwire and carbonate matrix material surrounding these structures all have smaller positive Eu anomalies than most of the other samples. The Eu in the sample of calcified gypsum vein material is so low, that it is the only REE in this sample below detection. This indicates that the brine from which the evaporates precipitated was more likely formed from meteoric waters, though a marine influence cannot be totally discounted as the samples do have minor Eu anomalies.

2.2　Mapleward Railway Cut (MP)

2.2.1　Lithofacies Description

The Mapleward Railway Cut outcrop (Figure 53) is located in Thunder Bay, Ontario, Canada at UTM coordinates 326420.10E and 5363808.48N 16 N NAD 83. Refer to Figures 52 and 62 for stratigraphic column representations of the two areas logged in the outcrop at the Mapleward Railway. The paleovalley portion of the outcrop is on the southwest side of the outcrop, and consists of a depression filled in with rubble from the base surge flow from the Sudbury impact. The paleohill portion was logged a few meters to the northeast of the paleovalley. Addison et al. (2010) previously found and described this site calling it the Grand Trunk Pacific (GTP) site in their paper.

At the very bottom of the paleovalley portion (Figure 54), there is 40cm of non-magnetic hematitic shale with 1cm thick and 20cm long very fine, hematite grainstone lenses forming a lenticular bedded unit. A 7cm thick lens of fine-grained hematitic grainstone (MP1 ▲), about 60cm in length, lies on top of the lenticular bedded unit. This is followed by 60 cm of lenticular bedding with one larger grainstone lens. On top sits a 50cm unit of hematitic, medium-grained grainstone that contains secondary black chert veins. This unit is a series of dunes, with a wavelength of approximately 7 meters. Above is a 12cm thick unit of carbon-rich black shale followed by 193 cm of lenticular bedding with five larger grainstone lenses. This succession is capped by a 37cm thick unit of medium-grained grainstone (Figure 55) (MP2 ☐), followed by 308 cm of lenticular bedding with scattered larger lenses. From this point on, layers become gently folded and there is a fault at the end of this sequence of layers. The following 150cm thick unit consists of ankeritic grainstone (MP3 ☐) lenses, hematite layers 2-3cm thick that are also lenses, and chert layers (Figure 56); but all these layers are either badly fractured or
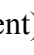
shattered (Figure 57).   Above the shattered unit rests a 6cm thick chert lens approximately

130cm in length. The proceeding 38cm unit consists of long lenses of hematite alternating with

medium-grained ankeritic grainstone. A 7cm unit of white chert lenses approximately 160cm in

length lies on top, followed by 120cm of long black chert lenses that are wispy and ribbon-like in

nature, with alternating medium-grained ankeritic grainstone layers. There were only a few

hematite layers present in this unit. Another 100cm thick unit lies on top and consists of similar

material to below, but with some hematitic medium grainstone lenses (MP4B ◇). Also, there

are areas of erratic amoeboid chert fragments that are surrounded by ankerite (Figure 58). There

are many areas of fracturing present in this unit and layers are very irregular. On top of the

fractured unit in the paleovalley portion of the outcrop lies approximately 300cm of very chaotic

rubble that consists of broken up Gunflint formation (Figures 59, 60). Figure 61 interestingly

shows a block of botryoidal chert.   Samples taken from this rubble unit are: MP5 ◆ (medium-

grained hematitic grainstone), MP6 ◯ (fine, dark-grained material - very likely devitrified

vesicular impact glass) , MP7 ● (white, blocky calcite cement), MP8A ✛ (white, blocky calcite

cement), MP8B ✳ (white blocky calcite cement), MP9 ☆ (white blocky calcite cement),

MP15 ◆ (black chert).

Figure 52. Stratigraphic Representation of Mapleward Railway Cut: Paleovalley.

11

10

9
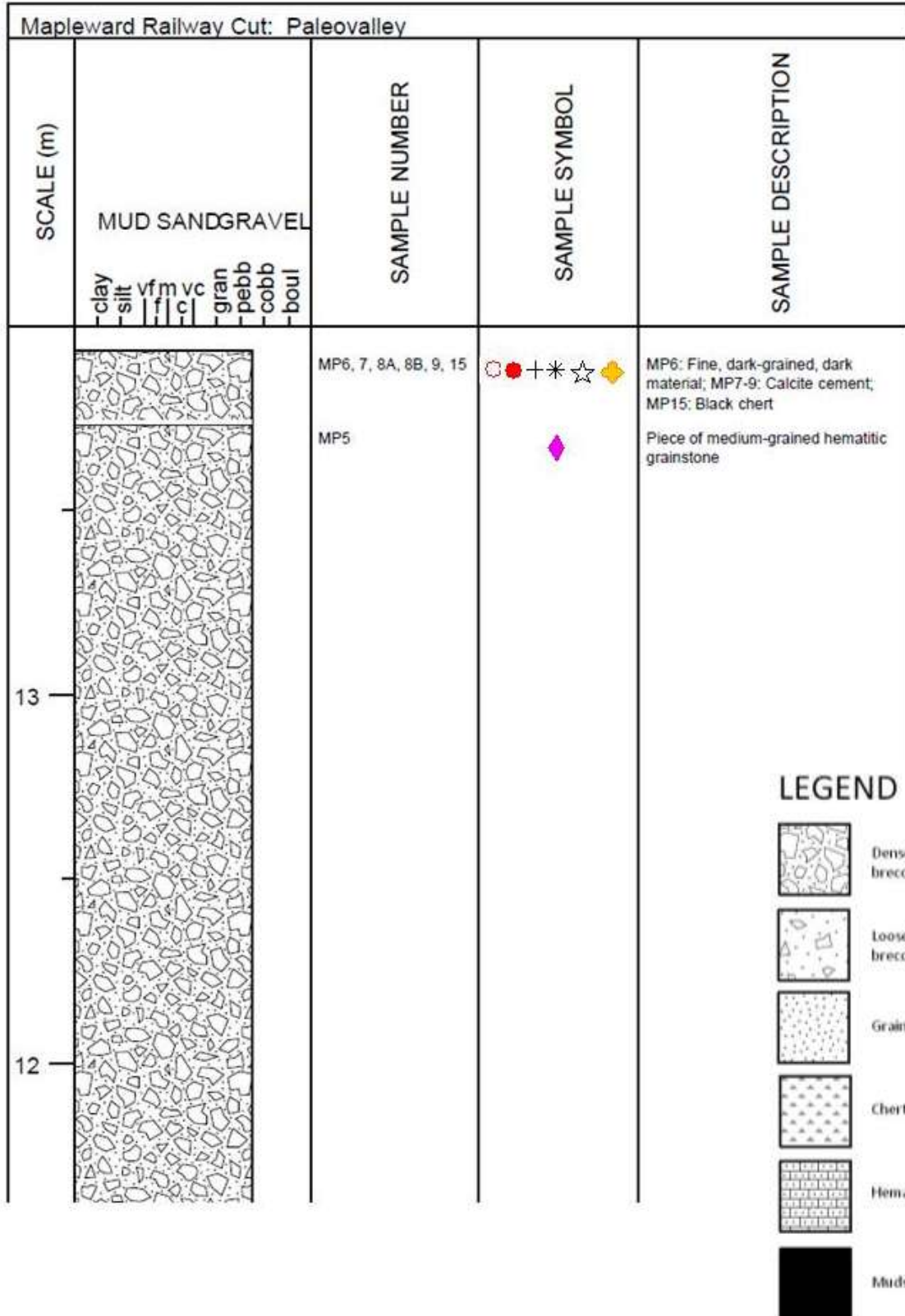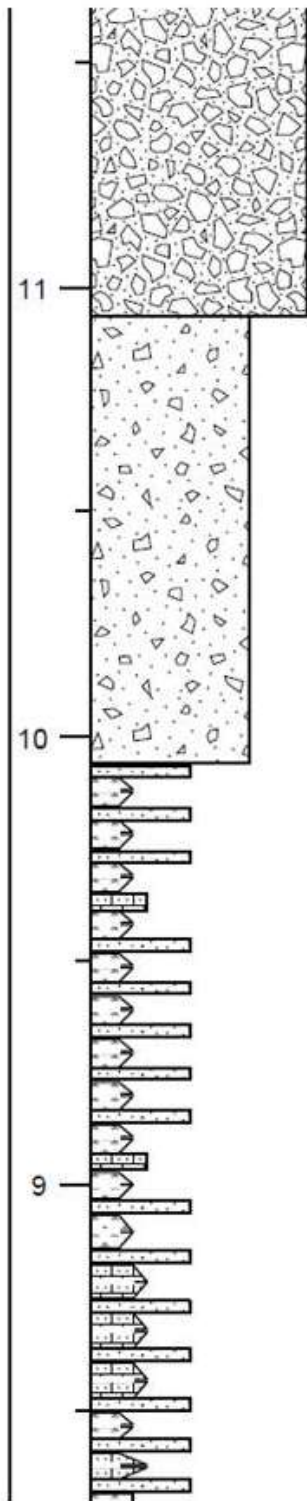
MP4B

◇

Fine-grained ankeritic grainstone;
unit is badly fractured

8

MP3

Medium-grained ankeritic grainstone

7

6

5

4

MP2

☐   Medium-grained grainstone

3

2

1

MP1 △ Fine-grained hematitic grainstone
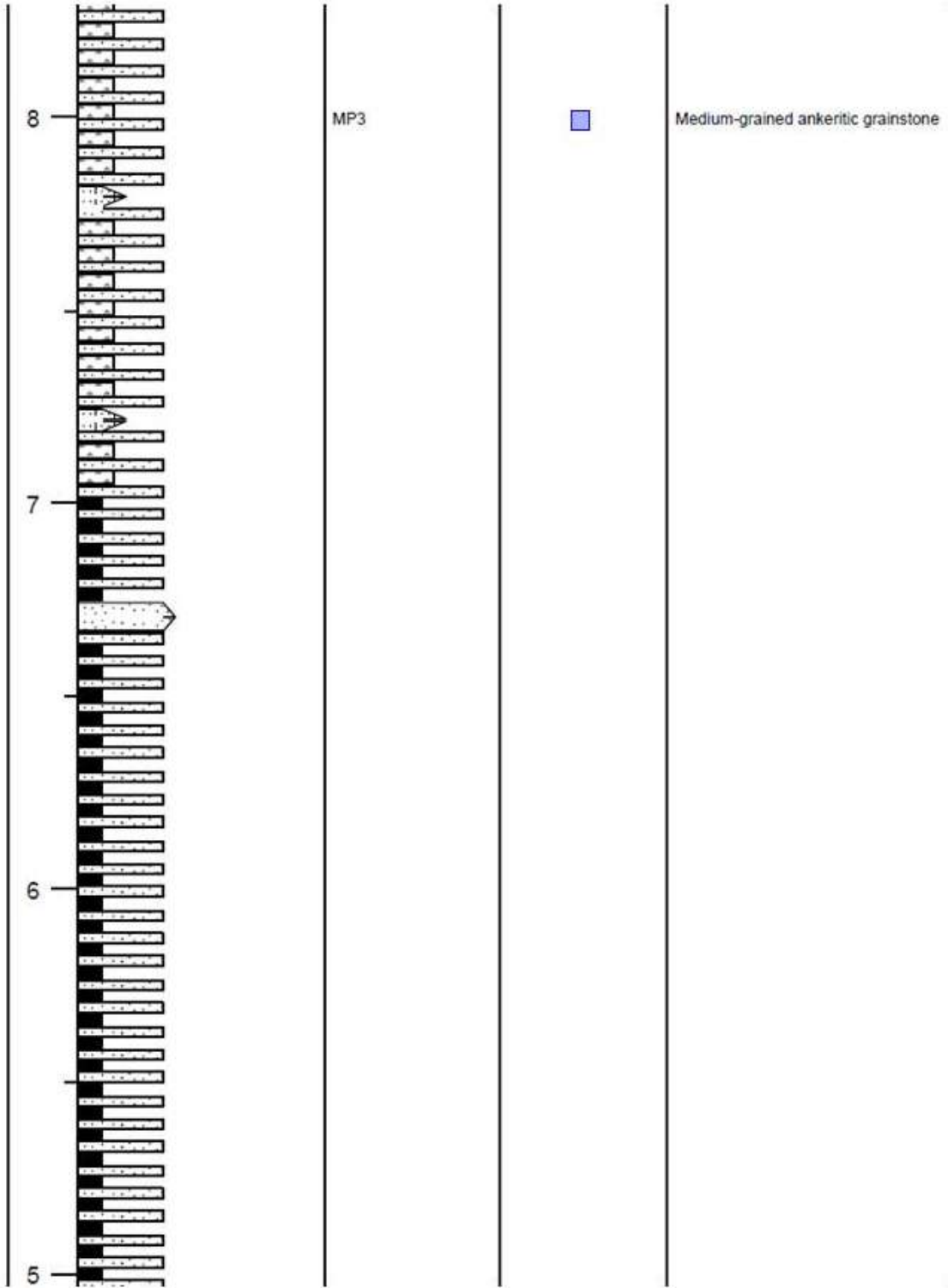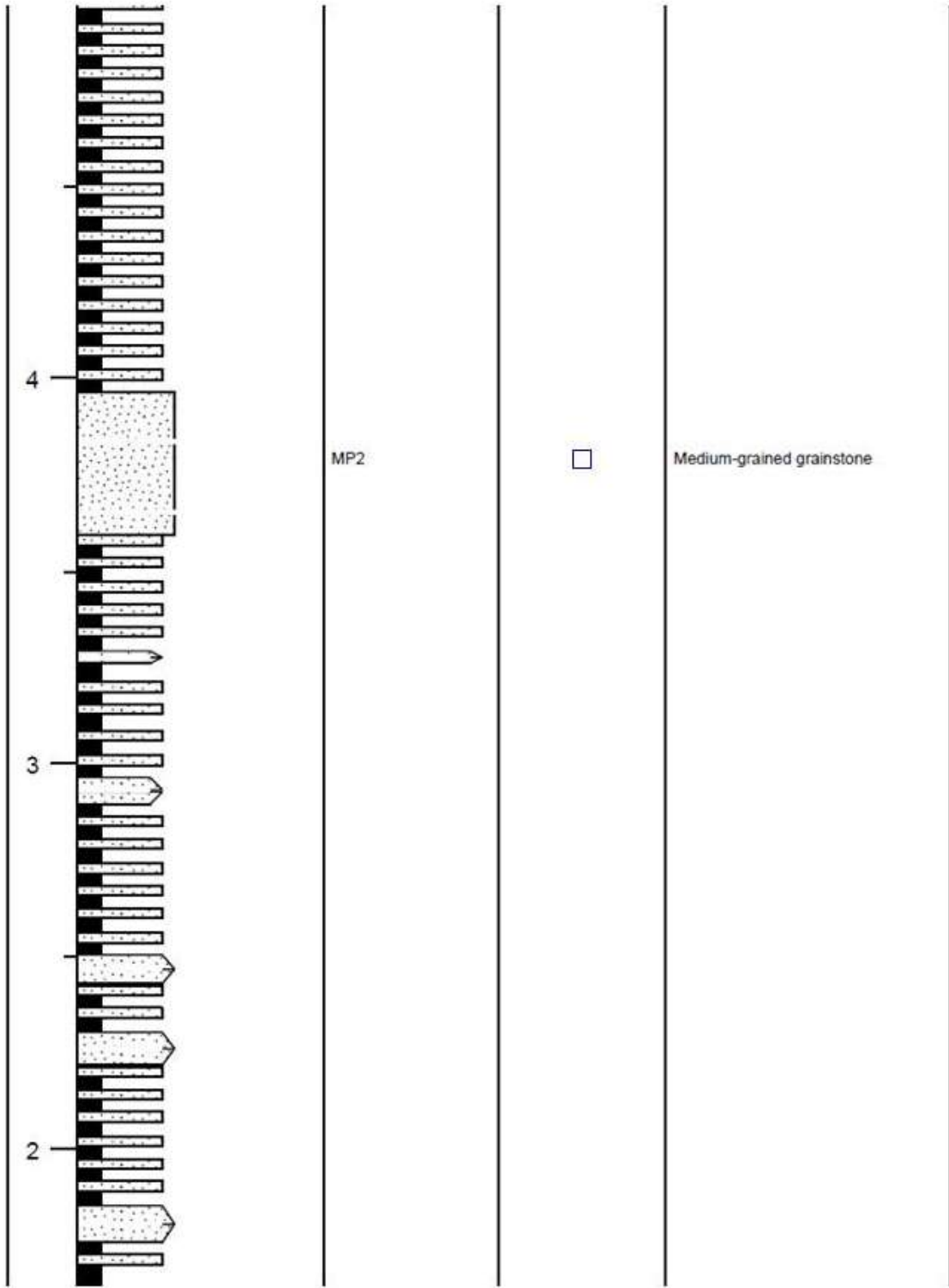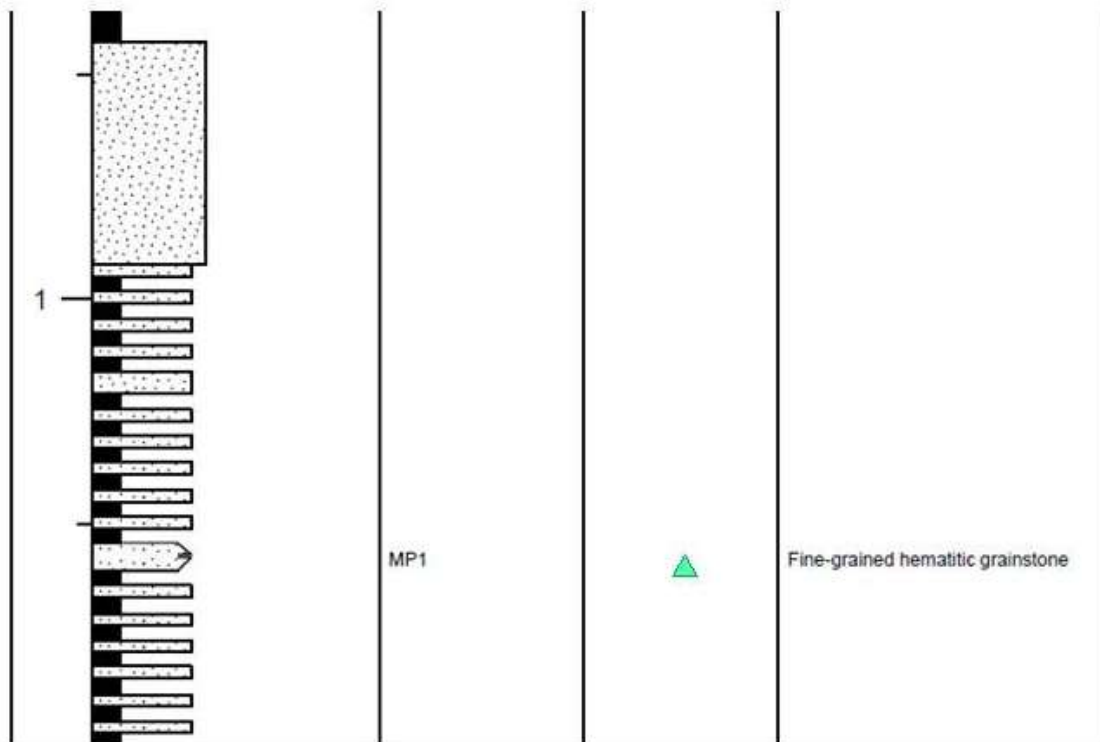
Figure 53. Panoramic, wide-angle view of Mapleward Railway Cut outcrop broken into 3 photos due to its lateral extent. Top photo is left-most side of outcrop, while bottom photo is the right most side of outcrop.

Figure 54. Outcrop of paleovalley with rubble sloping down upon the previously silicified layers (Scale indicated by hammer).
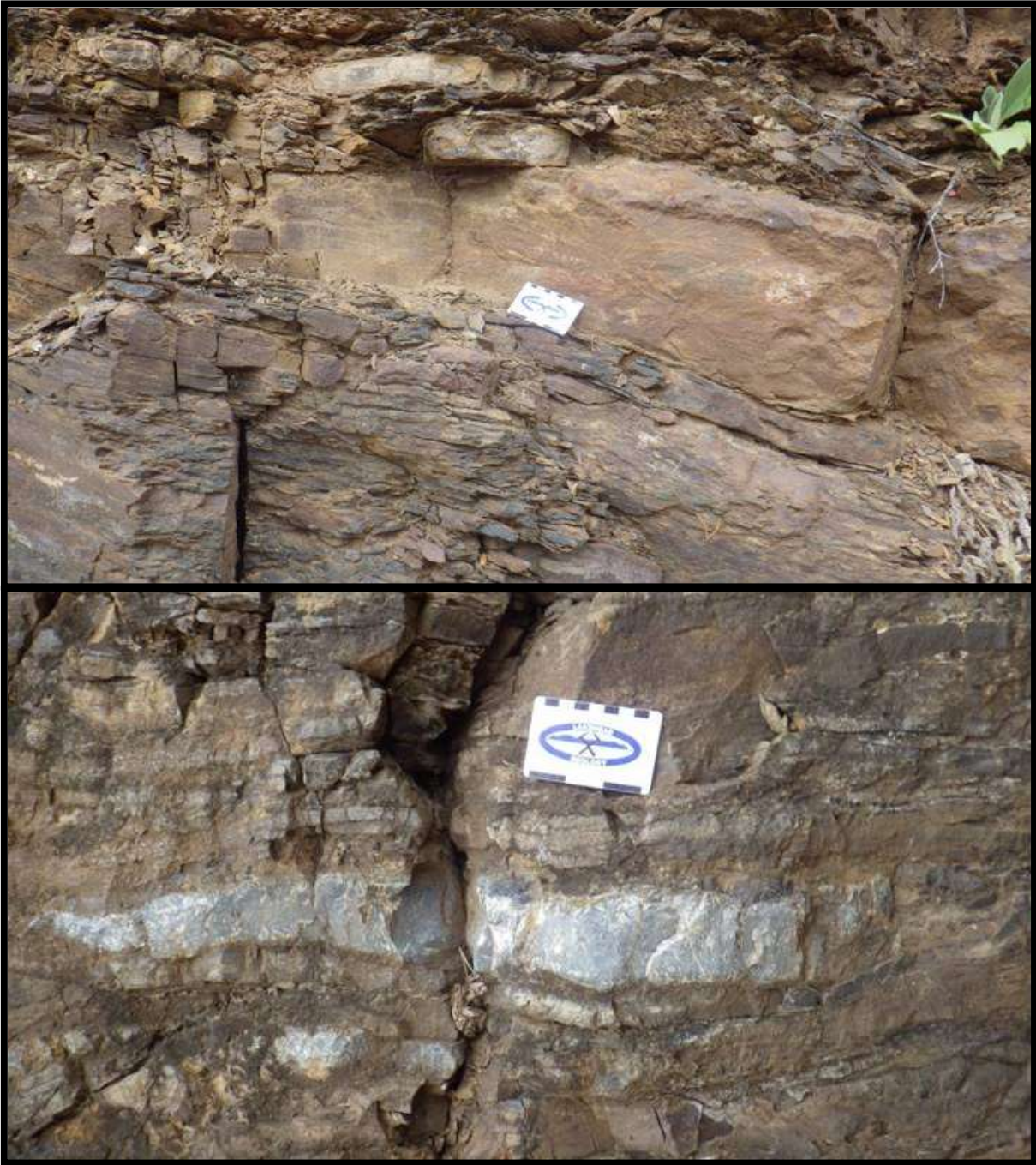
Figure 55. (Upper) Lenticular bedded facies consisting of shaley material and fine-grained grainstone, with fine-grained hematite grainstone lens situated on top.
Figure 56. (Lower) Chert layers, specifically white chert lens in this photo.
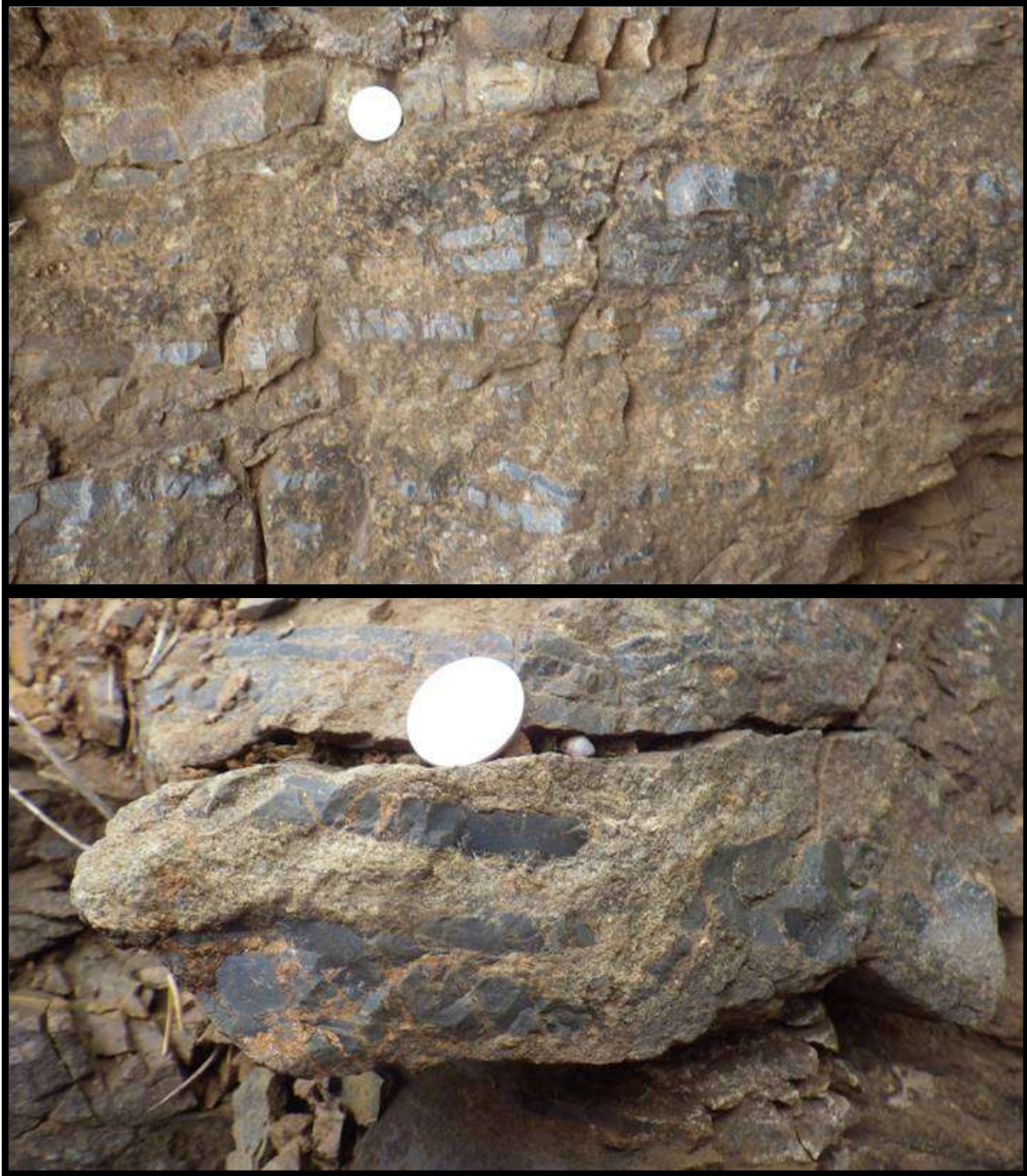
Figure 57. (Upper) Ankeritic grainstone lenses, hematite layers and lenses, and black chert, but all these layers are near the top of the intact outcrop and are either badly fractured or shattered. (Canadian 25 cent piece used for scale).

Figure 58. (Lower) Erratic amoeboid areas of chert fragments that are surrounded by ankerite. (Canadian 25 cent piece used for scale).
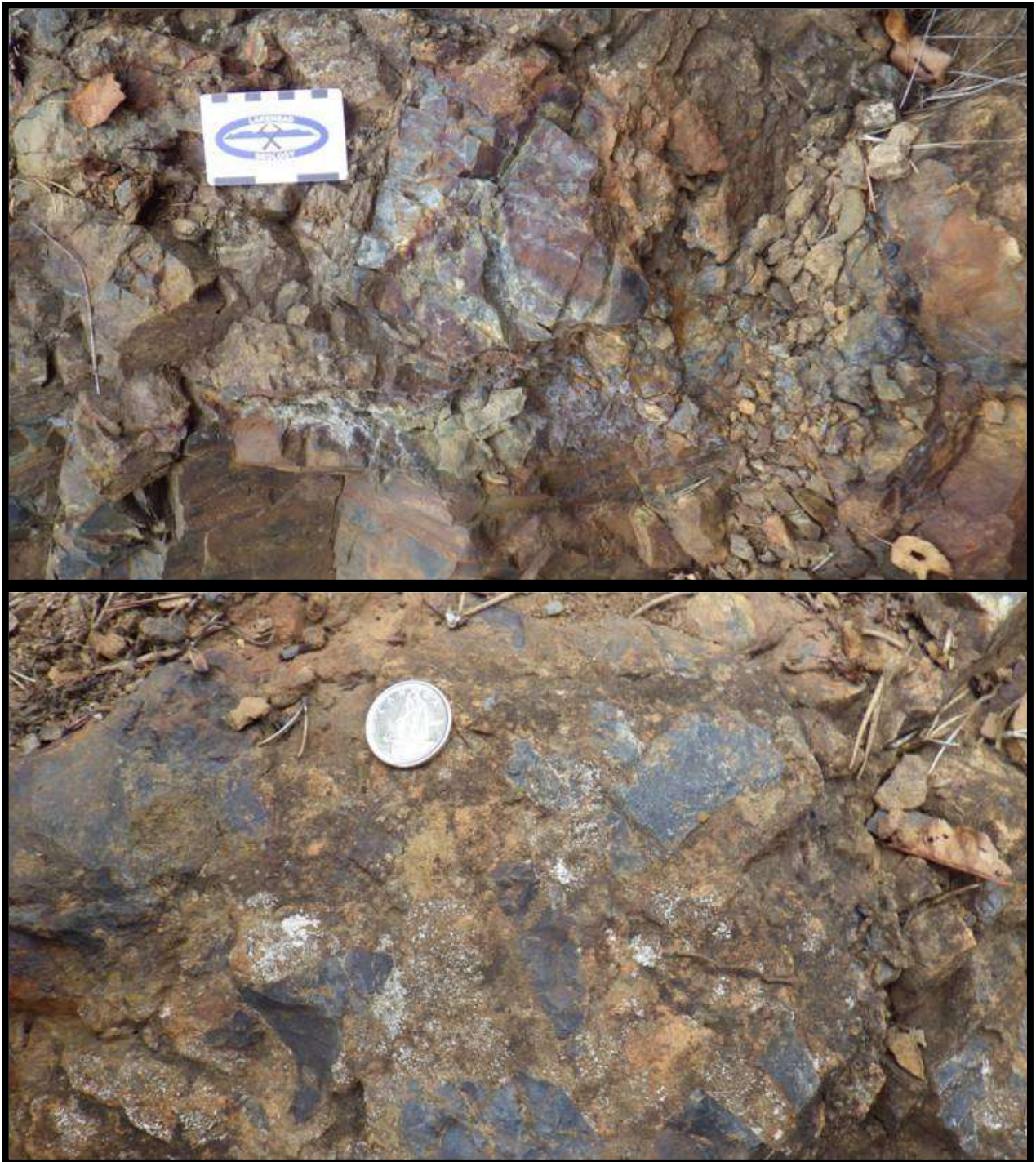
Figure 59. (Upper) Rubble pile in paleovalley consisting of Gunflint Formation cherts, grainstones, and hematitic shale.
Figure 60. (Lower) Rubble pile of Gunflint Formation close up of rip-up chert surrounded by grainstone.

Figure 61. Block with botryoidal chert layer present in Gunflint rubble in the paleovalley.

The paleohill outcrop was logged only a few meters to the right of the paleovalley outcrop as it is a continuation of it laterally. Only the top section of the paleohill is exposed, consisting of approximately 115cm of silicified Gunflint Formation, which is composed of fine-grained grainstone layers, black chert lenses and lenses of fine-grained hematite. On top rests a black chert layer approximately 15cm thick. Two samples were taken laterally from the chert layer; MP11A ✛ was taken from the west side and MP11B was taken from the east side ✛. Overlying the black chert layer is a 65cm layer of stromatolitic limestone (Figure 63) (MP10 ★). The layer that rests directly above the stromatolitic unit is the Sudbury Impact Layer, which consists of ejecta material, devitrified vesicular impact glass and white blocky calcite cement (Figure 64) (MP12 ✖, MP13 ✖, and MP14 ✛). The Paleohill portion of the outcrop does not contain any fractured blocks from the underlying Gunflint Formation.

Figure 62. Stratigraphic Representation of Mapleward Railway Cut: Paleohill.
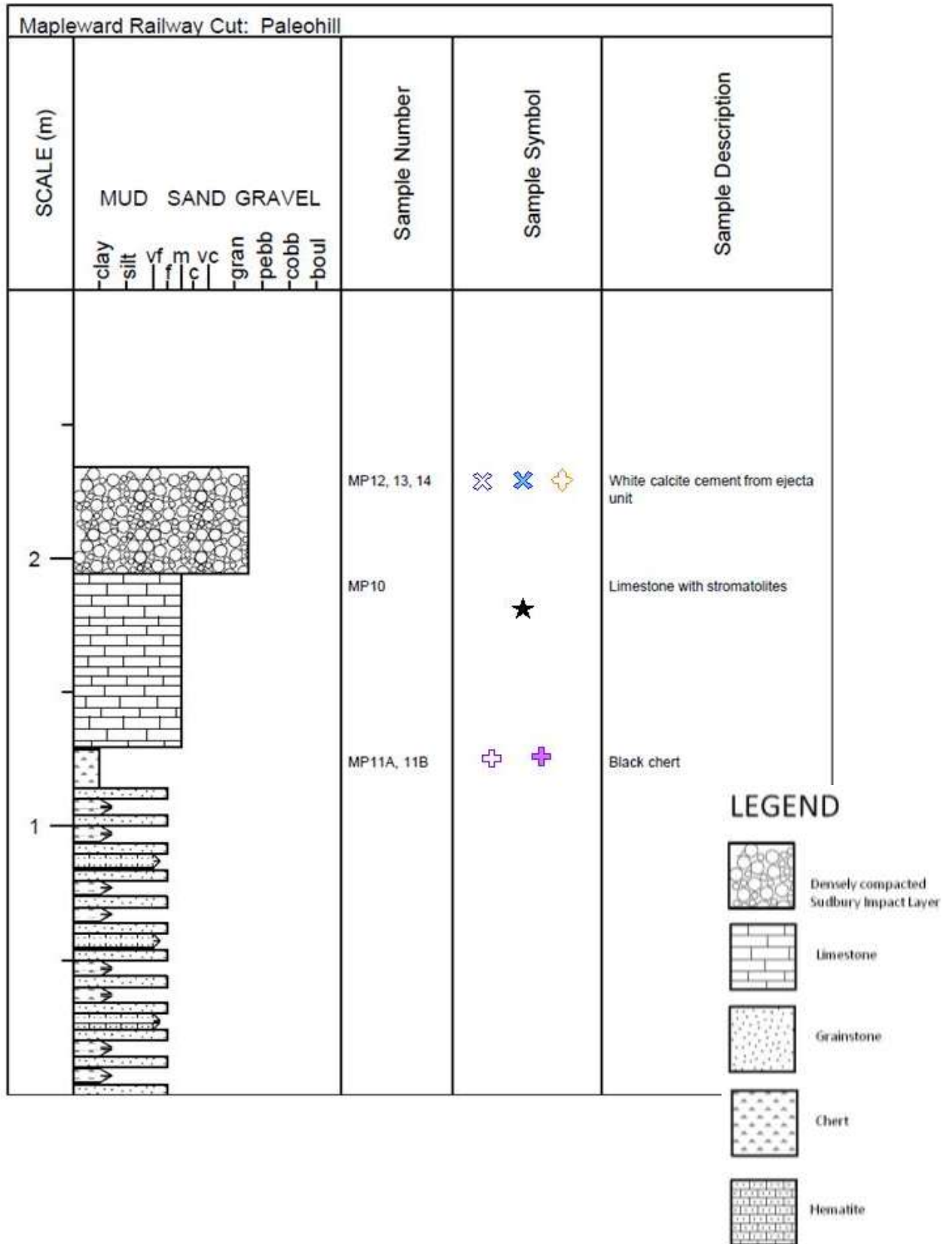
Figure 63. (Upper) Chert unit from paleohill overlain by stromatolitic limestone unit.
Figure 64. (Lower) Sudbury Impact Layer material consisting of devitrified vesicular impact glass surrounded by white blocky calcitic cement.

2.2.2   Geochemistry

View Table 2 for Mapleward Railway Cut geochemistry. Figure 65 shows that for most samples there is not a direct correlation between TiO_2 and Al_2O_3 and that, except for sample MP6, significant amounts of siliciclastic sediment is mixed in with the chemical sediments. There is a slight positive correlation between Al_2O_3 and REE Total and Al_2O_3 and vanadium. MP10 and MP14 have the highest values in both REE Total and vanadium. Molybdenum once again has generally very low values in most samples, except for MP8B (white blocky cement), which has a value of approximately 27ppm (Figure 65D). There appears to be a positive correlation between the cerium anomaly and vanadium and Y/Ho, at least in a sub-set of the samples. All samples except MP10 and MP14 have moderate to high positive europium and gadolinium anomalies. There is no correlation between cerium and gadolinium anomalies due to different levels of confidence, but with europium and gadolinium there seems to be a slight positive correlation. Samples MP10, MP 9, MP11A, and MP14 all have larger negative cerium anomalies.
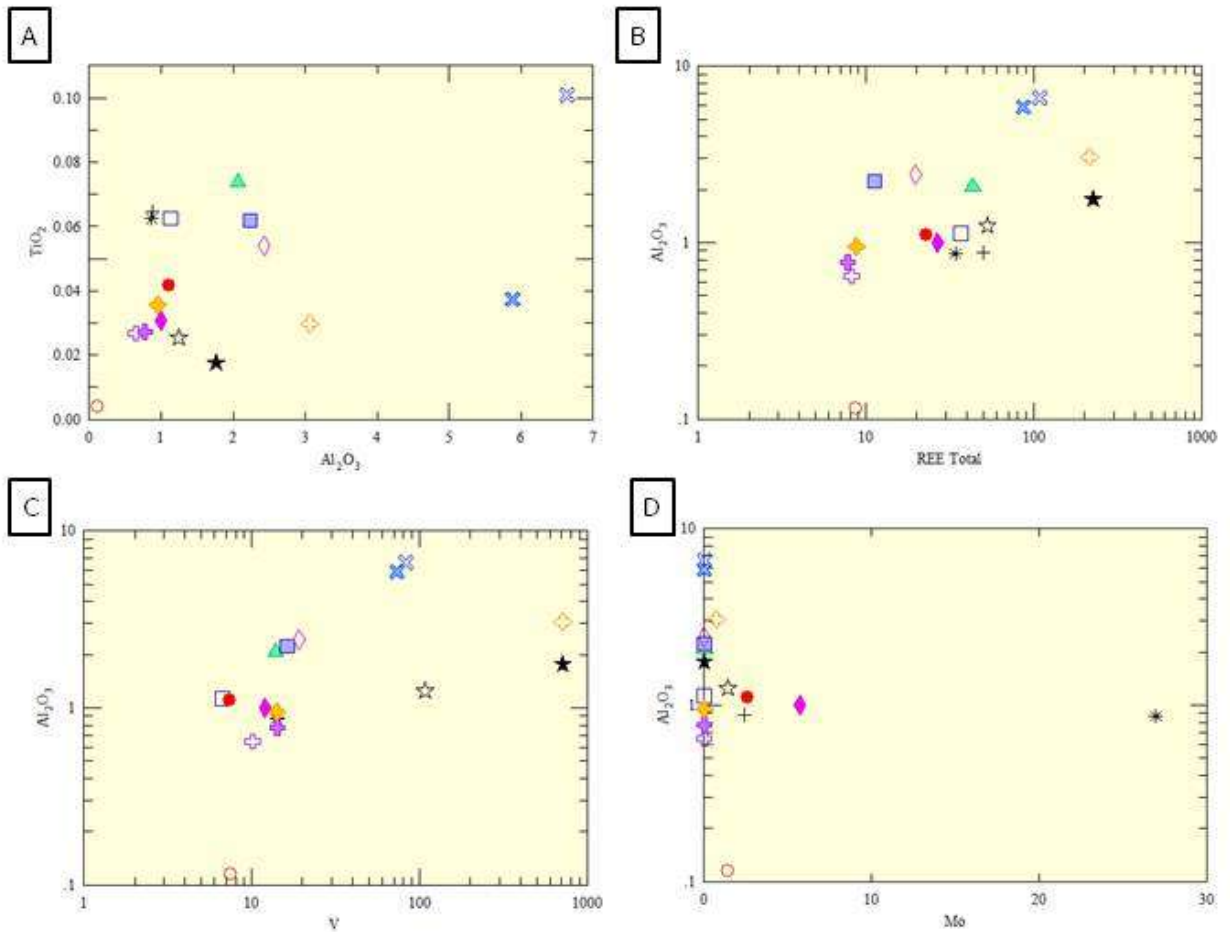
Figure 65. Bivariate plots of samples from Mapleward Railway Cut. A) No linear relation exists between TiO$_2$ vs Al$_2$O$_3$. B) No positive correlation is present for Al$_2$O$_3$ vs REE Total, with outlier sample MP6 low in Al$_2$O$_3$ and containing one of the smallest amount of REE Total. C) A cluster exists between Al$_2$O$_3$ and vanadium with MP6 once again one of the samples that has the smallest amounts of both Al$_2$O$_3$ and vanadium. D) There is no linear relationship between Al$_2$O$_3$ and molybdenum; many samples have a value near zero for molybdenum, while MP8B (calcitic cement from top of paleovalley) has the highest amount of molybdenum, approximately 27ppm.
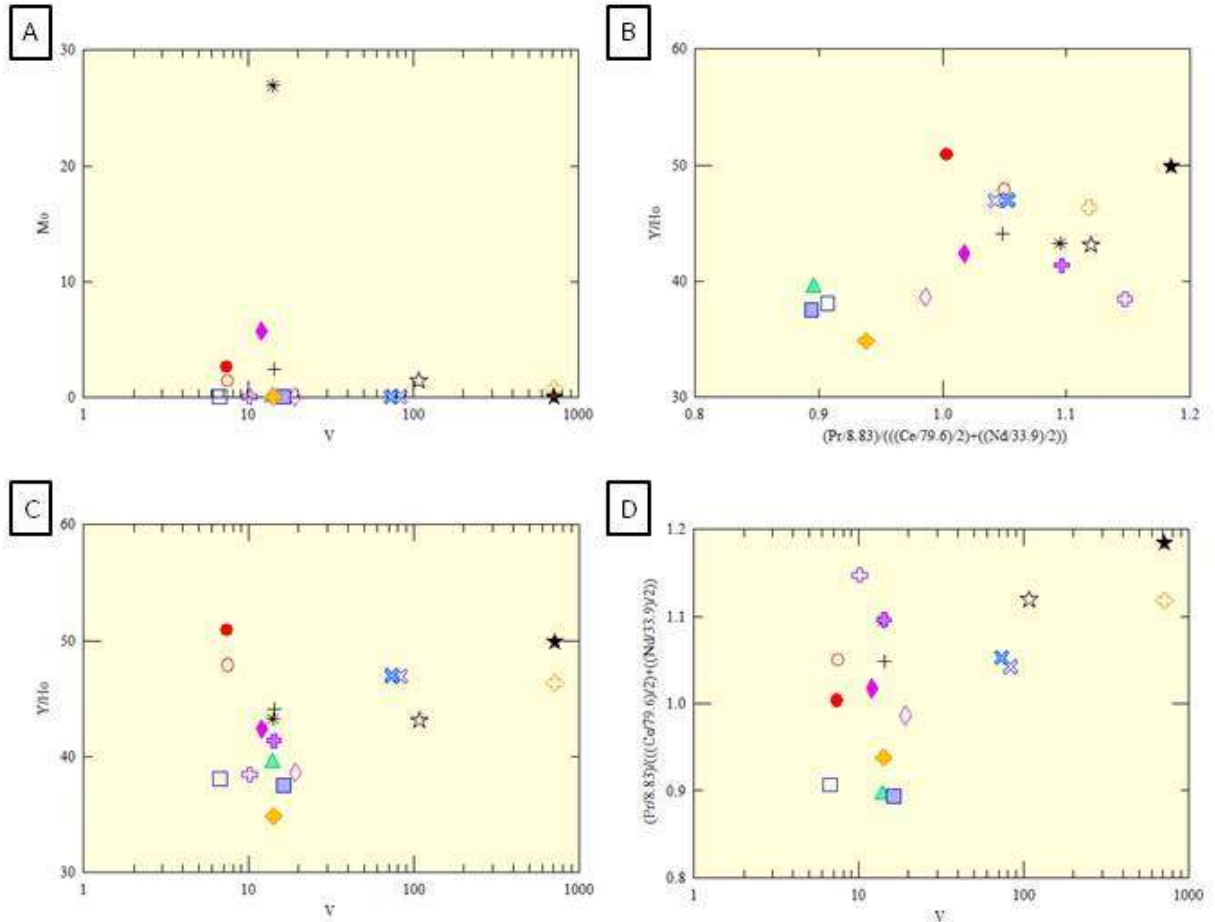
Figure 66. Bivariate plots of samples from the Mapleward Railway Cut. A) No correlation between molybdenum and vanadium. Once again outlier sample MP8A is shown with highest molybdenum values from the sample set. MP9 (calcite cement from atop paleovalley), MP12 and MP13 (both of white calcite cement from ejecta unit atop paleohill) have high vanadium values ranging from 70-110ppm, while MP10 (limestone with stromatolites from paleohill section) and MP14 (white calcite cement from ejecta unit atop paleohill) contain the highest amount of vanadium in the 700ppm range. B) Slight positive correlation between Y/Ho vs cerium anomaly. C) No linear correlation between Y/Ho vs vanadium. D) Linear regression line can be plotted in a positive correlation between cerium anomaly and vanadium with exceptions of samples MP6 (fine, dark chert from paleohill), MP11A (black chert from paleohill) and MP11B (black chert from paleohill).
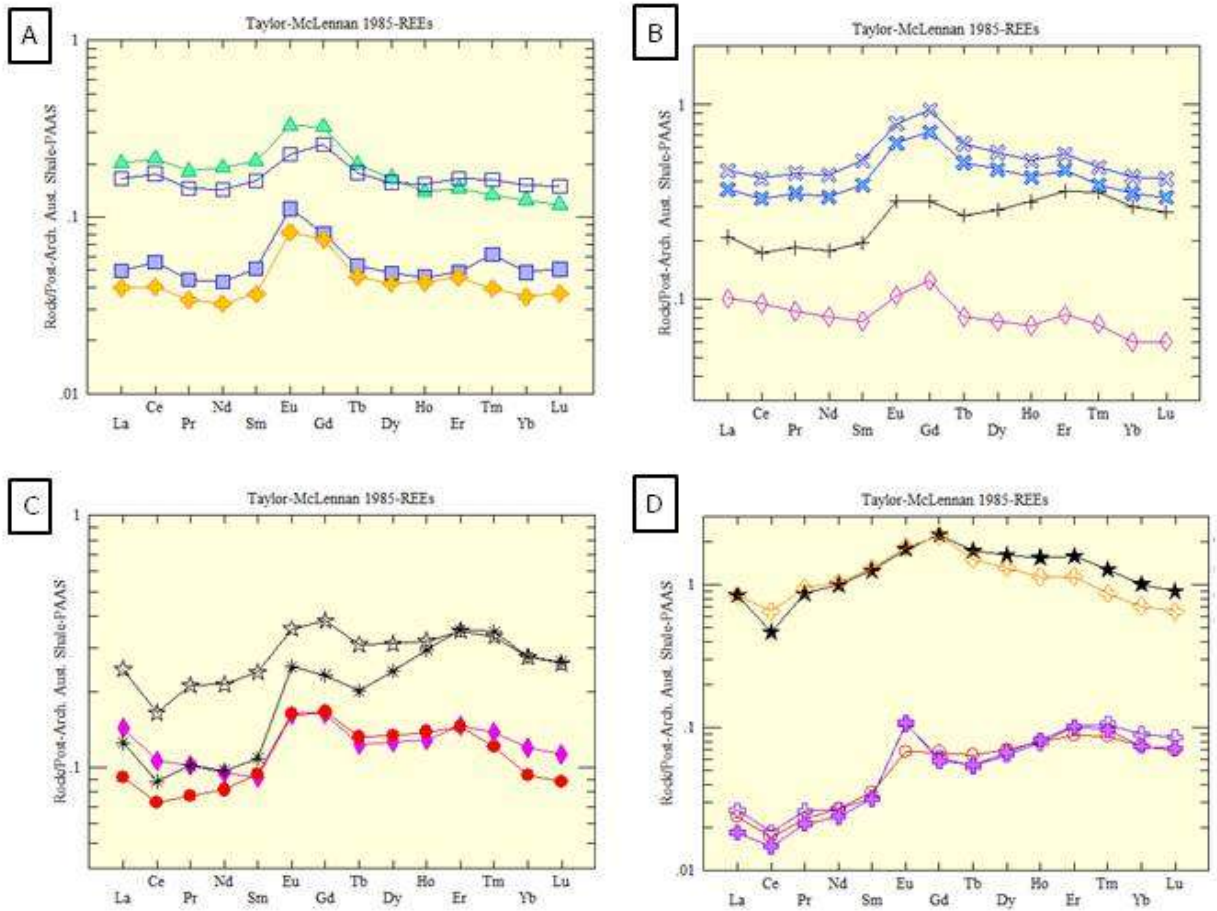
Figure 67. Rare earth element spider plots standardized to Taylor and McLennan (1985) PAAS. A) MP1 and MP2 have similar curves with similar values, while MP3 and MP15 have similar curves and similar values, with a sharper increase in europium values. B) MP12 and MP13 exhibit almost exactly the same patterns with elevated europium and gadolinium, while MP8A displays a similar pattern as well, but with a smaller positive gadolinium anomaly. MP4B has a similar curve, but this time gadolinium is the element with the largest positive anomaly. C) Samples MP5, MP7, MP8B, and MP9 have similar curves, all with slight cerium depletions, and elevated levels in both europium and gadolinium (except MP9). D) Samples MP10 and MP14 have similar hat shaped curves, with depletions in cerium and no Eu anomaly. MP11A, MP11B, and MP6 are also similarly shaped and all have cerium deficiencies, but moderate to large positive europium anomalies.
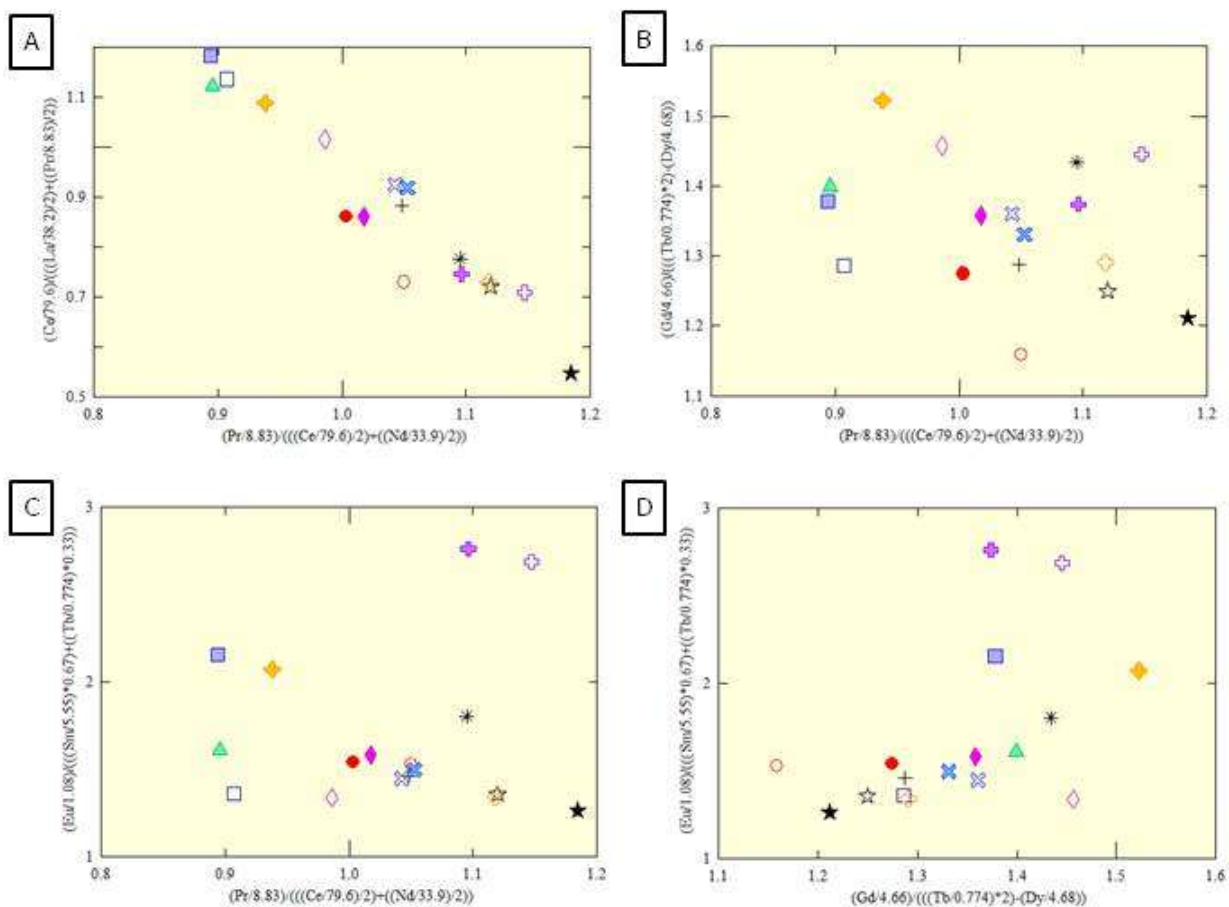
Figure 68. Bivariate plots exhibiting rare earth element anomalies of Mapleward Railway Cut samples. All values were normalized to PAAS before anomaly calculations. A) Linear correlation exhibited between lanthanum (y-axis) and cerium (x-axis) anomalies. This relationship is probably due to cerium being present in both equations. B) No correlation between gadolinium and cerium anomalies. C) No correlation between europium and cerium anomalies. D) Linear positive correlation between europium and gadolinium anomalies, exception of outlier samples.

2.2.3   Interpretations

The lenticular bedded unit with grainstone dunes lying below the Sudbury impact layer is

very similar to the unit at the same stratigraphic position as the Expressway site previously

described. The same interpretation of upper shoreface deposits in the Gunflint Sea can be applied

(Pufahl, 1996; Pufahl and Fralick, 2000). The tilting of the strata becomes markedly steeper as

the ejecta layer is approached and low angle faults appear. Immediately below the impact layer

the bedrock is shattered and the transition to the pebble-boulder breccia is gradational. Thus, it is

reasonable to assume that the deformation was caused by the seismic waves generated by the

impact. Silicification of the rock units directly underlying the impact layer occurred prior to the

impact as silicified fragments are present in the debris. Silicification at other locations is

associated with sub-aerial exposure (Burton and Fralick, 2007; Fralick and Burton, 2008), and as

the impact layer was deposited sub-aerially (Addison et al., 2010), it is reasonable to assume the

same applies at Mapleward Railway Cut. Large fragments of stromatolitic limestone contained

in the impact debris are located between the impact layer and the silicified surface. Remnants of

this layer are present on the paleohill-top. A sample from a stromatolitic limestone fragment in

the impact layer had both the largest V enrichment (over 700 ppm) and the largest negative Ce

anomaly. These both indicate precipitation of the abundant blocky calcite cements in the

limestone from oxygenated water capable of transporting the V and that went through a previous

period of Ce oxidation and precipitation. This is similar to other limestone occurrences where the

cements were precipitated by oxygenated meteoric waters (Burton and Fralick, 2007; Fralick and

Burton, 2008). Also, the limestone fragment has no Eu anomaly, a characteristic that indicates

meteoric water, not seawater. Samples from the Sudbury impact layer also have negative Ce

anomalies and enrichment in V probably also indicating deposition of their blocky calcite

cements from oxygenated water. It is interesting to note that a number of samples from directly

underlying lenticular bedded Gunflint have positive Ce anomalies indicating oxidation and precipitation of Ce in that nearshore environment. It is possible that oxygenated meteoric water was entering the nearshore and causing preferential precipitation of the Ce in seawater, leading to the positive anomalies.

2.3   Hillcrest Park (HCP)

2.3.1   Lithofacies Description

Hillcrest Park is located in Thunder Bay, Ontario, Canada, at UTM coordinates 334721.79E and 5366946.62N 16 N NAD83. Five outcrops were logged at Hillcrest Park, starting from HCP1 being the north most outcrop, and travelling south to HCP5, HCP5 being the south most outcrop logged. Refer to Figures 69, 70, 71, 72, and 73 for stratigraphic representations of the five Hillcrest Park outcrops. Addison et al. (2010) previously found and described this site calling it Site 1 (unnamed) in their paper, later on calling it Hillcrest Park in Addison and Brumpton (2012).

At the bottom of Hillcrest Park outcrop 1 (HCP1), is a 17cm unit of black chert (Figure 74) (HCP1A △), followed by a 13cm unit of fine-grained ankeritic grainstone (HCP1C ☐), followed by another unit of chert that is 15cm thick. This is overlain by 10cm of an ankerite-altered stromatolitic limestone (Figure 75) (HCP1B ☐), with a few chert veins dispersed within measuring approximately 2cm thick. This is all overlain by the Sudbury Impact Layer which is approximately a minimum of 115cm thick here. The S.I.L. has a very pebbly appearance (Figure 76), with large clasts of underlying material, approximately 15cm chert pieces dispersed with other cobbles from 4cm-12cm, all which are surrounded in a fine-grained ejecta matrix with blocky, white, carbonate cement (HCP1D ◇) (Figure 77). Figure 5 shows a small fragment of green material embedded in the ejecta layer. It is important to note that green fragments, ranging in size from 1mm to 2cm, have been found throughout the ejecta layer at different fieldsites (Figure 78, 79). A sample was taken of a piece, crushed, and given to the Lakehead University Instrument Laboratory for X-ray power diffraction (XRD) analysis. The XRD results indicated the green fragment is the mineral glauconite, an iron potassium phyllosilicate (mica group). The

glauconite fragments are found in pieces, denoting that lithification had occurred prior to the

shear blast wave that scraped bedrock off the landscape.
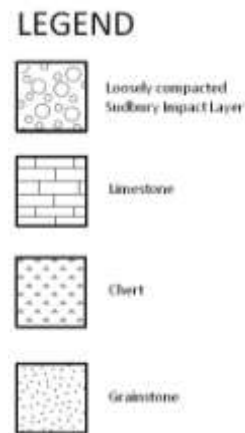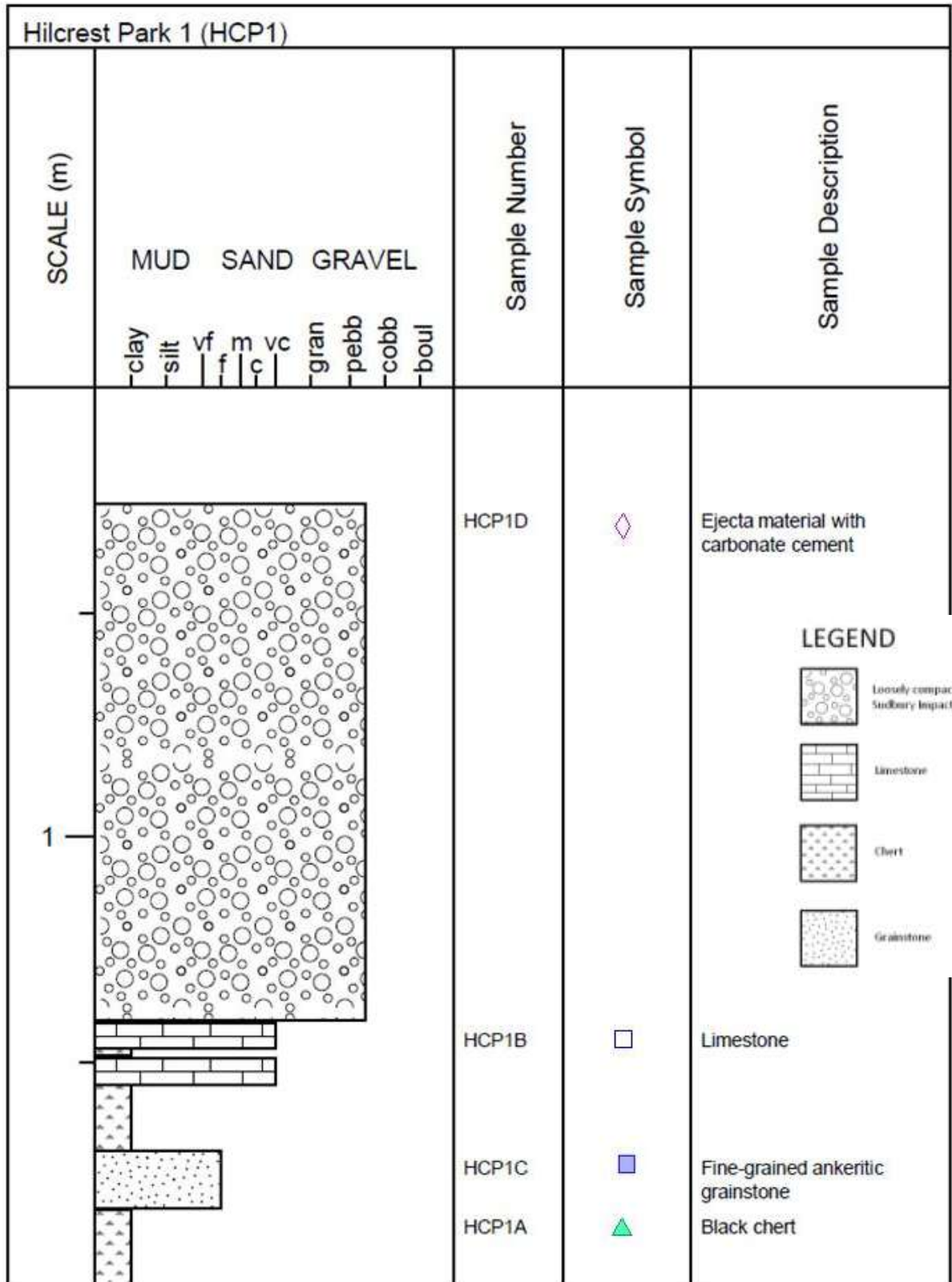
At the bottom of Hillcrest Park outcrop 2 (HCP2) is a 17cm thick unit of medium-grained ankeritic grainstone, followed by a 5cm thick unit of black chert, followed by a 5cm unit of fine-grained grainstone. This is overlain by a 3cm layer of black chert (HCP2A ♦). Overlying the chert layer is a 32cm unit of fine-grained grainstone, followed by another 10cm unit of black chert. On top is a 2cm layer of medium-grained grainstone, followed by another 9cm unit of black chert. A 7cm unit of medium-grained grainstone lies on top, followed by a 6cm unit of black chert (HCP2C ●), overlain by a 9cm unit of coarse-grained limestone (HCP2B ○). The underlying chert units are fractured and in-filled with orange ankeritic cement (Figure 80). This is topped off by the Sudbury Impact Layer measuring approximately a minimum of 34cm in thickness at this point in the outcrop (Figure 81).

Figure 70. Stratigraphic Representation of Hillcrest Park 2
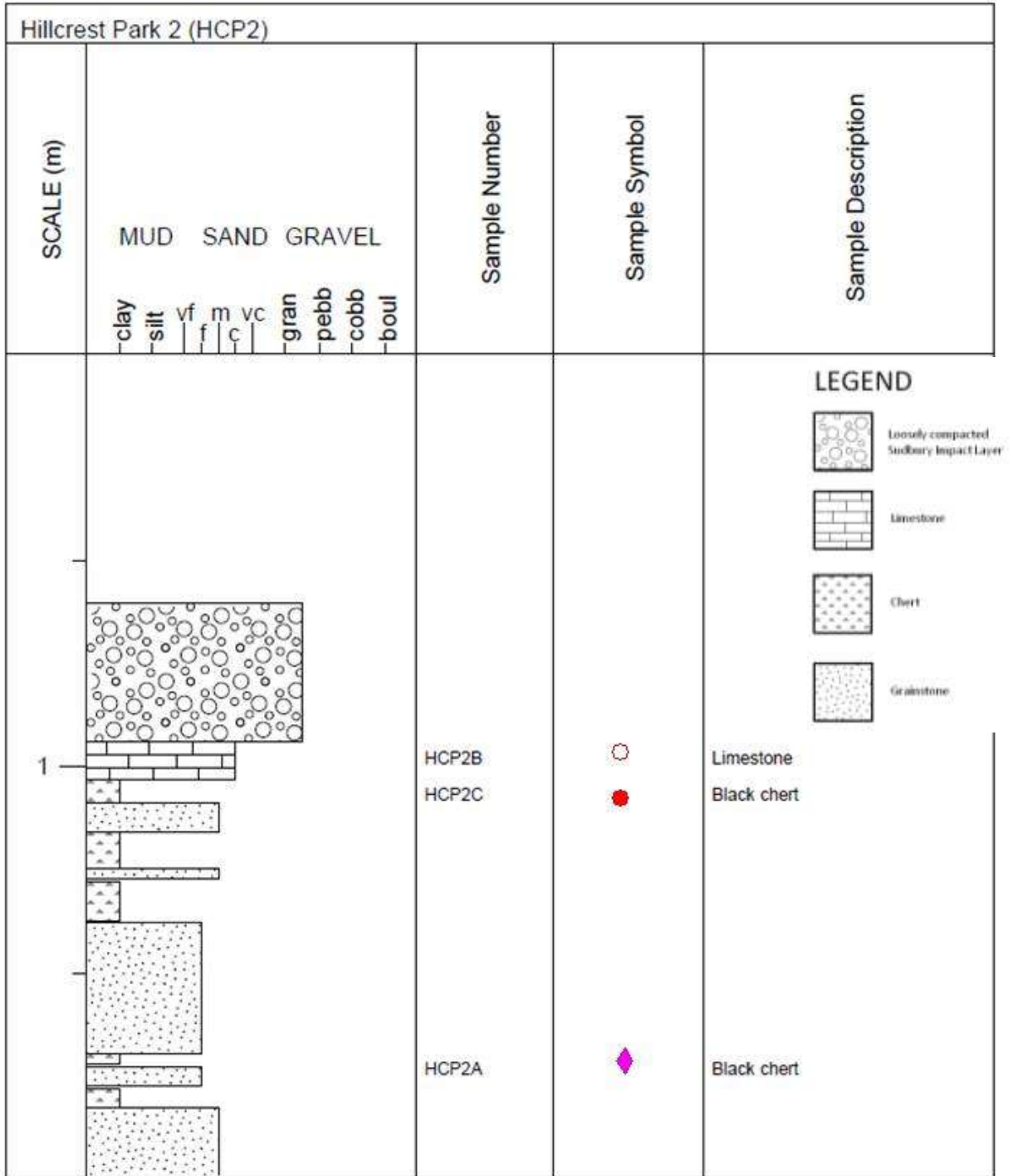
At the bottom of Hillcrest outcrop 3 (HCP3) is a 44cm thick unit of fine-grained grainstone with imbedded large chert fragments, averaging up to 20cm in size. On top lies a 4cm unit of fine-grained grainstone, followed by an 8cm unit of black chert. This is in turn followed by a 14cm unit of medium-grained grainstone. The following layer is approximately 85cm thick, and consists of a medium-grained grainstone with chert veins throughout the layer, averaging about 1-2cm in thickness, (Figure 82) and includes a limestone fragment approximately 7cm in length. The chert veins in the upper 10cm of this unit are fractured, unlike those 75cm below. The Sudbury Impact Layer overlies this unit, partially draping over it, and is approximately 23cm in thickness. The ejecta unit also displays chert veining (Figure 83). No samples were taken from this outcrop.

Figure 71. Stratigraphic Representation of Hillcrest Park 3.
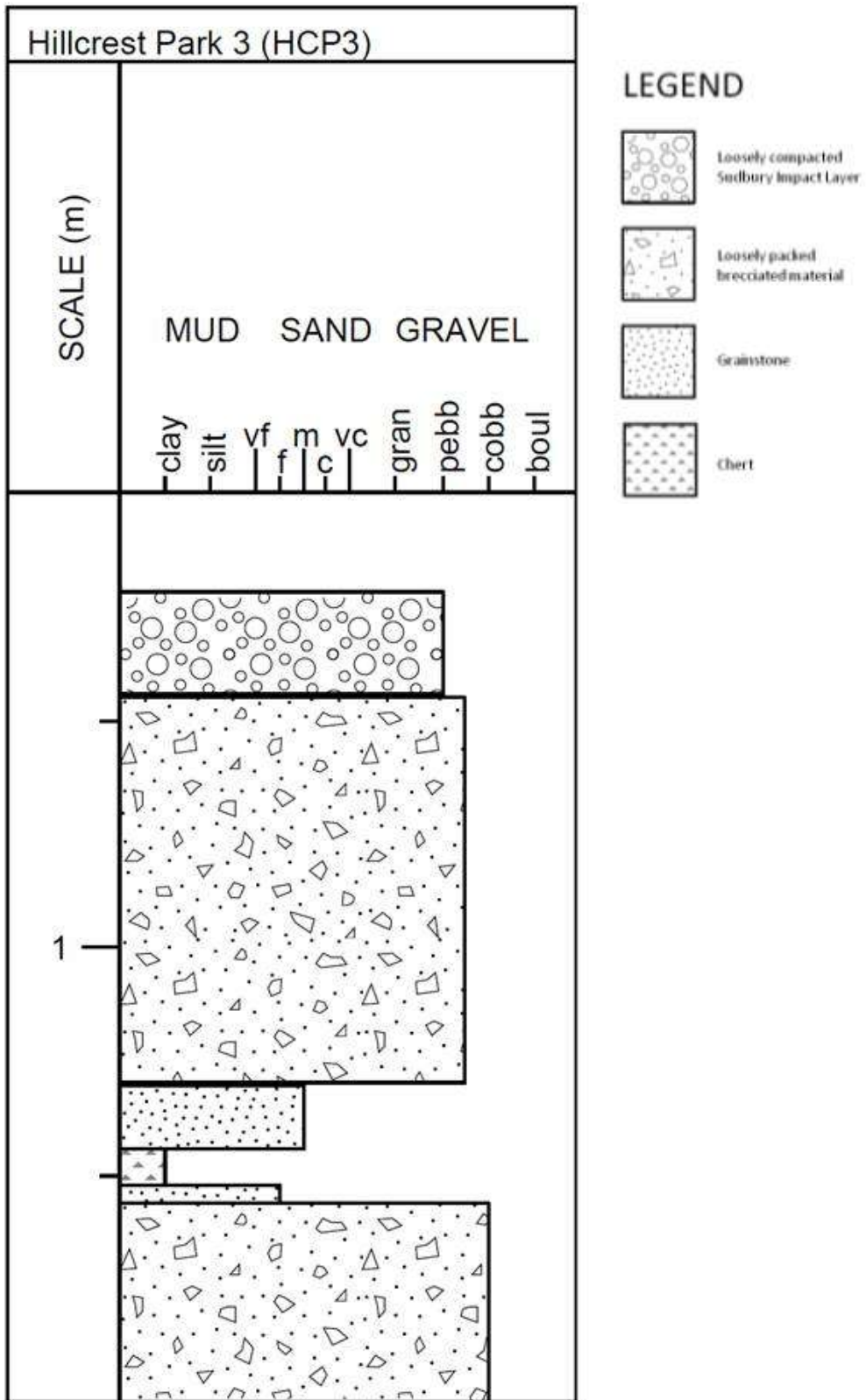
At the bottom of Hillcrest outcrop 4 (HCP4), is a 5cm unit of black chert with an ankeritic block situated in it. This is followed by 12cm of fine-grained ankeritic grainstone, with a 10cm unit of chert lying on top. Overlying the previous unit is a 9cm thick fine-grained ankeritic grainstone layer. On top is situated a 37cm lens of the Sudbury Impact Layer, with carbonate cement (HCP4B✳) and black chert veins (HCP4A✛). On top lies another lens of the S.I.L., approximately 28cm in thickness, consisting of the same carbonate cement, chert veins, but with abundant pebble-sized ankerite fragments. Overlying this is yet another Sudbury Impact Layer lens approximately 94cm thick (Figure 84). It consists of ejecta material in an ankeritic cement (HCP4C☆), chert veins 0.5cm-2cm thick (Figure 85), pebble-sized ankerite ranging from 0.5-4cm, other pebble-sized material, and fine-grained ankeritic grainstone cobbles averaging 17cm in length.

Figure 72. Stratigraphic Representation of Hillcrest Park 4.
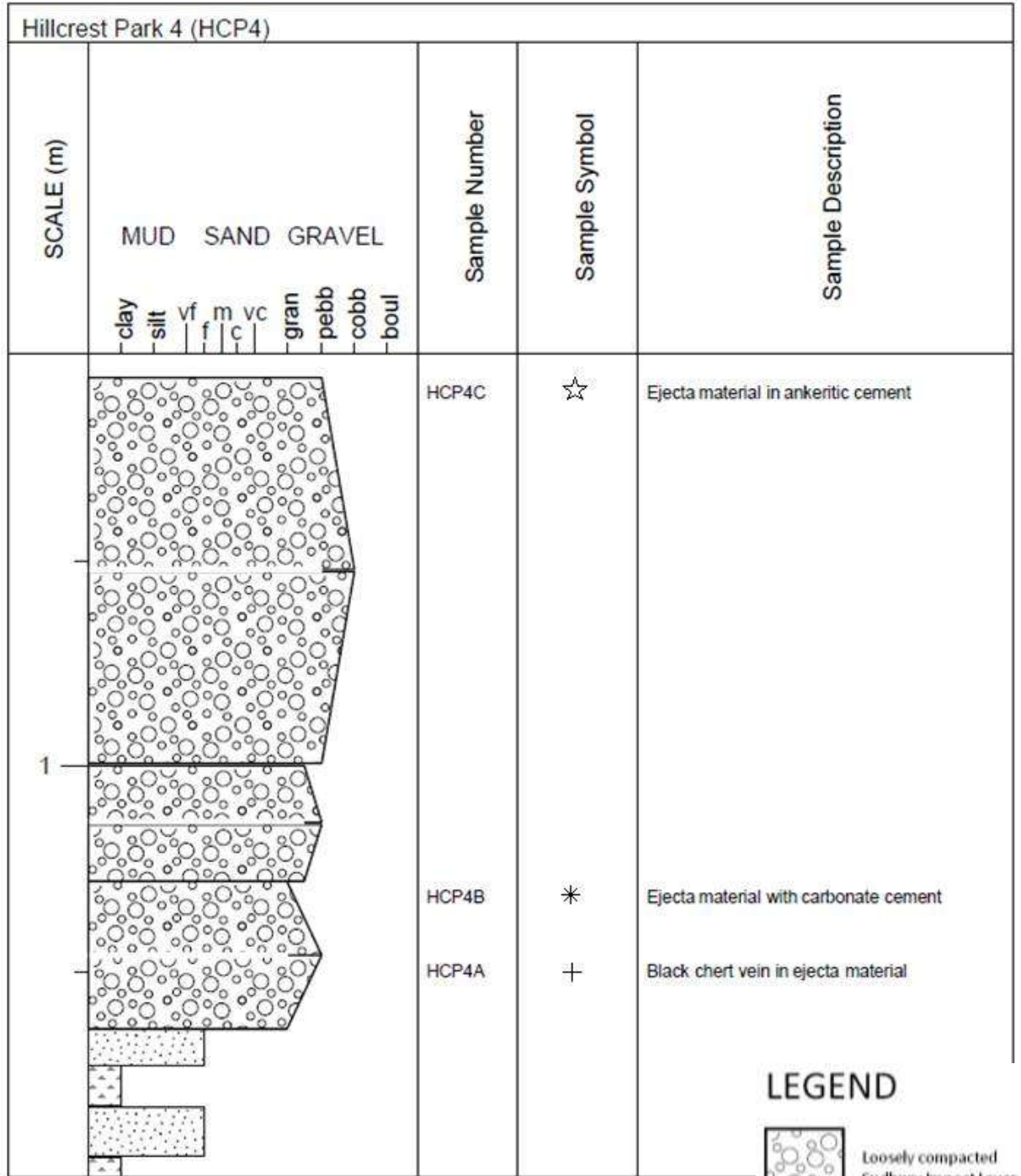
At the bottom of Hillcrest outcrop 5 (HCP5), is 7cm of black chert (HCP5F ⬦), followed by 9cm of medium-grained ankeritic grainstone. This is succeeded by 3cm of black chert (HCP5A ★), and 8cm of medium-grained ankeritic grainstone. On top lies a jumbled lens of the Sudbury Impact Layer measuring 105cm in thickness, draping over the underlying rock, and consisting of ejecta material in ankeritic cement, chert fragments up to 25cm in length, and lapilli (Figure 86, 87). Samples consist of: HCP5C ✚ (ejecta material above lapilli lens), HCP5D ✖ (ejecta material touching lapilli lens) and HCP5E ✖ (ejecta material laterally near lapilli). It is vital to note that in this outcrop, as the Sudbury Impact Layer (Figure 88) was being sampled with a rock hammer, and finally removed (Figure 89), a layer of fan-shaped crystal rosettes was discovered (HCP5B ✚) (Figure 89). Samples of the rosettes have been determined to be composed of calcite.

Figure 73. Stratigraphic Representation of Hillcrest Park 5.
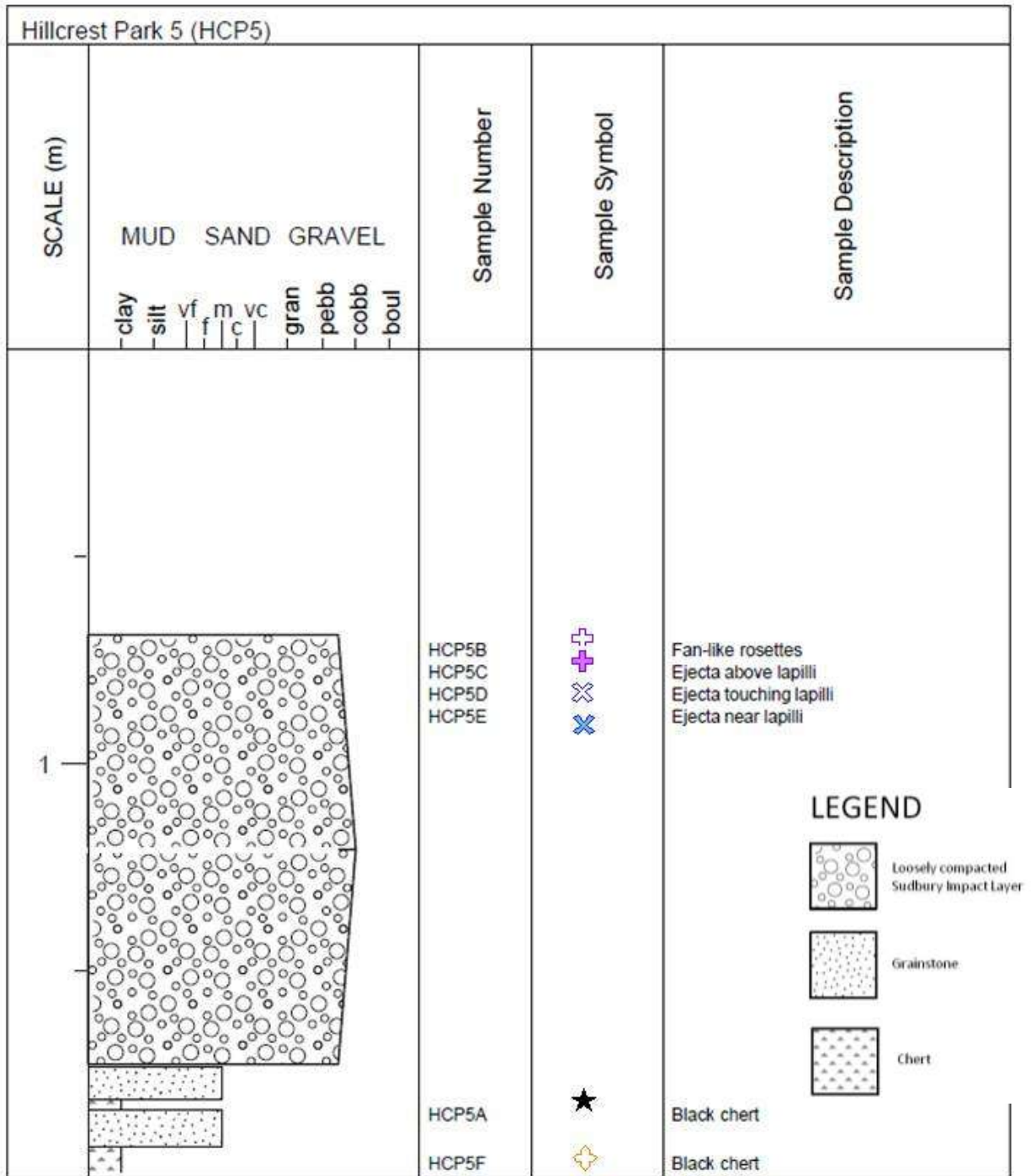
It is also important to note that at the top of Hillcrest Park at UTM coordinates

334682.39E and 5366958.78N 16N NAD83, a sample of stalactites (HCP STALACS) formed in a vug (Figures 90, 91) was collected and analyzed.

Figure 74. (Upper) Black chert unit from HCP1.
Figure 75. (Lower) Ankeritic-altered stromatolitic limestone from HCP1. It overlies a chert vein and its top is truncated by the Sudbury Impact Layer.

Figure 76. (Upper) Sudbury Impact Layer containing large clasts of underlying material (HCP1).
Figure 77. (Lower) Sudbury Impact Layer containing cobbles of chert (HCP1).
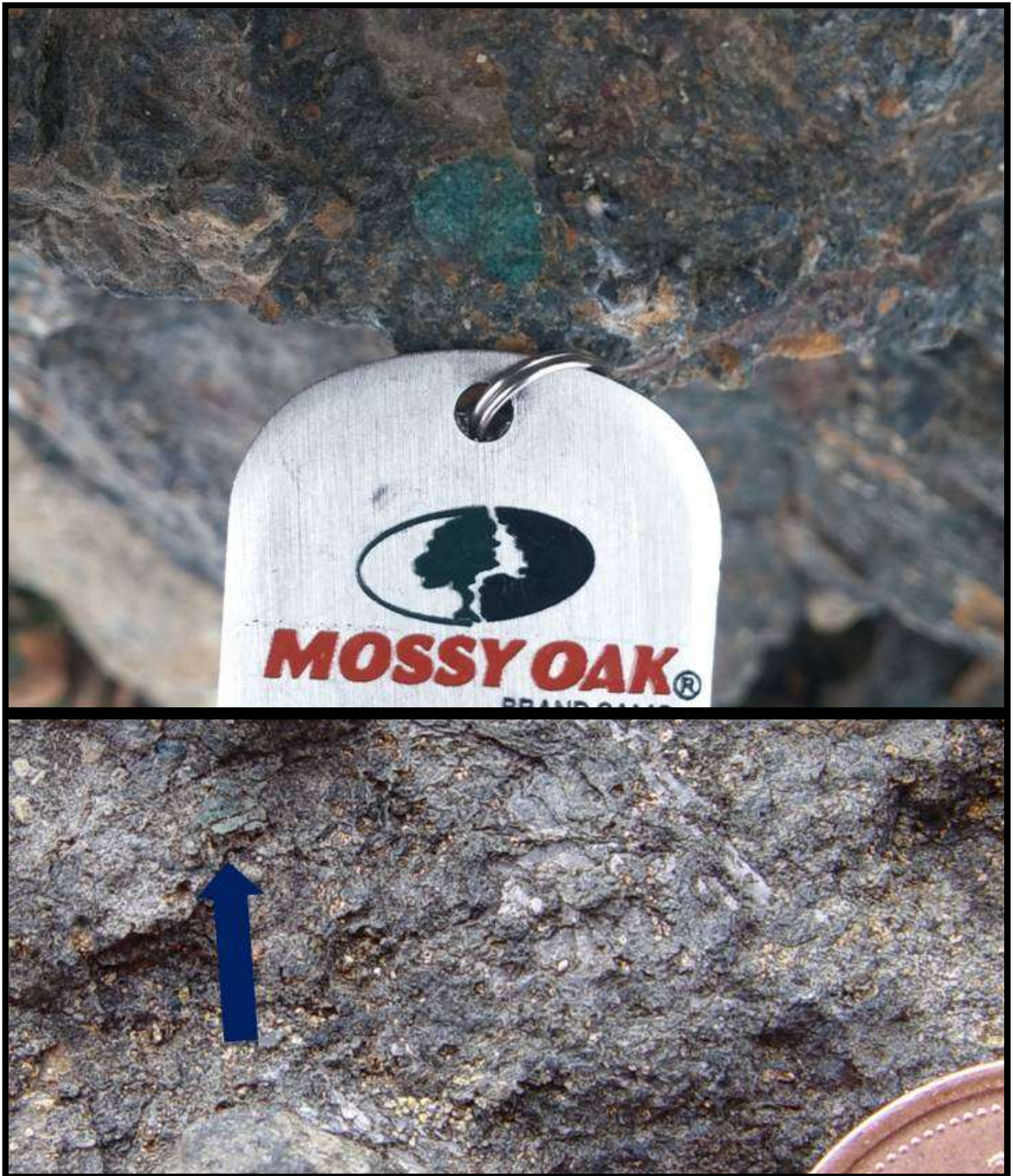
Figure 78. (Upper) Glauconite fragment in ejecta layer at HCP1 (Mossy Oak 3 cm wide beer opener used for scale).
Figure 79. (Lower) Blue arrow pointing to fragments of glauconite in the ejecta layer at Hillcrest Park.

Figure 80. (Upper) Fractured chert unit underlying the ejecta layer that has been infilled with ankerite cement.
Figure 81. (Lower) Ejecta layer with white calcite and yellow ankerite cement (HCP2).

Figure 82 (Upper) Chert veining in medium-grained grainstone unit in HCP3.
Figure 83. (Lower) Chert veining in ejecta unit in HCP3.

Figure 84. (Upper) Sudbury Impact Layer ejecta material in overlapping large lenses (HCP3).
Figure 85. (Lower) Ejecta unit containing lapilli with chert veins throughout (HCP3).

Figure 86. (Upper) Sudbury Impact Layer containing ankeritic-replaced accretionary lapilli.
Figure 87. (Lower) Sudbury Impact Layer containing larger accretionary lapilli.

Figure 88. (Upper) Sudbury Impact Layer containing mini accretionary lapiili. S.I.L. with fan-shaped crystal rosettes.
Figure 89. (Lower) Fan-shaped crystal rosette in the Sudbury Impact Layer.

Figure 90. (Upper) Silica stalactite formations in vug at top of Hillcrest Park.
Figure 91. (Lower) Silica stalactite formations on top of Hillcrest Park that are badly weathering.

2.3.2   Geochemistry

View Table 3 for Hillcrest Park geochemistry. The samples in Hillcrest Park have low amounts of siliciclastic material mixed in with the chemical sediments (Figure 92). Samples HCP1B (limestone), HCP1C (fine-grained ankeritic grainstone), and HCP2B (limestone) are highest in vanadium. Samples HCP1B, HCP2B, and HCP4B (carbonate cement from ejecta material) are highest in REE Total, while HCP2B and HCP4B are the samples that are most enriched in molybdenum.   Sample HCP2B is the only sample that has high combined levels of both molybdenum and vanadium as compared to other samples.

In Figure 94A samples HCP1B and HCP2B exhibit a hat-shaped REE curve with high levels of gadolinium and negative cerium anomalies. Figure 94B shows samples HCP1A and HCP4B with a similar curve with high levels of europium and even higher gadolinium values. Figure 94C shows all samples with a positive europium anomaly but only samples HCP2A and HCP STALACS have large negative cerium anomalies. In Figure 94D, both samples exhibit similar curves with positive europium anomalies and high levels of gadolinium, but HCP1C exhibits a negative cerium anomaly while HCP4C does not. Figure 94E and 94F show six samples with similar, but not exactly matching, REE curves. All samples show high levels of europium and also high, but lesser values of gadolinium.

In Figure 95, every graph except for 95A shows samples in a clustered manner. Samples HCP2A (black chert), HCP2B (limestone), and HCP STALACS (stalactites) exhibit the highest negative cerium anomalies, while HCP2C (black chert) shows the highest levels of cerium of the samples. There seems to be a relationship between samples that exhibit high levels of europium also exhibiting high levels of gadolinium. HCP2A exhibits a negative cerium anomaly but the highest europium anomaly.

Figure 92. Bivariate plots of samples from Hillcrest Park (HCP). A) Positive linear correlation exists between TiO$_2$ and Al$_2$O$_3$. B) Loose linear positive correlation between Al$_2$O$_3$ and REE Total with HCP1B and HCP2B showing extreme REE enrichment. C) All samples have low to near-zero values of vanadium except for HCP1B, HCP1C, and HCP2B which display extreme vanadium enrichment. D) All samples exhibit low molybdenum values with the exception of HCP2B and HCP4B that display molybdenum enrichment.
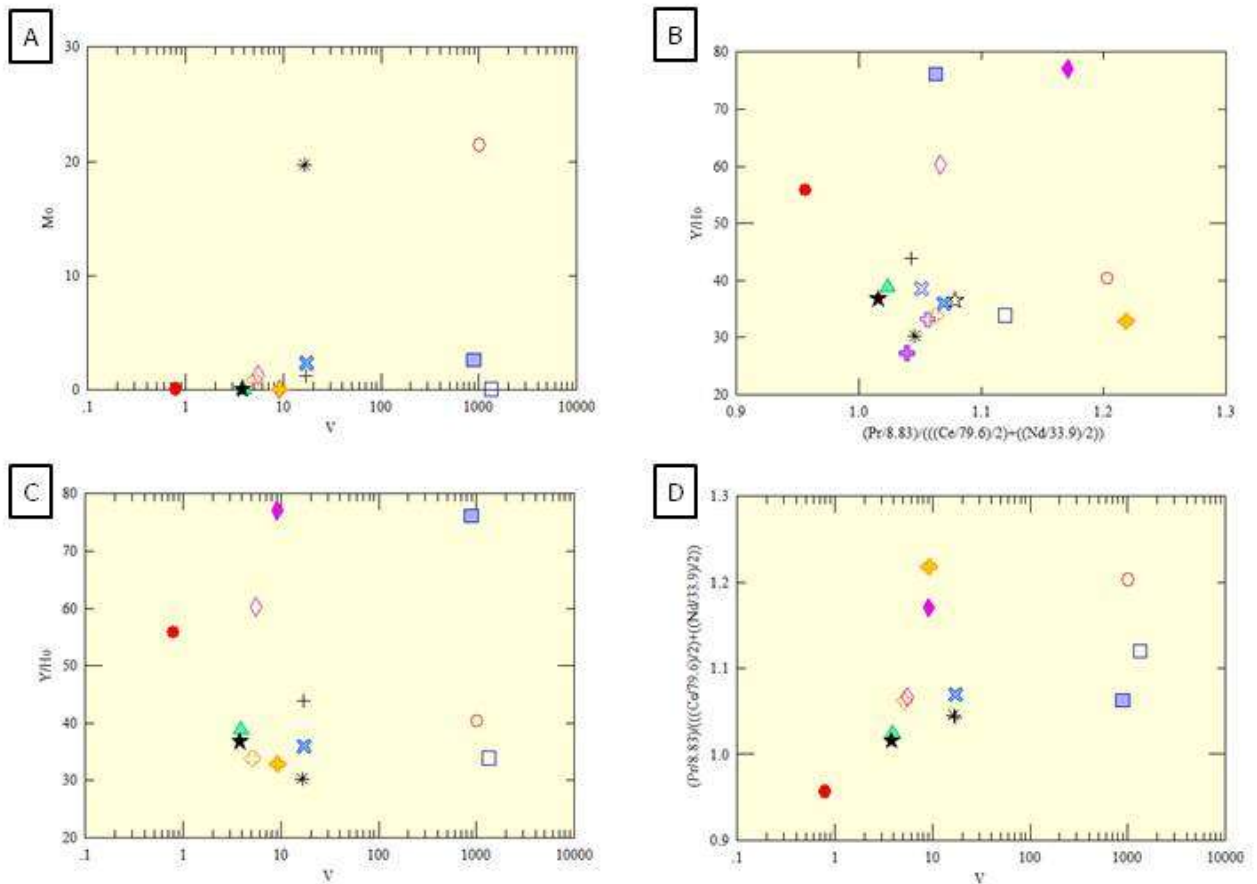
Figure 93. Bivariate plots of samples from Hillcrest Park (HCP). A) No correlation exists between Mo and vanadium. Most samples exhibit near-zero to low values of molybdenum and vanadium while HCP4B exhibits the highest molybdenum value, and HCP1B and HCP1C exhibit extreme vanadium enrichment. Sample HCP2B displays both elevated levels of Mo and V. B) Clustered pattern of samples. C) Samples HCP1B, HCP1C, and HCP2B which show enriched levels of vanadium. HCP2A shows low levels of vanadium but highest level of Y/Ho ratio, followed by HCP1D, then HCP2C. Sample HCP1c shows the highest levels of both Y/Ho and V. D) No correlation between Ce and V. Sample HCP2B exhibits one of the highest V levels and one of the most pronounced negative Ce anomaly.

Figure 94. Rare Earth Element spider plots standardized to Taylor and McLennan (1985) PAAS. A) HCP1B and HCP2B exhibit a hat-shaped REE curve with positive gadolinium anomalies, with negative cerium anomalies, and no Eu anomaly. B) HCP1A and HCP4B show similar curves, but with a positive europium anomaly, an even higher gadolinium anomaly, and much smaller negative Ce anomalies. C) All samples show a positive europium anomaly but only samples HCP2A and HCP STALACS show an extreme negative cerium anomaly. D) Both samples exhibit curves that

are similar but HCP1C shows a large negative cerium anomaly while HCP4C shows only slight to nill negative cerium levels. E) Rare Earth Element spider plots standardized to Taylor and McLennan (1985) PAAS. Samples HCP1D, HCP5C and HCP5D show similar curves, with high europium and gadolinium values, and minor to no negative cerium anomalies. F) Samples HCP4A, HCP5B, and HCP5E also show similar curves with high europium and gadolinium anomalies.

Figure 95. Bivariate plots of rare earth element anomalies of Hillcrest Park (HCP) samples. All values were normalized to PAAS before anomaly calculations. A) Linear correlation exhibited between lanthanum versus cerium anomalies. This relationship is probably due to Ce being present in both equations. B) There is no correlation between Ce and Gd anomalies. Sample HCP STALAC has the highest negative cerium anomaly and the lowest positive gadolinium anomaly. C) Samples that have higher positive europium anomalies also have more positive cerium anomalies, except for samples HCP1B, HCP2B, and HCP STALACS. Sample HCP2A on the other hand exhibits a high europium anomaly and a high negative cerium anomaly. D) There is loose correlation between samples when they have higher europium anomaly they have a higher positive gadolinium anomaly as well.

2.3.3   Interpretations

The Gunflint Formation directly underlying the stromatolites and Sudbury Impact Layer consists of ankerite grainstone that is silicified in places. Thick grainstone layers without interbedded fine-grained chemical muds are typical of the upper portions of shoaling upwards sequences in the upper Gunflint (Pufahl and Fralick, 2004). It is difficult to ascertain whether the chert layers are primary deposits, silicified areas of the deposit or veins. However, as there are abundant cross-cutting black chert veins in the deposit that is their most likely origin. The ankerite grainstone sample has extreme V enrichment and a negative Ce anomaly. Two of the five black chert samples also have negative Ce anomalies, one which is quite large. This indicates alteration by oxidized fluids that were carrying V and had leached REEs from a source where the Ce oxidized and was removed from solution.

The samples of coarse grainstone and stromatolites from the overlying limestone have some of the largest negative Ce anomalies and the smallest, virtually non-existent Eu anomalies. The stromatolite sample is highly enriched in V, and the grainstone sample is very enriched in both V and Mo. This strongly indicates formation of the calcite cements, which dominate the samples, from oxygenated meteoric waters. This unit was lithified by precipitation of the calcite cements prior to deposition of the Sudbury Impact Layer. Lithification prior to impact is evident because of the shattered chert immediately below the contact of the Sudbury Impact Layer and because of the rip-up boulders, blocks, and pieces of the underlying Gunflint units that are found mixed in with the ejecta layer that overlies the Gunflint formation. The green fragments of glauconite, marine sediments, are silicified, further denoting silicification prior to deposition in the ejecta layer.

Five of the eight samples that came from the Sudbury Impact Layer have negative Ce anomalies. Most of the samples are mixtures of resedimented ankeritic material, small chert fragments, devitrified glass and calcite cement. The geochemistry of the sample will be determined by which of these dominates. The sample of calcite cement is very enriched in Mo and does not have a Eu anomaly. The sample of chert stalactite has the largest negative Ce anomaly of any of the samples. This indicates that the calcite cements, which probably represent phreatic meteoric cements, and the vadose chert cements probably formed from oxygenated water; a similar conclusion to Burton and Fralick (2007) and Fralick and Burton (2008), which they developed after examining other outcrops of the Sudbury Impact Layer. The Sudbury Impact Layer at Hillcrest Park is organized into large lenses with smaller lenses of accretionary lapilli. This denotes either deposition or reworking by a fluid that carried the material in traction.

2.4   Waverly Towers

2.4.1   Lithofacies Description

Waverly Towers is located in Thunder Bay, Ontario, Canada, at UTM coordinates 335137.73E and 5367249.30N 16 N NAD83. Refer to Figures 96 and 105 for stratigraphic representations of the Waverly Towers outcrop. Addison et al. (2010) previously found and described this site calling it the Banning Street Bluff site in their paper.

At the bottom of the north side of the outcrop is a 90cm unit of ankeritic medium-grained grainstone, that is overlain by a badly silicified ankeritic grainstone approximately 30 cm in thickness (WT1 ▲) (WT2 ▢) (Figure 97). This unit sits directly below the ejecta layer and has abundant chert replacement (Figure 98). A 500cm thick layer of the Sudbury Impact Layer overlies the silicified unit. The ejecta layer can be divided into two layers: A bottom layer of 100cm that consists of small, pea-like sized melt fragments (Figure 99, 100) along with cobbles, some as large as 40cm, situated in an ankeritic matrix (WT3 ▢). The upper layer of 400cm consists of boulders and large blocks (Figure 101) of ejecta material similar to the underlying layer of small melt fragments. The blocks are disrupted and at various angles with pyritic black shale separating some of the larger blocks. Some blocks contain stromatolite fragments (Figure 102) (WT4 ◇), similar to those eroded from underlying layers at other sites. The sharp outer edges of the blocks attests to their lithification prior to disruption. In places black, pyritiferous shale forms the matrix between the blocks. One of the larger blocks has, on one side, about 10cm of large carbonate crystals appearing similar to chicken-wire texture (Figure 103, 104).

Figure 96. Stratigraphic Representation of Waverly Towers (WT) North Side
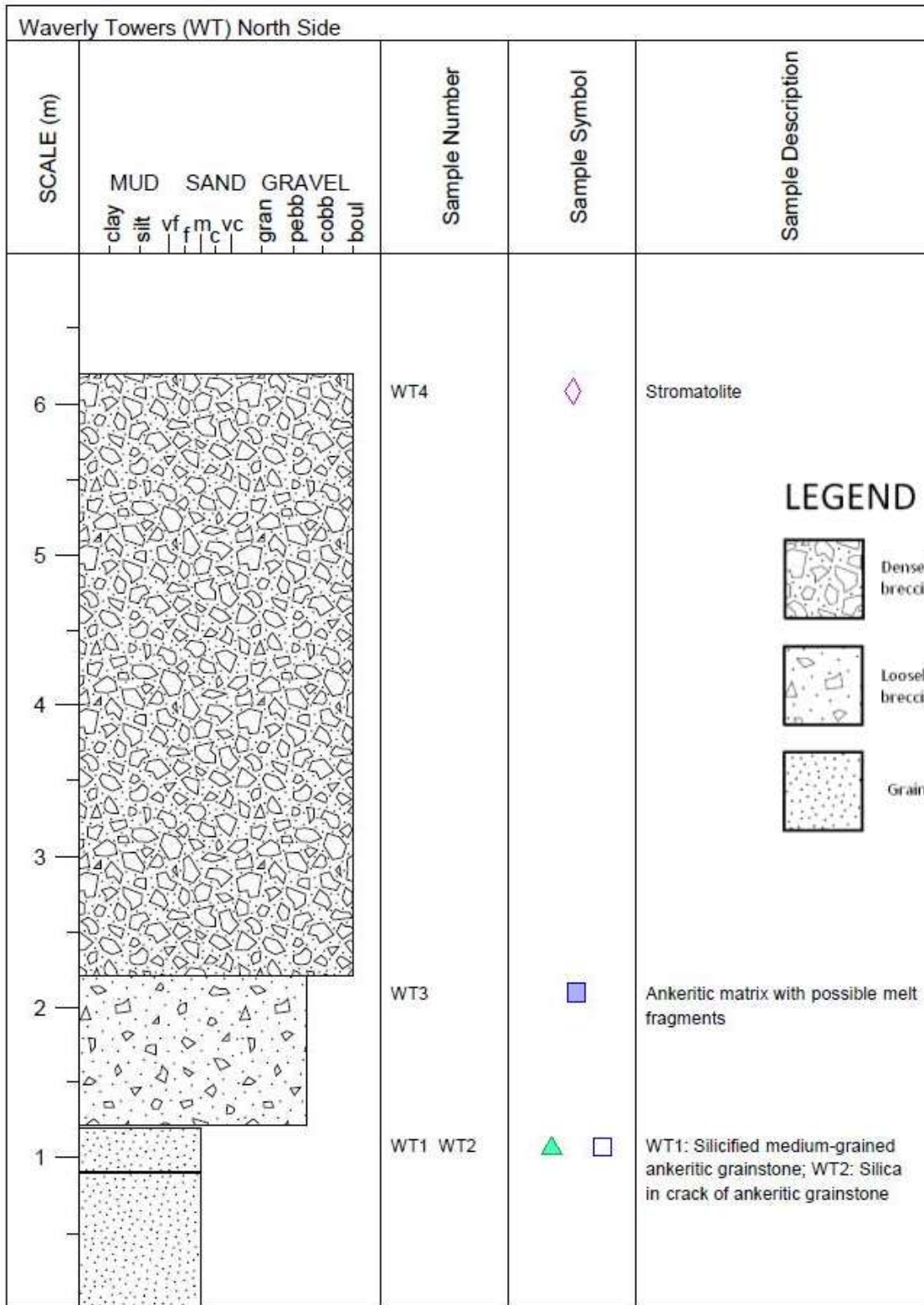
Figure 97. (Upper) Waverly Towers North Side succession of units starting with ankeritic medium-grained grainstone, in which the top 30cm of the unit is silicified with abundant chert replacement. This is overlain by the Sudbury Impact Layer.
Figure 98. (Lower) Silica veins in cracks in ankeritic grainstone.

Figure 99. (Upper) Devitrified vesicular impact glass in ejecta layer surrounded by ankeritic finer grains.
Figure 100. (Lower) Close-up of devitrified vesicular impact glass.

Figure 101. (Upper) Boulders and blocks in ejecta layer from Gunflint formation surrounded by smaller ejecta material and pyritiferous black shale in some places.
Figure 102. (Lower) Rip-up block from Gunflint formation containing stromatolite fragment.

Figure 103. (Upper) Block in ejecta layer containing large chicken-wire carbonate crystals.
Figure 104. (Lower) Different angle of block in ejecta layer containing large chicken-wire carbonate crystals.
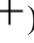
Starting at the bottom of the south side of the outcrop, there is a 2cm layer of fine-grained grainstone that rests under 2cm of shale. This is overlain by 3cm of fine-grained grainstone that extends approximately 100cm laterally becoming approximately 20cm thick. Overlying this layer is a 1cm layer of hematite. Twenty centimeters of shale (WT5 ◆ , WT6 ○) overlies the previous unit, although an 11cm thick fine-grained grainstone lens (WT7 ●) sits in the middle of the shale unit, making the entire layer ~31cm thick (Figure 106). This grainstone lens extends ~110cm laterally. Above this unit sits a 60cm carbonate grainstone (WT8 ✛) with chert veins. The chert veins are protruding out of the weathered carbonate grainstone. The top of this unit is very silicified (Figure 107). Stringers of silica intrude down into the top of this layer.

Figure 105. Stratigraphic Representation of Waverly Towers (WT) South Side.
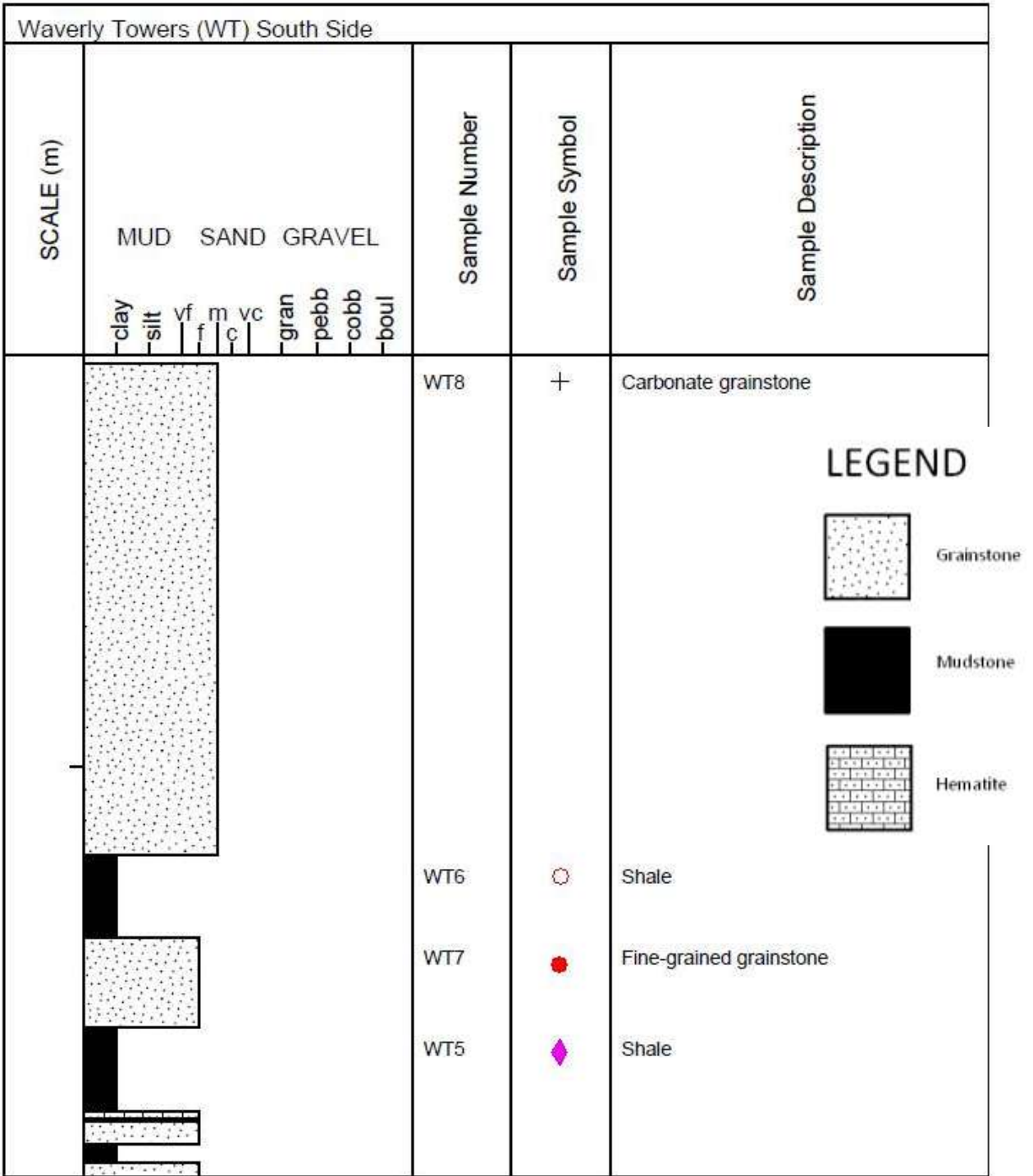
Figure 106. (Upper) Shale layer overlain by a grainstone lens, overlain by another shale layer from Waverly Towers South Side.
Figure 107. (Lower) Carbonate grainstone unit where the top of the unit is very silicified from Waverly Towers South Side.

2.4.2   Geochemistry

View Table 4 for Waverly Towers geochemistry. The samples from Waverly Towers (WT) have medium to high amounts of siliciclastic sediments mixed in with the chemical sediments. Figure 108B has a cluster of points indicating that most samples have siliciclastic sediments mixed in with the chemical sediments, although samples WT1 and WT2 exhibit low levels of siliciclastic material but high levels of REEs. Figure 108C displays the same concept, but replacing REE Total with vanadium. Samples WT3, WT4, WT7, and WT8 have the highest values of Mo with medium amounts of Al_2O_3, while all other samples have near-zero values or undetectable amounts of Mo. WT5 and WT6 have near zero amounts of Mo but high levels of siliciclastic material.   Sample WT4 has the high amounts of both Mo and V, where samples WT3, WT7 and WT8 have both high values of Mo and lower levels of V, while the other samples have little to undetectable amounts of Mo but range from low to extreme amounts of V. WT6 has the most amount of vanadium, around 800ppm. Most samples in Figure 109B exhibit a correlation between Y/Ho and negative cerium anomaly, except for WT2 which exhibits a positive cerium anomaly and a medium Y/Ho ratio. Figure 109C shows that as Y/Ho increases so does vanadium in a sample, with the exception of WT6. Figure 109D shows no correlation between negative cerium anomaly and high levels of vanadium in samples. Figure 110 displays that all samples exhibit both positive Eu and Gd anomalies and that WT2 shows a large positive Ce anomaly. Figure 111 shows that all samples that display a negative cerium anomaly exhibit a positive gadolinium anomaly except for WT2 which displays a positive cerium anomaly with an extremely positive gadolinium anomaly. WT1 also displays a slightly positive cerium anomaly. All samples show a negative cerium anomaly and a europium anomaly, except for WT1 which exhibits a slightly positive cerium anomaly and an extreme high europium anomaly, and WT2, which has an extreme positive cerium anomaly with only a positive europium anomaly.
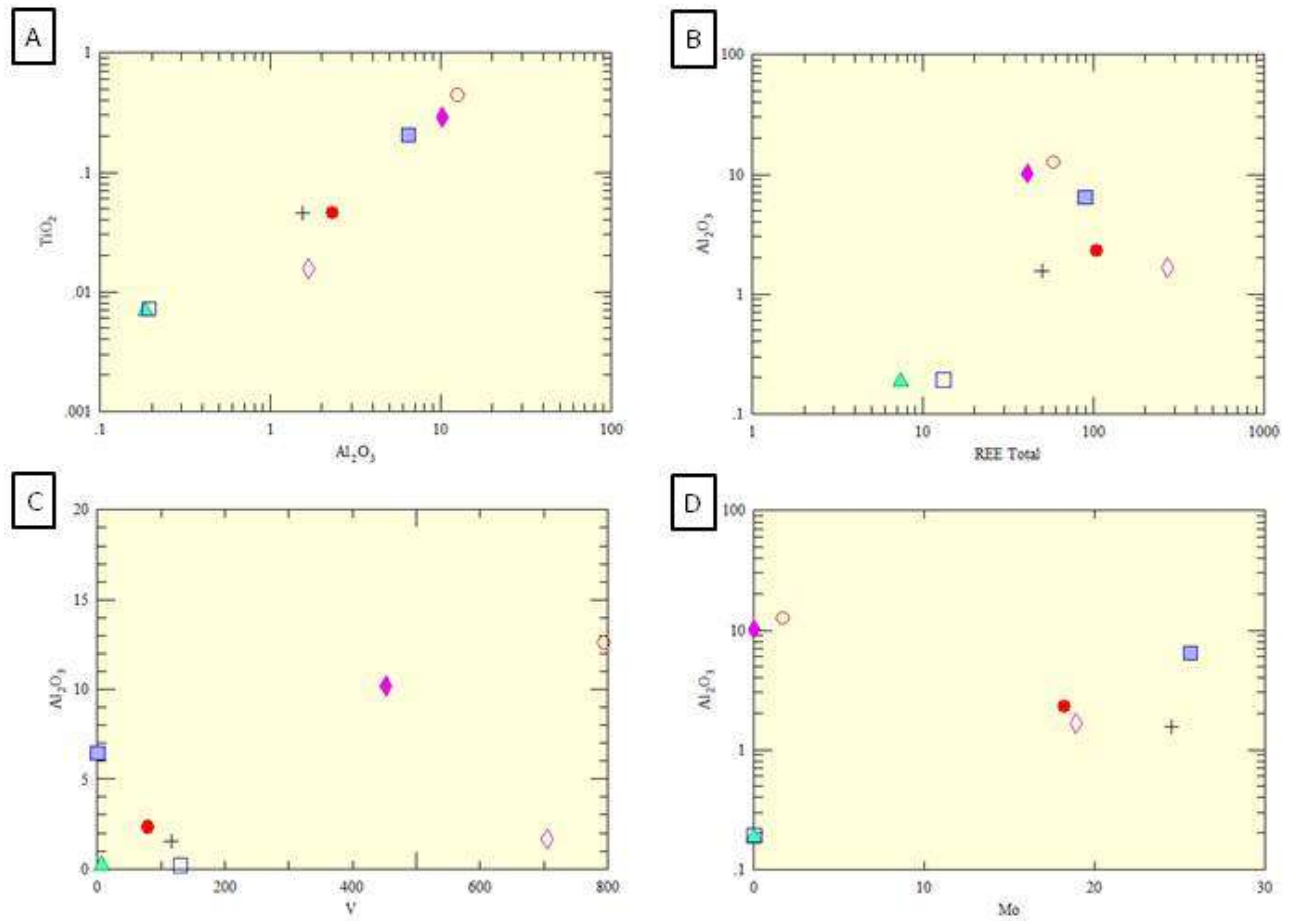
Figure 108. Bivariate plots of samples from Waverly Towers (WT). A) Positive linear correlation exists between TiO_2 and Al_2O_3. B) Weak correlation between Al_2O_3 and REE Total. C) No correlation between Al_2O_3 and V. While almost all samples, except for WT1, WT2 (silica in crack of grainstone), and WT4, increase in Al_2O_3 they also increase in V. D) No correlation exists between Al_2O_3 and Mo for samples WT3, WT4, WT7, and WT8. Other samples have near-zero values of Mo but increasing Al_2O_3 levels.
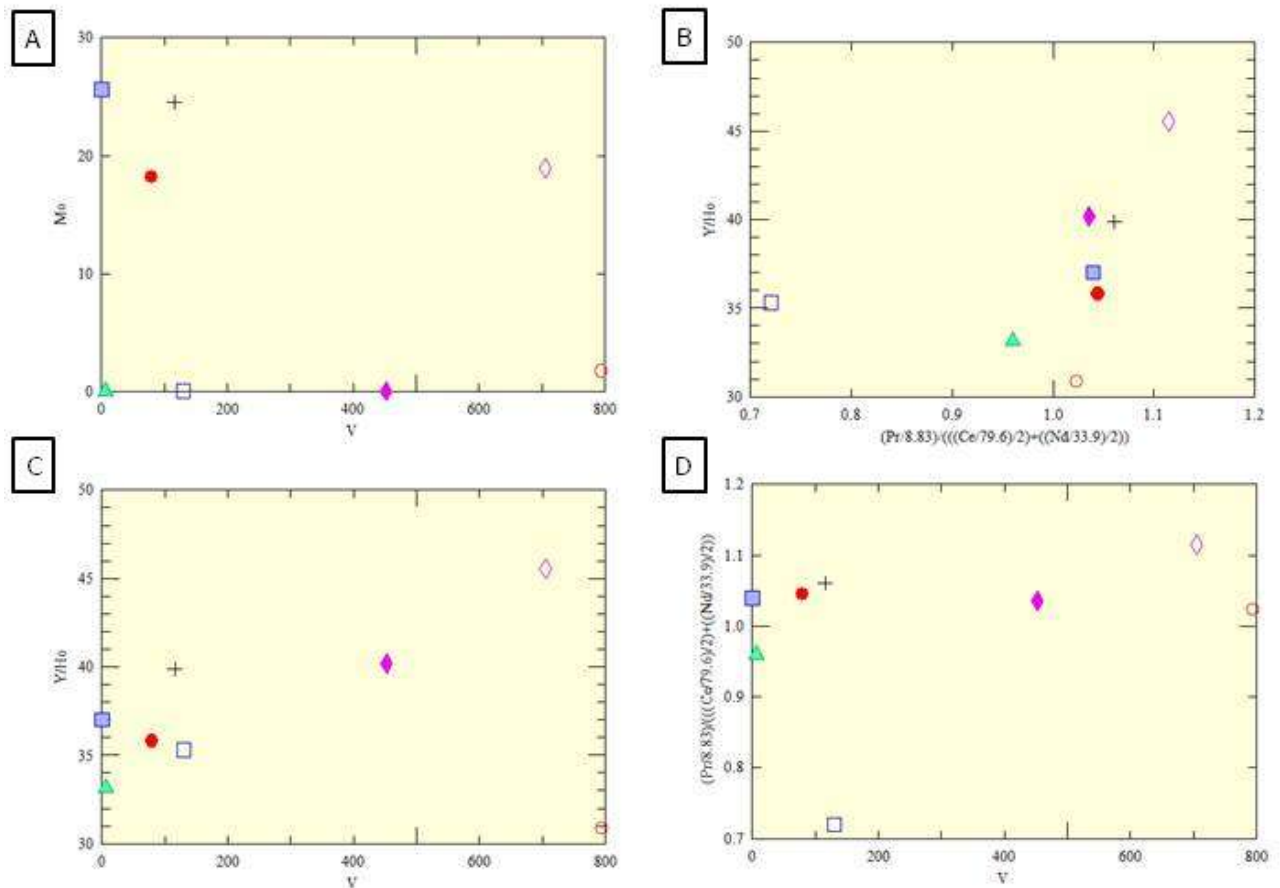
Figure 109. Bivariate plots of samples from Waverly Towers (WT). A) A scattered relationship exists between Mo and V; for samples WT4, WT7, and WT8 where Mo increases, V increases as well. The other samples have near-zero values for Mo, except for WT3 where it exhibits the highest amounts of Mo from the sample set. B) There is a positive linear relationship between Y/Ho ratio and cerium anomaly for most samples where as Y/HO increases, samples increases in negative cerium anomalies. The exception is for outlier samples WT2 and WT6 where WT2 has an elevated Y/Ho ratio but has a positive cerium anomaly, and WT6, which has elevated cerium levels but low Y/Ho ratio. C) Loose positive linear correlation between Y/Ho ratio and V for all samples except for WT6 where it is low in Y/Ho ratio but has the highest amount of vanadium (~800ppm). D) No correlation between cerium anomaly and V.
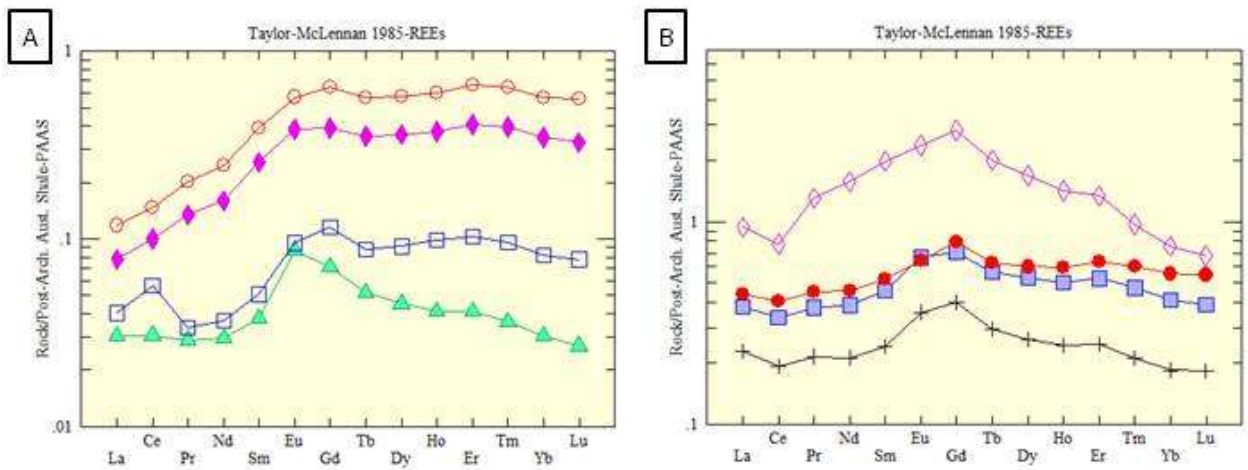
Figure 110. Rare earth element spider plots standardized to Taylor and McLennan (1985) PAAS. A) WT5 and WT6 (diamond and circle, shale samples) display similar REE curves depleted in LREEs. WT2 also displays a similar curve to WT5 and WT6, but it contains a large positive cerium anomaly. WT1 displays a different REE curve showing a pronounced positive europium anomaly, and a lesser, yet large gadolinium anomaly. B) All samples show a hat-shaped REE curve with elevated levels of both europium and gadolinium, and decreased levels of cerium. WT4 (stromatolite fragment) has the most pronounced hat-shaped REE curve with the largest gadolinium anomaly, and largest negative cerium anomaly.
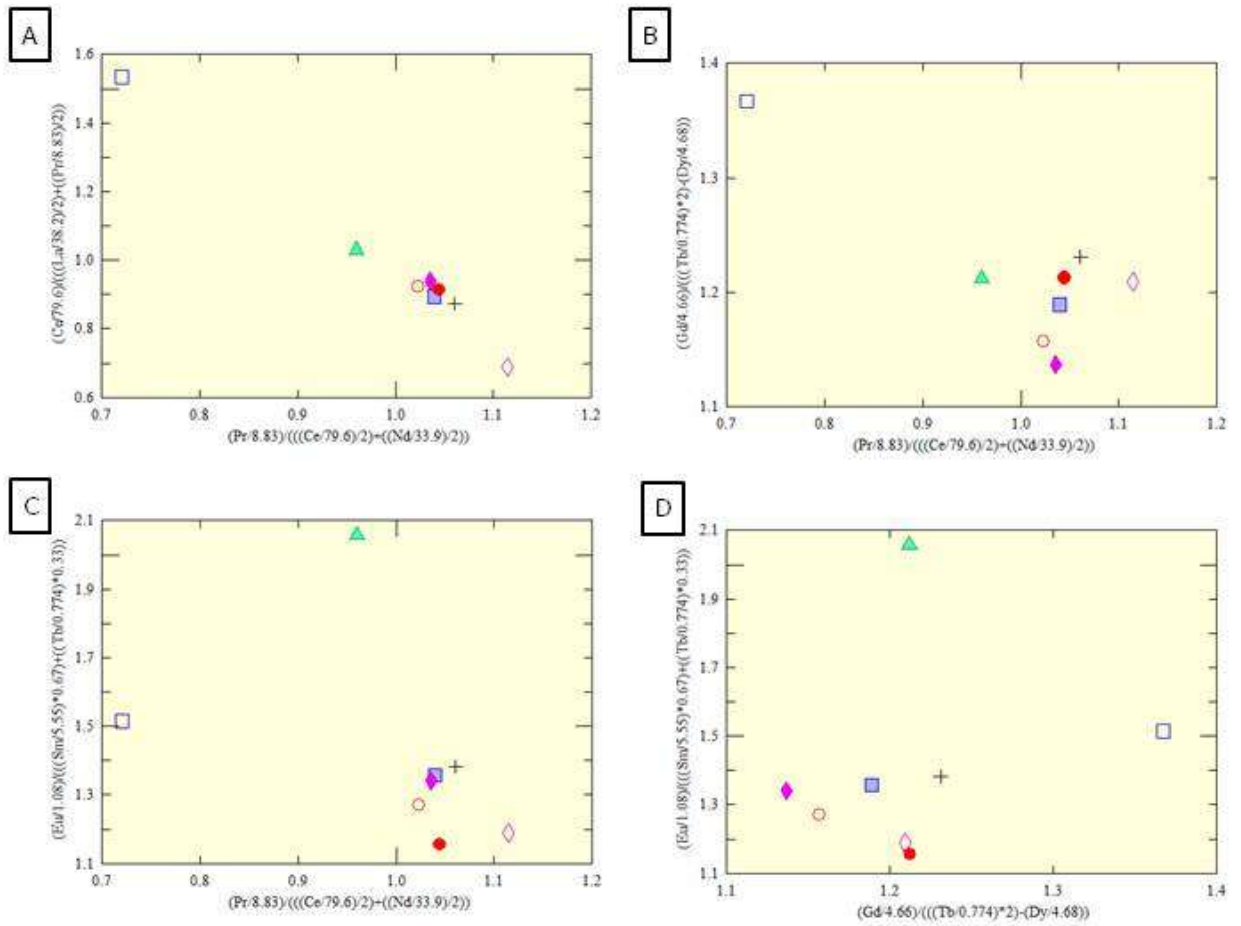
Figure 111. Bivariate plots exhibiting rare earth element anomalies of Waverly Towers (WT). All values were normalized to PAAS before anomaly calculations. A) Linear correlation is exhibited between lanthanum versus cerium anomalies. This relationship is probably due to Ce being present in both equations. B) Cluster of points with no trend. C) Cluster of points with no trend. WT1 (silicified grainstone) exhibits a slightly positive cerium anomaly but exhibits a very large europium anomaly. D) Cluster of points with no trend.

2.4.3   Interpretations

What can be interpreted from grainstones is that they were very likely deposited by storm events on the shallow shelf (Fralick, 1988; Pufahl and Fralick, 2004). Quiet water periods would be represented by the interbedded siliciclastic shale. The shale is depleted in LREEs when compared to PAAS. This indicates a more mafic source than the average post-Archean Australian shale composite. Basaltic volcanic tuffs and reworked tuffs are present in the upper Gunflint (Fralick et al, 2004) and this is probably the source of this material. The large V concentration in the shale also points to a mafic source. Of the four grainstone samples one has high V and Mo with a negative Ce anomaly, one has high V and Mo with a very small positive Eu anomaly, one has high V with a large positive Ce anomaly and one is non-descript. These grainstones show evidence of alteration by oxidized fluids that transported both V and Mo to where the reductants in the Gunflint sediments caused precipitation.

The Sudbury Impact Layer was deposited on the previously lithified Gunflint Formation. The stromatolite fragment, whose blocky calcite cement predates the Sudbury Impact Layer, has an extreme amount of V (705ppm), a large amount of Mo (18ppm), and a large negative Ce anomaly (61.41). This is similar to other limestone samples, and related to calcite cement formation in the meteoric phreatic zone by oxidized fluids (Burton and Fralick, 2007; Fralick and Burton 2008). The sample of fine-grained ankeritic debris with melt fragments contains large amounts of both V and Mo indicating its cements probably formed in a similar manner. The north side of the Waverly Tower outcrop consists of a large pile of boulder material, with individual boulders composed of SIL material and separated by thin seams of black shale. How this chaotic jumble of boulders formed is unknown, though they were pre-lithified and must have eroded from a proximal steep slope prior to Rove Deposition. Some of the ripped up boulders contain large crystals growing in a chicken-wire structure. This is indicative of a sabkha

environment where the crystals were able to precipitate in the sediment from saline groundwater. This is indicative that after the time of deposition of the S.I.L., the ocean or a saline lake must have been close to this site. It is likely that the chicken-wire texture overprints the white blocky calcite cement that grew in the ejecta material, though this was not able to be ascertained in the samples.

2.5   Hill and Markland Streets (HM)

2.5.1   Lithofacies Description

The outcrop logged at the corner of Hill and Markland Streets is located at UTM coordinates 334158.56E and 5366310.45N 16 N NAD83 and is 609cm by 2072cm in size. Figure 112 displays the stratigraphic representation of the Hill and Markland Streets outcrop. Addison et al. (2010) previously found and described this site calling it the Private Yard site in their paper. At the bottom of the section is a 30cm unit of medium-grained ankerite grainstone that is not silicified (Figure 113). It contains some ankeritic intraclasts and chert fragments (HM1 ▲). Above this lies 18cm of silicified medium-grained ankeritic grainstone that is very weathered (Figure 114) (HM2 ☐). This is overlain by 78cm of coarse-grained ankerite grainstone beds (HM3 ◼). A 5cm limestone unit that includes domal stromatolites (Figure 115) with coarse and fine-grained grainstone between, and banked up against the stromatolites, overlies the coarse-grained grainstone layer. Gullies are formed between some stromatolites, which then have been in-filled with both fine-grained and very coarse-grained grainstone (Figure 116). A 6cm thick very coarse-grained calcite grainstone layer overlies the stromatolitic limestone unit. A very sharp erosive contact cuts into the limestone unit with the Sudbury Impact Layer overlying it. The Sudbury Impact Layer averages about ~50cm in thickness, though its top has been eroded so the absolute thickness is unknown. The S.I.L. consists of pea-sized melt fragments and carbonate cement (Figure 117) (HM4 ◇, 5 ◆, 6 ⬡). The western portion of the top of the outcrop displays a more chaotic version of the Sudbury Impact Layer. It consists of large blocks, boulders, and cobbles (Figure 118) that have been ripped up from the underlying Gunflint Formation; the debris was deposited in a chaotic manner.

Figure 112. Stratigraphic Representation of Hill and Markland Streets (HM) Outcrop
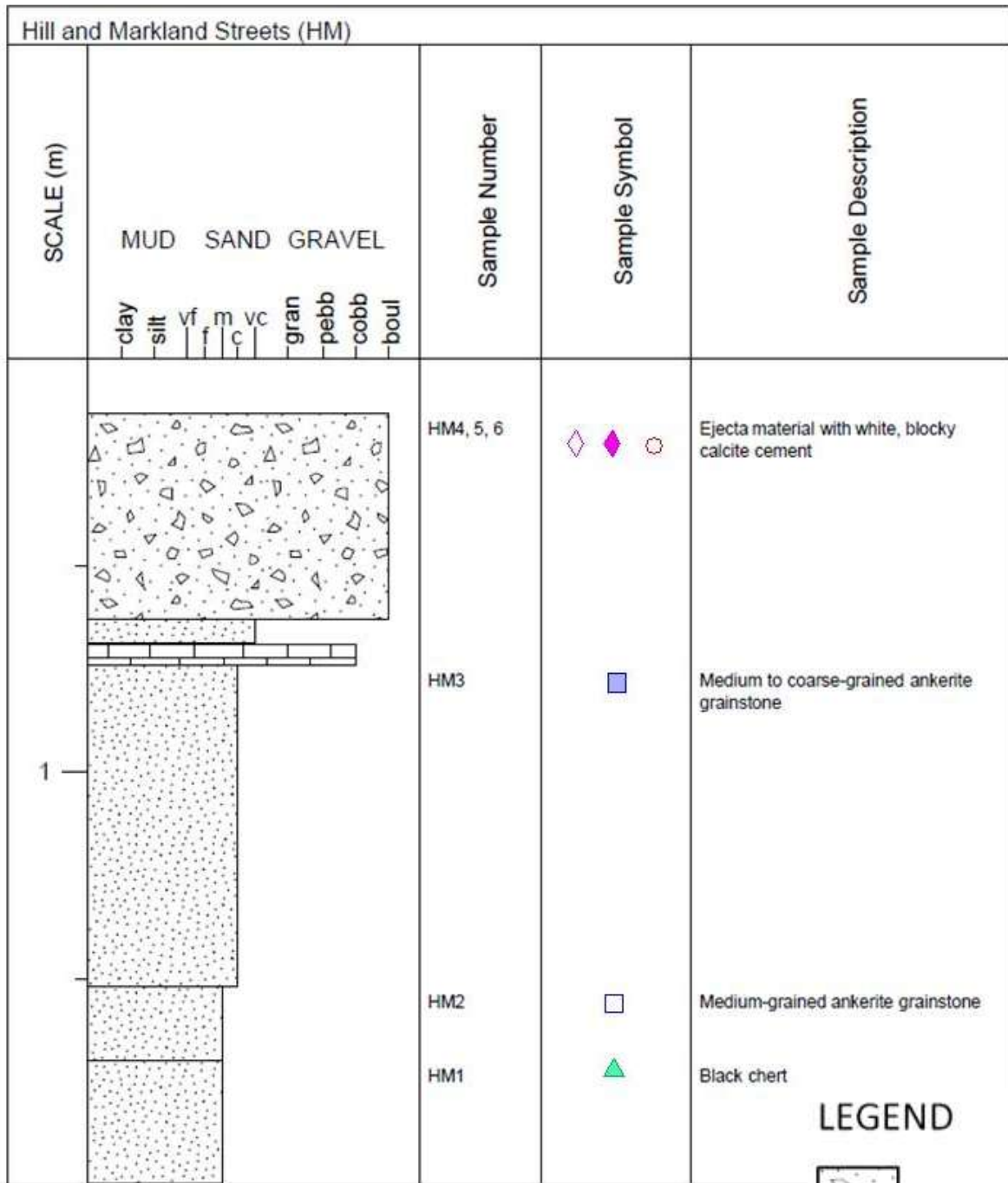
Figure 113. (Upper) Medium-grained ankeritic grainstone.
Figure 114. (Lower) Silicification of medium-grained ankeritic grainstone that overlies the non-silicified underlying grainstone.
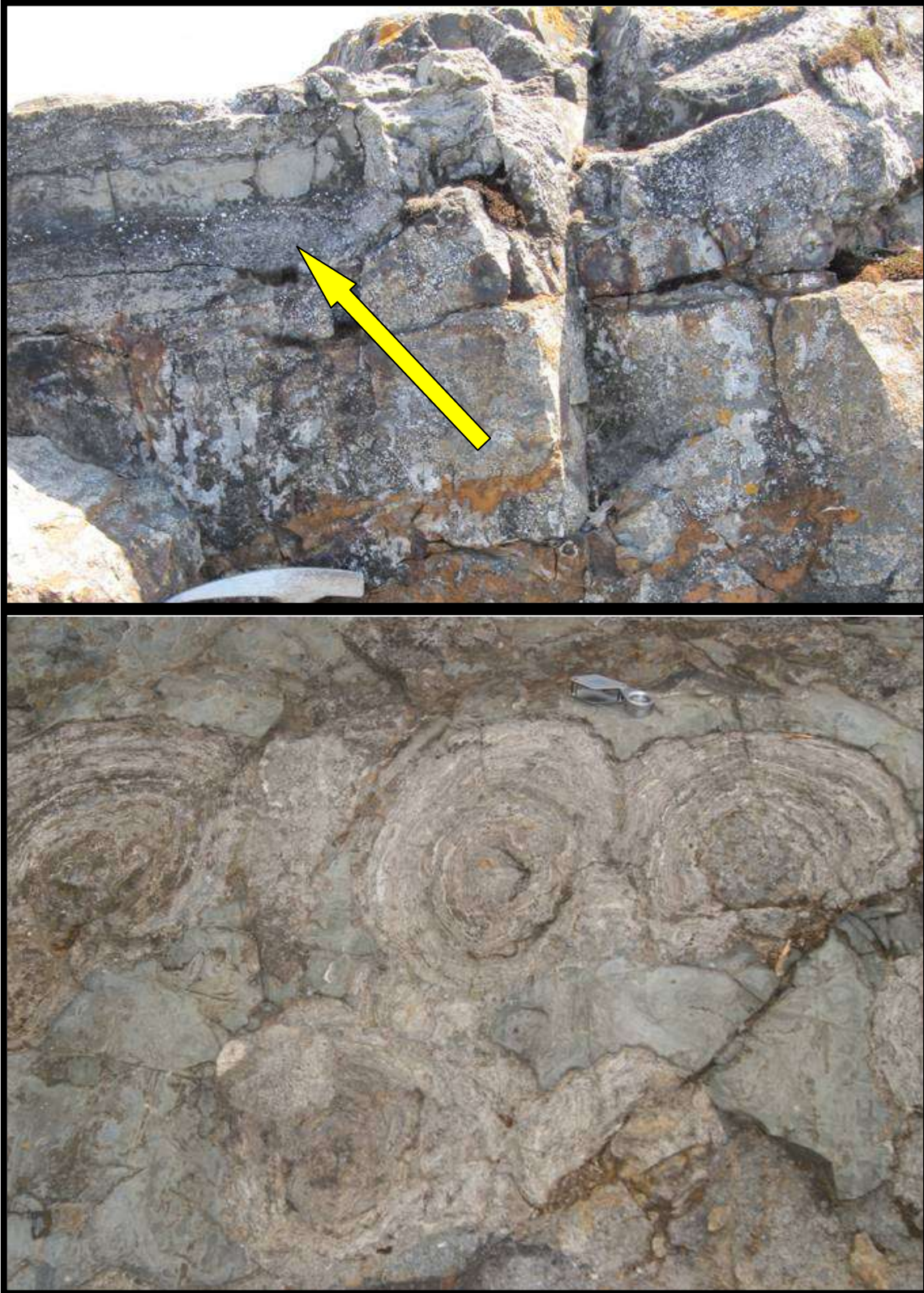
Figure 115. (Upper) Cross-section of domal stromatolites (yellow arrow); coarse grainstone underlies the stromatolite and fine and very coarse grainstone overlie it.
Figure 116. (Lower) Domal limestone stromatolites with gullies in between them filled with very fine, and very coarse-grained grainstone.

Figure 117. (Upper) Sudbury Impact Layer consisting of pea-sized devitrified vesicular impact glass and white blocky calcite cement.
Figure 118. (Lower) Chaotic outcrop consisting of large blocks, boulders, and cobbles of underlying ripped up Gunflint formation.

2.5.2   Geochemistry

View Table 5 for Hill and Markland geochemistry. The samples from Hill and Markland

(HM) have either low (grainstones) or large (S.I.L.) amounts of siliciclastic material mixed in

with the chemical sediments. Figure 119B shows no correlation, but samples HM4, HM5, and

HM6 showing high REE enrichment. Figure 119C shows that HM1 and HM2 have near-zero or

low amounts of V and Al_2O_3, while HM5 and HM6 have near-zero to low amounts of V but are

slightly enriched in Al_2O_3. Sample HM4 is slightly enriched in V and Al_2O_3 while HM3 has a

low level of Al_2O_3 but is enriched in V. Figure 119D shows HM4 has a larger amount of Mo,

while all other samples have below detection to near below detection Mo values. Figure 120A

shows that HM4 is enriched in Mo, with a slight V enrichment, while HM3 has a near-zero Mo

level, but a larger amount of V. Figure 120B shows no correlation, but sample HM3 has the

most distinct and high Y/Ho ratio and negative Ce anomaly. In Figure 120C, samples HM2,

HM5, and HM6 have increasing Y/Ho ratios but ear-zero amounts of V, while samples HM1,

HM3, and HM4 tend to show a linear positive correlation where as V increases, Y/Ho ratios

increase, with HM3 being enriched in both. In Figure 120D, no correlation is observed between

Ce anomaly and V, but samples HM1 and HM4 show higher vanadium levels with a negative

cerium anomaly, while HM3 exhibits highest levels of both. In Figure 121A, HM2 and HM3

have similar shaped REE curves, both with positive Eu and Gd anomalies, but HM3 exhibits a

high negative Ce anomaly while HM2 does not. Samples HM4, HM5, and HM6 show similar

REE shaped curves with larger Gd anomalies than Eu, and slight negative Ce anomalies. Figure

121B shows HM1 with an REE pattern spiking with a positive Eu anomaly, along with a positive

Ce anomaly. Figure 122B shows that most samples with a negative Ce anomaly tend to exhibit

higher Gd levels, with the exception of HM2 where it has a positive Ce anomaly and an even

higher positive Gd anomaly. On the contrary, HM1 exhibits a positive Ce anomaly but lower

positive Gd anomaly. In Figure 122C, samples HM4, HM5, and HM6 cluster around the same area, exhibiting slight negative Ce anomalies, and slight positive Eu anomalies, while HM3 exhibits the highest positive Eu and highest negative Ce anomalies in the sample set. Samples HM1 and HM2 both have roughly the same medium Eu anomaly within the positive Ce anomaly range. Figure 122D shows that samples that have positive Eu anomalies also have positive Gd anomalies.
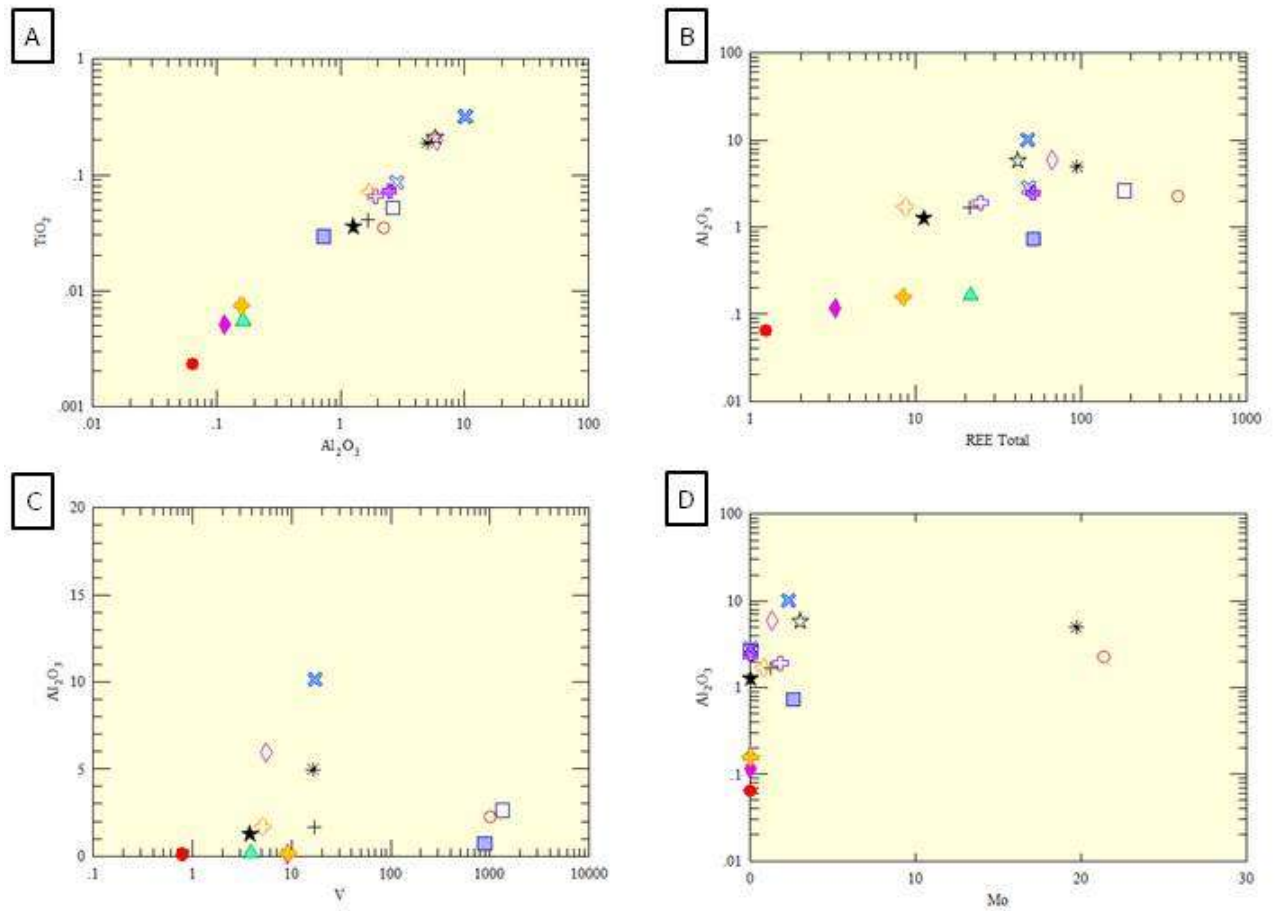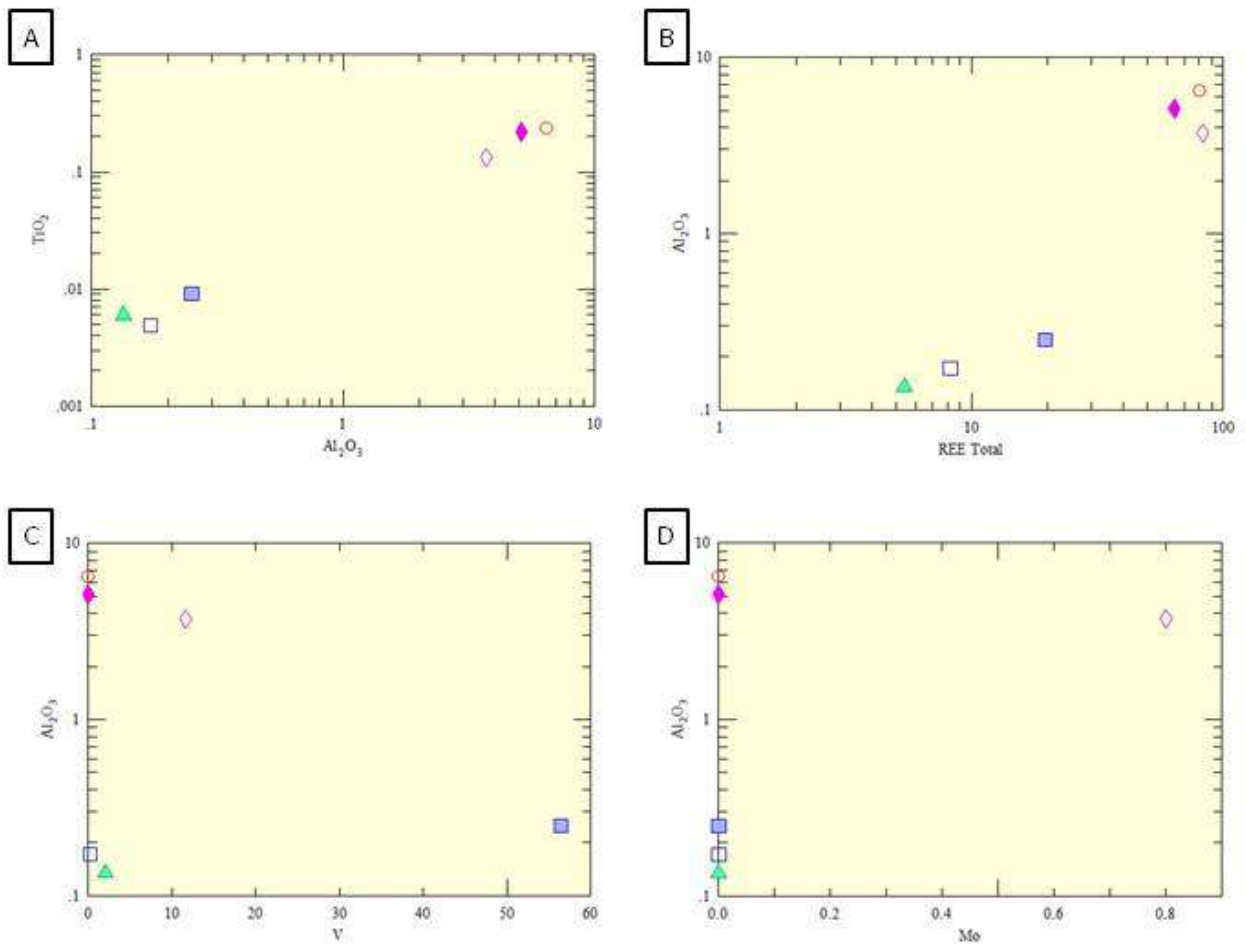
Figure 119. Bivariate plots of samples from Hill and Markland (HM). A) A positive linear correlation exists between TiO$_2$ and Al$_2$O$_3$. B) No correlation exists between Al$_2$O$_3$ and REE Total. As REE Total enrichment increases for HM1, HM2, and HM3, they also show enrichment in Al$_2$O$_3$ but to a lesser degree. Samples HM4, HM5, and HM6 exhibit high enrichments in both Al$_2$O$_3$ and REE Total. C) All samples except for HM1, HM3, and HM4 have near-zero vanadium values. Samples HM3 exhibits the highest amount of vanadium. D) All samples have near-zero or undetectable amounts of Mo except for HM4, which is still very low.

136
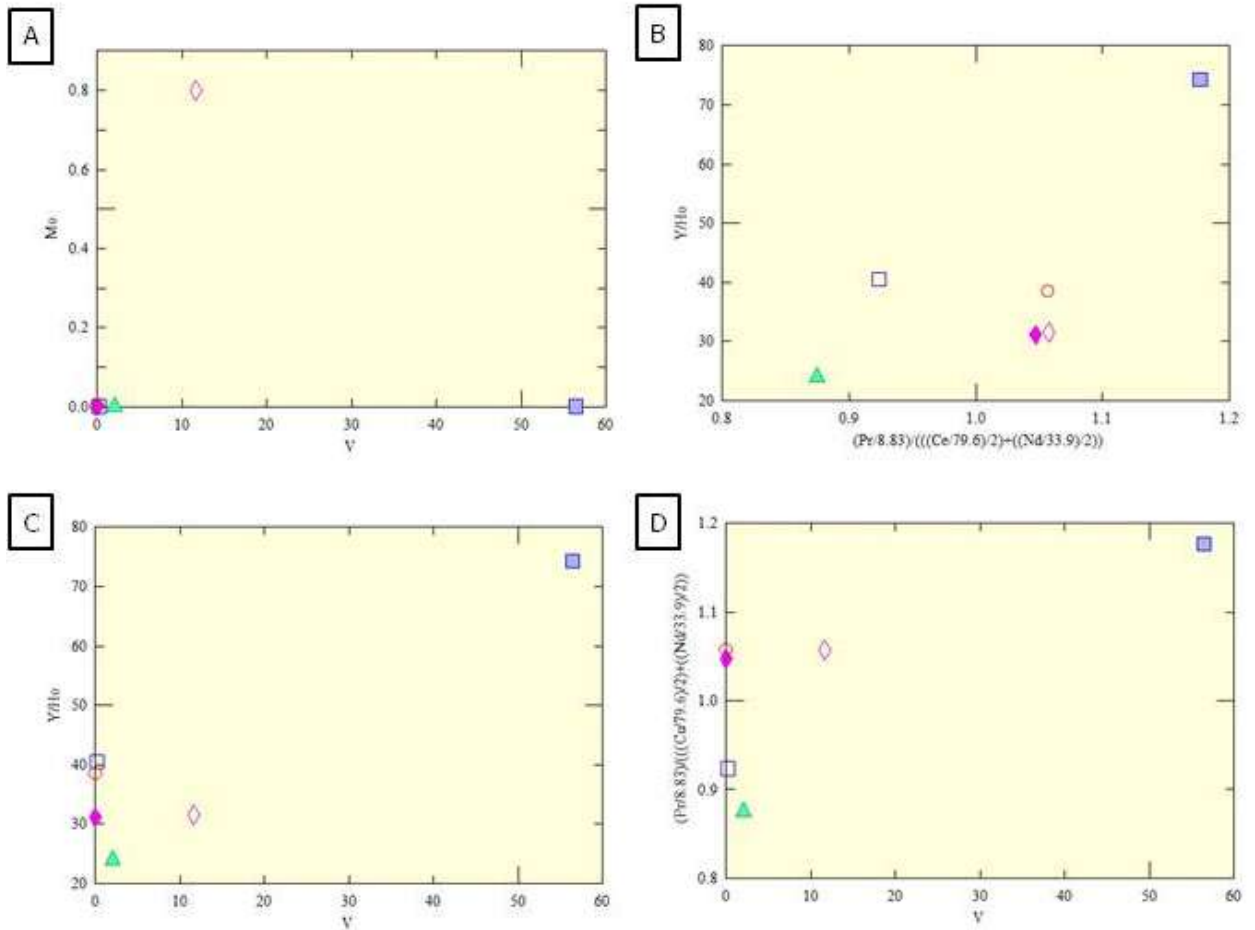
Figure 120. Bivariate plots of samples from Hill and Markland (HM). A) No correlation is evident between Mo vs V, but all samples are clustered around the zero mark for both elements, except for HM3 which exhibits near-zero amounts of Mo, but highest amount of V of the samples, and HM4 which exhibits the highest of the samples in Mo (although still a low amount), with a low amount of V. B) No correlation between Y/Ho ratio and cerium anomaly. HM3 exhibits the highest Y/Ho ratio and negative cerium anomaly. C) All samples except for HM1, HM3, and HM4 have near-zero values of V. Sample HM3 is the only sample that exhibits a high Y/Ho with a high value of V. D) No correlation is evident between Ce anomaly and V, but samples HM1 and HM4 show higher vanadium levels with a negative cerium anomaly, while HM3 exhibits the highest levels of both.
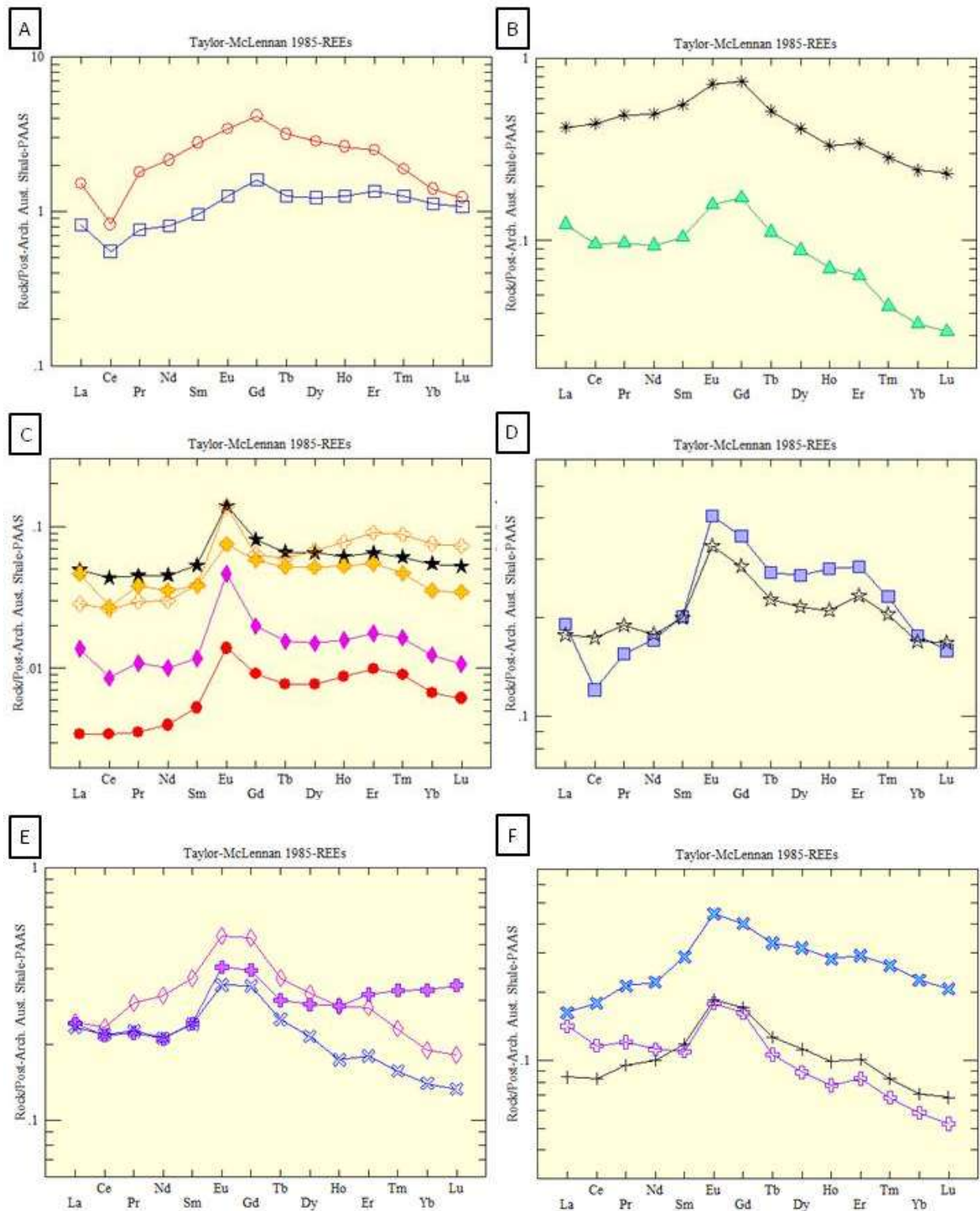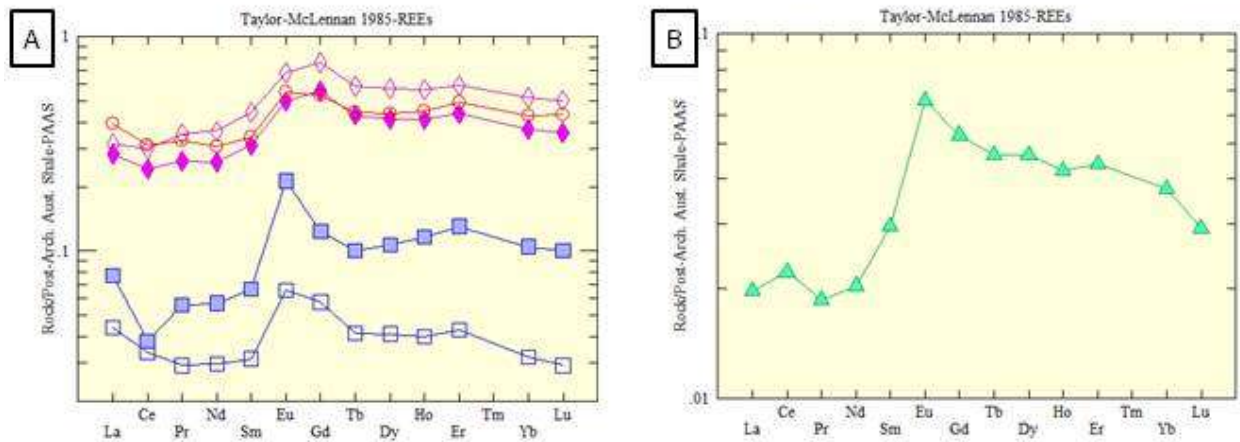
Figure 121. Rare Earth Element spider plots standardized to Taylor and McLennan (1985) PAAS. A) HM2 and HM3 exhibit similar REE curves, but HM3 (ankerite grainstone) exhibits an extreme positive Eu anomaly and a large negative cerium anomaly. Samples HM4, HM5, and HM6 exhibit similar REE curves, each having a slight negative cerium anomaly, with elevated levels of europium and gadolinium. B) Sample WT1 exhibits a positive europium anomaly with elevated levels of gadolinium and a positive cerium anomaly.
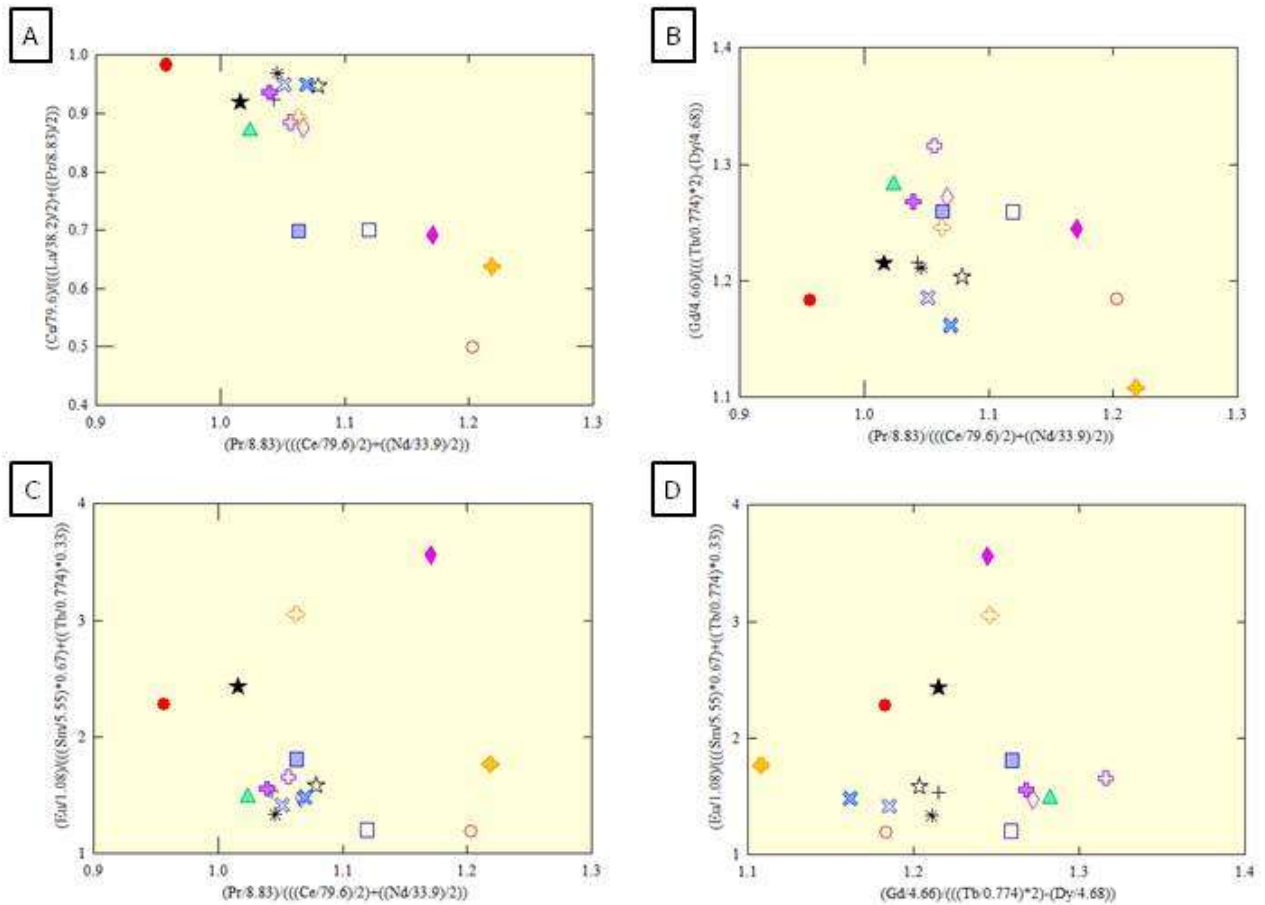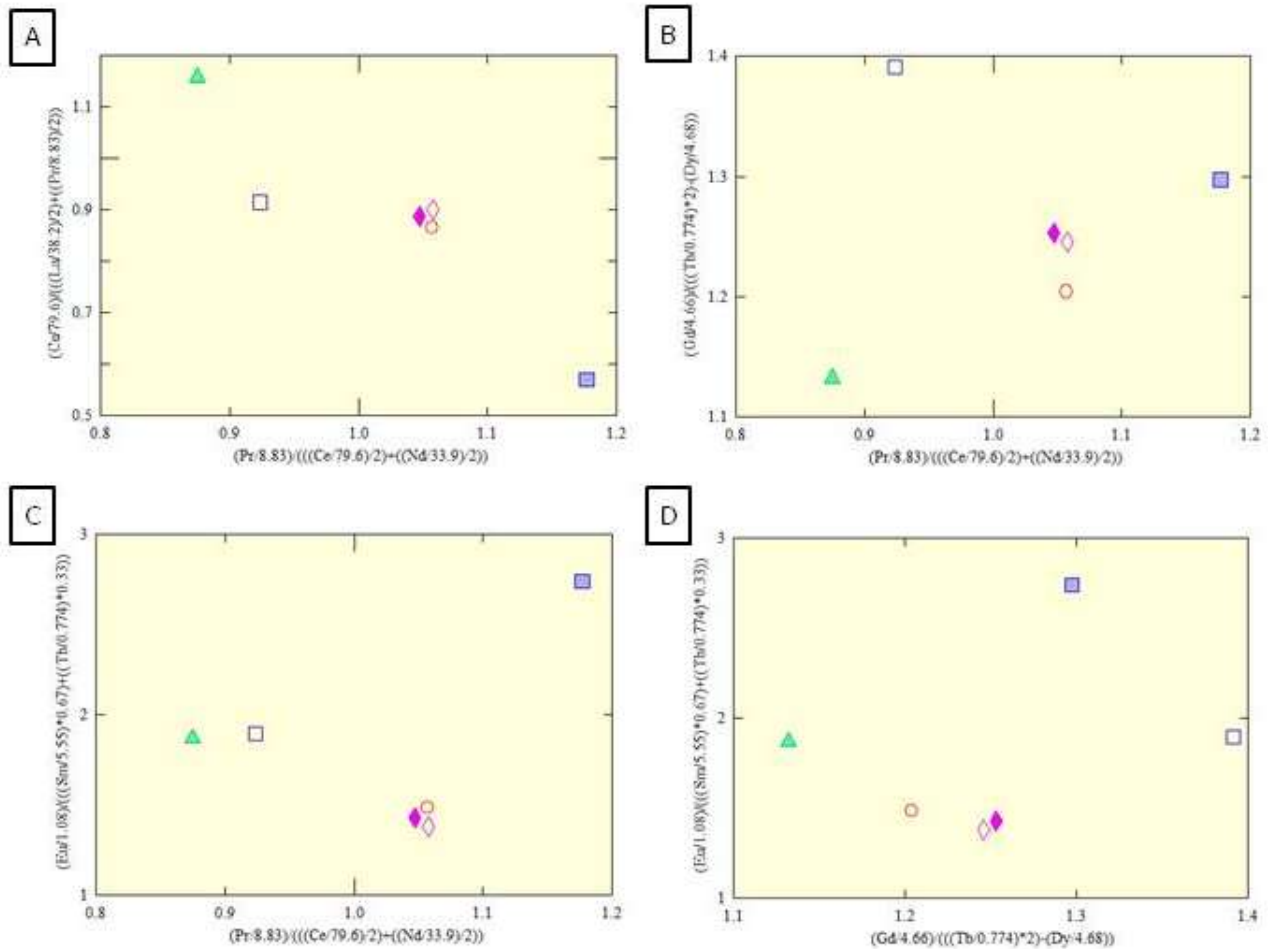
Figure 122. Bivariate plots exhibiting rare earth element anomalies of Hill and Markland (HM) samples. All values were normalized to PAAS before anomaly calculations. A) Linear correlation exhibited between lanthanum vs cerium anomalies. This relationship is probably due to Ce being present in both equations. B) Samples from the S.I.L. with medium Gd anomalies have small cerium anomalies, whereas HM2 shows both a positive Gd and Ce anomaly. HM1 on the other hand shows a small Gd anomaly but a large positive Ce anomaly. C) No correlation is evident between Eu and Ce anomalies, but HM4, HM5, and HM6 are clustered around the same point where they exhibit a slight negative Ce anomaly and a low positive Eu anomaly. HM1 displays a large positive Ce anomaly along with a positive europium anomaly. HM3 on the other hand displays a large negative Ce anomaly and a large positive Eu anomaly. D) No correlation is evident between Eu and Gd anomalies, but all samples that have higher Eu anomalies also exhibit medium-to-high Gd anomalies.

2.5.3   Interpretation

The grainstone facies has a silicified portion at the top of it at the Hill and Markland fieldsite; this is probably due to the regression of the ocean which led to sub-aerial exposure as discussed at other sites (Poulton et al., 2004; Addison et al., 2010). The limestone stromatolites overlying the ankerite grainstone unit are surrounded by fine- and coarse-grained grainstone with erosive channel-ways between the stromatolite clumps filled with the coarse grainstone, possibly indicative of a near-shore environment with enough wave action to deposit the large grains. The Sudbury Impact Layer contains ripped up pieces and boulders from the underlying Gunflint formation, including pre-lithified limestone, that had been swept by the impact blast. The S.I.L. contains white blocky calcite cement, the same as in other S.I.L. units elsewhere, indicating that meteoric water ran through the unit depositing the cement rather than oceanic water (Burton and Fralick, 2007; Fralick and Burton, 2008). Samples HM4, HM5, and HM6 (samples of blocky white calcite cement from the ejecta) all exhibit a minor negative cerium anomaly denoting that the groundwater went through a period of oxidation prior to precipitation of the calcite cement (Burton and Fralick, 2007; Fralick and Burton, 2008). One of the grainstone samples from under the limestone has a large negative Ce anomaly and an elevated amount of V, indicating that the oxygenated groundwater penetrated into these units as well.

2.6   Baseball Central (BC)

2.6.1   Lithofacies Description

Baseball Central is located in Thunder Bay, Ontario, Canada at the UTM coordinates

332389.26E and 5364254.64N 16 N NAD83. Refer to Figure 123 for a stratigraphic column

representation of the outcrop logged at Baseball Central. Addison et al. (2010) previously found

and described this site in their paper. The very bottom of the outcrop consists of 41 cm of chert

veins, which are in some places fragmented, and are situated in a very fine-grained, dark matrix

(BC6 ▲). Above lies a 3cm unit of medium-grained, ankerite grainstone overlain by 22 cm of

alternating layers of dark chert bands averaging 2 cm thick and fine-grained, ankerite grainstone

(BC7 ☐). Situated on top of the alternating grainstone and chert unit is a 7cm unit of silicified

coarse-grained grainstone (Sample BC8 ■), followed by 10 cm of whitish chert with vertical

cracks, plausibly syneresis cracks (Sample BC9 ◇ , BC10 ◆). This is followed by 4 cm of

silicified fine-grained grainstone with mud clasts (Sample BC11 ⬡). A 2cm thick layer of

whitish chert lies on top of the preceding layer and is overlain by 4 cm of silicified coarse-

grained grainstone (Sample BC12 ✹), followed by 6 cm of silicified fine-grained grainstone with

stylolites present (Sample BC13 ✚). Next follows a 13cm thick unit of fine-grained grainstone

with unaltered ankerite (Figure 124) and fractured black chert resulting in chert pieces ranging in

size from 1 to10 cm in length. Directly above lies 126 cm of the Sudbury Impact Layer

consisting of fine- to medium-grained, black chert fragments 1-4 cm in length scattered

throughout, with random cobble-sized material, all of which is surrounded by a white blocky

calcite cement (Figure 125) (Sample BC14 ✳).

Figure 123.   Stratigraphic representation of Baseball Central field site.
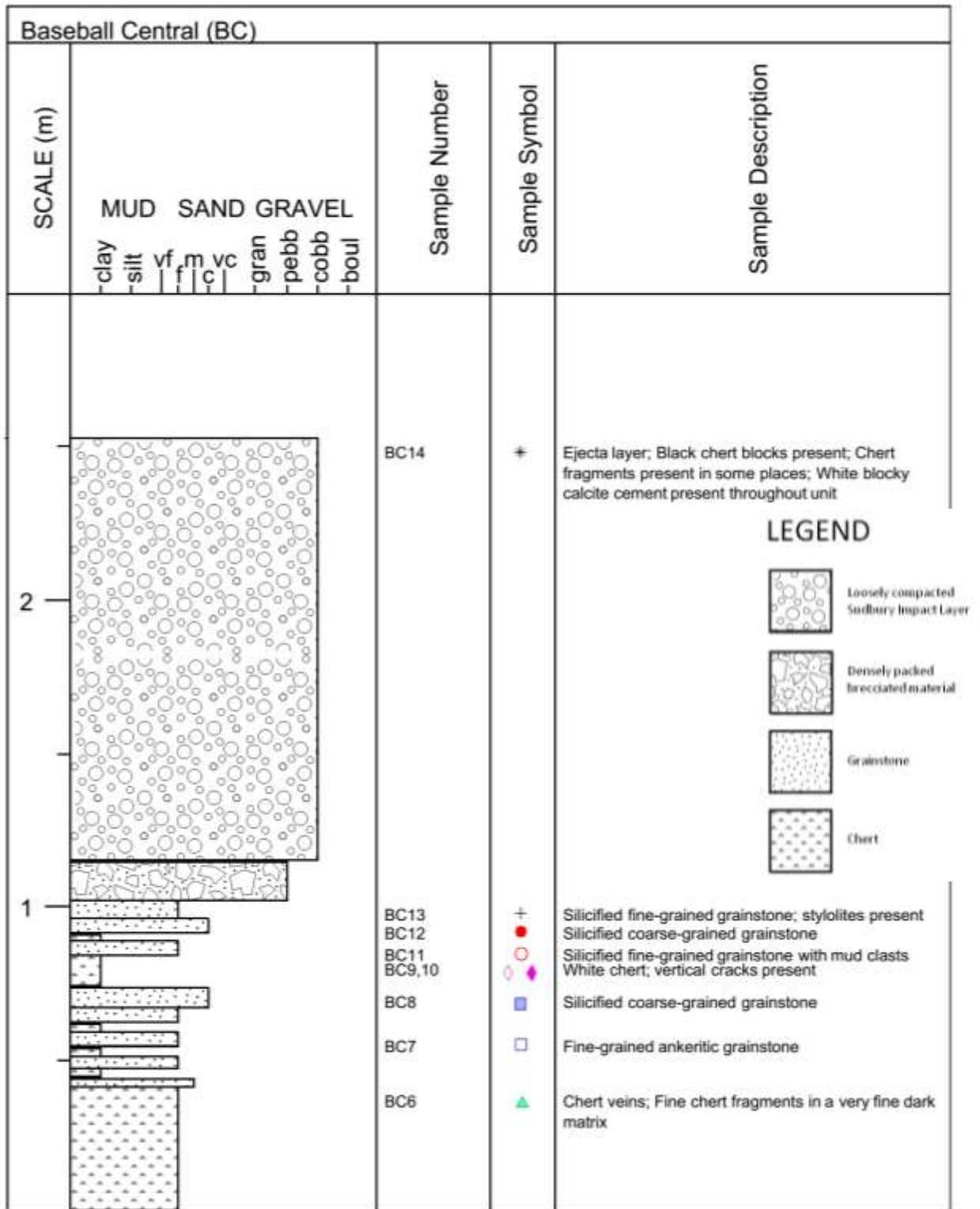
Figure 124. (Upper) Silicified medium-grained grainstone with some unaltered ankerite.
Figure 125. (Lower) Fine-grained, dark ejecta material with cobble-size chert pieces and white blocky calcite cement. Uneroded ejecta unit is present a meter away from original logged outcrop.

2.6.2   Geochemistry

View Table 6 for Baseball Central geochemistry. The samples in Baseball Central have very low to minor amounts of siliciclastic material mixed in with the chemical sediments. Samples BC7 (fine-grained ankerite grainstone), sample BC10 (white chert with vertical cracks) and BC11 and BC13 (silicified fine-grained grainstone) are slightly enriched in TiO_2 and Al_2O_3, but still have less than 0.03 and 1 percent, respectively. Sample BC14 (calcite cement from the ejecta unit) exhibits the greatest amount of TiO_2 and Al_2O_3 enrichment, but again only has 0.05 and less than 2 percent, respectively. The bivariate plots for Al_2O_3 versus REE Total and Al_2O_3 versus vanadium (Figure 126B and 126C) display similar patterns with a slightly scattered positive correlation, and with samples BC10, BC11, BC13, and BC14 showing elevated levels of vanadium. These are 30 times higher for BC10, BC11 and BC13, and 1000 times higher for BC14 than the other samples. Sample BC14 has 50 times higher Total REEs than the other samples. Figure 126D and 127A shows that BC11 has considerably more Mo than the other samples, which are all below 2ppm. Figure 127B shows no correlation between Y/Ho ratio and Ce anomaly. Another exception is sample BC10, which has a slight negative Ce anomaly but shows a high Y/Ho ratio. Figure 127C shows that as V levels increase, Y/Ho ratios decrease. In figure 127D, BC14 exhibits a negative Ce anomaly and extreme enrichment in V levels. In Figure 128A, samples BC6 and BC12 show similar REE curves with high Gd levels but extreme Eu enrichment. Figure 128B shows BC9, BC10, and BC11 exhibits similar REE curves with high levels of Eu and Gd. Figure 129C shows that BC8 and BC13 have similar REE curves with high Eu enrichment, but BC8 shows a positive Ce anomaly. Figure 128D shows that BC14 exhibits a hat-shaped REE curve with a positive Gd enrichment and a sharp negative Ce anomaly. Figure 129B and 129C tends to show that when samples have a positive Ce anomaly,

Gd and Eu anomalies tend to become increasingly more positive as well. Samples BC9 and

BC14 both have negative Ce anomalies but lower Gd and Eu anomalies.
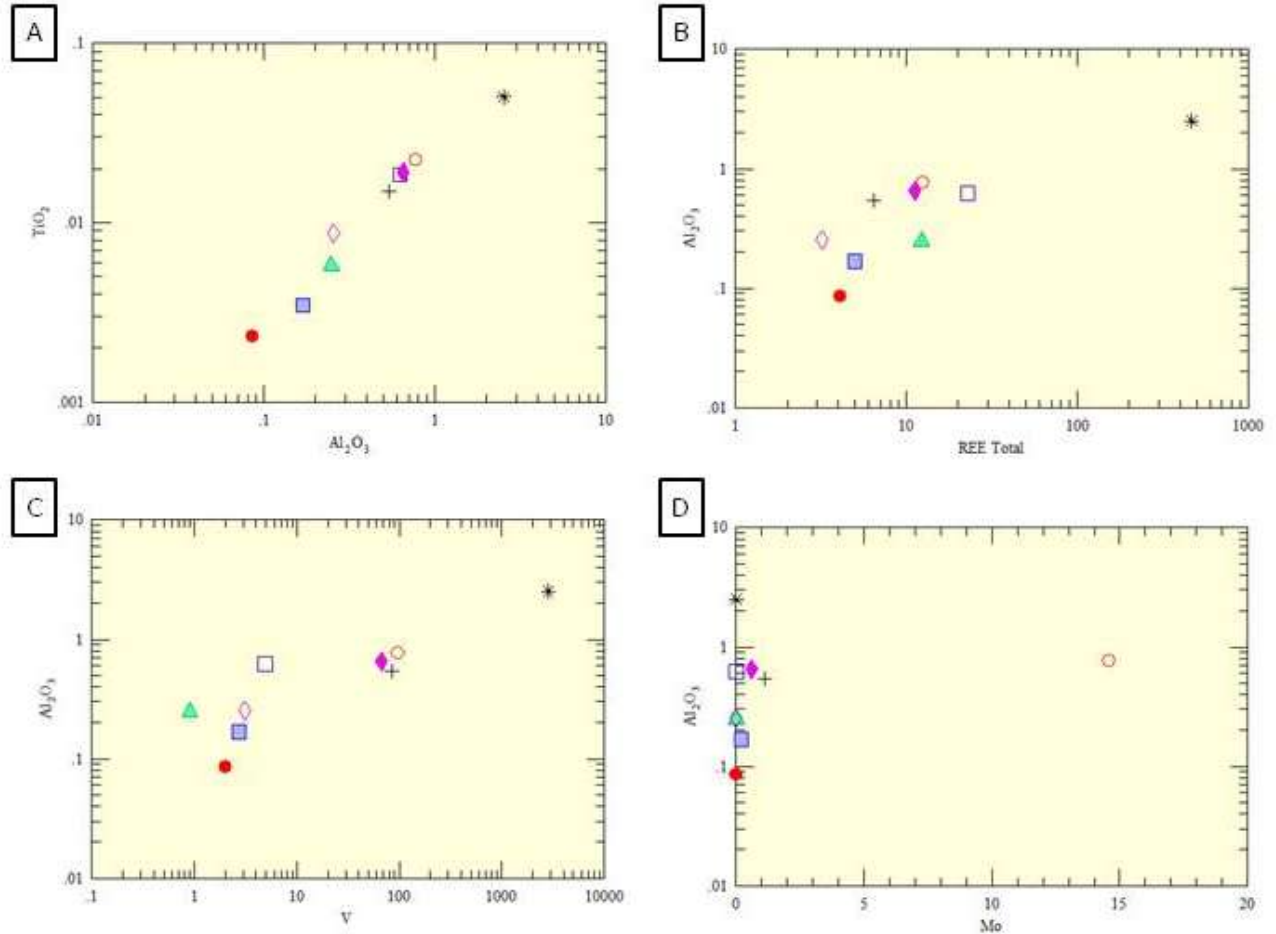
 Figure 126. Bivariate plots of samples from Baseball Central. A) Positive linear correlation exists between TiO$_2$ vs Al$_2$O$_3$. B) Cluster of points with a slight positive correlation exist between Al$_2$O$_3$ vs REE Total with sample BC14 (ejecta layer calcite cement) showing a slightly elevated level of Al$_2$O$_3$ and extreme (2848ppm) REE enrichment. C) Cluster of points exhibiting a positive correlation with sample BC 14 exhibiting an extreme amount of vanadium enrichment. D) No correlation exists between Al$_2$O$_3$ vs Mo. Samples with undetectable amounts of molybdenum are shown as zero values. All samples except BC8, BC10, BC11, and BC13 have undetectable molybdenum values. Sample BC11 exhibits an extreme enrichment in molybdenum as compared to the rest of the samples.
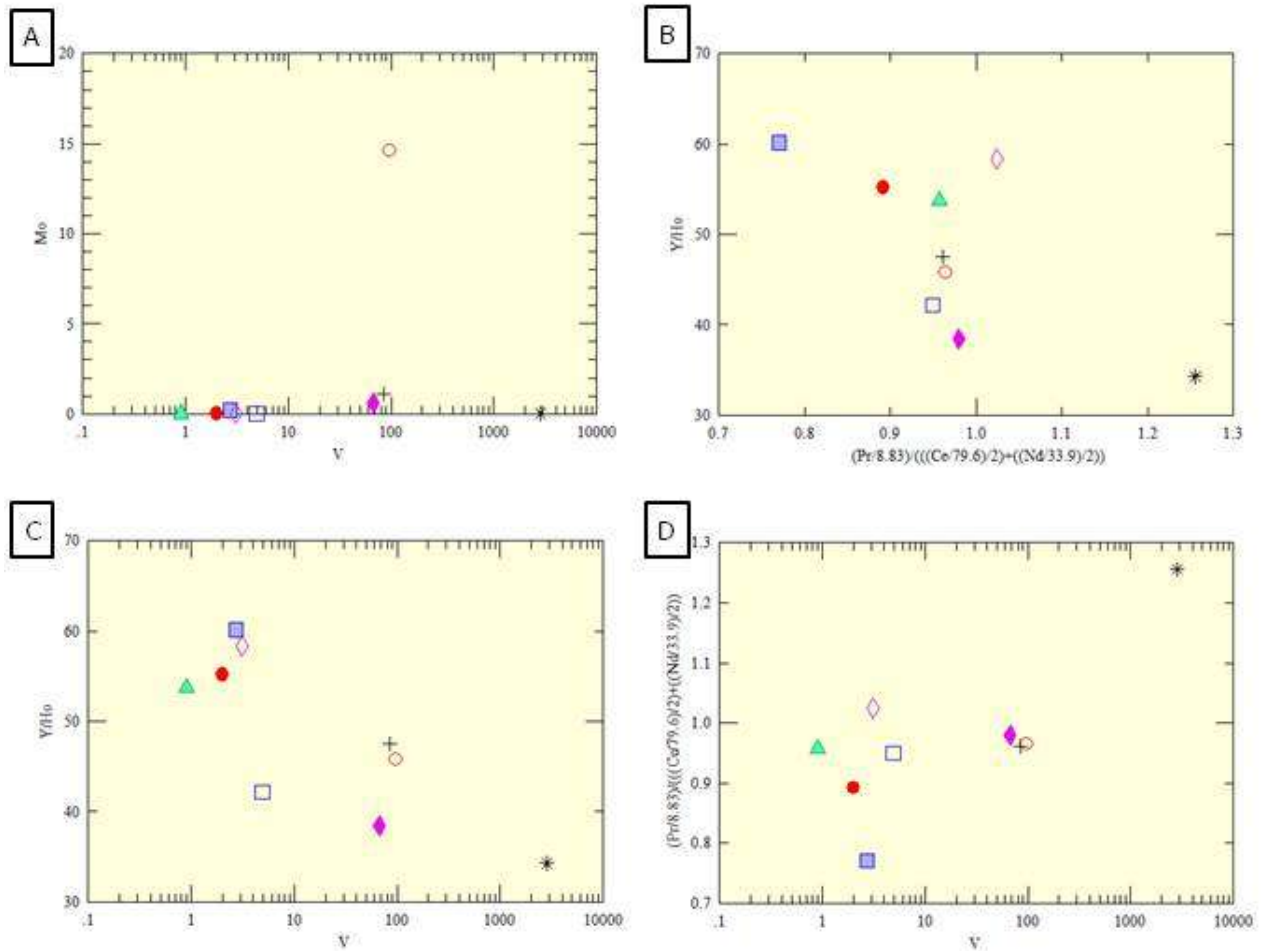
Figure 127. Bivariate plots of Baseball Central samples. A) No correlation exists between Mo and V. All samples except for BC8, 10, 11, and 13 show undetectable Mo values, with BC11 exhibiting an elevated molybdenum value. Samples 10, 11, and 13, show elevated vanadium levels, with sample BC14 (ejecta unit calcite cement) exhibiting the highest vanadium content. B) No correlation exists between Y/Ho versus cerium anomaly. C) Loose linear regression between Y/Ho ratio and vanadium is apparent, with Y/Ho ratios decreasing as vanadium levels increase. D) No correlation exists between cerium anomaly versus vanadium except for sample BC14, which has the highest values of both.

Figure 128. Rare Earth Element spider plots standardized to Taylor and McLennan (1985) PAAS. A) Sample BC6 and 12 exhibit similar REE curves with a large positive europium anomaly and elevated gadolinium levels. B) Samples BC9, 10, and, 11 exhibit similar REE curves with a pronounced europium anomaly and elevated gadolinium levels, though less than BC6 and 12. C) BC8 and 13 exhibiting similar REE curves both showing a pronounced positive europium anomaly, and high levels of gadolinium, but BC8 has a positive cerium anomaly, while BC 13 has no cerium anomaly. D) Sample BC14 exhibits a hat style REE curve with a positive gadolinium anomaly at the peak of middle rare earth enrichment. It also has a pronounced negative cerium anomaly.

 Figure 129. Bivariate plots exhibiting Rare Earth Element anomalies of Baseball Central samples.
All values were normalized to PAAS before anomaly calculations. A) Linear correlation exhibited
between lanthanum (y axis) versus cerium (x axis) anomalies. This relationship is probably due to
Ce being present in both equations. B) Samples with the largest Gd anomalies (y axis) have positive
Ce anomalies (x axis), whereas BC14 with a negative Ce anomaly has a small positive Gd anomaly.
C) No correlation exists between europium and cerium anomalies, but the sample with the negative
Ce anomaly, BC14, is the only one that has no significant Eu anomaly. D) No correlation exists
between europium versus gadolinium.

2.6.3 Interpretations

The outcrop at Baseball Central alternates between chert and ankerite grainstone, but these units have been silicified, probably from subaerial exposure once the ocean finally regressed enough to expose the land. The Sudbury Impact Layer was deposited here in a subaerial environment (Addison et al., 2010). Immediately below the impact layer, the chert is shattered, denoting that deformation was caused by seismic waves generated by the impact. Pieces of the silicified underlying Gunflint Formation are embedded in the Sudbury Impact Layer, denoting that silification of the underlying bedrocks had already taken place (Burton and Fralick, 2007; Fralick and Burton, 2008). Sample BC14 (white blocky calcite cement from the ejecta layer) exhibits an extremely large negative Ce anomaly along with extreme vanadium enrichment and no Eu anomaly indicating that the pore waters that percolated depositing the ejecta cements were meteoric and oxygenated instead of seawater. The meteroric waters were depleted in Ce compared to other REEs indicating that when the water went through an oxic environment, Ce (III) oxidized to Ce (IV), and went out of solution. These groundwaters also altered the rocks underlying the S.I.L. as two of these layers have large V enrichments and one has a large Mo enrichment.

2.7   Highway 588 Roadcut (588)

2.7.1   Lithofacies Description

The Highway 588 fieldsite is located at UTM coordinates 307423.89E and

5357873.32N 16 N NAD83. Addison et al. (2010) previously found and described this site in

their paper. Because of the destruction of the outcrop at this site due to highway blasting, an

accurate stratigraphic representation was unable to be drawn. Using deducing capabilities, and

observations from other outcrops containing Sudbury Impact Layer debris, the following

lithofacies description can be assembled in a plausible manner: The fieldsite consists of

stromatolites and grainstone similar to what is present in the Hill and Markland Street outcrop,

which is underlain by black chert and silicified ankeritic grainstone. Sample 588A2 ☐ is a

sample of ankerite grainstone taken from a boulder. Some of the medium- to coarse-grained

grainstone and chert has been shattered and infilled with ankerite (588A1 ▲) (Figure 130).

Sample 588B1 ◊ is a sample of fine-grained calcite grainstone, which is then overlain by lapilli.

The limestone stromatolites (588B2 ◆) (Figure 131) at this site were lithified and then erosively

truncated and overlain by at least 60cm of accretionary lapilli grading upwards to sand-sized

devitrified glass. This unit contains blocks of the underlying Gunflint lithologies. Figure 132 is

a picture of a slabbed sample showing stromatolites on the bottom followed by dark, fine calcite

grainstone, followed by fine-grained layered calcite, and finally topped by lapilli.

Figure 133 shows a sample of oxidized lapilli surrounded by medium- to coarse-grained

ejecta material (588A3 ☐) that consists of devitrified vesicular impact glass (DVIG), green

glauconite fragments, calcite cement, and other fine-grained material.   Figure 134 shows a

slabbed and polished sample of ejecta consisting of very large lapilli reaching approximately

2.5cm in width, the largest observed to date. Banding is visually present in the lapilli along with

a large core, with smaller lapilli with fragments of other material torn up and deposited along the way. Figure 135 shows another slabbed and polished sample of ejecta material specifically showing the concentrically banded lapilli.

Figure 130. (Upper) Shattered chert infilled with ankerite in cracks.
Figure 131. (Lower) Lithified stromatolite piece underlying ejecta at top of slab.

Figure 132. (Upper) Slabbed boulder with stromatolite on bottom followed by dark, fine calcite grainstone, overlain by fine-grained layered calcite, and overlain by lapilli.
Figure 133. (Lower) Oxidized lapilli surrounded by medium- to coarse-grained ejecta consisting of DVIG, green glauconite fragments, calcite cement and other fine-grained material.
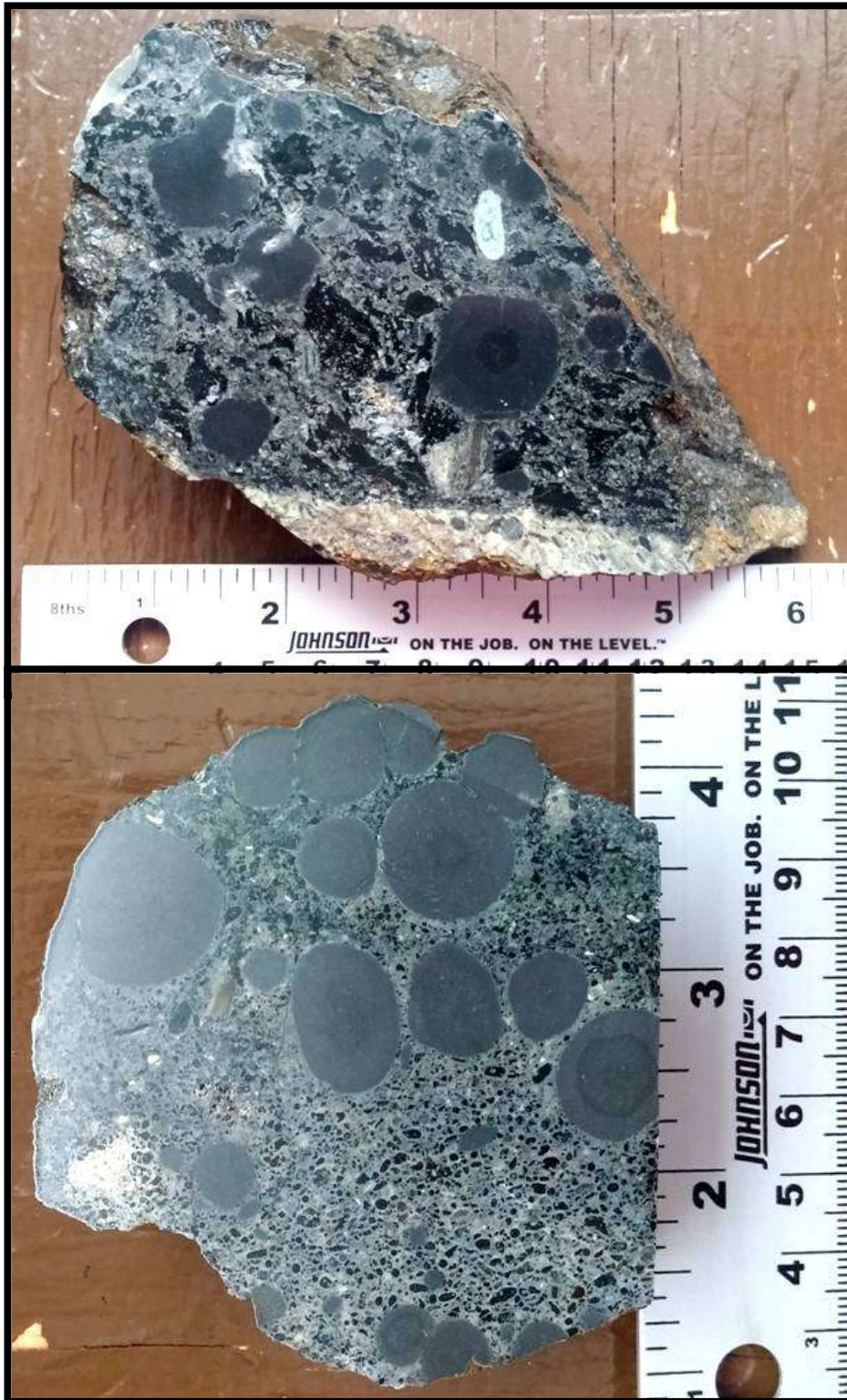
Figure 134. (Upper) Slabbed and polished sample of 2.5cm diameter lapilli.
Figure 135. (Lower) Slabbed and polished piece of ejecta material containing accretionary lapilli.

154

2.7.2   Geochemistry

View Table 7 for Highway 588 geochemistry. The samples from Highway 588 (588) have low to medium amounts of siliciclastic sediments mixed in with the chemical sediments. Figure 136 shows samples 588A3 (ejecta) and 588B2 (stromatolite) are both enriched in TiO_2 and Al_2O_3. In Figure 136B, samples 588A3, 588B1 (calcite grainstone), and 588B2 are highly enriched in total REEs. In Figure 136C, samples 588A2 (ankerite grainstone), 588B1, and 588B2 are greatly enriched in vanadium, while 588A1 (chert) is enriched in neither, and 588A3 has high Al_2O_3 but low vanadium. In Figure 136D, samples 588A1, 588A3, and 588B2 have undetectable amounts of molybdenum, while 588B1 displays slight enrichment in Mo and Al_2O_3 and 588A2 displays high molybdenum enrichment and slight Al_2O_3 enrichment.   Figure 137A reveals no distinct relationship between Mo and V, but sample 588B1 exhibits high levels of vanadium and medium amounts of Mo, while 588A2 exhibits high levels in both Mo and V. Figure 137B seems to indicate that samples that have a negative Ce anomaly tend to have higher Y/Ho ratios except for 588A3. Figure 137C shows that most samples that increase in V levels also commonly increase in Y/Ho ratio. Figure 137D shows that 588B1 and 588B2 have high levels of V and also have negative Ce anomalies. In Figure 138A, samples 588A2 and 588A3 show similar REE curves as both have only slight positive Eu and Gd anomalies, but 588A2 has a slight positive Ce anomaly while 588A3 has a slight negative Ce anomaly. The general shapes of the REE patterns for samples 588A1, 588B1, and 588B2 are similar to 588A2 and 588A3, but 588B2 has a large negative Ce anomaly and no Eu anomaly, 588B1 has a large positive Eu anomaly and no Ce anomaly, and 588A has a large positive Eu and a positive Ce anomaly.
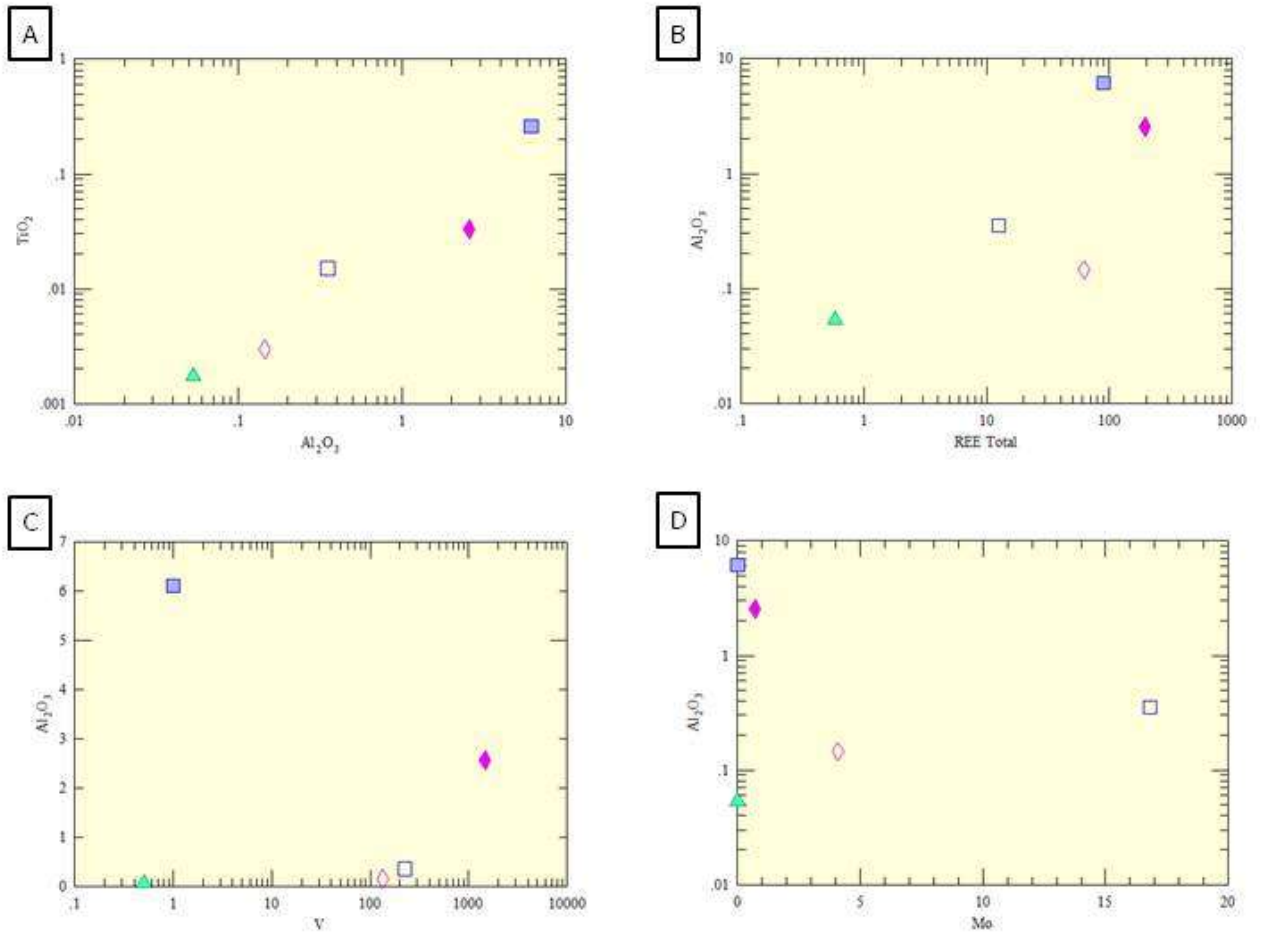
Figure 136. Bivariate plots of samples from Highway 588 (588). A) Positive linear correlation exists between TiO_2 vs Al_2O_3. B) Weak linear correlation is evident between Al_2O_3 and REE Total. C) No correlation between Al_2O_3 and V exists. Sample 588A3 is enriched in Al_2O_3, while being low in V, and 588B2 is enriched in V, while exhibiting low levels of Al_2O_3. D) No correlation exists between Al_2O_3 vs Mo, but samples 588A1, 588A3, and 588B2 are all near zero in Mo, while 588A2 is extremely enriched in Mo and 588B1 is somewhat enriched.
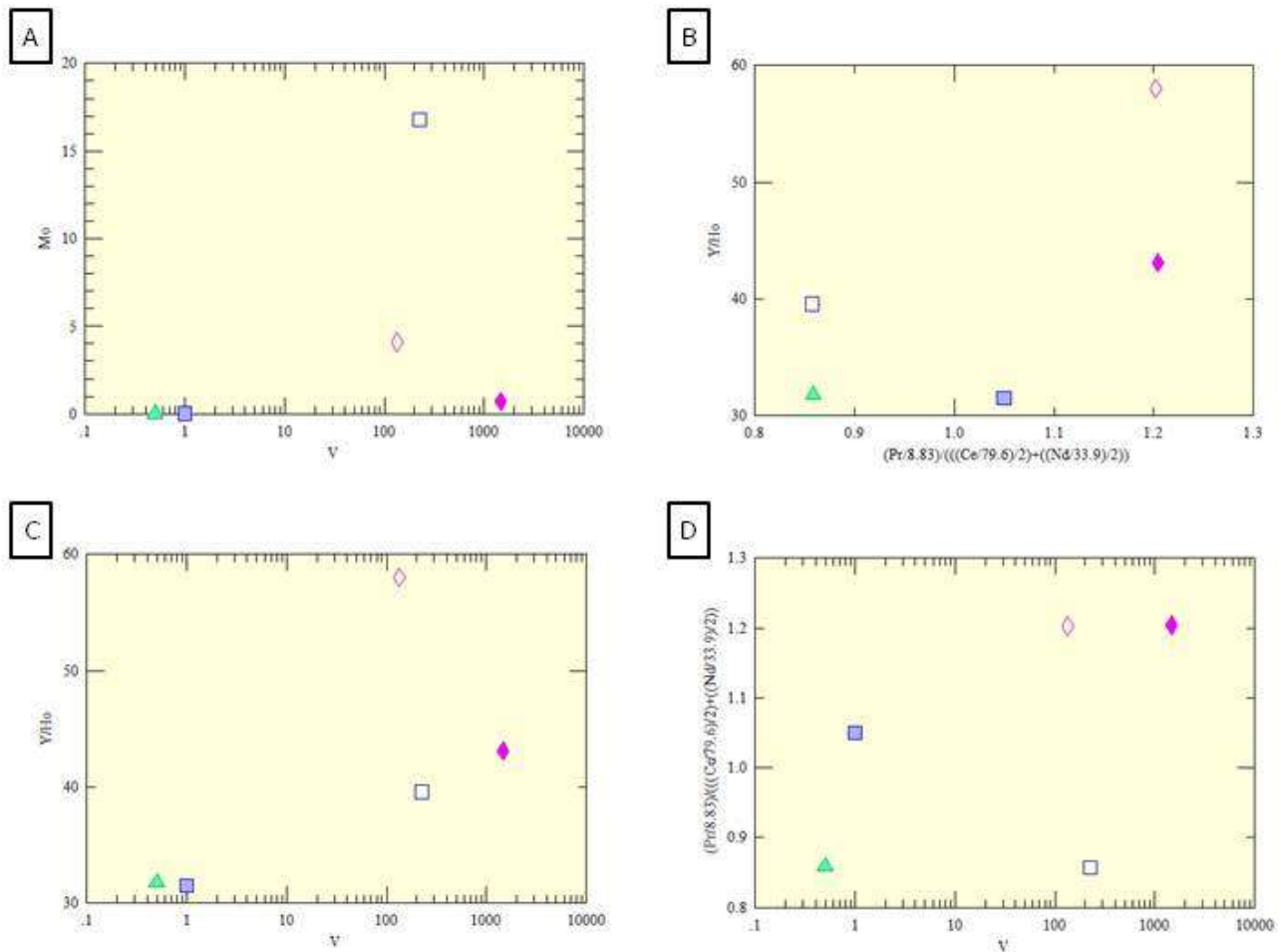
Figure 137. Bivariate plots of Highway 588 samples. A) No correlation exists between Mo and V. Samples 588A1, 588A3, and 588B2 show near-zero or undetectable amounts of Mo, while 558A2 and 588B1 are elevated in Mo and enriched greatly in V. B) No correlation exists between Y/Ho ratio and Ce anomaly. Samples 588B1 and 588B2 exhibit a negative cerium anomaly with medium to high Y/Ho ratios. C) There seems to be a slight loose positive correlation between Y/Ho ratio and V. Samples 588A2, 588B1, and 588B2 increase in Y/Ho ratio and also increase in V amounts. D) No correlation observed between Ce anomaly and V, although with samples 588B1 and 588B2, Ce anomaly is negative, and V amounts increase, but the opposite occurs with sample 588A2 where it exhibits a positive cerium anomaly and an enrichment in vanadium.
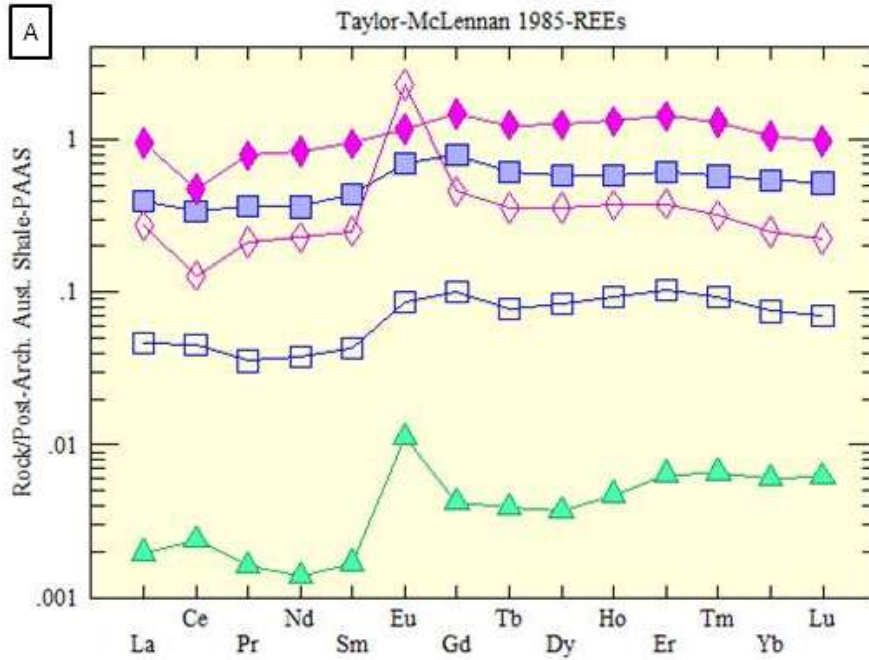
Figure 138. Rare earth element spider plots standardized to Taylor and McLennan (1985) PAAS. A) Samples 588B1 and 588B2 both exhibit a similar REE curve with negative Ce anomalies, but 588B1 displays an extreme positive Eu anomaly, while 588B2 does not. Sample 588A2 and 588A3 exhibit almost identical REE curves with slight Eu and Gd enrichments. Sample 588A1 exhibits a positive Eu anomaly, and also a slight positive Ce anomaly.
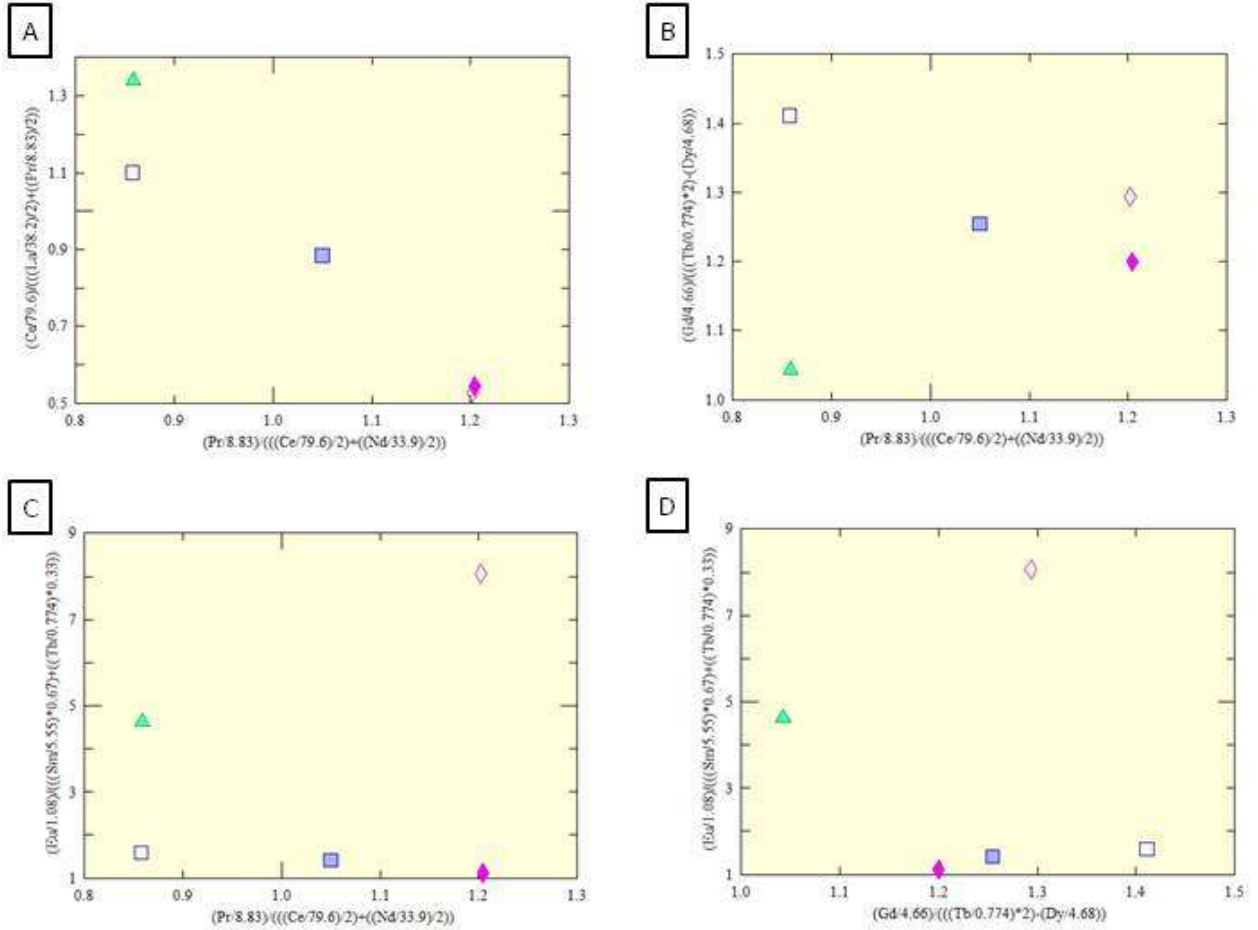
Figure 139. Bivariate plots exhibiting rare earth element anomalies of Highway 588 samples. All values were normalized to PAAS before anomaly calculations. A) Linear correlation exhibited between La and Ce anomalies. This relationship is probably due to Ce being present in both equations. B) Samples 588B1 and 588B2 have large negative Ce anomalies with moderate Gd anomalies, while 588A1 and 588A2 both display a positive Ce anomaly but 588A1 has a small positive Gd anomaly while 588A2 exhibits an extreme Gd anomaly. Sample 588A3 has a very small to no Ce anomaly and a moderate Gd anomaly. C) There is no relationship between Eu and Ce anomalies. D) There is no relationship between Eu and Gd anomalies.

2.7.3   Interpretations

Even though the outcrop at Highway 588 is only partial due to highway blasting resulting in blocks and boulders instead of a full intact outcrop, it is apparent that the ankerite grainstone has been silicified due to sub-aerial exposure (Burton and Fralick, 2007; Fralick and Burton, 2008), and in some areas shattered by the seismic waves generated by the impact. It can be concluded that the underlying Gunflint formation ankeritic grainstones were silicified prior to the time of impact because silicified large blocks and smaller rip-ups are present within the Sudbury Impact Layer. Samples 588B1 (fine-grained calcite grainstone associated with the stromatolites) and 588B2 (stromatolite) exhibit negative Ce anomalies and the highest enrichments in vanadium. Sample 588B1 is also enriched in V and has a large positive Eu anomaly, whereas 588B2 has no Eu anomaly. These samples with high vanadium levels and negative Ce anomalies indicate precipitation occurred from oxygenated water that transported the vanadium and had previously gone through a stage of Ce oxidation and precipitation (Burton and Fralick, 2007; Fralick and Burton, 2008). It is interesting to note though, that 588B1 also exhibits a large positive Europium anomaly indicating that it may have originally precipitated from seawater, or the plagioclase in the mafic tuff, from which the sand grains were formed, may have been enriched in Eu. The underlying ankerite grainstone is also highly enriched in Mo and enriched in V, indicating that it was also affected by infiltration of the oxidized fluid. The SIL, though very enriched in REEs and with a very small positive Eu anomaly, only has a very small to negligible negative Ce anomaly and is not enriched in V or Mo. The abundant exotic melt fragments and lapilli, and absence of calcite cement in the sample may account for this.

2.8 Gunflint Trail (GT)

2.8.1 Lithofacies Description

This fieldsite, a large boulder at the base of a cliff (Figure 141), is located near the Gunflint Trail at UTM coordinates 5328091N and 665212E 15N NAD 83, and contains the layers overlying the Sudbury Impact Layer. Jirsa et al. (2008) previously found and described this site in their paper. The stratigraphic representation of the site is shown in Figure 140. The lithofacies descriptions starting from bottom are as follows: There is a 20cm dark and light banded chert (Figure 142) at the very bottom at the outcrop (GT1 ▲), followed by a 10cm layer of iron carbonate (GT2 ☐) with pieces of chert imbedded within it. The pieces of chert are rounded with some platy pieces included. This layer is also irregular, ending laterally and longer than it is thick. Above rests a 2cm wavy chert layer (GT3 ■) that is probably a vein. Next lies a 6cm carbonate layer with a few pieces of chert near the top of the layer, with a thin chert vein in the middle of the layer (Figure 143). Above is a 3cm chert/agate layer, very likely a secondary replacement with mini stalactite formations (Figure 144). This 3cm agate layer and the 2cm chert layer below the carbonate unit join together laterally (Figure 145). A 12cm unit of carbonate overlies the chert layer. Soft platy fragments, possibly of siltstone, are imbedded in the carbonate (Figure 146). Above lies a 3cm of chert/agate (GT4 ◇). Overlying the chert is a 9cm unit of ankerite (GT5 ◆). On top lies a 17cm of siltstone (GT6 ⬡). Another layer of carbonate (GT7 ●) is 23cm thick and overlays the siltstone. There are pieces of siltstone floating in the carbonate layer (Figure 147), and agate surrounding the carbonate layer. Overtop lies a 55cm layer of Rove siltstone that is baked and silicified (Figure 148).

Figure 140. Stratigraphic Representation of Gunflint Trail (GT) Boulder by Cliff
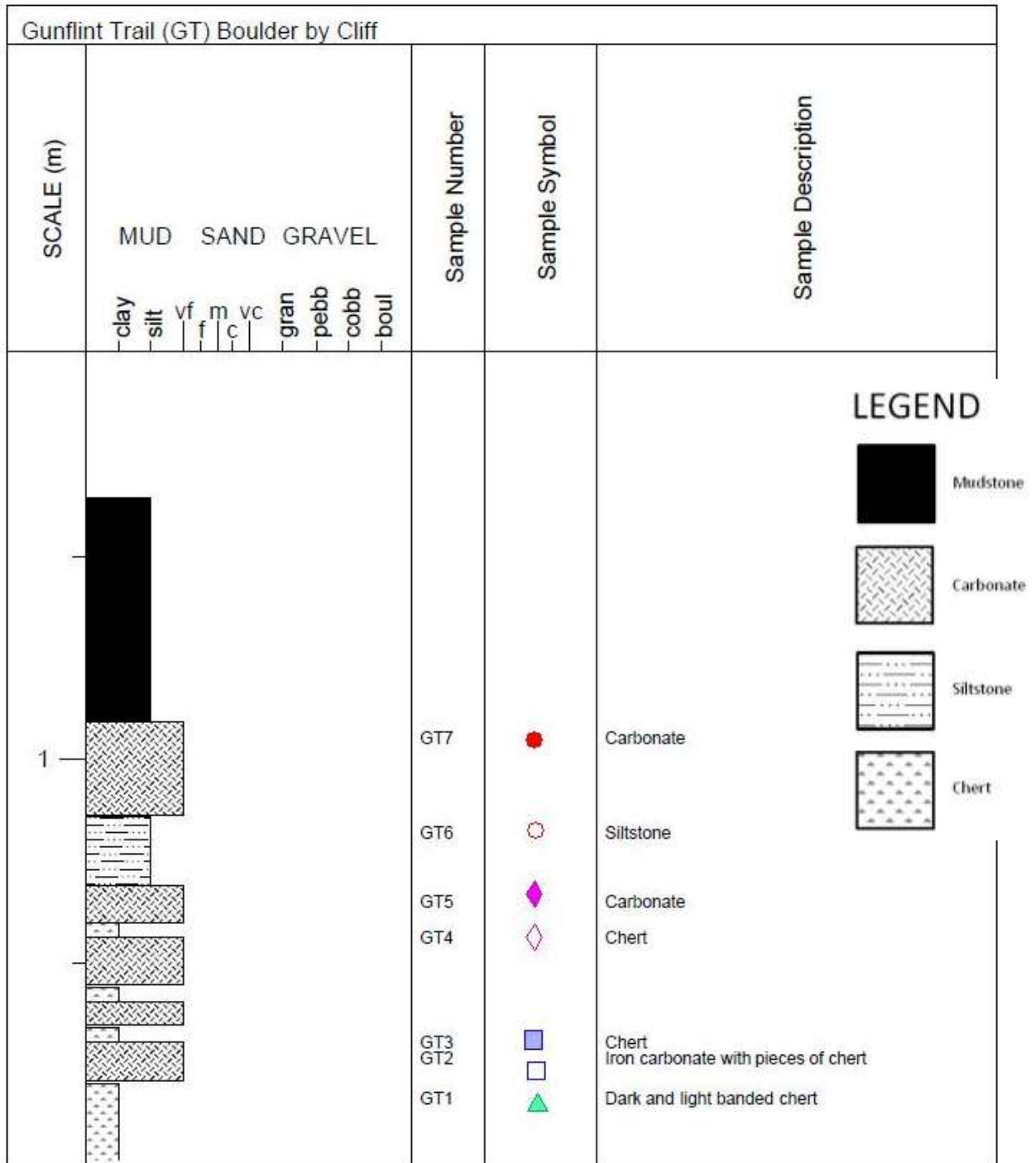
Figure 141. (Above) Gunflint Trail boulder by the cliff outcrop.
Figure 142. (Below) Dark and light banded chert.

Figure 143. (Above) Succession of chert and carbonate layers.
Figure 144. (Below) Mini stalactite formation within the chert-carbonate succession.

Figure 145. (Above) Chert and agate layers joining laterally.
Figure 146. (Below) Platy fragments imbedded in carbonate.

Figure 147. (Above) Pieces of siltstone floating in carbonate layer.
Figure 148. (Below) Silicified Rove siltstone.

The Gunflint Trail Cliff face fieldsite, containing the S.I.L. and layers under it, is located roughly at UTM coordinates 662473E and 5329219N 15N NAD 83. Figure 149 shows the stratigraphic representation of the Gunflint Trail Cliff face fieldsite. The lithofacies description starts from bottom as follows: At the very bottom of the outcrop is a 10cm layer of cherty material that is parallel laminated, this is followed by 42cm of green material which is also parallel laminated (Figure 150). XRD analysis has shown that the very fine-grained green material is grunerite; the proximity of an overlying thick diabase sill caused thermal metamorphism of this outcrop. Above lies 80cm of green material with cherty blocks approximately 10cm thick that are imbedded in it, with only a few of them broken up (Figure 151). The bedding in this layer is convoluted. Overlying the convolute bedding is 35cm of parallel laminated green material (GT8 ╋). This is followed by 10cm of parallel laminated chert that grades laterally into the green material. This is overlain by 15cm of chert that is parallel laminated, followed by 30cm of parallel laminated green material, with a 13cm thick chert on top. It appears that the green material was silicified during formation of this unit, which also includes a water escape structure cutting into it. Above rests 105cm of green material (which Jirsa et al., 2011 describes as Gunflint Iron Formation iron-silicate) with broken up pieces of cherty material imbedded within it. The bedding is very contorted in this unit. Above lies 20cm of parallel laminated green material (GT9 ✳), followed by 15cm of silicified green material. This is overlain by 50cm of parallel laminated green material, and once again overlain by 10cm of silicified cherty green material. Overlying this unit is 50cm of mostly parallel laminated green material, which includes a boudinage-looking chert layer in the upper 8cm portion of the green material (Figure 152). This is overlain by 100cm of mostly green material, but here the parallel laminations are absent. Chert blocks within this unit are almost all laying horizontally (Figure 153). Overlaying this is a chaotic unit 220cm in thickness consisting of

shattered chert blocks (GT10 ☆) that are mostly horizontal, with the exception of a few blocks

standing up vertically or at an angle (Figure 154). Overlying is a 130cm very chaotic unit

consisting of chert fragments and blocks with some rounded pieces, all of which are imbedded in

green material (GT11 ★) that is contorted around some of the chert blocks (Figure 155).

Finally, 30cm of devitrified glass overlay the chaotic unit. Lenses of lapilli are present in this

unit.

Two samples were taken just a little way off from the cliff face exposure located at UTM

coordinates 663660E and 5329108N 15N NAD83. Sample GT13 ✛ was a sample of the

green convolute bedded material, and GT14 ✛ was a sample of grey-white chert (Figure 156).

Figure 149. Stratigraphic Representation of Gunflint Trail (GT) Cliff Face

4

3

2

GT9   *   Parallel laminated green material

GT8   +   Parallel laminated green material
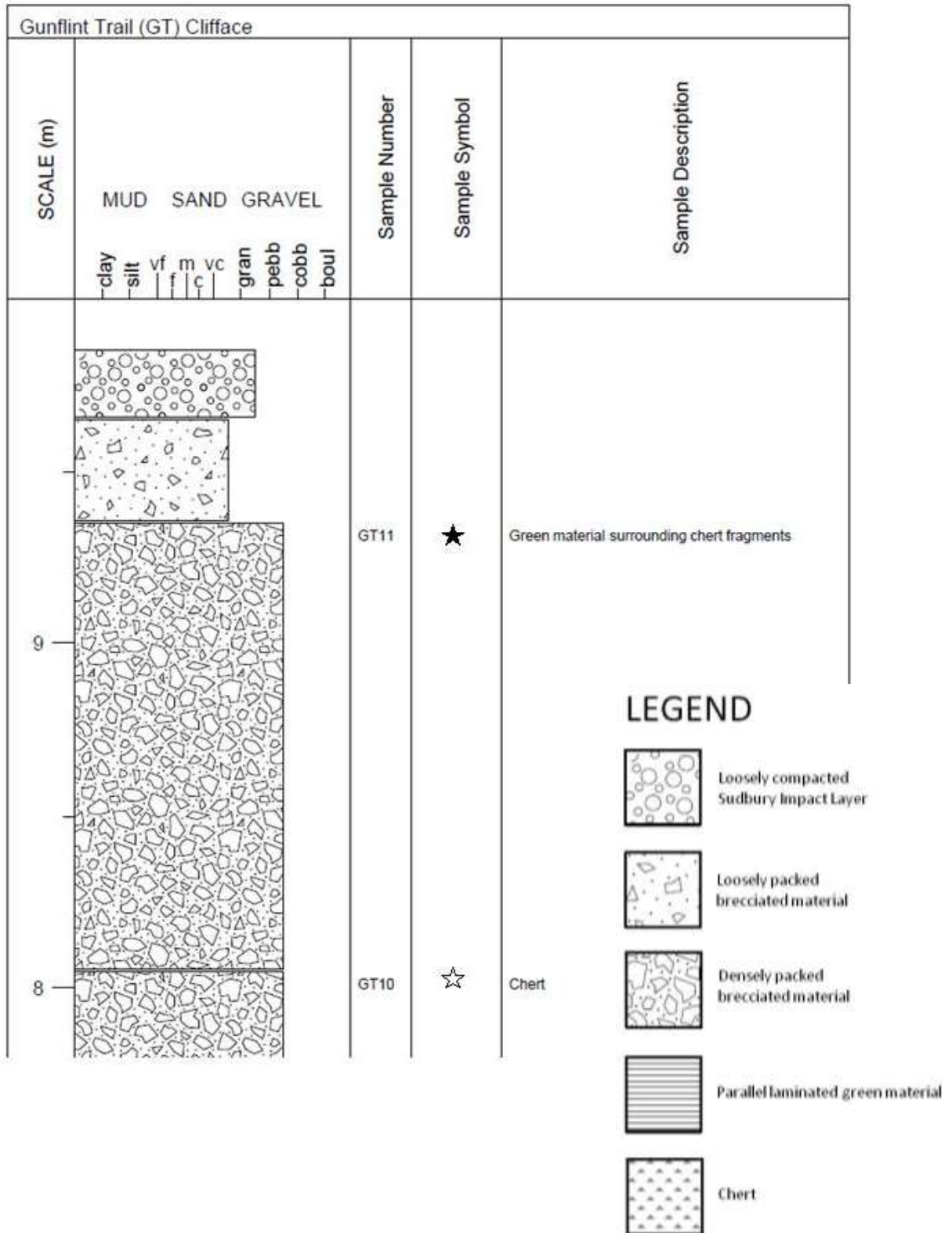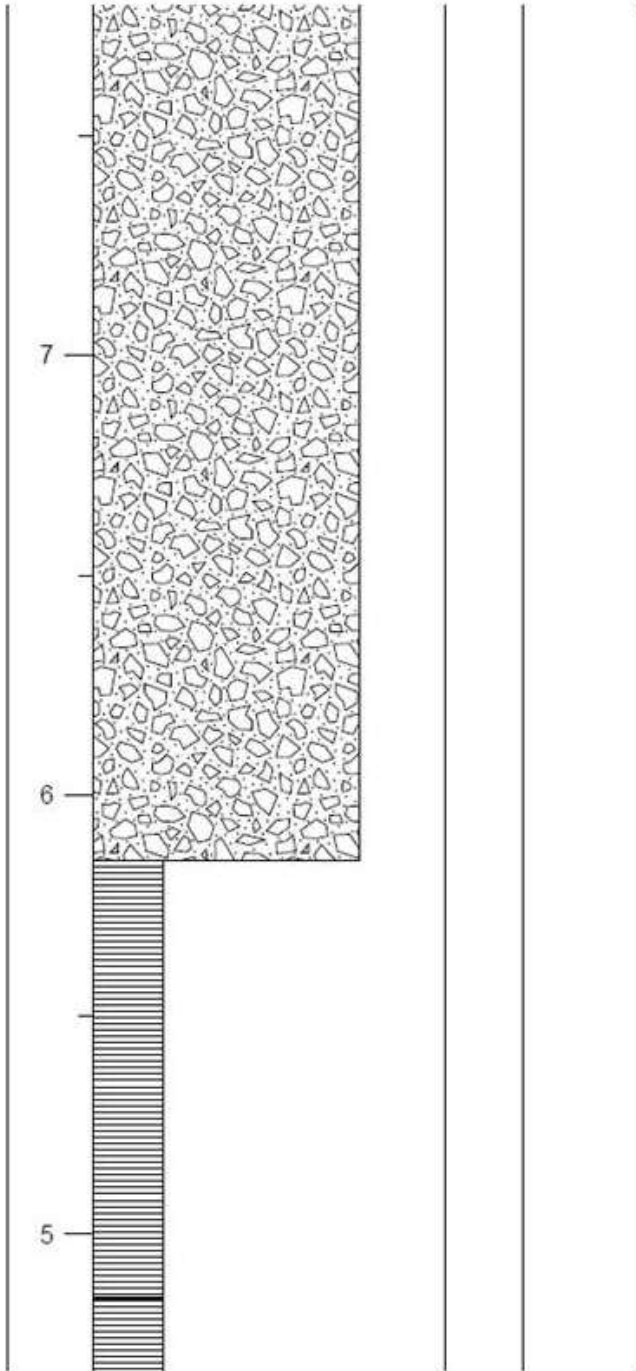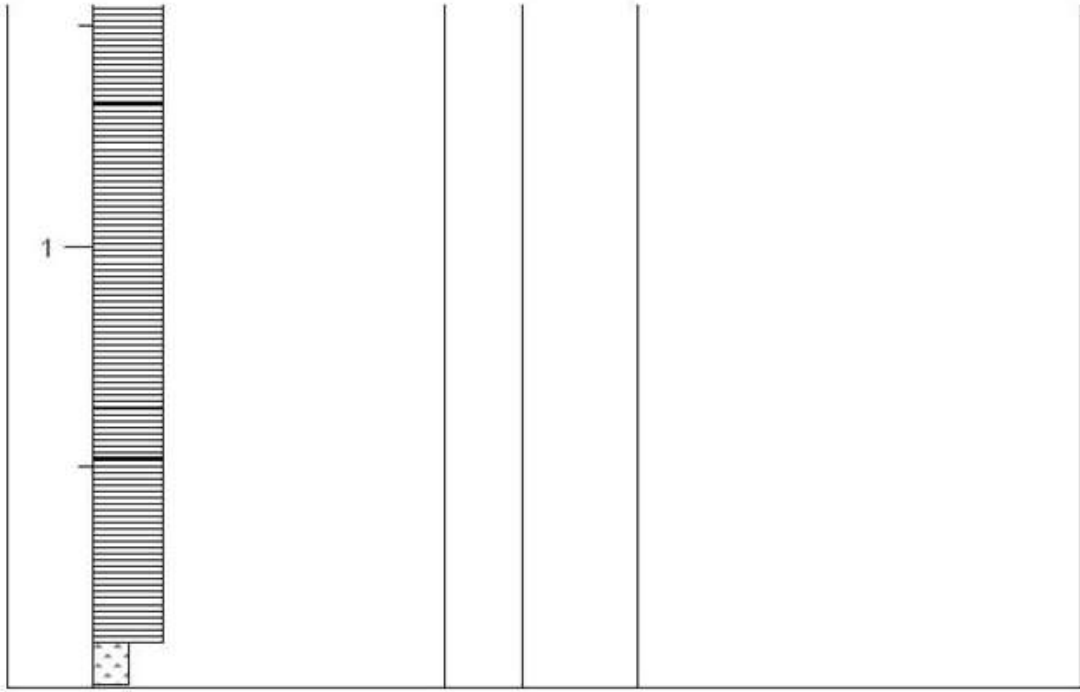
Figure 150. (Above) Parallel laminated cherty material, followed by parallel laminated green material.
Figure 151. (Below) Green material with chert blocks embedded, only few are broken up.
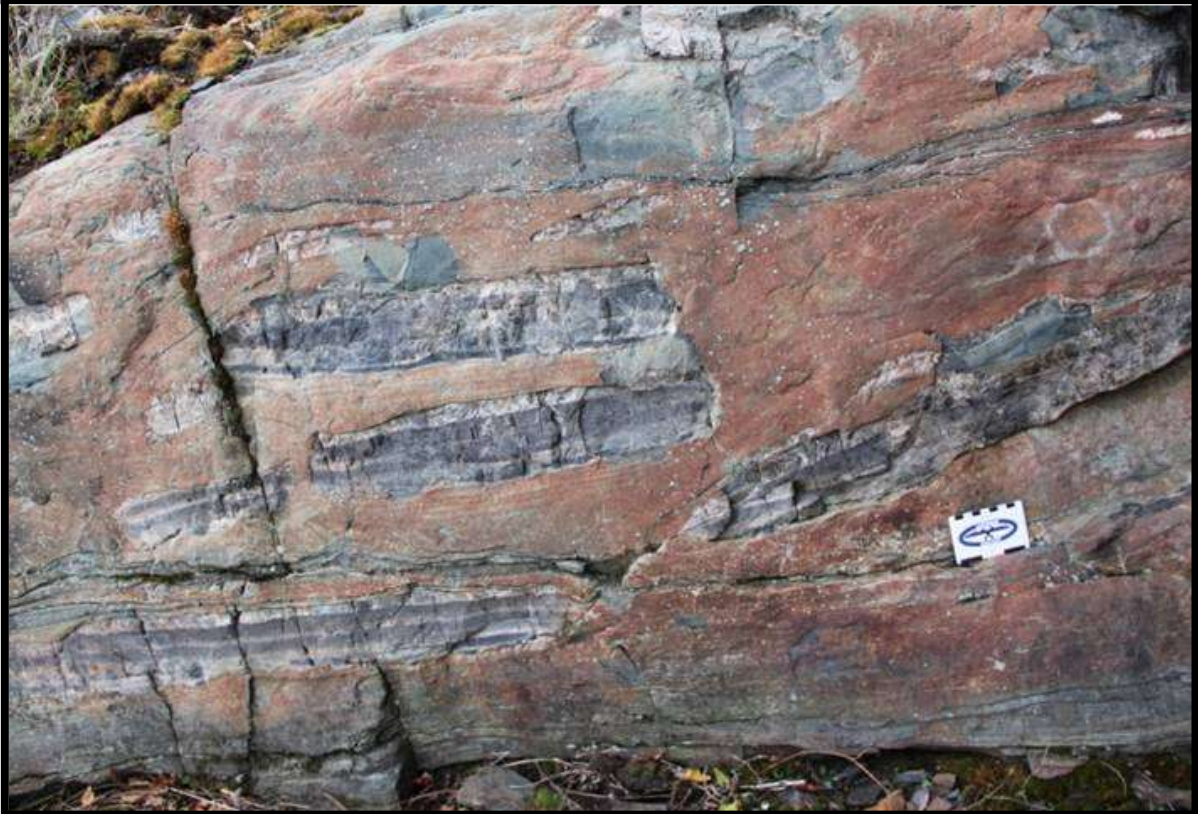
Figure 152. (Above) Water escape structure cutting into the sediment.
Figure 153. (Below) Horizontally lain chert blocks.

Figure 154. (Above) Shattered chert blocks, many horizontal but many also vertical and on an angle.
Figure 155. (Below) Chert fragments and blocks with some rounded pieces, all of which are imbedded in green material that is contorted around some of the chert blocks.

Figure 156. (Above) Green convolute bedded material (GT13), next to grey-white cherty material (GT14).

2.8.2   Geochemistry

View Table 8 for Gunflint Trail geochemistry. The samples from the Gunflint Trail have medium to high amounts of siliciclastic material mixed in with the chemical sediments. The layers above the S. I. L. have higher amounts of siliciclastic material. There is a correlation between Al_2O_3 and Total REE indicating that a large amount of siliciclastic sediment mixed in with the chemical sediments, especially in samples GT2, GT4 and GT6, is probably effecting the REE concentrations, though GT14 exhibits low levels of both Al_2O_3 and Total REE. Sample GT2 is most enriched in vanadium, with GT1 and GT7 also showing some enrichment. Sample GT14 has the lowest amount of V. In Figure 157D, samples GT1, GT3, GT4, GT5, GT6, GT7, and GT11 show an increase in Mo values as Al_2O_3 increase, whereas the rest of the samples exhibit near-zero to undetectable amounts of Mo. Sample GT14 exhibits the most positive Ce anomaly of the sample group, while GT3 and GT7 exhibit the most negative Ce anomalies. In Figure 160B, there seems to be a correlation between Gd and Ce anomalies, where samples that have a positive Ce anomaly tend to have higher Gd anomalies, while samples with negative Ce anomalies display lower Gd anomalies. The same is true with Eu vs Ce anomalies in Figure 160C, where samples that display a positive Ce anomaly tend to have higher positive Eu anomalies, while samples with negative Ce anomalies tend to display smaller positive Eu anomalies.   The exception in this case is GT3 where it displays the largest positive Eu anomaly with one of the largest negative Ce anomalies. Samples GT2, GT5, and GT6 all display negative Eu anomalies and samples GT2, GT5, GT7 and GT13 are all very depleted in light REEs. In Figure 160D, when comparing Eu and Gd anomalies, most samples are clustered in the positive Gd anomaly and positive Eu area.
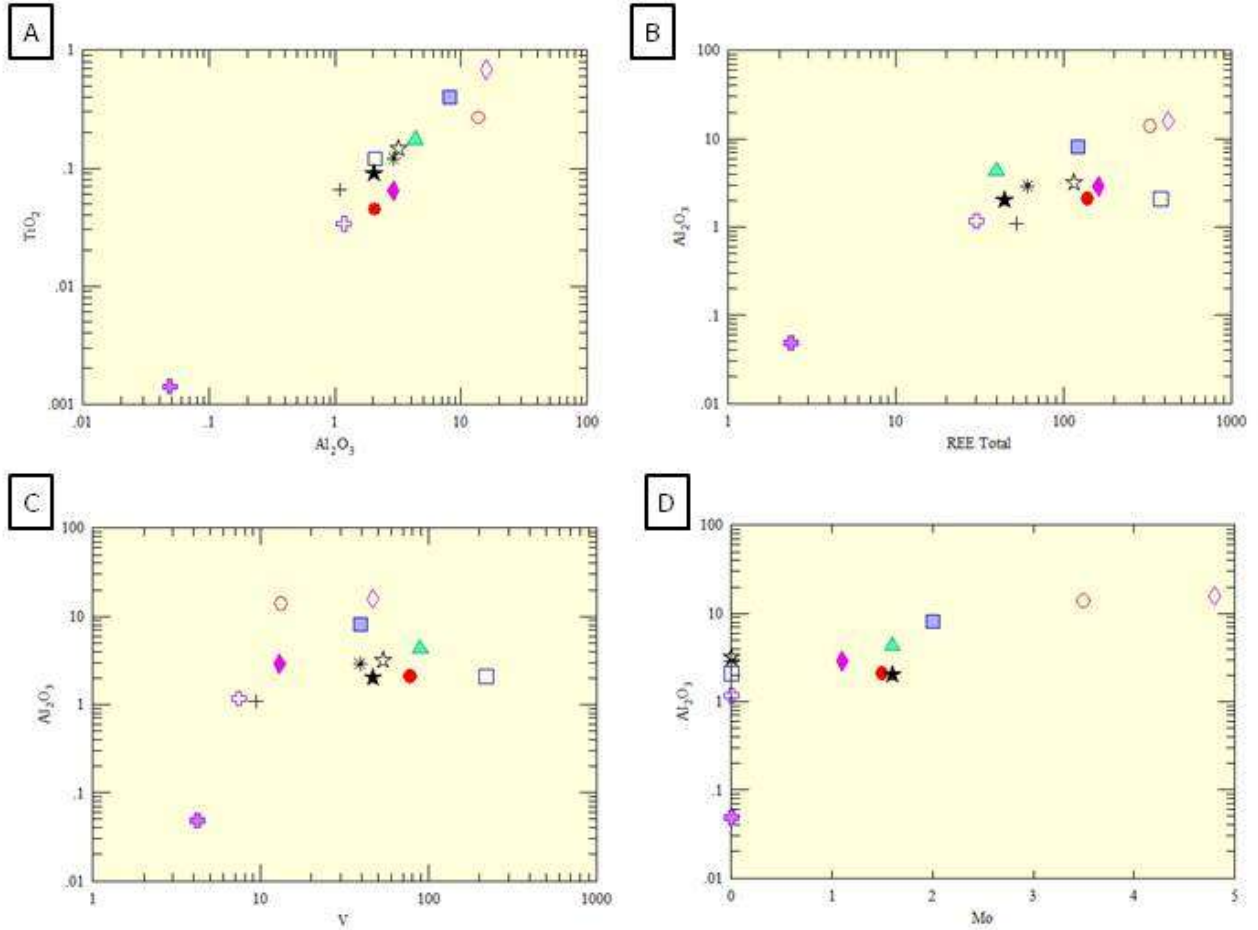
Figure 157. Bivariate plots of samples from Gunflint Trail (GT). A) Positive linear, and slightly clustered, correlation exists between TiO_2 vs Al_2O_3, with sample GT14 having extremely low values in both. B) Clustered positive linear relationship exists between Al_2O_3 vs REE Total where as Al_2O_3 levels increase, so do levels of REE Total. Sample GT14 has the lowest levels of both Al_2O_3 and REE Total. C) A cluster of samples exists between Al_2O_3 vs V, where the majority of samples are in the medium to high range in Al_2O_3 and also exhibit higher V values. D) A weak positive linear correlation in Al_2O_3 and Mo exists for samples GT1, GT3, GT4, GT5, GT6, GT7, and GT11, while the other samples have below detection Mo values.
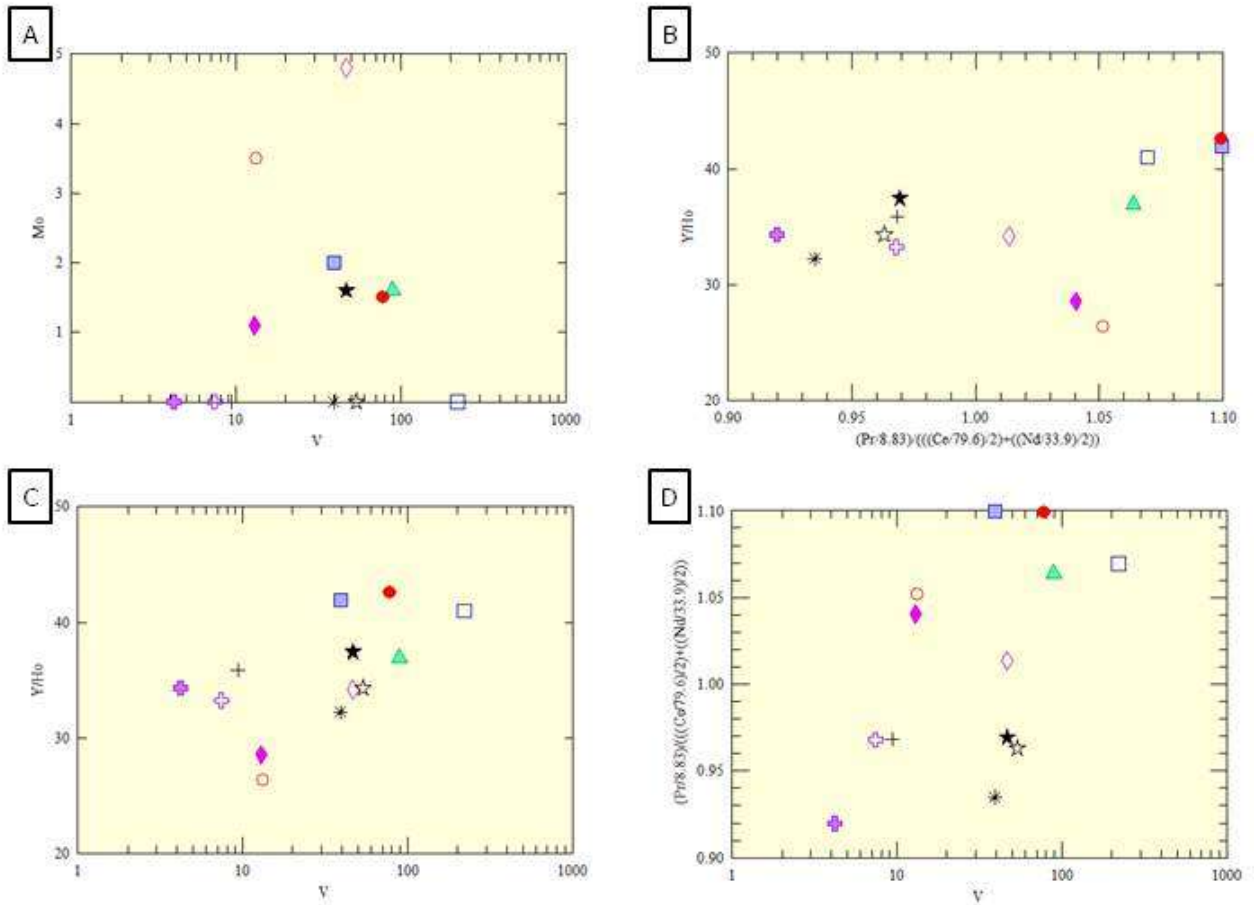
Figure 158. Bivariate plots of samples from Gunflint Trail (GT). A) No correlation exists between Mo and V. B) Slight low-gradient linear relationship between Y/Ho and Ce anomaly. Many samples with rising Y/Ho ratios also go from having a positive Ce anomaly to a negative Ce anomaly, except for outlier samples GT5 and GT6 which display a slight negative Ce anomaly but low Y/Ho ratios. C) Cluster of samples exists between Y/Ho ratio and V that display a very slight positive correlation. D) Loose positive correlation between Ce anomaly and V. As most samples' vanadium levels increase, their Ce anomalies become more negative.
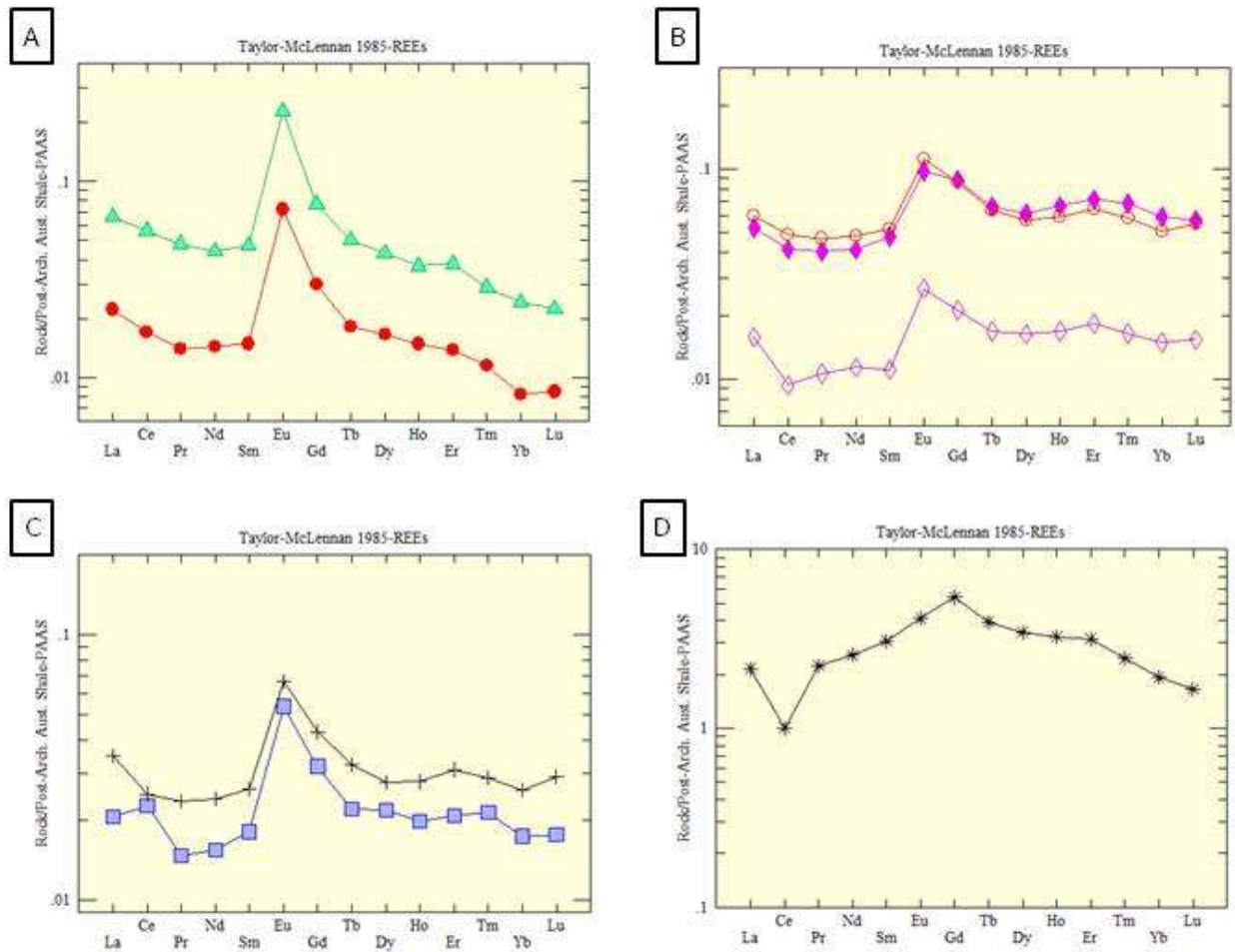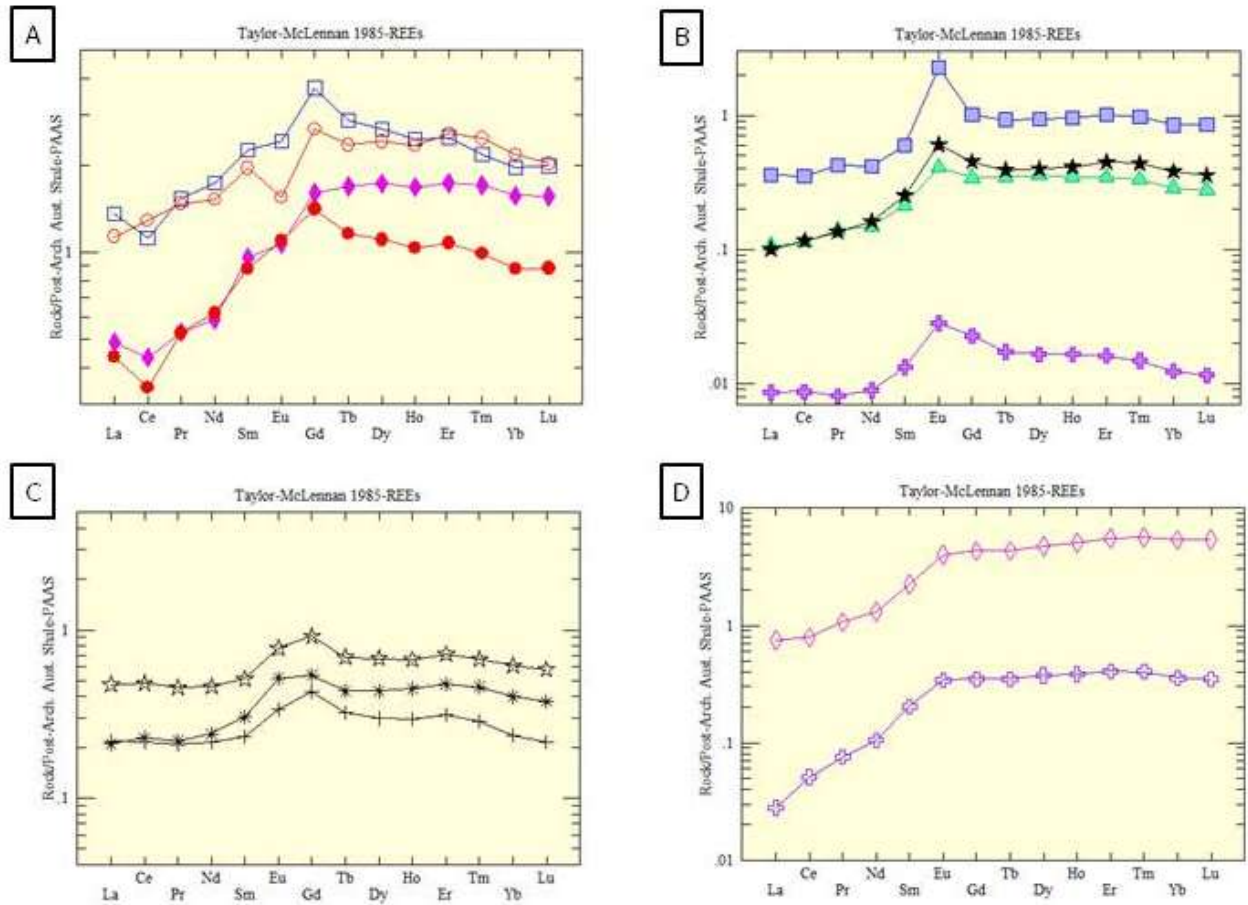
Figure 159. Rare Earth Element spider plots standardized to Taylor and McLennan (1985) PAAS. A) Samples GT2, GT5, and GT7 show similar REE curves with high positive Gd anomalies, sharp negative Ce anomalies and minor Eu anomalies. Sample GT6 displays a different REE curve with a sharp negative Eu anomaly along with a positive Gd anomaly. B) Samples GT1, GT3, GT11, and GT14 display similar REE curves with high positive Eu and Gd anomalies, but GT3 exhibits the highest positive Eu anomaly. C) Samples GT8, GT9, and GT10 exhibit similar REE curves with slight elevated Eu and Gd anomalies. D) Sample GT4 and GT13 display low LREE amounts and higher MREE and HREE amounts.
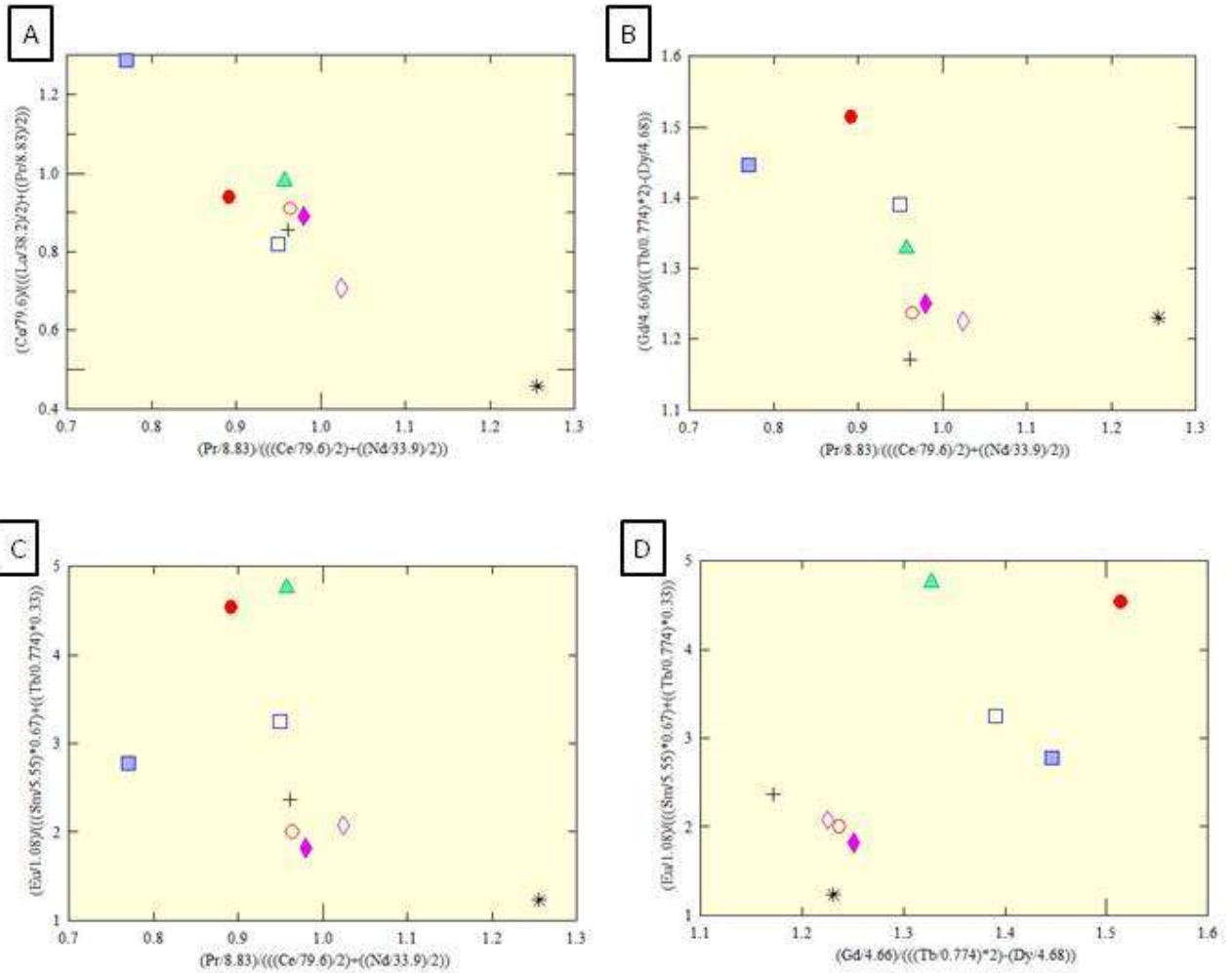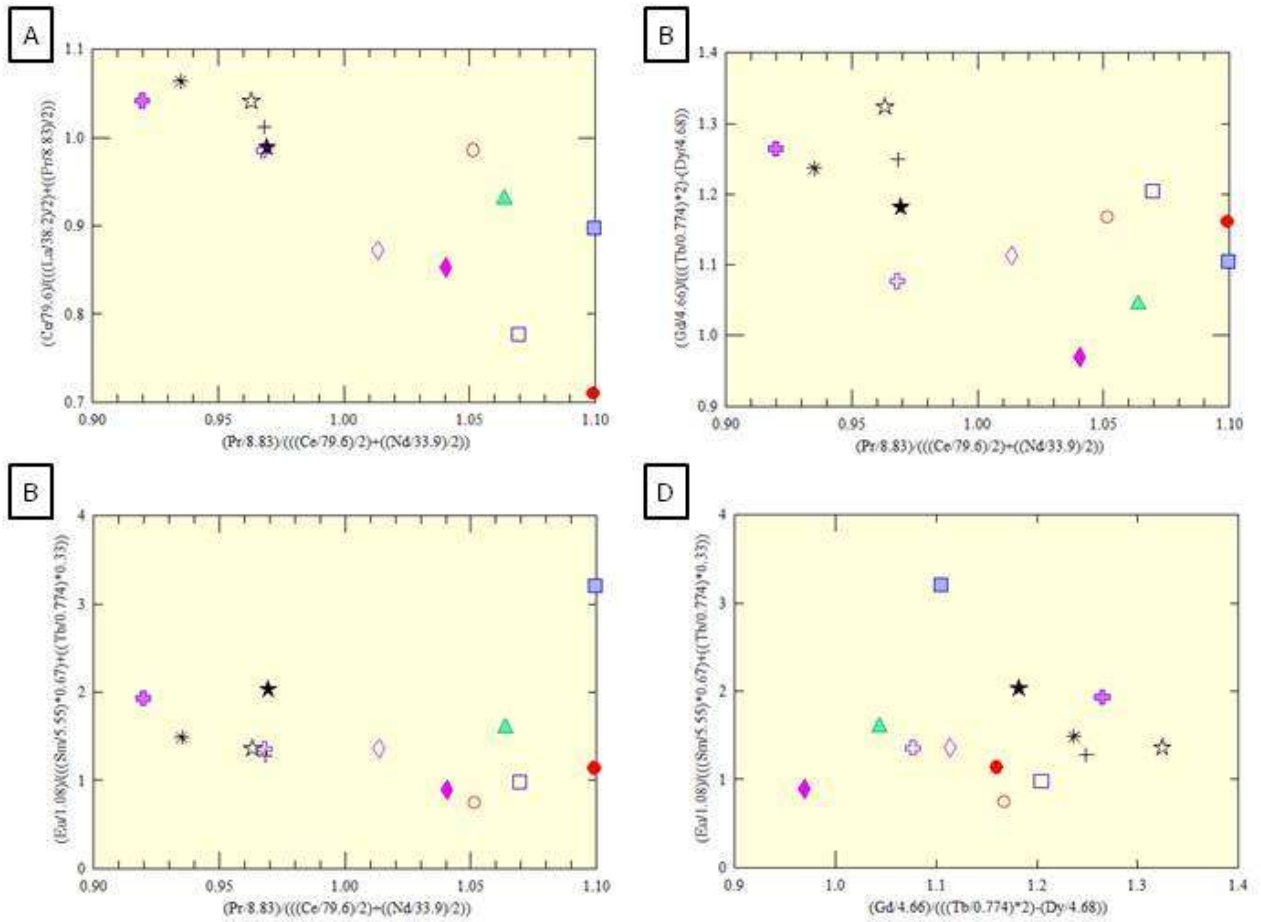
Figure 160. Bivariate plots exhibiting rare earth element anomalies of Gunflint Trail (GT) samples. All values were normalized to PAAS before anomaly calculations. A) Wide linear correlation exhibited between La vs Ce anomalies. This relationship is probably due to Ce being present in both equations. B) A scattered slight linear relationship between Gd and Ce anomalies. Many samples with positive Gd anomalies also have positive Ce anomalies, while other samples with lesser positive Gd anomalies have negative Ce anomalies. C) Linear relationship between Eu and Ce anomalies, where samples with larger positive Eu anomalies also have larger positive Ce anomalies, whereas samples with lesser positive Eu anomalies also have larger negative Ce anomalies. D) Clustered relationship between Eu and Gd anomalies.

2.8.3   Interpretations

The high metamorphic grade precludes an in depth discussion of the depositional environment of the strata below the S.I.L.. The green material is an iron-silicate (Jirsa et al., 2011). The high iron content indicates deposition in the ocean. The sample from a shattered chert block has a minor element chemical signature very similar to the green layers, indicating it is probably silicified iron-silicate, grunerite-rich material. The white chert from the deformed assemblage has very low amounts of minor elements compared to the other samples, signifying it is probably a primary chert deposit. Going up through the succession the chert layers become more brittle and broken and begin to be displaced downward. The top of this succession is chaotic with the green material swirled plastically around fragments of white chert. This is overlain by layers and lenses of devitrified glass and lapilli that are not affected by the deformation. It appears that this was an assemblage of unlithified iron-rich sediment interlayered with silicified zones and chert layers that was fluidized by a shock. The obvious shock was the Sudbury impact event as its debris directly overlies the deformed assemblage. This implies that the sea had recently been in the area depositing the iron-rich sediment, most samples have positive Eu anomalies, and that the sediment was still water saturated. It is difficult to ascertain if there was lateral movement, but some deformation at a lower level in the cliff may represent a slide plain.

The layers of ankerite with chert veins and capped by the Rove siltstone that overlie the S.I.L. have quite large amounts of Al_2O_3 resulting from large amounts of siliciclastic material being mixed in. This results in higher than normal amounts of REEs and Mo. Samples GT2, GT5 and GT6 all have slight negative Eu anomalies, which may be the result of their siliciclastic content, as represented by GT6, causing this negative anomaly. However, GT3 and GT4, which have very high Al_2O_3, do not have negative Eu anomalies, throwing into question whether the

negative anomalies are caused by the siliciclastic component. The ankerite composition of the carbonate strongly indicate that these sediments were precipitated in the ocean, as a source of dissolved iron is needed, though at this time it appears that an increased flux of siliciclastics was making its way to the sea. Although the ocean did deposit these sediments, there is evidence of oceanic regression, due to the silicification of the units and secondary chert veins, common in rocks below other exposure surfaces in this study. The transgression depositing the basal Rove ends deposition in the area.
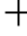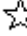
Field evidence indicated that much of the deformation in the uppermost layers of iron formation occurred during and after silicification, but prior to complete lithification. Assuming that brecciation and folding are the products of seismic waves that were formed by the Sudbury impact, it implied that during the impact, Gunflint Lake was at or only slightly below sea level, or just freshly subaerially exposed (Jirsa et al., 2011).

3   Lithofacies and Geochemistry of Drill Core

3.1 TFBH2 Drill Core

3.1.1   Lithofacies Description

Terry Fox Bore Hole 2 (TFBH2) is located at approximately at 339871.42 E and

5372370.69 N 16U NAD83. There is no previous publication of TFBH2, but Addison et al.

(2010) previously researched the Terry Fox fieldsite location, from which this drillcore came.

Figure 161 is a stratigraphic representation of drill core TFBH2. Starting from the bottom of the

drill core there is 1070cm of Gunflint Formation. Sample TFBH2-1 ▲ was taken from 80cm

above the base of the drill core which, at this area, consists of silicified, parallel laminated, fine

sand-sized material (Figure 162). Samples TFBH2-2 □ was taken 525cm above the base of the

drill core and consists of layers of silt-sized carbonate with fine sand-sized carbonate layers 4mm

in thickness (Figure 163). Sample TFBH2-3 ■ was taken 1070cm above the base of the drill

core and consists of carbonate grainstone with rounded rip-ups composed of siliceous mudstone

and black chert. This unit is 21cm in thickness. Above this unit lies 8cm of coarse-grained silica

grainstone then a 9cm carbonate grainstone with rounded rip ups that are composed of grey,

siliceous mudstone, with black chert rip-ups. Above this lies 46 cm of carbonate grainstone with

dark grey to black layers and blobs of siliceous material (Figure 164). Sample TFBH2-4 ◇ is of

the black chert. Overlying this unit is a 15cm thick unit of silicified carbonate grainstone with

dark grey to black layers and blobs. Distinct stylolites are present in this unit. Overtop lies 5cm

of similar silicified carbonate grainstone but here it is broken and in-filled with sand and granule

sized carbonate debris between the irregular pieces (Figure 165). Overlying this unit is 35cm of

fine-grained carbonate (Figure 166) with broken pieces of chert in a fine carbonate matrix

(Figure 167). There are a few 1cm thick layers of agate in the fine grainstone. Above lies a

10cm siliceous grainstone. Sample TFBH2-5 ◆ is taken from the overlying 55cm unit that consists of fine-grained carbonate with large blotchy popcorn-sized areas of light carbonate, surrounded by dark grey carbonate. Above this lies 9cm of crystalline carbonate layers that are greyish and fine-grained. A few layers include hematite in them with agate filling large voids (Figure 168). Above this lies 48cm of chaotically broken ankerite grainstone with some blotchy silicified areas (Figure 169). Overlying this unit is 23cm of fine-grained crystals that become large black crystal growths, which look like manganese flowers. This area contains somewhat silicified fine-grained carbonate. Sample TFBH2-6 ⬡ is a sample of the black growths (Figure 170). Overlying this is 13cm of silicified, fine-grained carbonate with extensive overgrowth of a green mineral. Sample TFBH2-7 ⬤ was taken from this unit. A 6cm unit of highly silicified fine-grained material with hematite lies on top, with sample TFBH2-8 ✛ taken from this unit. It is overlain by a 1cm layer of hematite then 39cm of the Sudbury Impact Layer, with ejecta material consisting mostly of devitrified vesicular impact glass granules with a white calcite cement. Sample TFBH2-9 ✳ is a sample of the white calcite cement. A 1cm layer of fine-grained carbonate overlies the ejecta material, which in turn is overlain by a 20cm unit of fine-grained carbonate with clasts in a pyritic matrix. Sample TFBH2-10 ☆ comes from this unit (Figure 171). Overlying this unit is a 7cm layer of fine-grained carbonate with clasts in a micritic matrix. An 18cm unit of shale and siltstone of the basal Rove overlies the previous unit, followed by a 2cm unit of chert. On top lays a 6cm unit of angular chert blocks in mudstone (Figure 172). Finally, the last unit consists of 60cm of siltstone and shale of the Rove formation (Figure 173).

An outcrop (Figure 174) of the S.I.L. approximately 200m west-southwest of the drill-hole site contained a similar silica flowerette features as seen at the Harbour Expressway

fieldsite. The difference between these silica flowerettes and the ones at Harbour Expressway is that these are intact and not eroded, therefore showing the full nature of the formation of the features, which have a similar appearance to stalactites. Samples were extracted and some faces were lapped for fine detail viewing. Figure 175 is a side-view of a sample of the silica flowerettes with botryoidal features around the flowerette. Figure 176 is a side-view of a sample from Terry Fox showing stalactite fingers dropping down surrounded by the peach-coloured botryoidal material. Figure 177 shows a lapped and detailed sample of the silica flowerette features with a side view to show the parallel laminated, silicified bottom. Figure 178 shows a lapped sample that gives more detail on the crypto-crystalline nature of the flowerettes, surrounding and radiating from the inner dark core, similar to stalactite formations.

Figure 161. Stratigraphic Representation of TFBH2 Drill Core.

TFBH2-10	☆	Fine-grained carbonate clasts in a pyritic matrix	
TFBH2-9	✳	White blocky carbonate cement from ejecta layer	
TFBH2-8	+	Highly silicified fine-grained grainstone with hematite	
TFBH2-7	●	Silicified fine-grained carbonate with extensive overgrowth of green mineral	
TFBH2-6	○	Black crystal growths in partially silicified fine-grained carbonate	

188

TFBH2-5   ◆   Fine-grained carbonate

TFBH2-4   ◇   Black material

TFBH2-3　　　□　　Fine-grained carbonate grainstone with rounded rip ups

Figure 162. (Upper) Parallel laminated, silicified fine sand-sized material.
Figure 163. (Lower) Layers of silt-sized carbonate with 4mm thick layers of fine-sand sized carbonate.
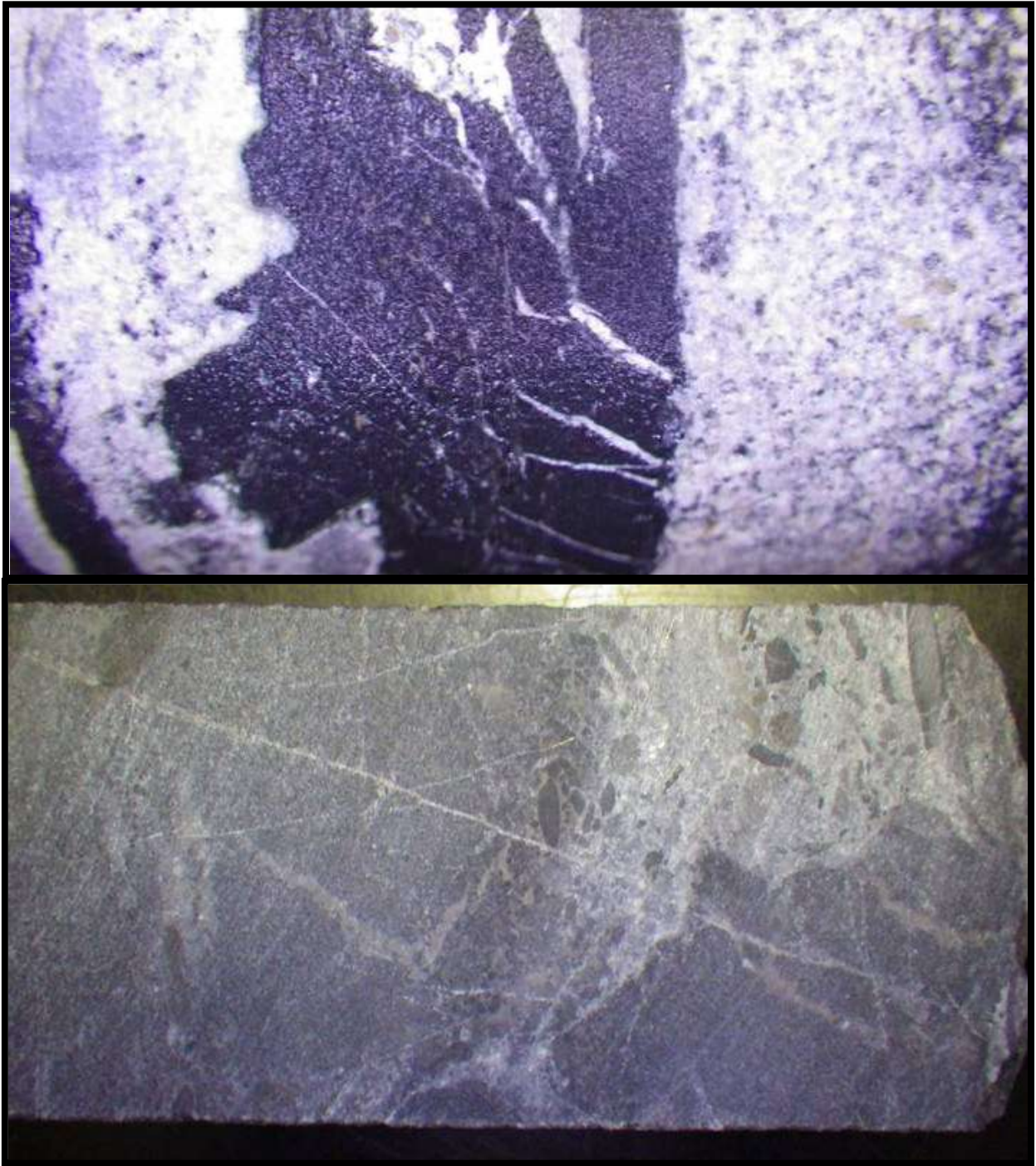
Figure 164. (Upper) Close up of carbonate grainstone with black, fractured silicified layers.
Figure 165. (Lower) Fractured, silicified grainstone in-filled with cement and granules.

Figure 166. (Upper) Close-up of fine-grained carbonate matrix showing popcorn-like texture.
Figure 167. (Lower) Broken up pieces of chert in carbonate cement.

Figure 168. (Upper) Crystalline carbonate and hematitic carbonate with agate veins.
Figure 169. (Lower) Blotchy, broken carbonate with some silicified areas.
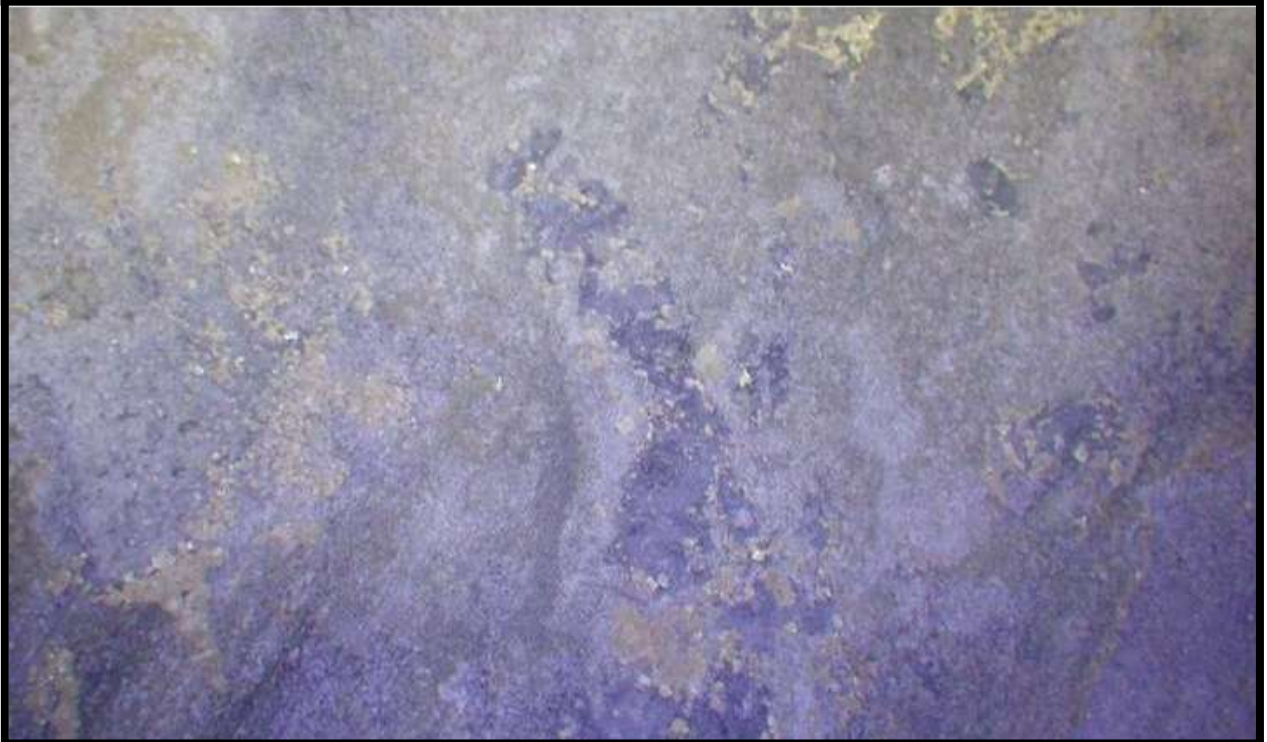
Figure 170. (Upper) Black mineral overgrowths on carbonate crystals.
Figure 171. (Lower) Fine-grained carbonate clasts in a pyritic matrix with silicified areas.

Figure 172. (Upper) Angular chert blocks in mudstone.
Figure 173. (Lower) Siltstone and shales of the Rove Formation.

Figure 174. (Upper) Outcrop at Terry Fox of the ejecta layer overlain by ankerite grainstone, Rove siltstones and a diabase sill.
Figure 175. (Lower) A sample from Terry Fox is similar to flowerette plaque at Harbour Expressway.

Figure 176. Side view of silica stalactite sample extracted from Terry Fox. Stalactites hang from 'ceiling' and develop a botryoidal coating on each stalactite finger.

Figure 177. (Upper) Lathed and lapped sample from Terry Fox of silica stalactite formation, with detail of side and top. The bottom of the sample displays a siliceous open-space fill.
Figure 178. (Lower) Lathed and polished sample of silica flowerettes from Terry Fox. Flowerettes show cryptocrystalline banding and growth with a central dark core.

3.1.2   Geochemistry

View Table 9 for TFBH2 drill core geochemistry. The samples at Terry Fox have low to medium amounts of siliciclastic material mixed in with the chemical sediments. In Figures 179B and 179C, samples TFBH2-9 (S.I.L.) and TFBH2-10 (above S.I.L.) are elevated in both REE and V respectively. All samples except for TFBH2-4, TFBH-6, and TFBH2-8 have below detection amounts of Mo. Samples TFBH2-8, TFBH2-9, and TFBH2-10 exhibit the highest V levels (Figure 180C, 180D). Samples TFBH2-4, TFBH2-6, and TFBH2-7 display similar hat-shaped REE patterns that have slight positive Eu and Gd anomalies (Figure 181A). Samples TFBH2-8, TFBH2-9, and TFBH2-10 display similar REE patterns with slightly higher positive Eu anomalies than Gd anomalies (Figure 181B). Samples TFBH2-2 and TFBH2-5 display similar shaped REE curves with positive Eu and Gd anomalies but TFBH2-5 displays a drastic negative Ce anomaly (Figure 181C). Samples TFBH2-1 shows a hat-shaped REE curve peaking with a positive Gd anomaly, and TFBH2-3 displays a constant increase in the REE elements moving toward the HREEs (Figure 181D). Figure 182B shows that there is a cluster of samples situated in one area but outlier samples TFBH2-1 and TFBH2-2 show extreme positive Gd anomalies with positive Ce anomalies, while sample TFBH2-5 has an average Gd anomaly compared to the rest of the sample set, but exhibits an extreme negative Ce anomaly. In Figure 182C most samples have a Ce anomaly close to 1.0 but increase in Gd anomaly, with outlier sample TFBH2-5 that exhibits the extreme negative Ce anomaly. In Figure 182D, there is a positive correlation between Eu and, but sample TFBH2-1 is an exception to this.
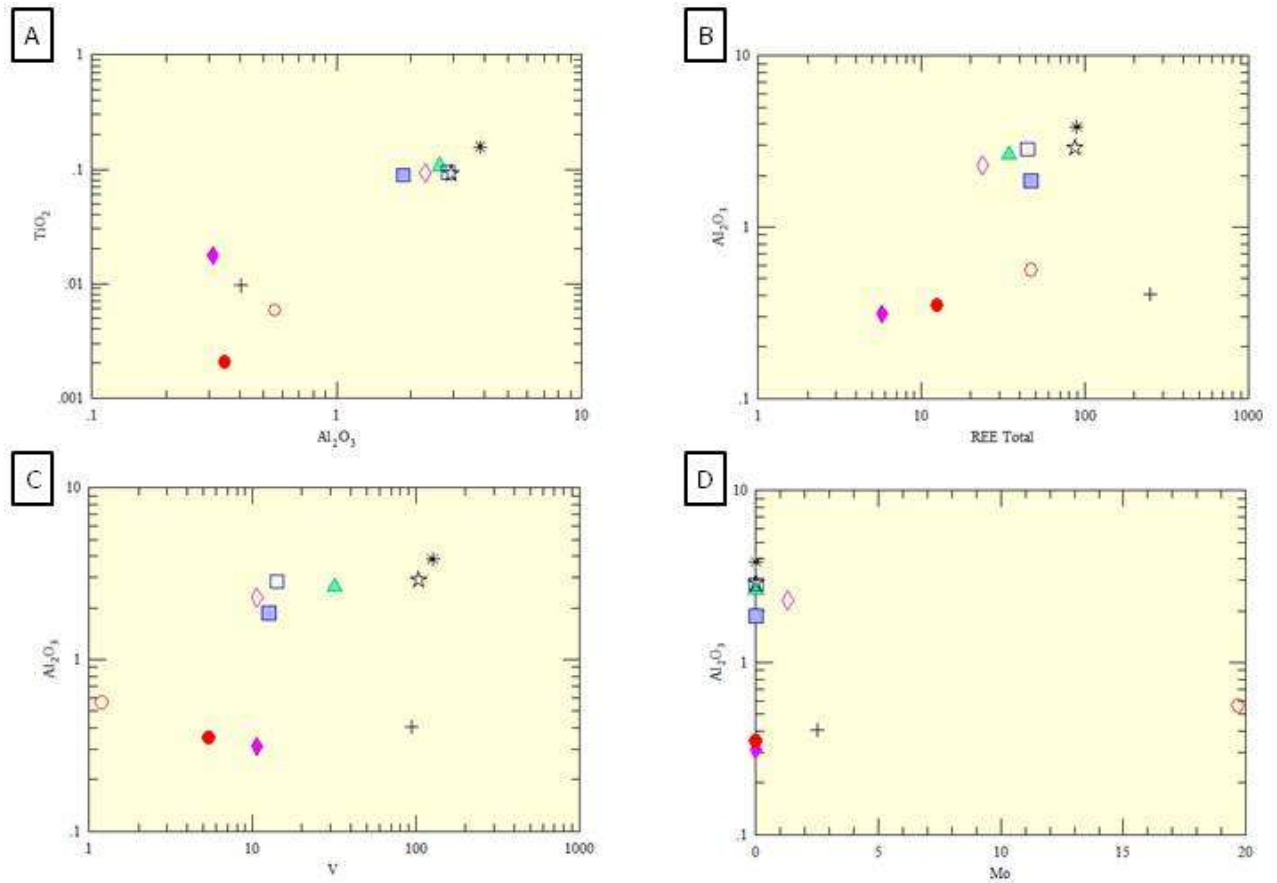
Figure 179. Bivariate plots of samples from TFBH2. A) Positive correlation exists TiO_2 and Al_2O_3 with slight outliers (samples TFBH2-5 and TFBH2-8). B) Slight clustering of samples between Al_2O_3 and REE Total with outlier point TFBH2-8 containing approximately ~175 ppm REE Total. C) No correlation exists between Al_2O_3 and V. D) No correlation exists between Al_2O_3 and Mo. All samples except for TFBH2-4, TFBH2-6, and TFBH2-8 have below detection amounts of Mo, sample TFBH2-6 had the most Mo, with almost 20ppm.
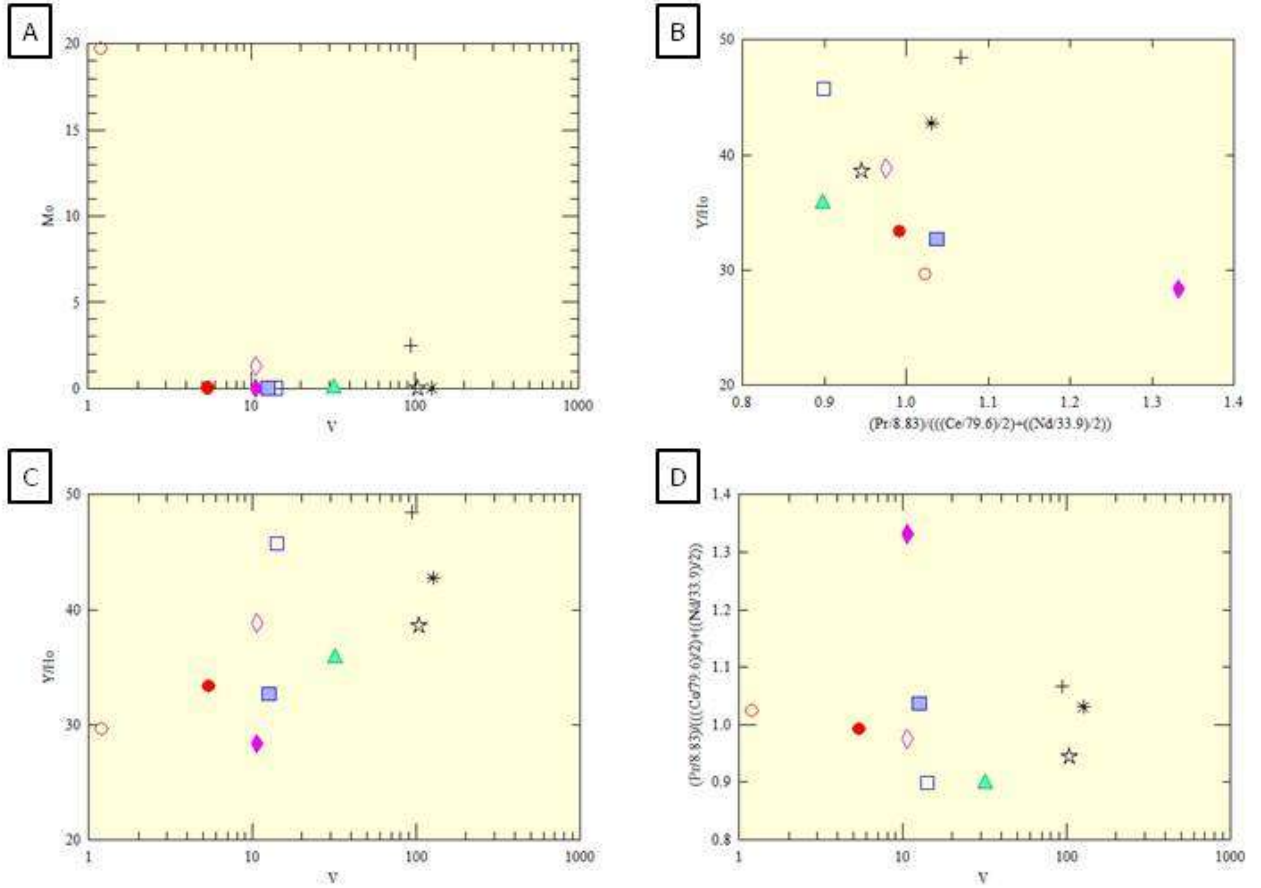
Figure 180. Bivariate plots of samples from TFBH2. A) No correlation exists between Mo and V. TFBH2-8, TFBH2-9, and TFBH2-10 are the samples with the highest levels of V. They represent the S.I.L. and samples immediately below and above. B) No clear correlation between Y/Ho and Ce anomaly. It appears that many samples that exhibit higher levels of Y/Ho ratios also exhibit Ce anomalies that are slightly more positive. C) Clustered yet positive correlation between Y/Ho and V. Most samples that have elevated levels of Y/Ho ratios also have more V. D) Cluster of samples in Ce anomaly vs V plot, with TFBH2-5 having the most negative Ce anomaly.
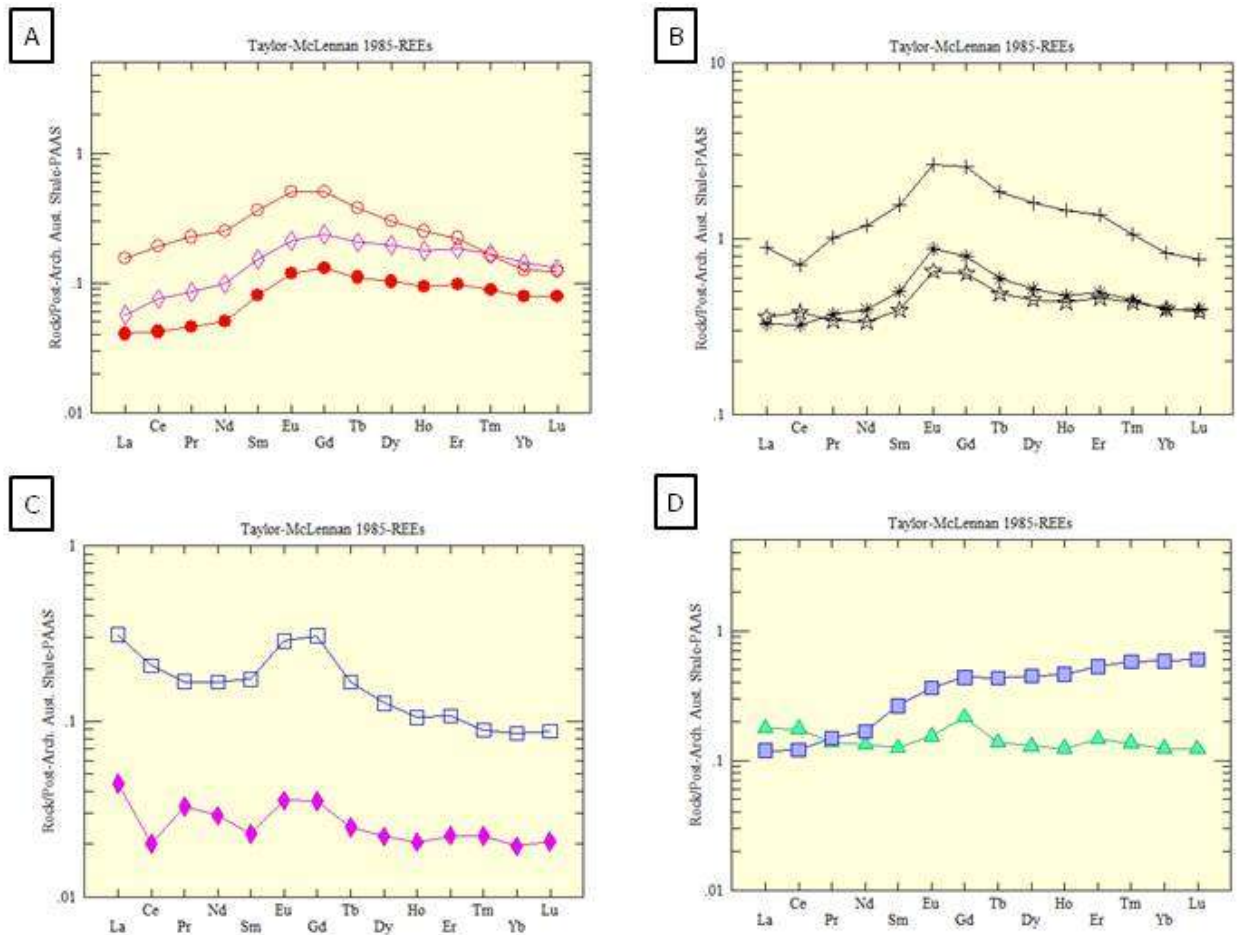
Figure 181. Rare earth element spider plots standardized to Taylor and McLennan (1985) PAAS. A) Samples TFBH2-4, TFBH2-6, and TFBH2-7 exhibit similar hat-shaped REE patterns with elevated levels of Eu and Gd. B) Samples TFBH2-8, TFBH2-9, and TFBH2-10 exhibit similar, hat-shaped REE patterns with positive Eu and Gd anomalies, but TFBH2-10 exhibits a positive Ce anomaly while the other two have negative Ce anomalies. C) Sample TFBH2-2 exhibits elevated positive Eu and Gd anomalies. Sample TFBH2-5 exhibits only slight positive Eu and Gd anomalies, but displays a sharp negative Ce anomaly. D) Sample TFBH2-1 displays a positive Gd anomaly. Sample TFBH2-3 displays enrichment in MREEs and HREEs.
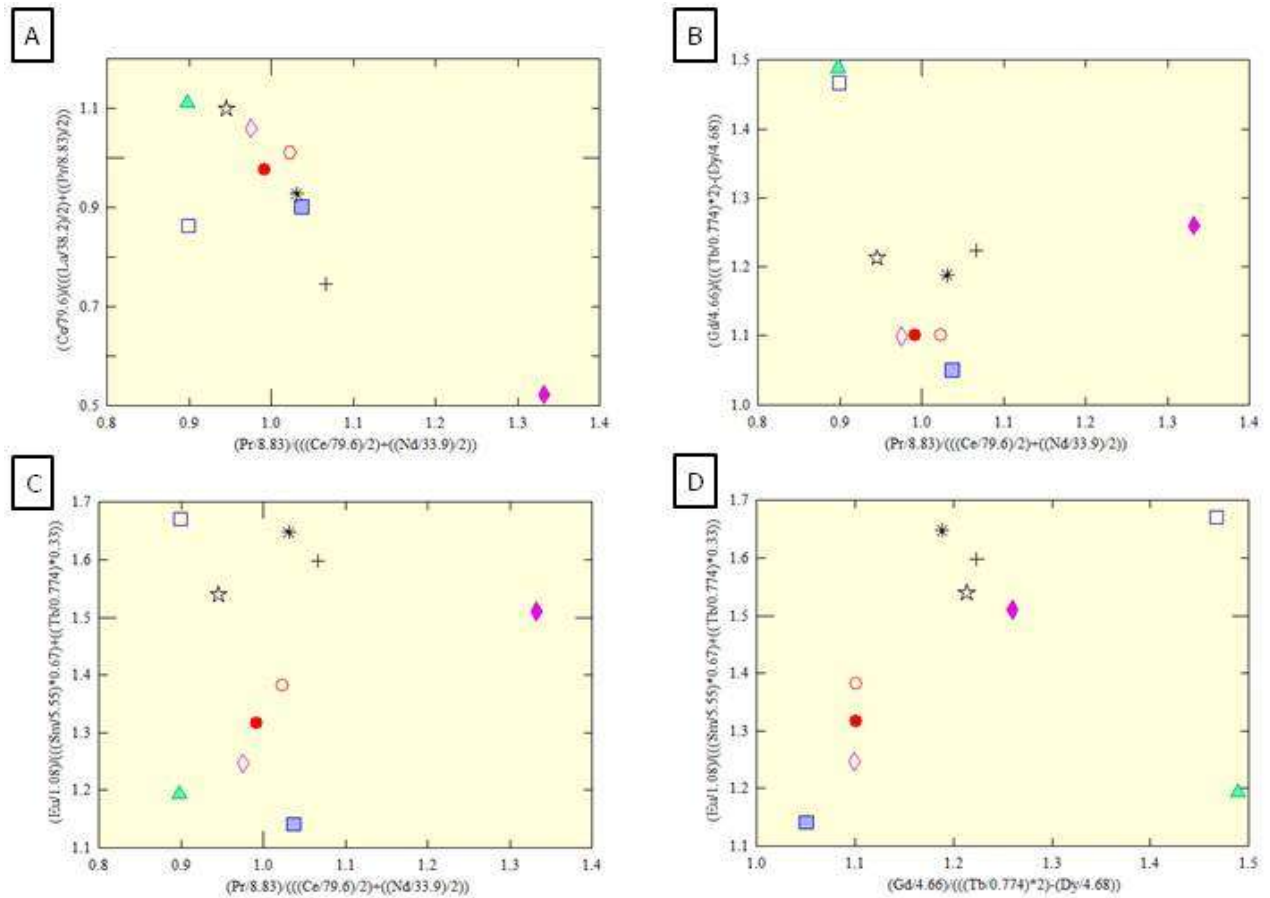
Figure 182. Bivariate plots exhibiting rare earth element anomalies of TFBH2 samples. All values were normalized to PAAS before anomaly calculations. A) Linear correlation exhibited between La and Ce anomalies. This relationship is probably due to Ce being present in both equations. B) Samples are clustered but TFBH2-1 and TFBH2-2 have the highest positive Ce anomalies and highest positive Gd anomalies, while TFBH2-5 has the highest negative Ce anomaly, and a medium positive Gd anomaly as compared to the rest of the samples. C) No relationship exists between Eu and Ce anomalies but there is a cluster in the 1.0 range of Ce anomaly, with TFBH2-5 being the outlier sample with the highest negative Ce anomaly. D) Correlation exists between Eu and Gd anomaly, where most samples that have a positive Eu anomaly, also have a positive Gd anomaly, with the exception of TFBH2-1, which displays the largest positive Gd anomaly but a small Eu anomaly.

3.1.3 Interpretations

Terry Fox drill core reflects an offshore environment where ankerite grainstones are interlayered with silty ankerite layers. These Gunflint Formation layers were exposed at one point in time prior to the Sudbury impact because silicification took place in the majority of the drill core turning carbonates into silica-rich facies. The presence of stylolites in some of the layers that are completely quartz indicates that they were originally carbonates and were diagenetically altered post-burial. It is evident that the area was silicified and subaerially exposed prior to impact because the chert layers were shattered and brecciated. The popcorn fabric in the carbonate one meter below the ejecta layer resembles chicken-wire structures which form on sabkhas with saline groundwater. The sample taken from this material has a large negative Ce anomaly indicative of cements precipitated from oxidized groundwater, further indicating subaerial exposure prior to the impact event. The V in the samples taken from the ejecta layer and the layers immediately adjacent to it is enriched indicating that the area was subject to infiltration by oxygenated water and V was able to precipitate out and into the cements of the S.I.L. and adjacent strata. The sample from directly below the S.I.L. also has a negative Ce anomaly, also indicating that the water this hematitic chert precipitated from was oxidized. The ejecta layer also contains small silica stalactites formed in open voids. These require vadose groundwater conditions to have prevailed. Fine-grained ankerite layers overlying the S.I.L. attest to pre-Rove flooding of the area and the initial Rove transgression is marked by the deposition of pure siliciclastic layers and reworked lithified material from the Gunflint formation.

3.2 BDQ-1 Drill Core

3.2.1   Lithofacies Description

Drill core BDQ-1 is located approximately 400m northwest of the Highway 588 site. This drill core has not been previously published. Figure 183 shows the stratigraphic representation of BDQ-1 drill core. Starting from the bottom of the drill core there is 8.5cm of coarse-to very coarse-grained grainstone. About 3.5cm from the bottom of this unit there are numerous silty shale drapes, approximately 1-2mm in thickness. The drapes are dipping at about 30º and highlight the cross-stratification. The grainstone grains are fractured, and the fractures are filled with quartz cement. Grains are replaced by quartz cement, with quartz cement also between some grains. Grains that are replaced are ghost-like, dark and sub-rounded. Above this unit lies 10cm of layers of very fine sand to silt grainstone, with one thick layer of medium-sized grainstone, with a stylolite. Average thickness of layers is 5mm with fairly sharp contacts. Overlying this unit is a 55cm layer of coarse grainstone with millimeter thick mud drapes and other fine-grained layers up to 7mm thick that may be chemical sediments such as chert or veins of quartz. The top 3cm of this unit is silicified with fractured angular pieces. Sample BDQ-1-1 ▲ is taken from the base of this unit. The overlying unit is 50cm thick and is a transition zone from mostly massive grainstone with a few layers, to approximately 70% of medium- to coarse-grained grainstone with layers averaging 2cm in thickness (with one 6cm thick layer near the bottom), containing an abundance of rip up clasts, and interlayered with fine-grained grey layers. The fine-grained layers are made of carbonate, specifically neomorphic spar, averaging 8mm in thickness. Carbonate rhombs are present in this unit, along with stylolites. This unit also has evidence of late-stage silicification. On top rests a 25cm thick unit consisting of 60% grainstone and 40% of fine-grained carbonate layers, with some stylolites present. Layers have sharp

contacts, and some grainstone layers are lensoid. There is a layer of rip-up clasts near the top with clasts of siltstone aproximately 2cm in width. On top rests a 4cm unit of dark grey medium- to coarse-grained grainstone that is silicified with a sharp contact at its base. A stylolite is present on its top contact. Above sits a 23cm thick unit of similar dark grey medium- to coarse-grained silicified grainstone. On top sits a 4cm thick grainstone layer, followed by a 10cm thick grainstone layer - both of which have quartz grains. On top is situated 23 cm of interlayered fine-grained carbonate siltstones, with grainstones consisting of quartz and carbonate. Above is 18cm of interlayered fine-grained carbonate siltstones with grainstones consisting of quartz and carbonate but now is a creamy colour that possibly represents carbonate replacement of the quartz. This unit is cross-stratified near the base for approximately 4cm.

Sample BDQ-1-2 ☐ is located at this base of this unit. Over top of this lies 69cm of alternating coarse-grained grainstone with abundant interclasts and siltstone. Sample BDQ-1-3 ☐ was taken from the 31cm overlying layer that consists of coarse-grained grainstone with silty layers. Above this lies 78cm of medium and coarse grainstone layers interlayered with silt-sized grainstone. On top is a 22cm unit of badly altered medium-grained grainstone with irregular silt lenses with vertical fracture. Angular interclasts and stylolites are present in this unit, followed by a sharp contact. Sample BDQ-1-4 ◊ is taken from this unit. On top lies a 7cm thick very coarse-grained grainstone, followed by 12cm of cream-coloured medium-grained grainstone with rip-up clasts approximately 7mm in length. It is possibly cross-stratified. The silt layers in between are cream-coloured and silicified. Overlying this unit is 25cm of silicified, medium-grained grainstone with some silty layers approximately 0.5cm thick, and stylolites are present.

This unit is a brecciated zone, probably fractured from the impact event. Sample BDQ-1-5 ◆ is taken from this unit and consists of medium-grained grainstone with some carbonate. On top lays 10cm of brecciated silicified, coarse-grained grainstone, followed by 28cm of brecciated

dark coloured very coarse-grained grainstone, with not much silicification. Overlying this unit is 11cm of medium-grained grainstone with a spotted alteration pattern, followed by 4cm of silicified very coarse-grained grainstone with a quartz matrix. Above lies 13cm of silicified, cross-bedded, coarse-grained grainstone, followed by 15cm of dark, silicified coarse-grained grainstone. Next on top lies 11cm of silicified very coarse-grained grainstone. This unit is a transition zone, where the top of the unit is carbonate. The next unit is 86cm of brecciation. The bottom 6cm of the 86cm unit consists of agate, massive silica and fine-grained carbonate with vertical fracturing present. The next 7cm is medium-grained grainstone with agate, and is silicified in places. Vertical fracturing is present in this area as well. Sample BDQ-1-6 is taken from this 7cm unit of the 86cm unit. The 11cm thick unit overlying the 7cm unit consists of carbonate and silica patches. The carbonates are fine-grained and have graded contacts with each layer, and the silica contains granules. On top of the entire 86cm unit is 25cm of medium-grained ankerite that coarsens upward, with white and dark clasts, in a reddish matrix. There are approximately 1cm of rip-ups near the top of the unit, with some pyrite. The entire unit is vertically fractured. This is followed by 9cm of brecciated coarse-grained grainstone with agate veins. On top lays a 10cm medium-grained carbonate grainstone, followed by 5cm of siltone of which sample BDQ-1-7 is taken from. This is in turn followed by 5cm of fine-to-medium-grained grainstone. This is succeeded by three units of the Sudbury Impact Layer. The first unit is 4cm thick and consists of hard ejecta material, followed by 14cm of unsilicified ejecta material that is very soft and greenish-brown in colour with small pebbly and green inclusions. The final unit is 16cm in thickness and consists of hard ejecta material that contains lapilli that are 0.5-1.0cm wide, surrounded by carbonate cement. The overlying unit is 54 cm thick and consists of medium-grained, ankerite grainstone with layers of coarse-grained grainstone approximately 1mm-10mm thick. Cross-bedding is present in the lower half of the unit while in the top half of

the unit assymetrical ripples are present. Sample BDQ-1-8 ✛ is taken from the upper portion of this unit. The following unit is 23cm thick and consists of a chaotic mixture of broken pieces of siltstone and carbonate ranging in size from 0.1-0.5mm in with shale layers. There is a chicken-wire structure present in the top of this unit where sample BDQ-1-9 ✴ is taken from. There is another feature that has a rhomb (Figure 184) and lath (Figure 185) shape to it and samples BDQ-1-gyp1 ☆, BDQ-1-gyp2 ★, BDQ-1-gyp3 ✛, and BDQ-1-gyp4 ✛ are taken from this unit. Next is 13cm of parallel bedded siltstone that is overlain by fine-grained grainstone with layers of medium-grianed grainstone averaging 0.3mm in thickness. This is succeeded by 8cm of chaotic broken pieces of siltstone and fine-grained grainstone, followed by 8cm of brecciated and chaotic medium-grained grainstone with broken clasts. There are some domed structures present that consist of medium- to coarse-grained grainstone. Sample BDQ-1-10 ✖ is taken from this unit. The following unit is an 80cm thick carbonate unit of chicken-wire structure consisting of small crystals at the base of the unit, which coarsen upwards into large crystals at the top of the unit (Figures 186, 188, 189, 190, 191, 192, 193, 194, 195). There are a few mud layers in between. Samples BDQ-1-11 ✖ and BDQ-1-13 ✛ are taken from the crystals in this unit. 24-25cm above the base of this unit there is greenish material with 0.1-0.5cm long laths, and also similarily in the 47-48cm portion there is greenish material with longer green pieces. Above this is the contact with the Rove Formation (Figure 187). There is 10cm of siltstone that immediately overlies the previous carbonate crystal unit. Above sits a 155cm shale and siltstone thinly laminated unit, followed by a 95cm silty shale unit. This is succeeded by a 20cm thick green tuff layer, followed by a 6cm thick, fine-grained, carbonate grainstone with mud rip-ups. On top sits a 5cm green ash layer with fine green material embedded and is then followed by 17cm of greenish silt which is non-effervescent, but includes thin mud laminations. Following

this is 122cm of carbonate mud, mud rip ups, mud layers and carbonate crystals. Samples BDQ-

1-14 ⬥ (carbonate sediment) and BDQ-1-15 ▽ (large carbonate crystals) are taken from this

layer. After this unit is the contact with the black Rove shales.

Figure 183. Stratigraphic Representation of BDQ-1 Drill Core.

10

9

BDQ1-13
BDQ1-11

Chicken-wire carbonate crystals

BDQ1-10   ✖   Fine-grained carbonate

BDQ1-9   ✳   Rhomb-shaped crystals
BDQgyp4   ✚
BDQgyp3   ✚
BDQgyp2   ★
BDQgyp1   ☆

BDQ1-8   +   Medium-grained grainstone

8

BDQ1-7   ●   Siltstone

BDQ1-6

○ Medium-grained grainstone

5

BDQ1-5

◆ Medium-grained grainstone with some carbonate

BDQ1-4

◇ Medium-grained grainstone

4

3

2

BDQ1-3

☐ Silty carbonate

BDQ-1-2

☐ Cream-coloured fine-grained grainstone

1

BDQ1-1

△ Coarse-grained grainstone

Figure 184. (Above) Pseudomorph rhomb-shaped features after gypsum in carbonate.
Figure 185. (Below) Bladed pseudomorphs after gypsum in carbonate.

Figure 186. (Above) Chicken-wire structure forms a coarsening upward sequence of carbonate crystals at the top of the carbonate succession.
Figure 187. (Below) Contact between top of chicken-wire calcite unit and silts of the Rove formation.
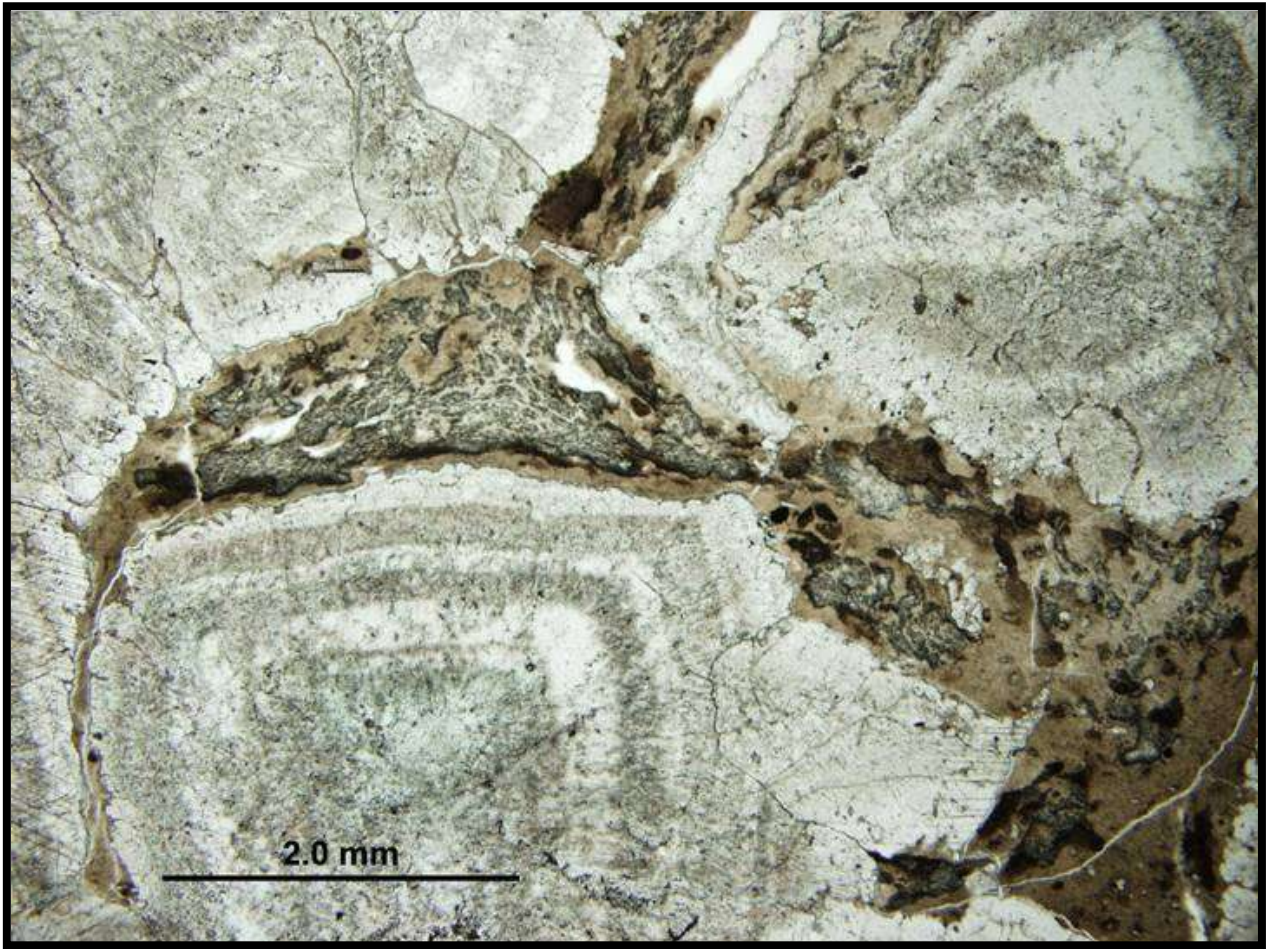
Figure 188. (Above) Thin section in plane polarized light of top of chicken-wire structure. Clearly defined growth lines are present in calcite crystals, with mud surrounding each crystal.
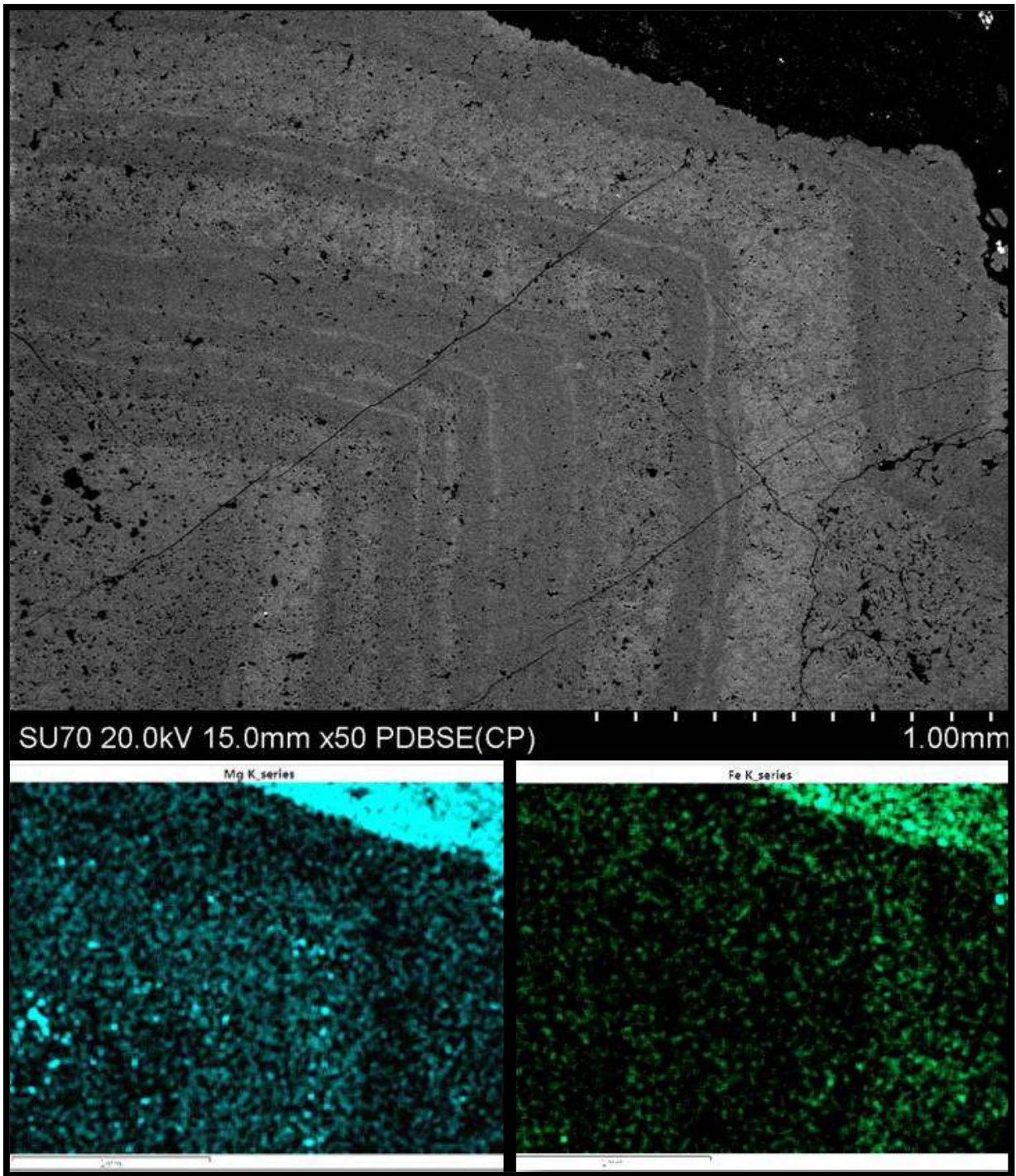
Figure 189. (Top) SEM backscatter electron image of banded calcite chicken-wire crystal.
Figure 190. Lower Left. False colour map of Figure 189. Blue bands are magnesium-rich.
Figure 191. Lower Right. Green bands are iron-rich.
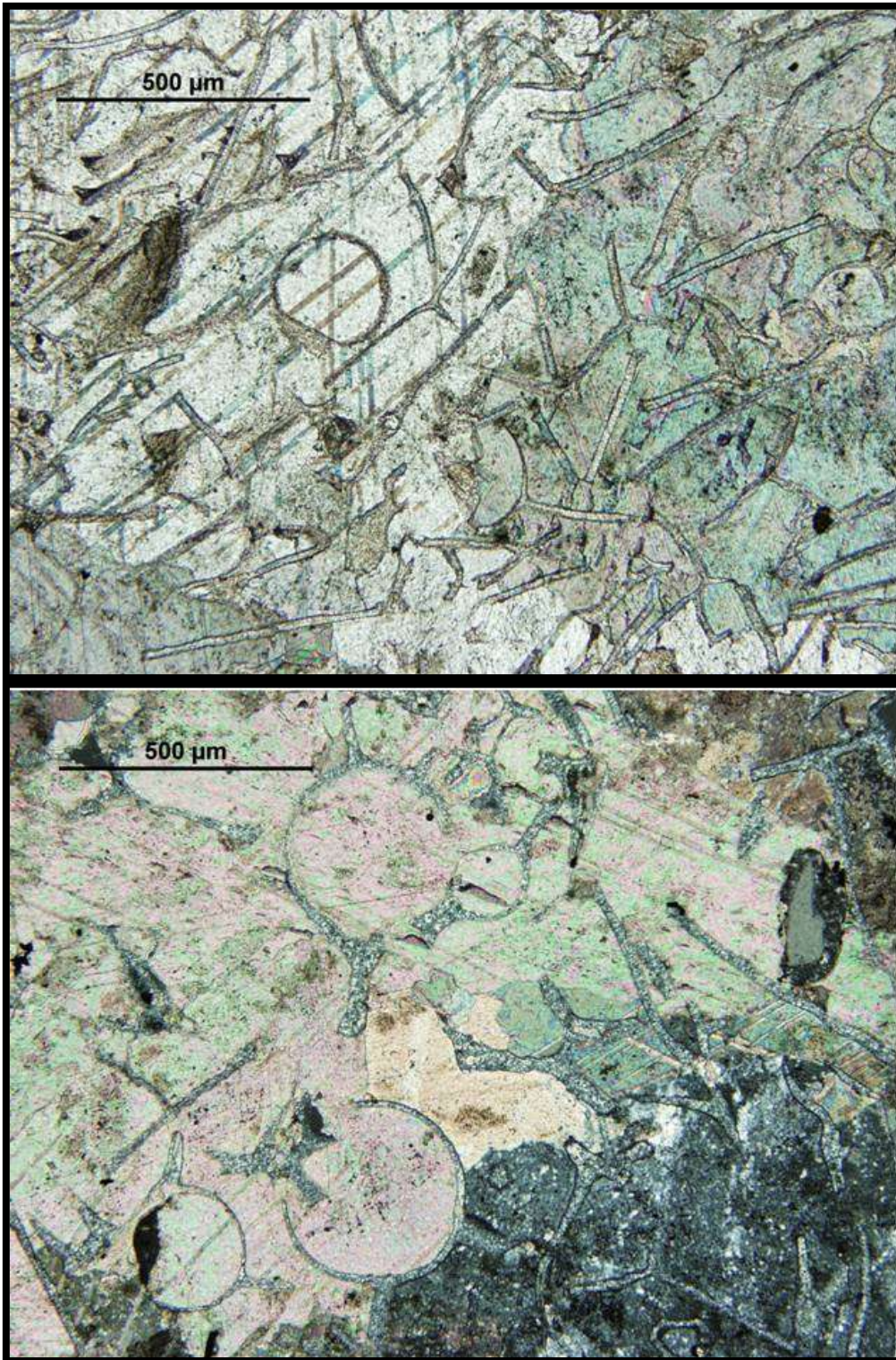
Figure 192. (Above) Thin section in plane polarized light of carbonate chicken-wire structure, with sphere and filament structures embedded within the carbonate.
Figure 193. (Below) Thin section in plane polarized light. Close up of chicken-wire structure with sphere and filament structures. Some sphere rims are intact and hold their shape, while others have partially collapsed or deteriorated.
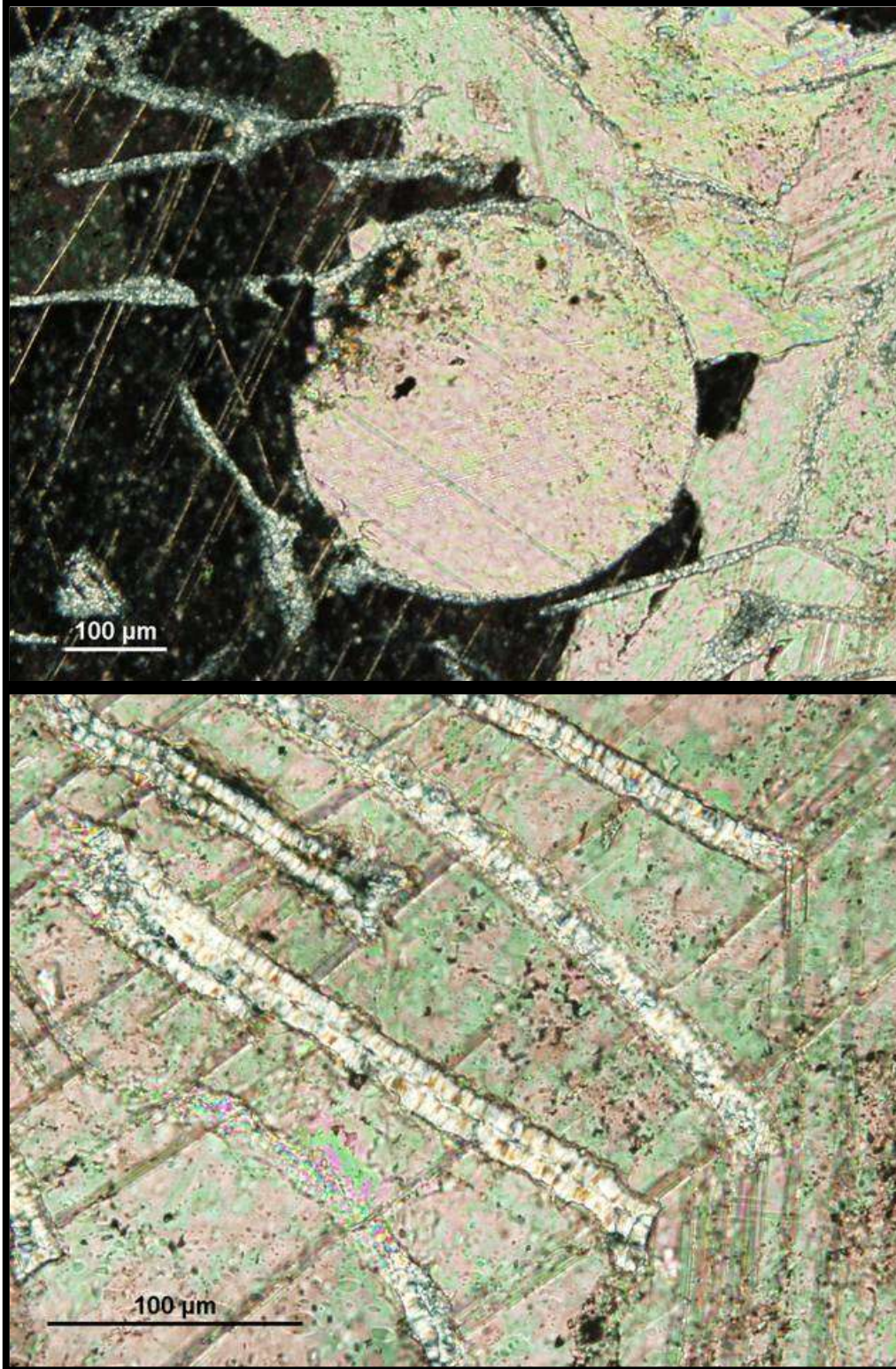
Figure 194. (Above) Close up of silica rimmed sphere infilled with carbonate. Initially the sphere was hollow.
Figure 195. (Below) Close up of silica collapsed spheres where rims are pressed together equally.

3.2.2   Geochemistry

View Table 10 for BDQ-1 drill core for geochemistry. The samples in BDQ-1have low

to medium-high amounts of siliciclastic material that is mixed in with the chemical sediment.

Sample BDQ-1-7 displays the highest amount of REE enrichment and is a slight outlier point in

Figure 196B. Figure 196C shows a general positive relationship between Al_2O_3 and V where

samples with larger Al_2O_3 concentrations also have large V concentrations. Sample BDQ-1-9

and BDQ-1-7 are extremely enriched in V. In Figure 196D, there is also a positive linear

relationship between Al_2O_3 and Mo, where the samples whose Mo values are not below

detection increase as Al_2O_3 increases. Sample BDQ-1-9 is most enriched in Mo. In Figure

197A, there is no relationship between Mo and V, but sample BDQ-1-9 is rich in both. In Figure

197B, there does not seem to be a relationship between Y/Ho and Ce anomaly. No correlation

exists in Figure 196C between Y/Ho and V. In Figure 196D, there seems to be a relationship

between Ce anomaly and V, where samples that increase in V also tend to have a negative Ce

anomaly. In Figure 198A, samples BDQ-1-gyp1, BDQ-1-gyp3, BDQ-1-gyp4, BDQ-1-10, and

BDQ-1-15 exhibit similar REE patterns with elevated Eu and Gd anomalies. In Figure 198B,

samples BDQ-1-3, BDQ-1-5, BDQ-1-8, BDQ-1-9, BDQ-1-14 and BDQ-1-gyp2 exhibit similar

REE curves with all samples exhibiting elevated positive Eu and Gd anomalies. In Figure 198C,

sample BDQ-1-7 exhibits a positive Gd enrichment and a negative Ce anomaly. In Figure 198D,

samples BDQ-1-11 and BDQ-1-14 display similar REE curves where both exhibit slight negative

Eu anomalies. In Figure 198E, samples BDQ-1-4 and BDQ-1-6 display similar REE patterns

with positive Eu and Ce anomalies. In Figure 198F, samples BDQ-1-1 and BDQ-1-2 display

similar REE patterns where there are positive Eu and Gd anomalies in both samples. In Figure

199B, samples with a positive Ce anomaly tend to have higher positive Gd anomalies, and

samples with negative Ce anomalies tend to have lower positive Gd anomalies. In Figure 199C,

samples with a positive Ce anomaly tend to have higher positive Eu anomalies, whereas samples

with a negative Ce anomaly tend to have lower positive Eu anomalies. In Figure 199D, it is

observed that as samples increase in positive Gd anomalies, their positive Eu anomalies increase

as well.
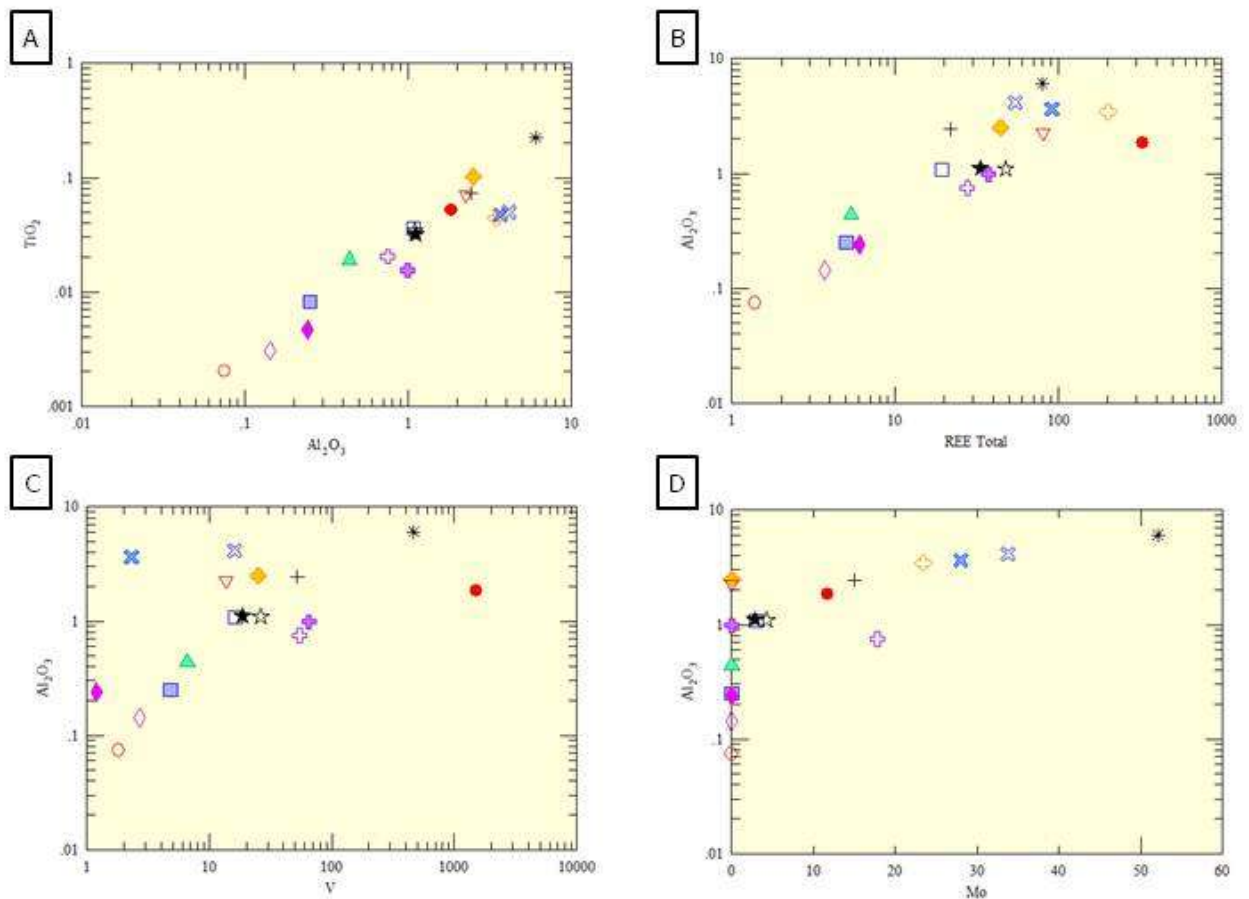
Figure 196. Bivariate plots of samples from BDQ-1. A) Positive linear correlation exists between TiO_2 vs Al_2O_3. Siliciclastic content varies from very low to moderately high. B) A positive linear relationship exists between Al_2O_3 and REE Total. C) Positive, yet slightly scattered linear correlation between Al_2O_3 and V, with BDQ-1-7 and BDQ-1-9 (samples from immediately below and above the ejecta layer) having higher Al_2O_3 levels and extreme V enrichment. D) Positive correlation between Al_2O_3 and Mo, except for samples that have below detection Mo levels.
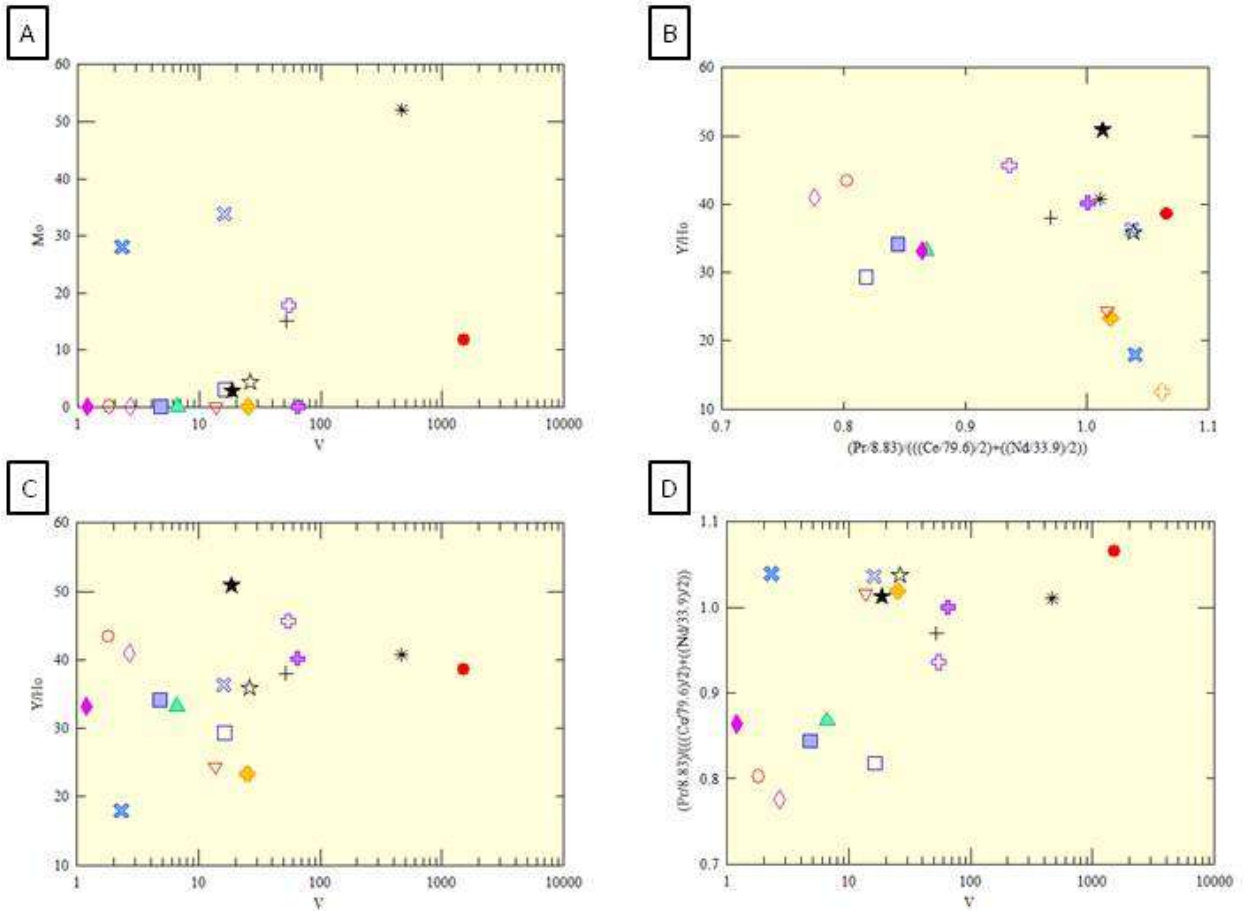
Figure 197. Bivariate plots of samples from BDQ-1. A) No correlation exists between Mo and V. B) No correlation exists between Y/Ho ratio and Ce anomaly. C) No correlation exists between Y/Ho and V. D) Positive correlation exists between Ce anomaly and V. Many samples that have higher or increasing V concentrations exhibit the transition from a positive to a negative Ce anomaly.

227
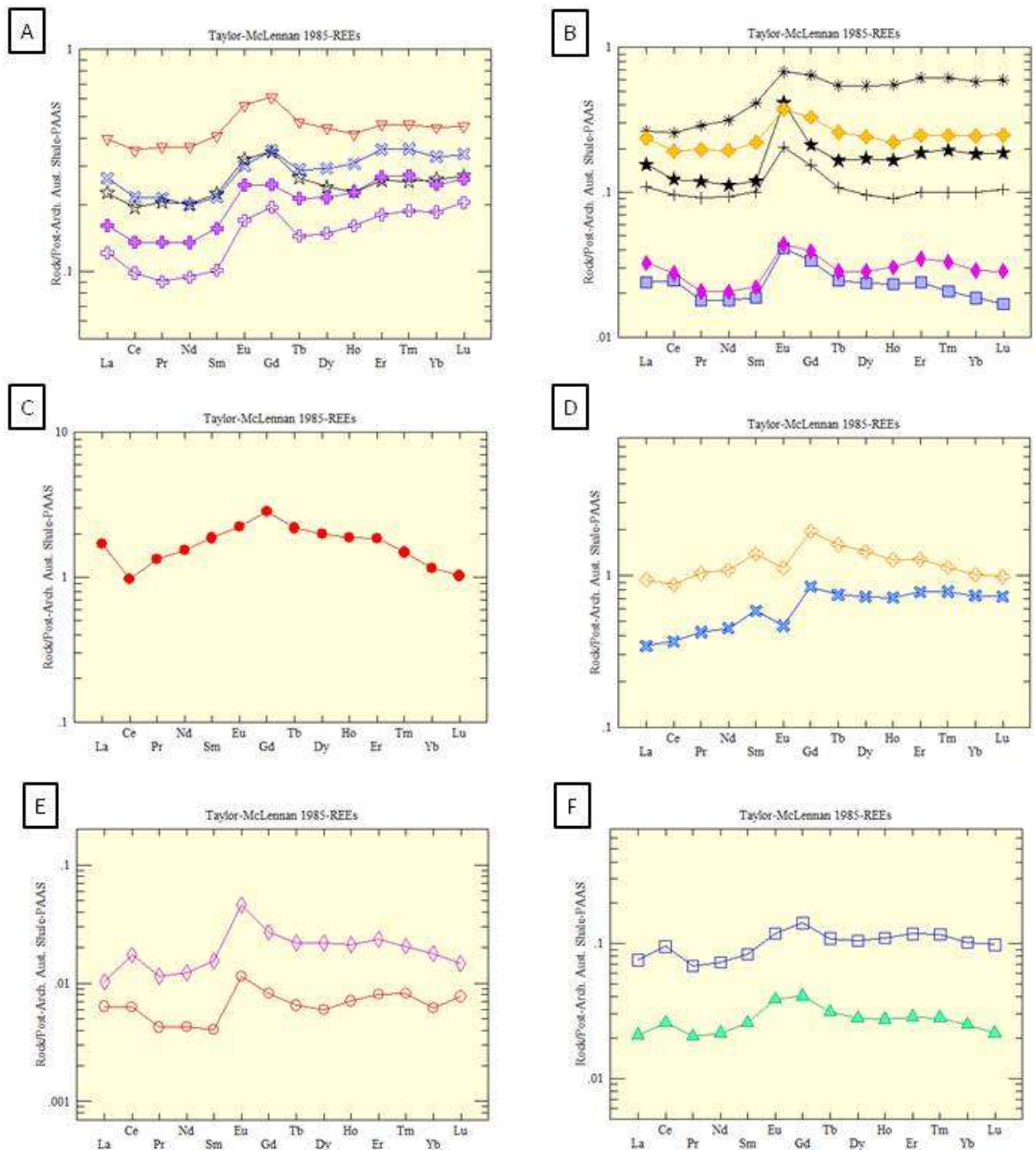
Figure 198. Rare earth element spider plots standardized to Taylor and McLennan (1985) PAAS. A) Samples BDQ-1-gyp1, BDQ-1-gyp3, BDQ-1-gyp4, BDQ-1-10, and BDQ-1-15 exhibit similar REE shapes curves with elevated Eu and Gd anomalies, and LREE depletion. B) Samples BDQ-1-3, BDQ-1-5, BDQ-1-8, BDQ-1-9, BDQ-1-gyp2, and BDQ-1-14 exhibit similar REE patterns with all samples exhibiting larger Eu anomalies than Gd anomalies. C) Sample BDQ-1-7 exhibits Gd enrichment and a negative Ce anomaly. D) Samples BDQ-1-11 and BDQ-1-13 display similar REE patterns with negative Eu anomalies. E) Samples BDQ-1-4 and BDQ-1-6 display similar REE patterns with positive Eu and Ce anomalies. F) Samples BDQ-1-1 and BDQ-1-2 display similar shaped REE patterns with positive Eu, Gd, and Ce anomalies in both samples.

228
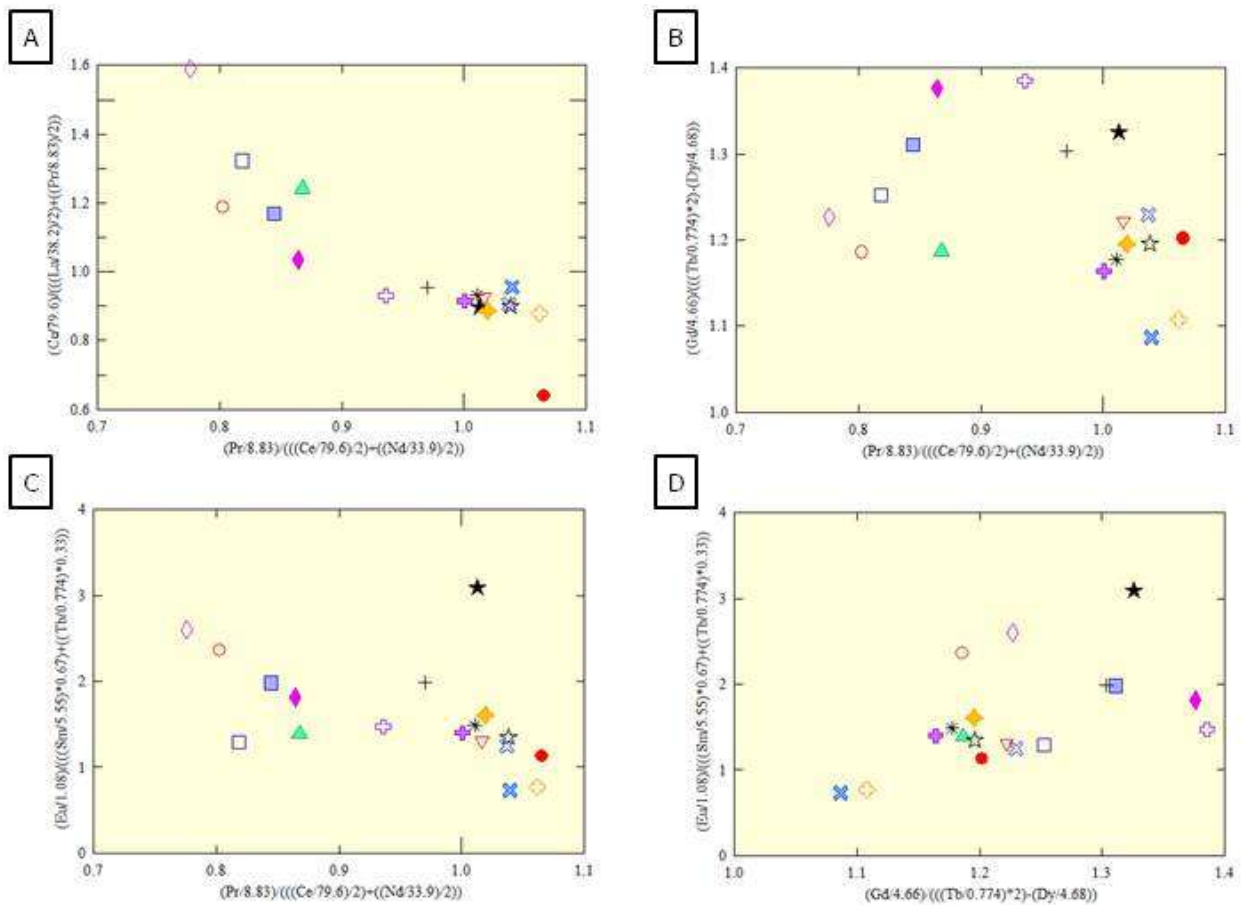
Figure 199. Bivariate plots exhibiting rare earth element anomalies of BDQ-1 samples. All values were normalized to PAAS before anomaly calculations. A) Linear correlation exhibited between La and Ce anomalies. This relationship is probably due to Ce being present in both equations. Only samples BDQ-1-7 (ankerite immediately below S.I.l.) and BDQ-1-13 (top of chicken-wire texture below Rove formation) show negative Ce anomalies. B) No relationship exists between Gd and Ce. C) Positive linear relationship between Eu and Ce anomalies, with the exception of BDQ-1-gyp2 which exhibits an extreme positive Eu anomaly as compared to the rest of the sample set. D) Linear relationship between Eu and Gd, where most samples that increase in Gd levels also increase in Eu levels.

229

3.2.3   Interpretations

The ankerite grainstones near the bottom of drillcore BDQ-1 denote deposition in an offshore location. Gunflint formation grainstones such as these commonly represent tempestites with intervening fine-grained carbonate deposited during fair-weather periods (Fralick, 1988; Pufahl and Fralick, 2000; Pufahl and Fralick, 2003). As the S.I.L. is approached, the amount of silicification of the grainstones increases to the point of total silicification with agate veins. Just prior to the deposition of the Sudbury Impact Layer, the silicified unit below the S.I.L. was shattered due to the shock waves generated by the impact, denoting silicification before impact. During deposition of the Sudbury Impact Layer, the land was subaerially exposed and the sediment developed high levels of vanadium from the cement that was precipitated, denoting oxidized groundwater. The material lying directly beneath the S.I.L. has a negative Ce anomaly as does the carbonate that overlies the S.I.L. and pseudomorphs gypsum forming a chicken-wire texture. Both the chicken-wire textured carbonate above the S.I.L. and the one below the Rove have extreme Mo enrichment, probably denoting delivery of Mo by oxidized continental groundwater and its precipitation in the organic-rich sabkha to intertidal sediment. The positive Eu anomalies of this sediment denote that seawater also formed a portion of the groundwater system. This mixed seawater continental groundwater system is typical of many modern marine sabkha systems. Bladed carbonate pseudomorphs of gypsum crystals are imbedded in the sediment above the chicken-wire texture denoting a progression from sabkha to uppertidal flat with time and probably forming a prelude to a flooding event represented by the overlying grainstone. This is capped off by another interval of chicken-wire texture immediately beneath the Rove Formation siltstones. The spherules in the chicken-wire carbonate layer below the Rove are similar to what Chadwick et al. (2001) describe in a dolomite layer they encountered in the Ketilidian orogen, in South Greenland. The Greenland spherules were first interpreted as

microfossils (*Vallencia* sp.) by Bondesen et al. (1967) because of their spheroid shape, but later the spherules were reinterpreted as replaced distal impact ejecta in the mid-Precambrian strata, either representing the Vredefort impact in South Africa at c. 2025 Ma or the Sudbury impact in Canada at c. 1850 Ma (Grieve 1998). So, the spherules in the carbonate layer below the Rove may represent reworked impact debris.

3.3 PR-98-1 Drill Core

3.3.1   Lithofacies Description

Drill core PR-98-1 is located at 48.057º N, 89.573º W.   Figure 200 shows the

stratigraphic representation of PR-98-1 drill core. Addison et al. (2005) previously researched

this drill core. At the bottom of the drill core is 88cm of fine-grained carbonate grainstone with a

few pronounced stylolites (Figure 201). There are low-angle truncations, most likely hummocky

cross-stratification where the sand is thicker, while other areas are composed of 0.2cm-1cm

thick, very fine-grained grainstone and sand layers that have a blotchy appearance and are

diagenetically altered (Figure 202). The quartz is situated along the stylolite boundary indicating

that it was present before dissolution. Blobs of micrite that are surrounded by stylolites are

present. Sample PR-98-1-1 ▲ was taken 40cm above the base of this unit. Overlying this unit

is 10cm of black chert in-medium-grained carbonate grainstone, with silicification eating into the

grainstone. Above lies 5cm of medium-grained carbonate grainstone, followed by 4cm of badly

silicified grainstone. This in turn is overlain by 27cm of medium-grained carbonate grainstone

with some carbonate rip-ups. Layers are approximately 1cm thick and are separated by dark

micritic layers. Everything is parallel laminated. Sample PR-98-1-2 ☐ comes from this unit.

On top lies 32cm of ejecta material from the Sudbury Impact Layer, which is fine-grained at the

bottom, with lapilli in the middle (Figure 203), and with medium-grained material on top.

Sample PR-98-1-3 ☐ was taken from this unit. On top rests a 12cm thick unit of parallel

laminated carbonate siltstone with some darker, organic-rich micrite layers less than 1mm thick.

Sample PR-98-1-4 ◇ is taken from the top of this unit. Following on top is 8cm of medium-

grained ankerite grainstone with faint cross-stratification, followed by a 6cm zone of salmon-

coloured, highly silicified material. This is overlain by 8cm of carbonate siltstone with small

lenses of medium-grained grainstone in the top 3cm. On top lies 10cm of interlayered medium-grained grainstone and micrite, followed by 7cm of wave-ripple laminated silt-sized carbonate (Figure 204). On top lies 3cm of dark-coloured, medium-grained grainstone, succeeded by 7cm of greenish micrite with cracks filled with medium-grained grainstone. Both bottom and top boundaries are cracked and broken. Following upwards is a 2cm layer of medium-grained ankerite grainstone that grades into 1cm of micrite, and another 2cm of medium-grained grainstone that grades into 3cm of green micrite. On top lies 4cm of coarse-grained green grainstone that grades into fine silt at its top (Figure 205). Sample PR-98-1-5 ◆ is taken from this layer. Overlying this layer is 1cm of coarse-grained grainstone that grades into fine-grained grainstone, followed by a sharp erosive contact with 7cm of rip-up conglomerate with pieces of the green micrite. Succeeding this unit is 6cm of cross-stratified medium-grained grainstone, followed by 7cm of black micrite that is partially silicified. This is in turn overlain by 4cm of coarse-grained grainstone with large ripped up pieces of green micrite at the bottom of the layer. Above lies 3cm of salmon-coloured chert (Figure 206) from which sample PR-98-1-6 ⬡ is taken, and on top lays a 5cm layer of medium-grained carbonate grainstone from which sample PR-98-1-7 ⬤ is taken. Finally, situated on top are the Rove Formation shales and tuffaceous layers (Figure 207).

Figure 200. Stratigraphic Representation of PR-98-1 Drill Core

PR98-1-2	□	Medium-grained carbonate grainstone
PR98-1-1	△	Fine-grained carbonate grainstone
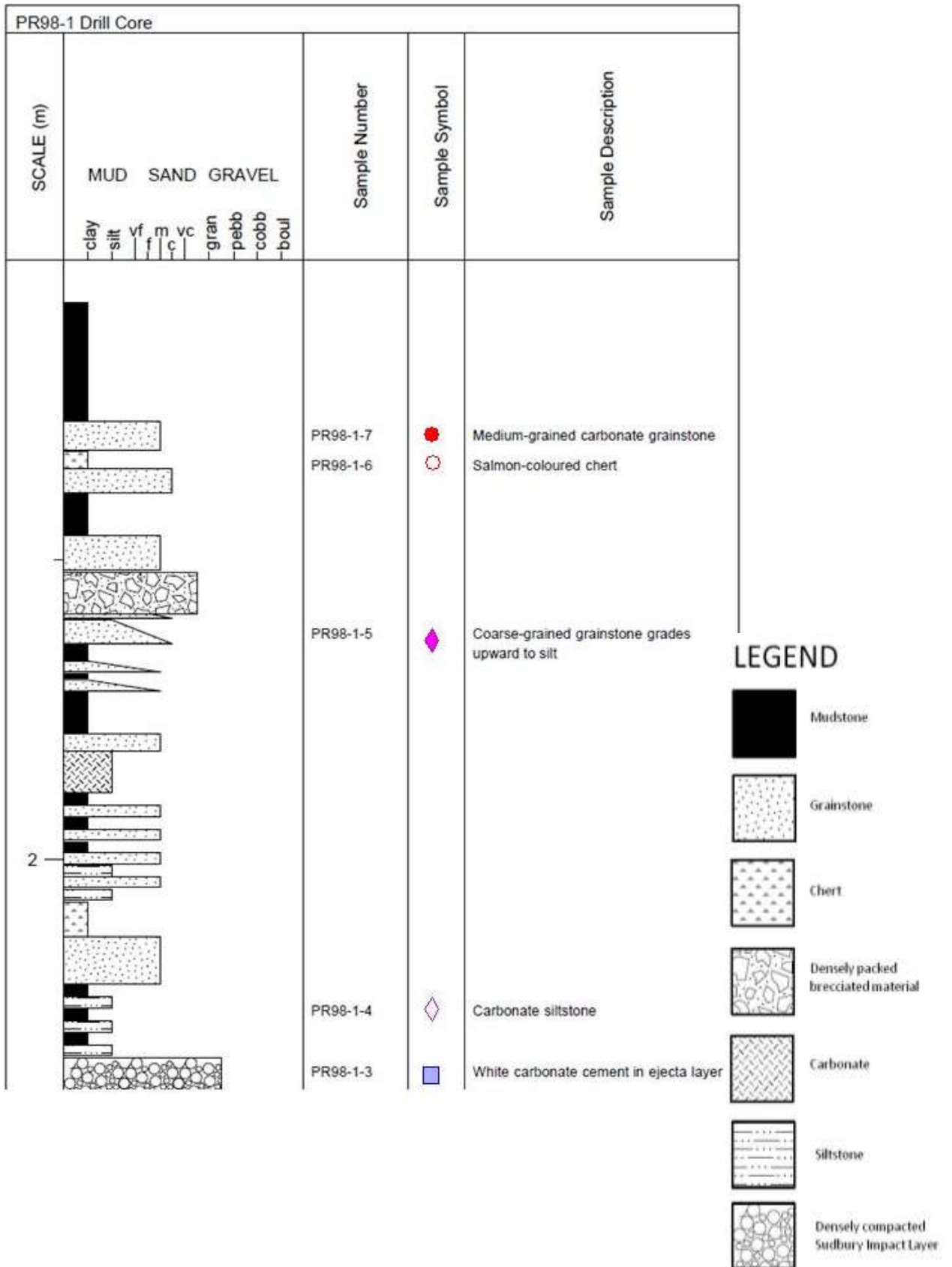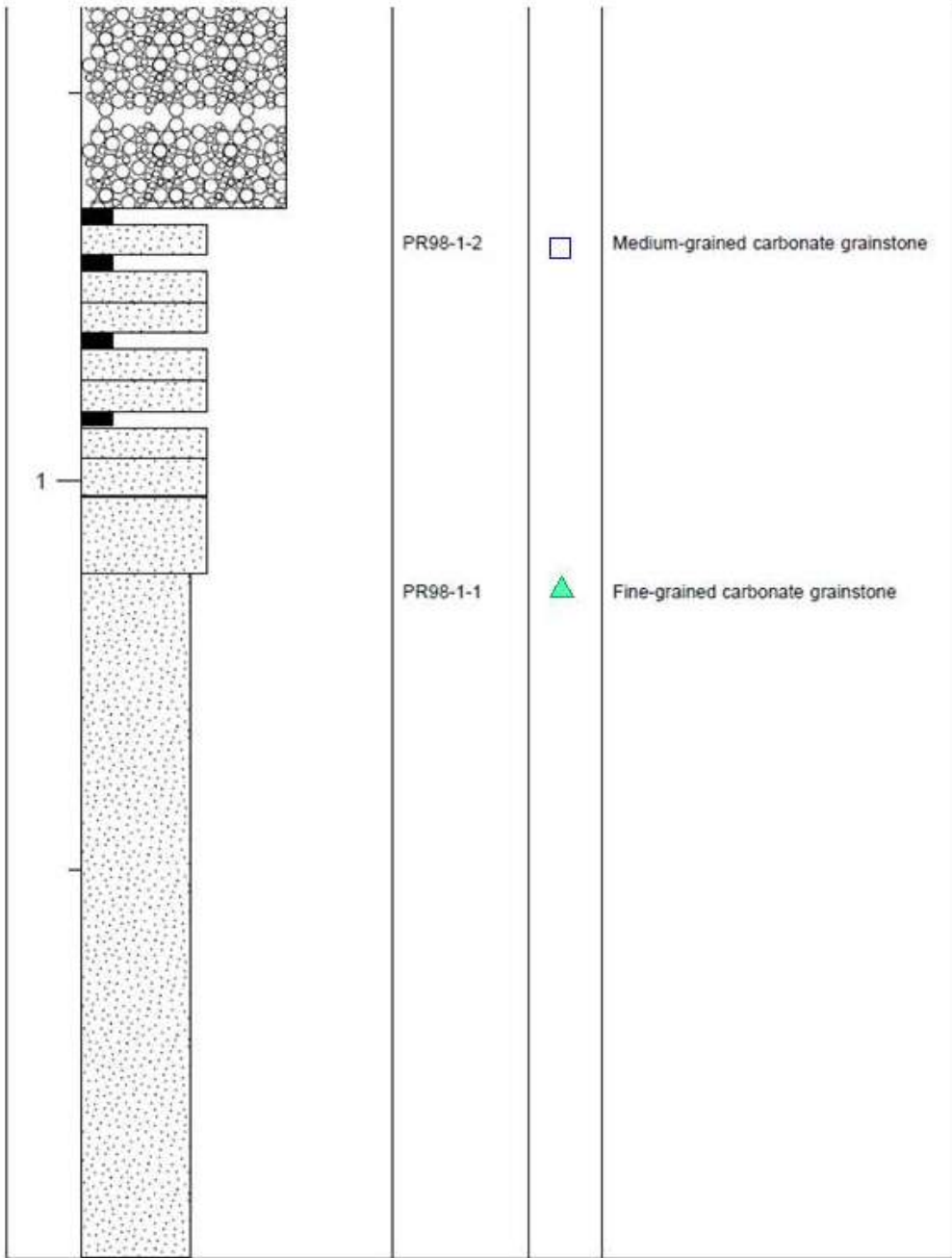
Figure 201. (Upper) Fine-grained carbonate grainstone with pronounced stylolites.
Figure 202. (Lower) Very fine-grained grainstone and silt layers that are very diagenetically altered.
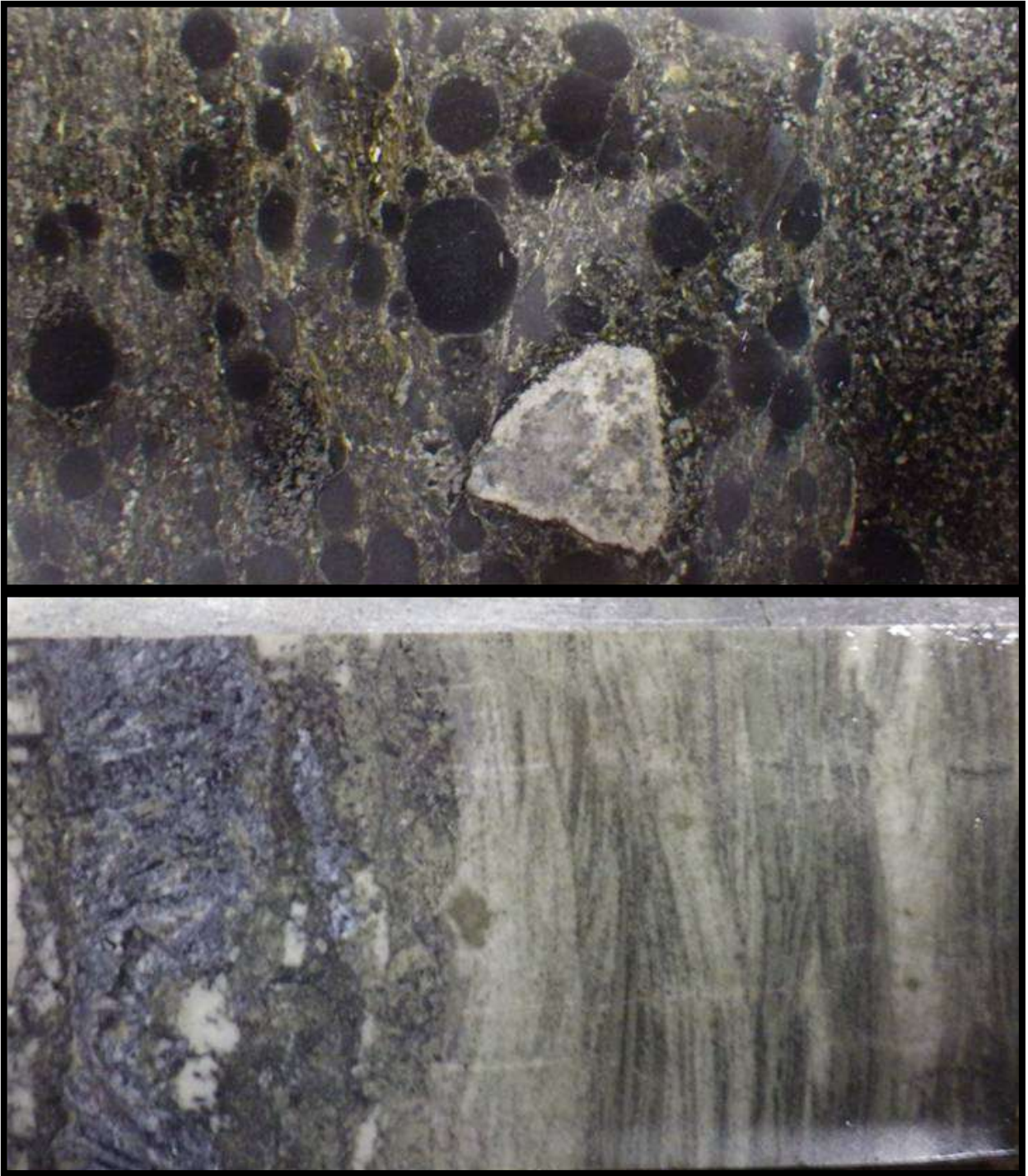
Figure 203. (Upper) Ejecta layer with lapilli, a pebble and a sandy matrix of devitrified glass.
Figure 204. (Lower) Wave-ripple laminations in silt-sized carbonate.
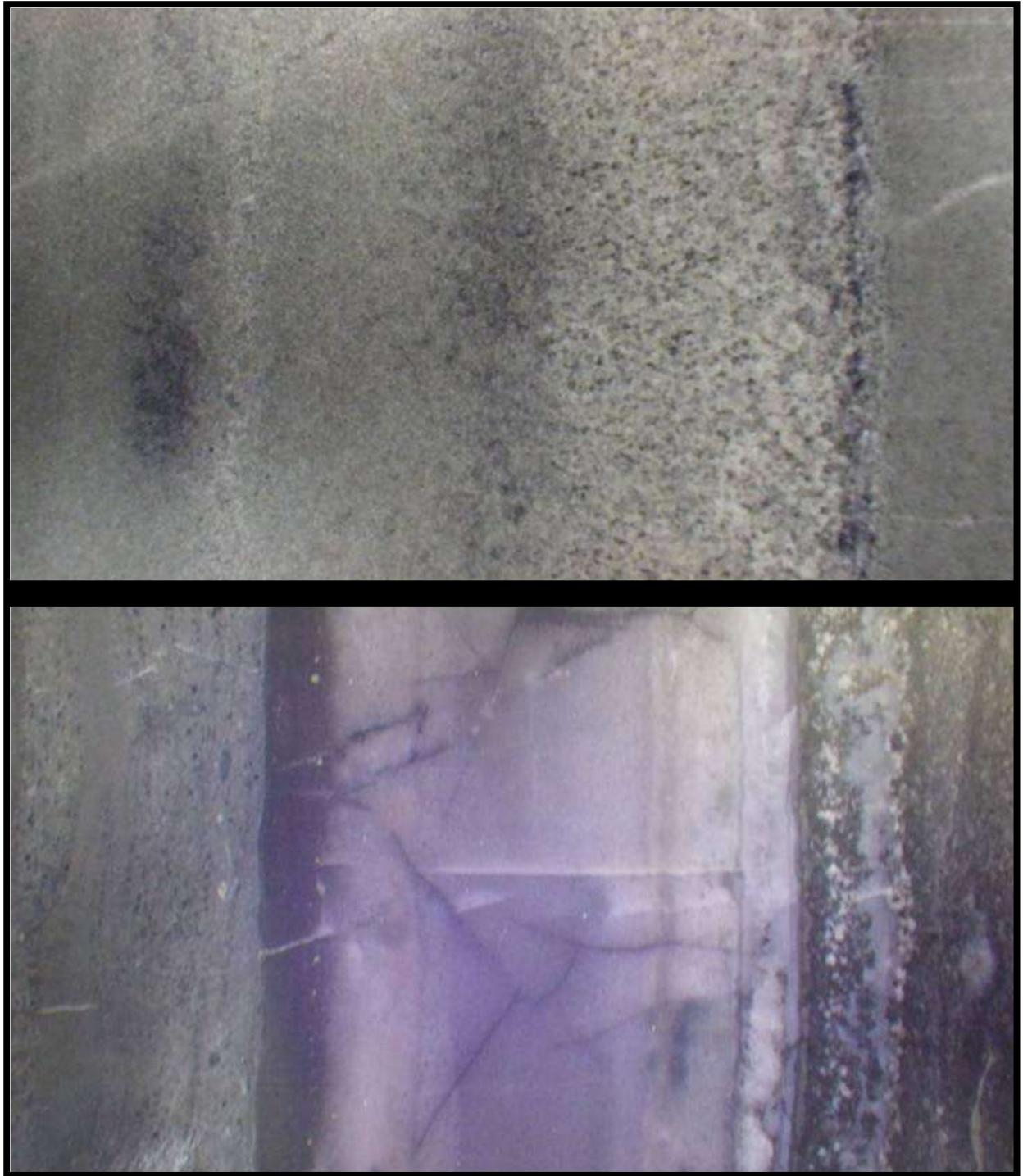
Figure 205. (Upper) Green coarse-grained material that grades to fine silt at top of unit (to left).
Figure 206. (Lower) Salmon coloured chert that is fractured and infilled with micrite.

Figure 207. (Above) Rove Formation silts and shales.

3.3.2   Geochemistry

View Table 11 for PR-98-1 drill core geochemistry. Samples from PR98-1 contain high

levels of siliciclastic sediment that is mixed in with the chemical sediment. Samples PR98-1-2,

PR98-1-3 PR98-1-4, PR98-1-5, and PR98-1-7 all have considerable REE enrichment and high

levels of Al_2O_3 (Figure 208B). In Figure 208C, all samples except for PR98-1-1 have high to

extreme levels of V. In Figure 208D, all samples except for PR98-1-2 and PR98-1-6 have below

detection levels of Mo. Sample PR98-1-2 is the most enriched in V and Mo in Figure 209A. A

relationship between Y/Ho and Ce anomaly is found in Figure 209B where samples that have a

positive Ce anomalies display a higher Y/Ho ratio, whereas samples with a negative Ce anomaly

display lower Y/Ho values. In Figure 209C, There is a possible very slight relationship between

Y/Ho and V, where samples PR-98-1-2, PR-98-1-4, PR-98-1-7 form a low angle positive

correlation. In Figure 209D, samples that increase in V also tend to head toward a more negative

Ce anomaly. In Figure 210A, samples PR98-1-1 and PR98-1-4 display similar shaped REE

patterns with elevated positive Eu and Gd anomalies. Samples PR98-1-2, PR98-1-4, PR98-1-3,

and PR98-1-5 all display similar hat-shaped REE curves with a positive Gd anomaly at their

peak. Sample PR98-1-6 displays an extreme positive Eu anomaly. In Figure 210B, sample

PR98-1-7 displays an REE curve that is enriched in the MREEs and HREEs with a slight

positive Gd anomaly. In Figure 211B, samples that go in the direction of a negative Ce anomaly

tend to decrease in positive Gd anomaly, and similarly in Figure 211C, samples that tend to go

toward a negative Ce anomaly also tend to decrease in positive Eu anomaly. In Figure 211D, as

samples increase in positive Eu anomaly, they also increase in positive Gd anomaly.
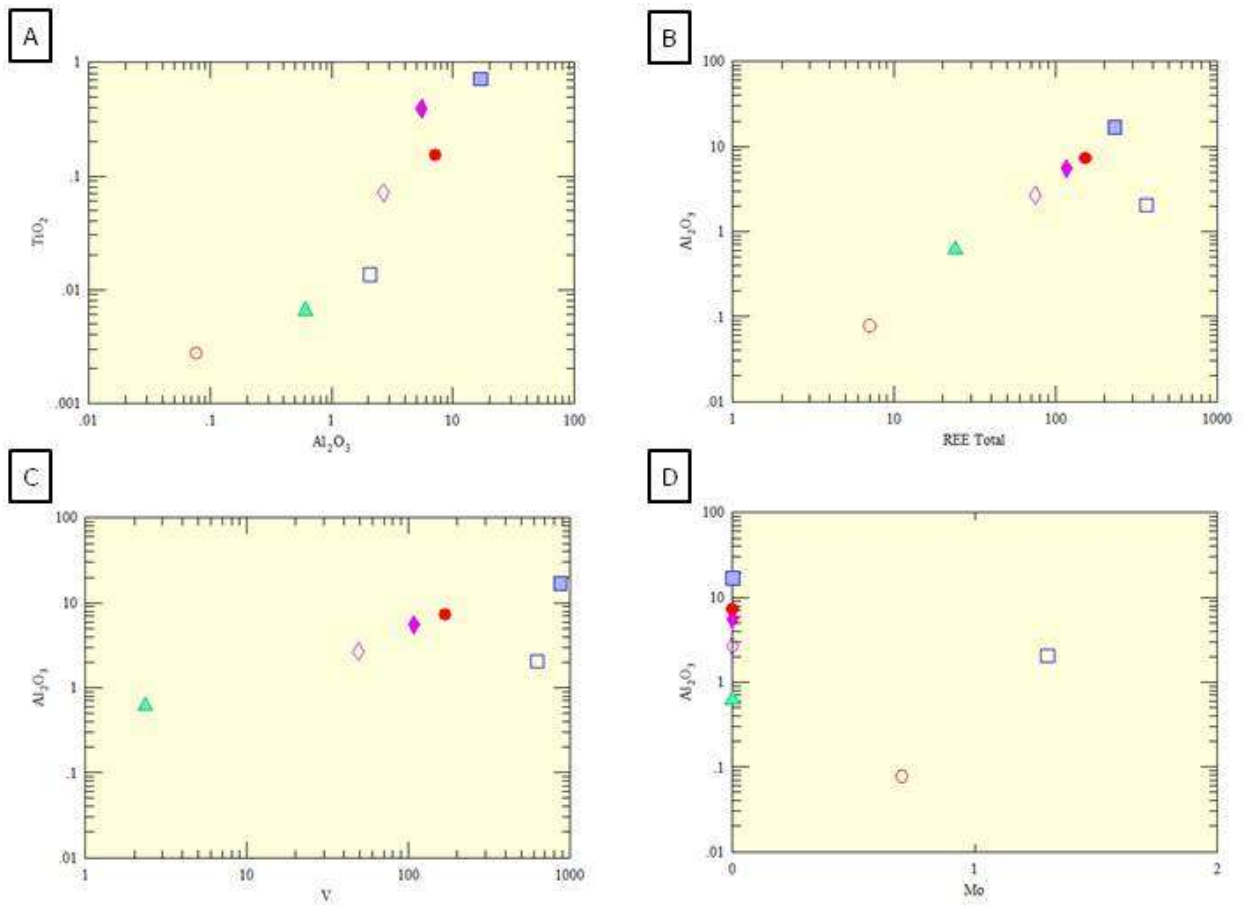
Figure 208. Bivariate plots of samples from PR-98-1. A) A positive linear correlation exists between TiO_2 and Al_2O_3. There is a low to high amount of siliciclastic material that is mixed in with the chemical sediments. **B)** A positive linear relationship exists between Al_2O_3 and REE Total with the exception of outlier sample PR-98-1-2 (from immediately below the S.I.L.). **C)** Linear correlation between Al_2O_3 and V, where as Al_2O_3 increases, so does V. Sample PR-98-1-2 is again an outlier. **D)** All samples except for PR-98-1-2 and PR-98-1-6 have below detection levels of Mo.
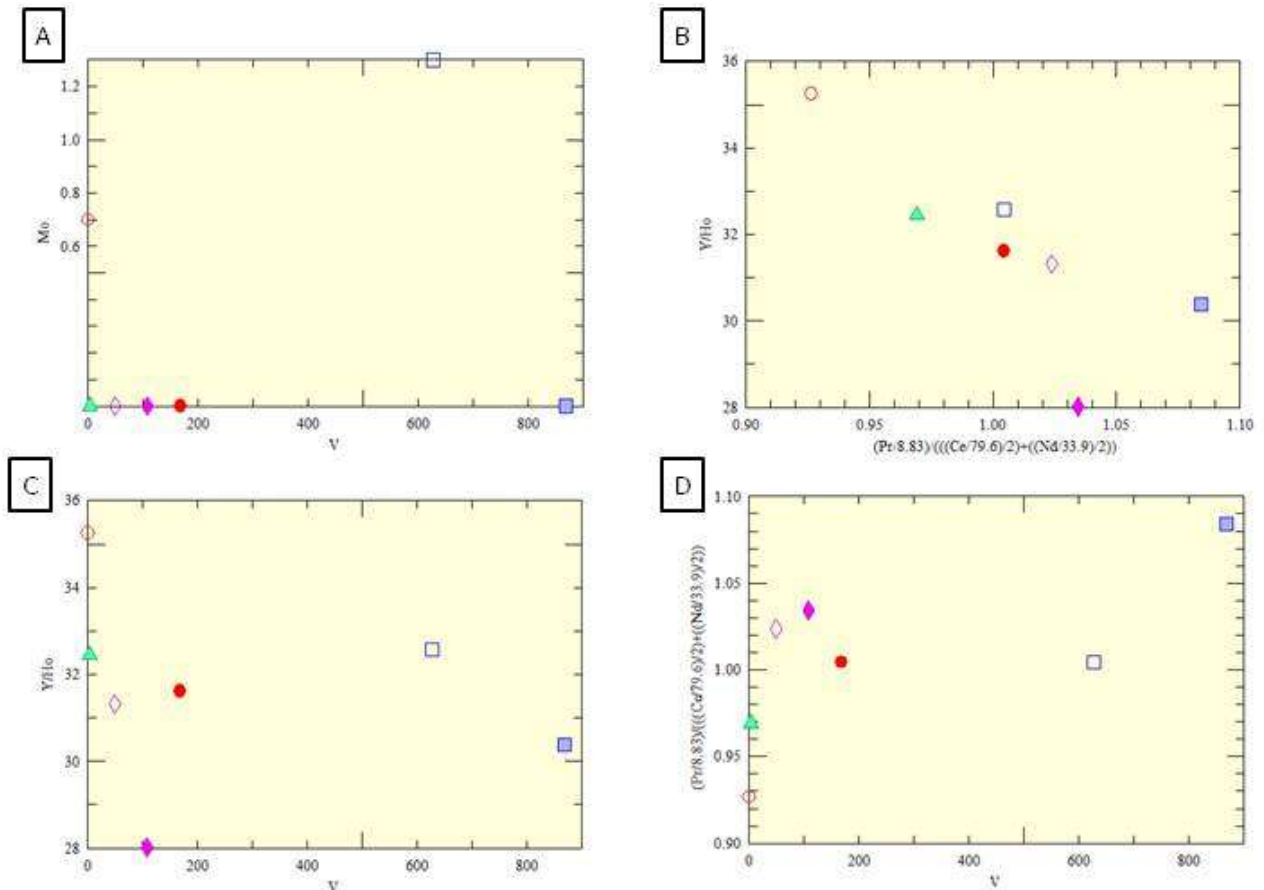
Figure 209. Bivariate plots of samples from PR-98-1. A) No correlation exists between Mo and V. All samples except for PR-98-1-2 and 6 have below detection amounts of Mo. B) A linear relationship exists between Y/Ho ratio and Ce for most samples. As samples tend toward negative Ce anomalies, there is a decrease in Y/Ho ratio. C) No correlation exists between Y/Ho and V. D) No correlation exists between Ce anomaly and V, where as samples increase in levels of V they tend to travel from a positive to negative Ce anomaly.
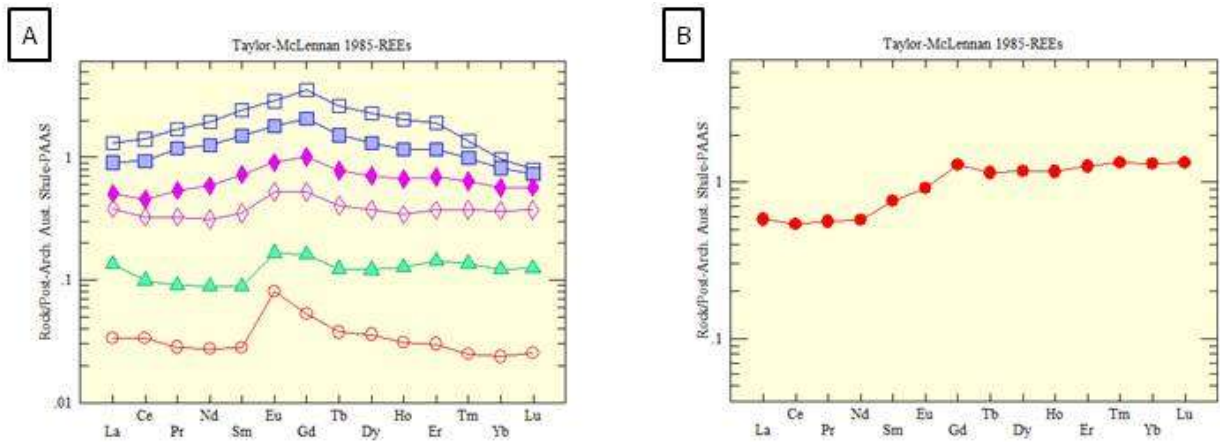
Figure 210. Rare earth element spider plots standardized to Taylor and McLennan (1985) PAAS. A) Samples PR-98-1-2, PR-98-1-3, and PR-98-1-5 exhibit similar hat-shaped REE patterns that peak in Gd anomalies. Samples PR-98-1-1 and PR-98-1-4 have similar REE curves with slightly enriched Eu and Gd anomalies. Samples PR-98-1-6 has a pronounced positive Eu anomaly. B) Sample PR-98-1-7 shows a peak positive Gd anomaly with enrichment in HREEs.
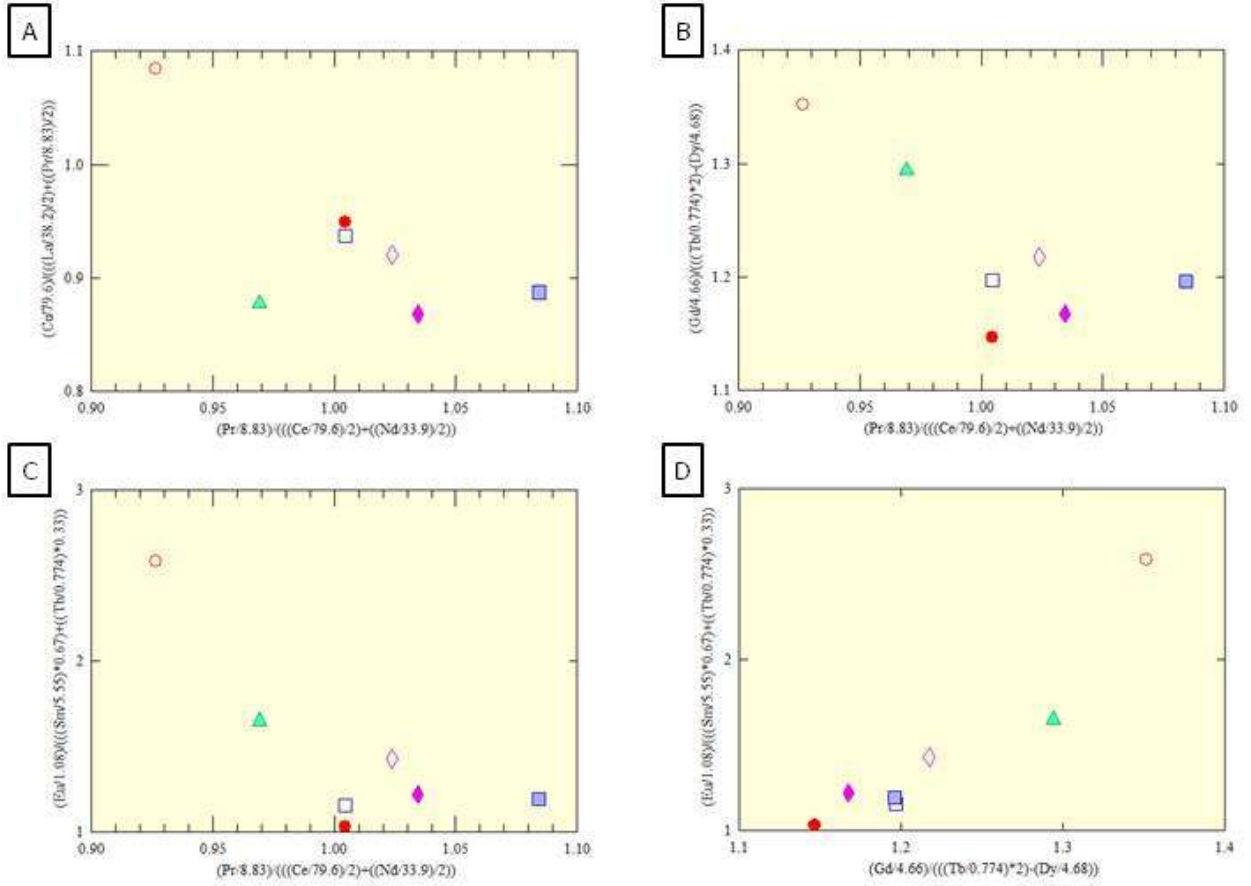
Figure 211. Bivariate plots exhibiting rare earth element anomalies of PR-98-1 samples. All values were normalized to PAAS before anomaly calculations. A) Linear correlation exhibited between La and Ce anomalies. This relationship is probably due to Ce being present in both equations. B) Samples with the largest positive Ce anomalies also have the largest Gd anomalies. When the samples reach the neutral to negative Ce anomaly area, they decrease considerably in Gd anomaly. C) Samples with positive Ce anomalies also have the largest positive Gd anomalies in the sample set. Samples that exhibit negative Ce anomalies exhibit decreased positive Gd anomalies. D) Correlation between Eu and Gd anomalies. Samples that increase in Gd anomalies also increase in Eu anomalies.

244

3.3.3   Interpretations

The Gunflint ankerite grainstones that form the bottom of drillcore PR-98-1 represent tempestites with interlayered fair-weather micritic facies. With the presence of the stylolites it is evident that the facies have been compacted under pressure. It is also evident that there was a period of subaerial exposure due to the fact that the facies were silicified and in some cases shattered. The grainstone directly beneath the S.I.L. has extremely high concentrations of V and slightly high levels of Mo, also probably highlighting the effects of oxidized groundwater. The Sudbury Impact Layer erosively overlies these ankeritic grainstones. It consists of a reverse graded lower section and a normal graded upper section, similar to BDQ-1 and probably representing deposition from a subaerial pyroclastic flow (Fralick et al., 2011). On top of the ejecta unit are upper flow regime parallel laminated ankerite grainstones and cross-stratified grainstones probably deposited above storm wave base in a near-shore marine setting. Silicilastic content increases upward toward the contact with the Rove Formation.

3.4   VHD-00-1 Drill Core

3.4.1   Lithofacies Description

Drill core VHD-00-1 is located in the Virginia Horn region in Minnesota at the only warehouse locations available of NW, NE, Sec 35, T. 58N., R.18W. Addison et al. (2005) previously researched this drill core. Figure 212 shows the stratigraphic representation of VHD-00-1 drill core. Starting at the bottom of the drill core, there is 40cm of dark, silicified, fine-grained carbonate grainstone, followed by 4cm of shattered and brecciated silicified dark grainstone. Overlying this unit is 20cm of the ejecta from the Sudbury Impact Layer that consists fine ejecta material with devitrified vesicular impact glass with white carbonate cement. This is followed by 34cm of silt-sized carbonate material with occasional black micritic rip-ups (Figure 213). After this unit, there is missing core. Following the gap, is 43cm of siltstone layers with black micritic tops, with layers averaging 3-5cm thick. Sample VHD-00-1-1 ▲ is taken from this layer. Another gap of missing core follows the previous unit, approximately 2m in length. The next section consists of 19cm of contorted, soft sediment injections (Figure 214), followed by 36cm of very fine grained grainstone and very coarse-grained silt that is parallel laminated. On top lays 10cm of fine-grained carbonate crystal layers, followed by 8cm of fine-grained carbonate with sprays of black vertical lines which are micritic infilled cracks (Figure 215). Next lies 18cm of parallel laminated silty material, followed by 18cm of large crystals in what was parallel laminated silty material, with crystals preferentially growing in layers. This is in turn succeeded by 6cm of parallel laminated micrite and silt, followed by a 9cm thick layer of rip-up mud granules that do not effervesce (Figure 216). On top lies a 23cm unit of large crystal-dominated layers with vertical stylolites, followed by 6cm of silicified micrite that cracks in an angular fashion. This is overlain by 6cm of silicified silty micrite, followed by 6cm of fine-

grained silicified green mud with very thin rip-up layers. On top lays 3cm of flat pebble

conglomerate (rip-ups) with a fine-grained matrix with clasts up to 4cm in length. This in turn is

followed by 10cm of parallel laminated silt, with thin layers of ripped up silt with a very fine -
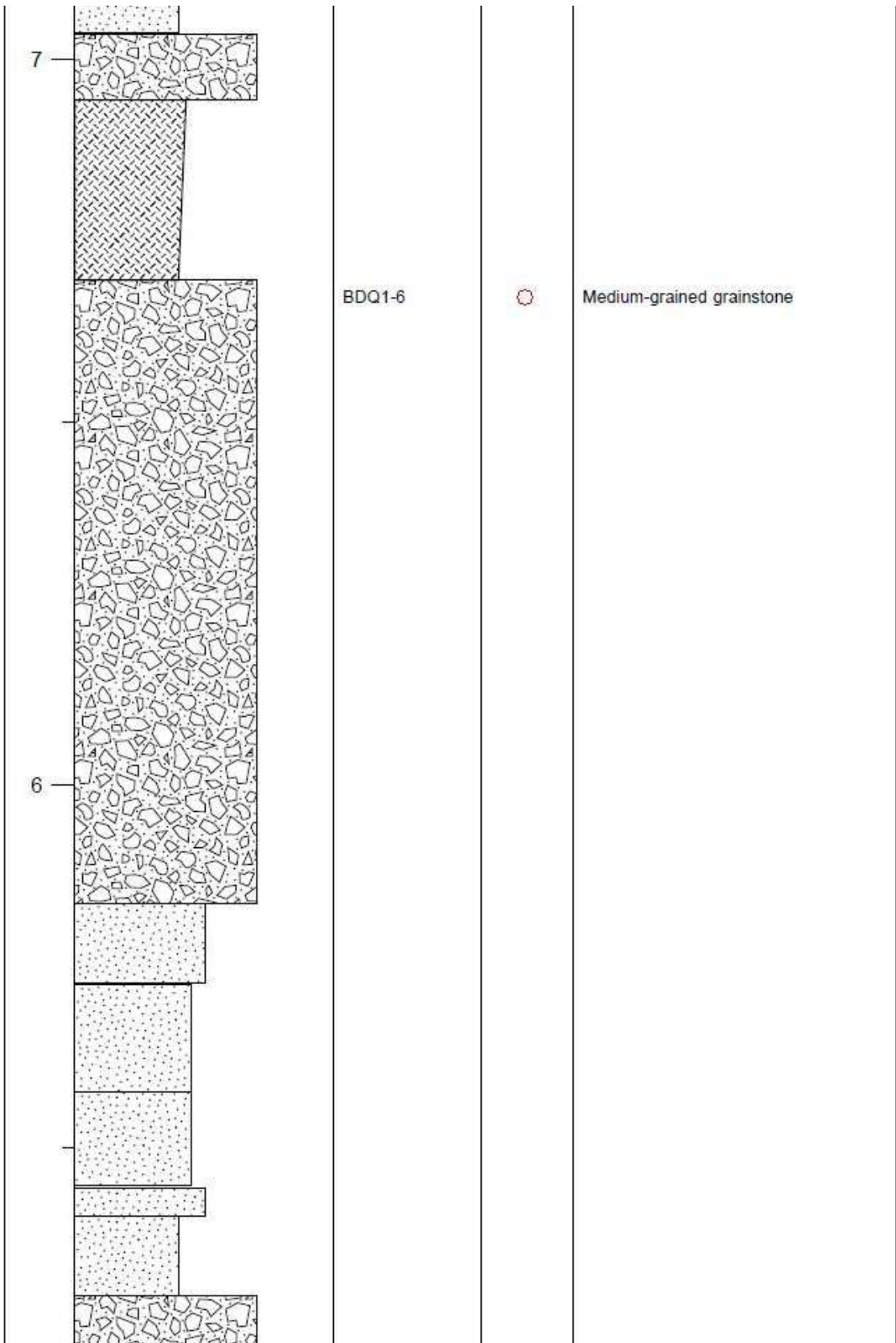
grained grainstone matrix (Figures 217, 218).
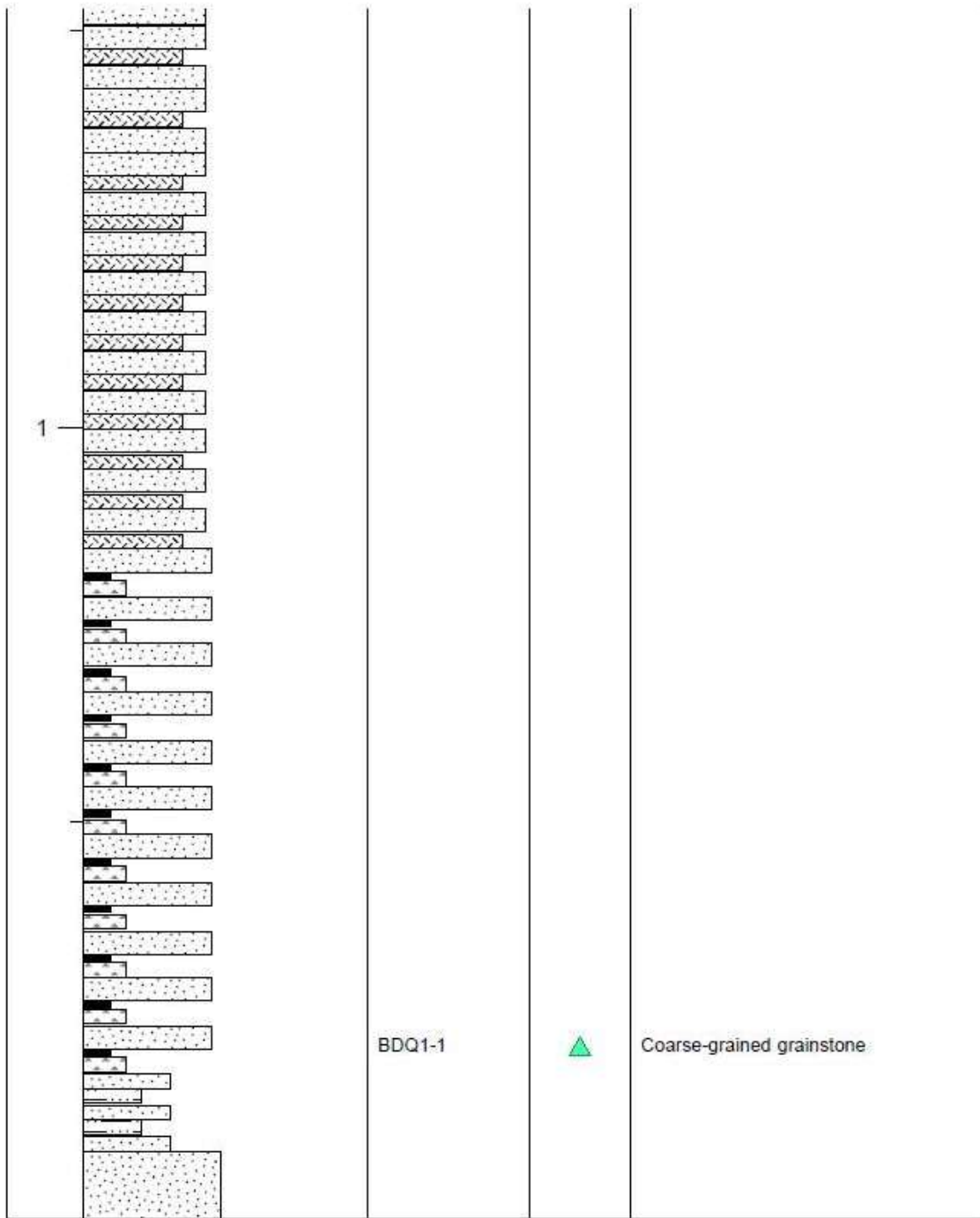
Figure 212. Stratigraphic Representation of VHD-00-1 Drill Core.

2

VHD-00-1-1   △   Carbonate siltstone

1
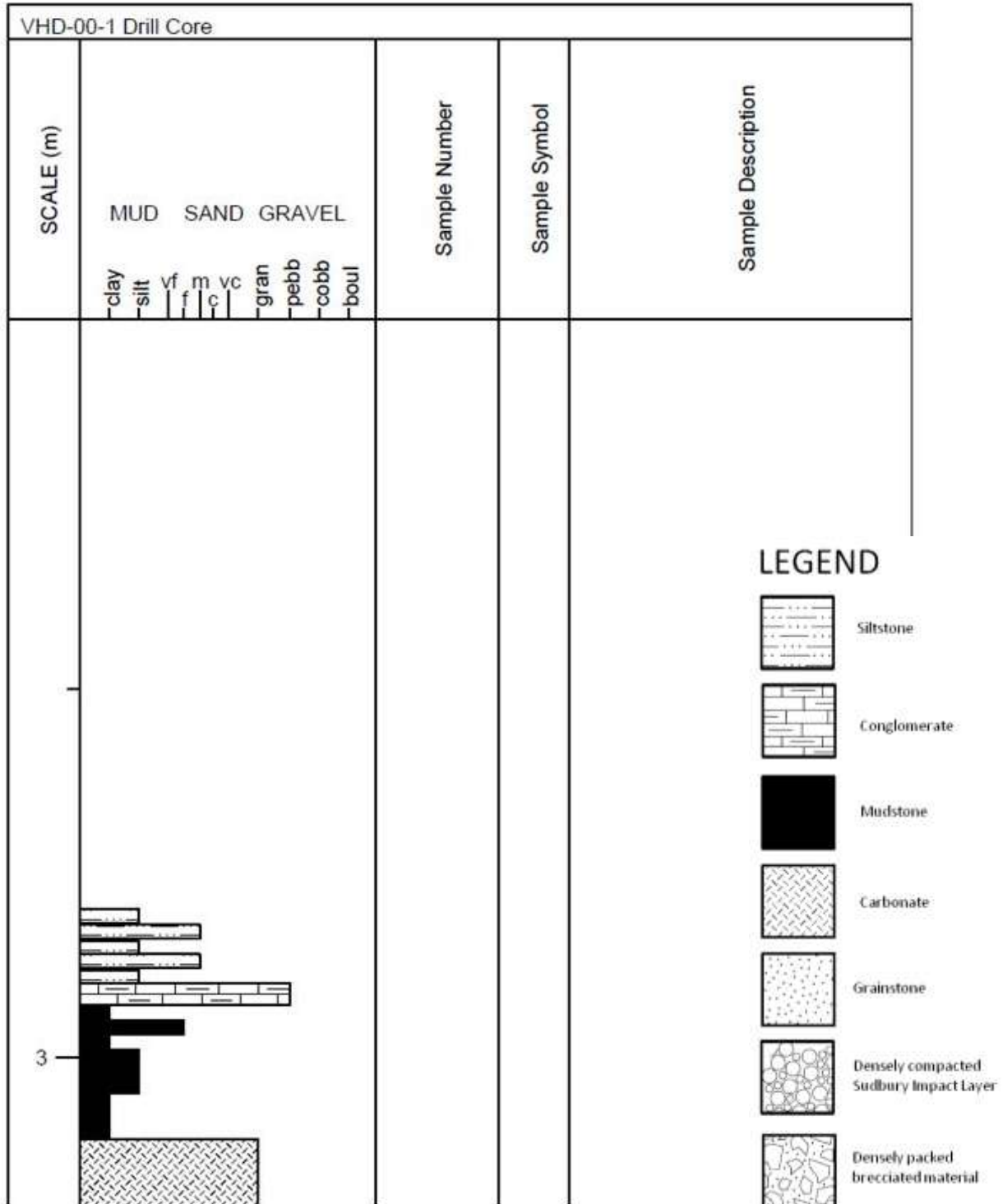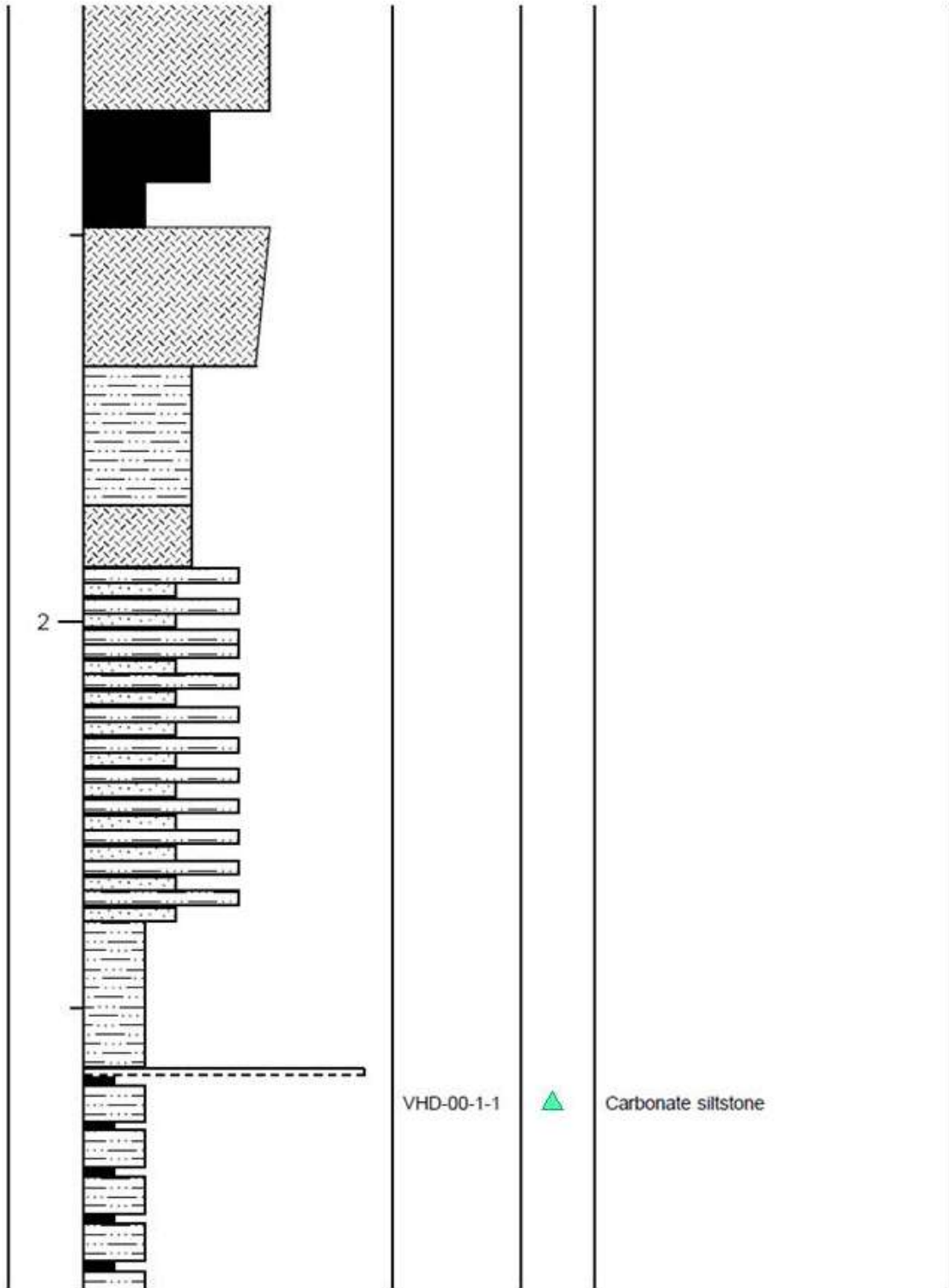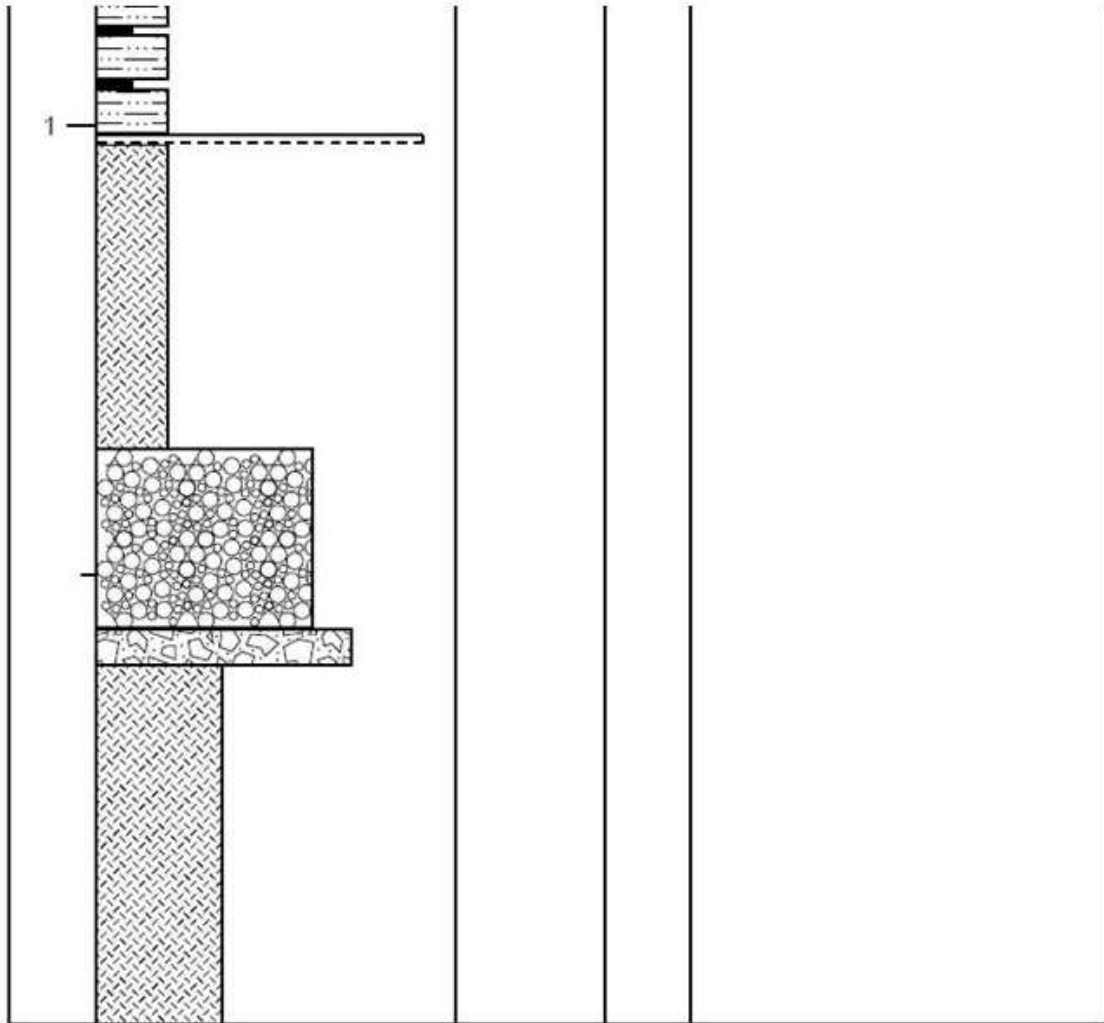
Figure 213. (Upper) Silt-sized carbonate layers with graded tops.
Figure 214. (Lower) Contorted, soft sediment deformed with injections.
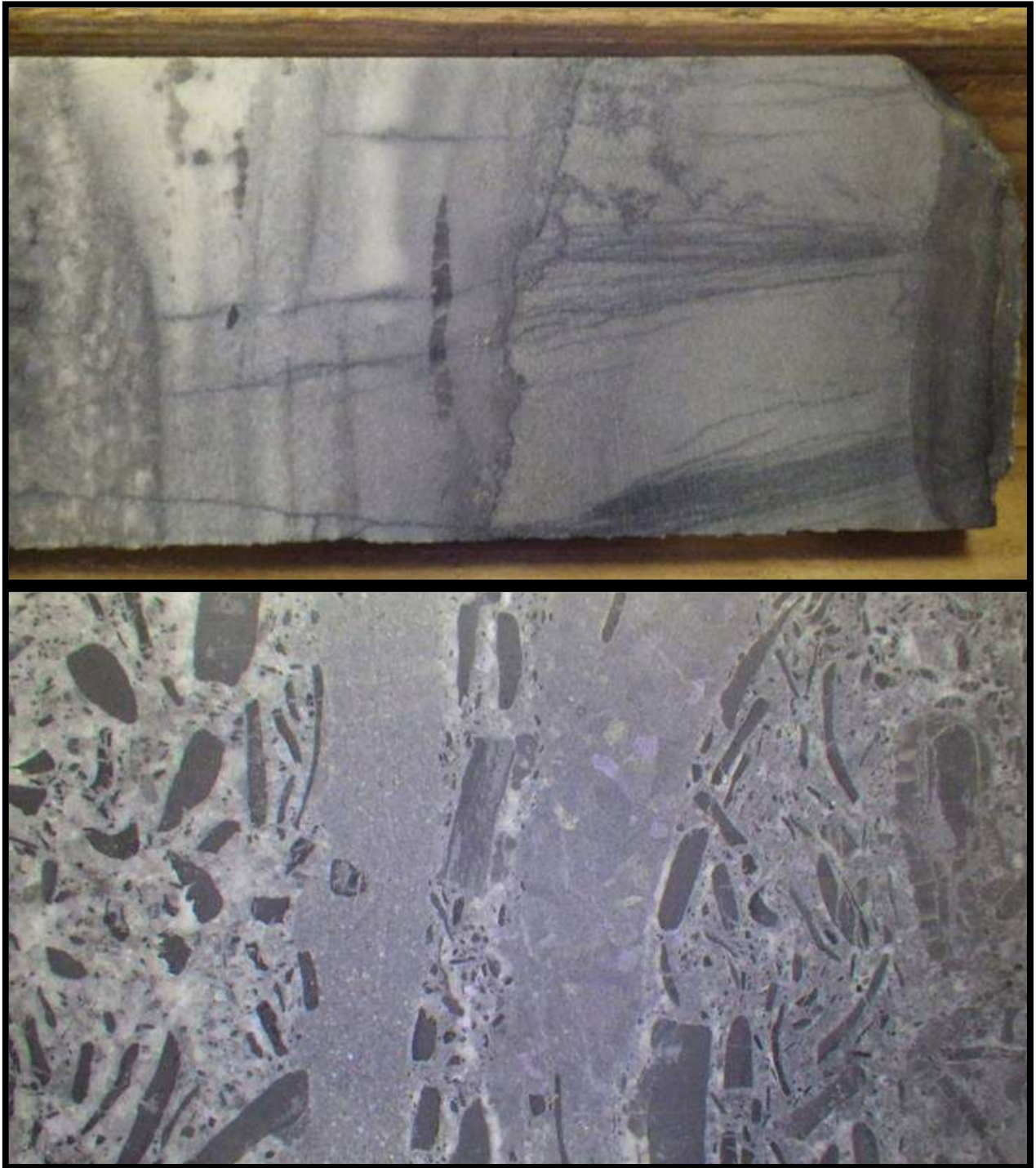
Figure 215. (Above) Fine carbonate with micritic material and sprays of vertical black cracks.
Figure 216. (Below) Rip-up layers of black micrite intraclasts.
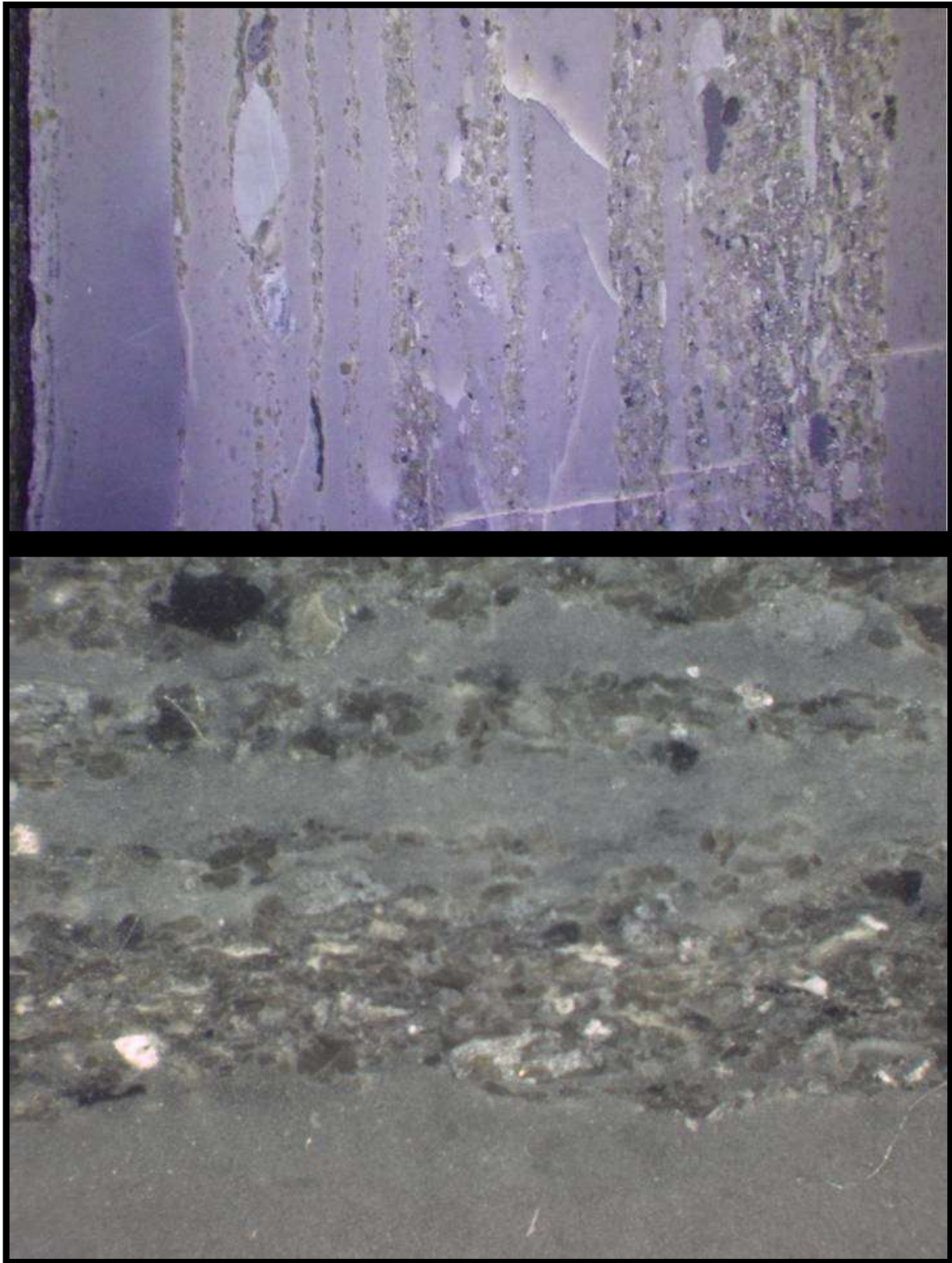
Figure 217. (Upper) Parallel laminated silt with layers of ripped up silt in a very fine matrix.
Figure 218. (Lower) Close up of rip up layers in above photo.

3.4.2   Geochemistry

View Table 12 for VHD-00-1 Drillcore geochemistry. Only one sample was taken from drillhole VHD-00-1, which is VHD-00-1-1. Sample VHD-00-1 exhibits REE total of 82 ppm, and is not very enriched in Al_2O_3. It is slightly enriched in V at 54.6 ppm, but is below detection for Mo. The Y/Ho ratio is around 31with a Ce anomaly situated near 1.0. The rare earth element spider diagram of VHD-00-1-1 displays a positive Eu and Gd anomaly.   For the bivariate plots of VHD-00-1-1, La is near 0.93, Ce is near 1.00, Gd is near 1.15, and finally Eu is near 1.40.
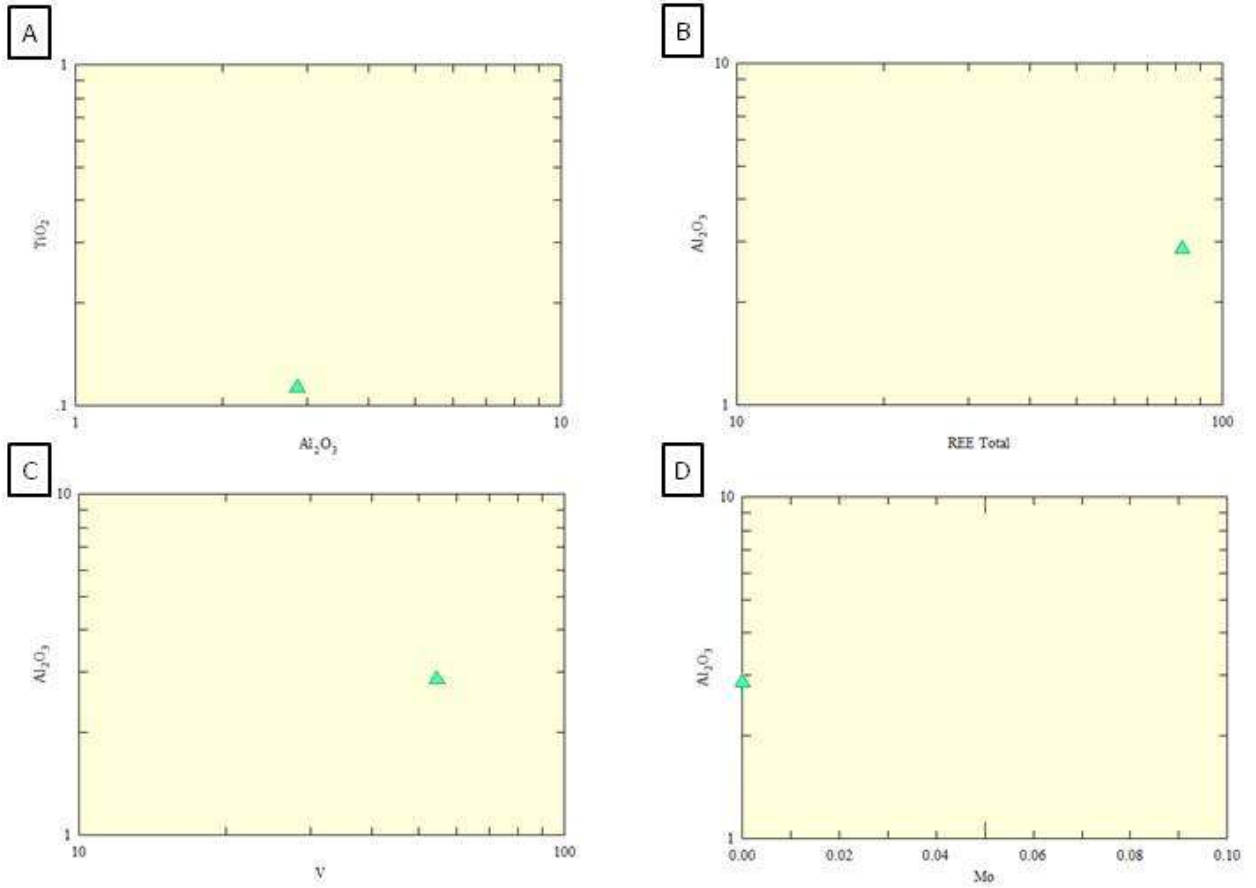
Figure 219. Bivariate plots of sample VHD-00-1-1 from VHD-00-1. A) Low levels of TiO$_2$ vs Al$_2$O$_3$. B) Low levels of Al$_2$O$_3$, but a high level of REE Total. C) Low levels of Al$_2$O$_3$ but a moderately high level of V. D) A below detection amount of Mo.
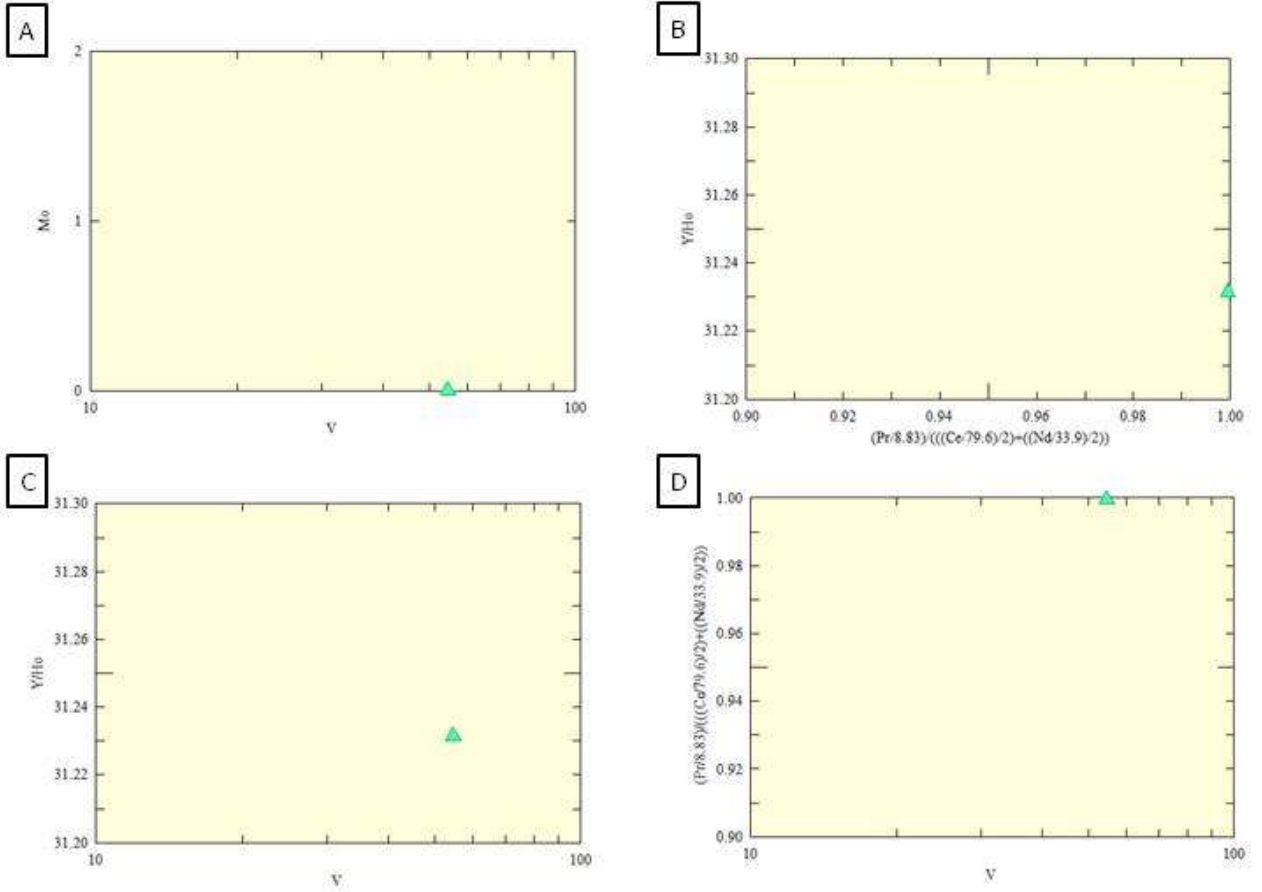
Figure 220. Bivariate plots of sample VHD-00-1-1 from VHD-00-1. A) Below detection amount of Mo, whereas V is ~55 ppm. B) Y/Ho ratio is situated at around 31. C) Y/Ho vrs V. D) Ce anomaly near 1, while V is situated at around ~55ppm.
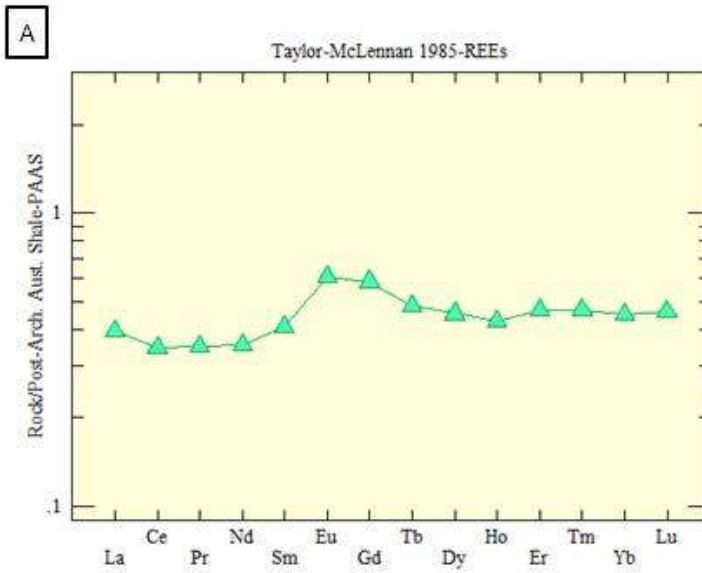
Figure 221. Rare earth element spider plot standardized to Taylor and McLennan (1985) PAAS. A) Sample VHD-00-1-1 exhibiting positive Eu and Gd anomalies. The REE pattern is typical of Gunflint chemical sediments not subject to alteration.
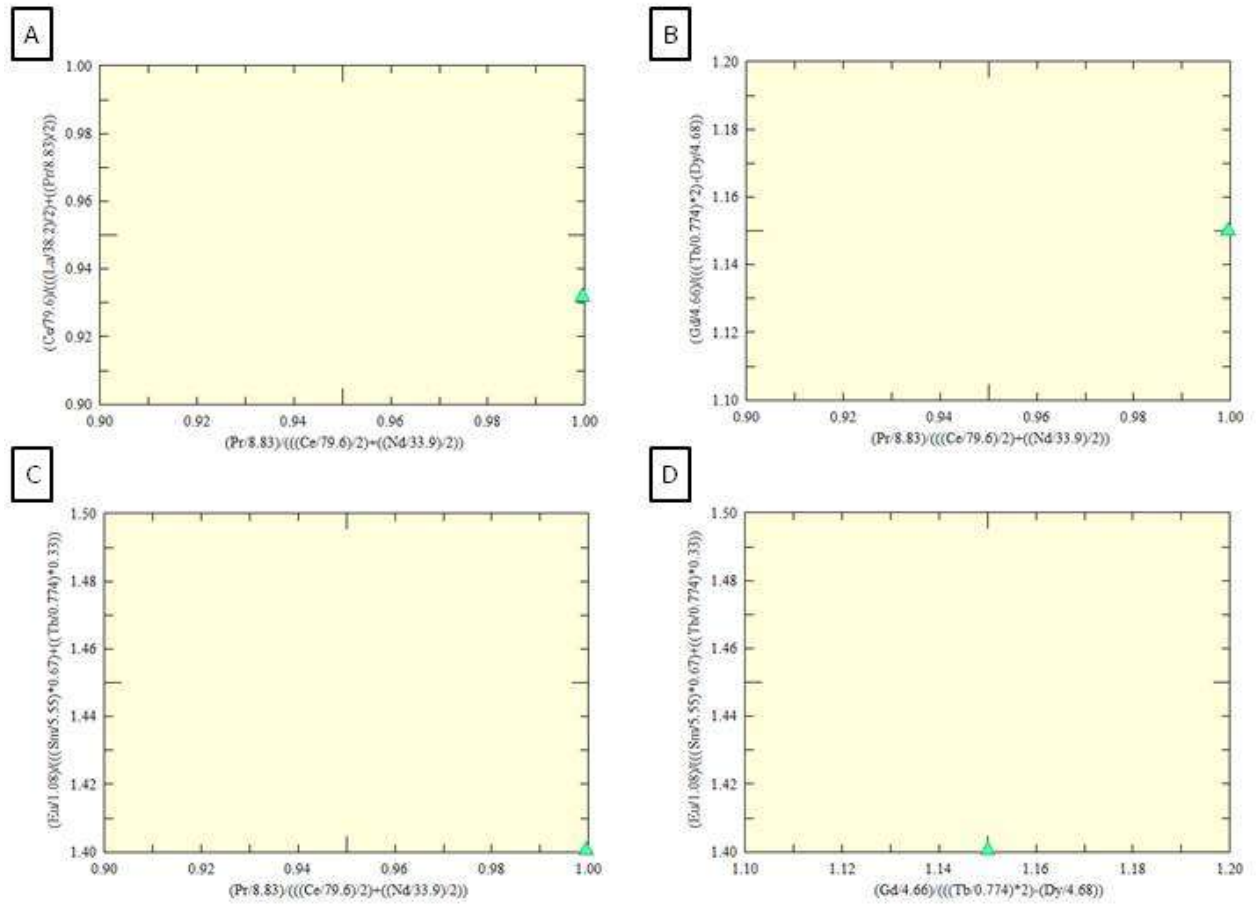
Figure 222. Bivariate plots exhibiting rare earth element anomalies of sample VDH-00-1-1 from VHD-00-1. All values were normalized to PAAS before anomaly calculations. A) La near 0.93, and Ce near 1.00. B) Gd near 1.15, and Ce near 1.00. C) Eu near 1.40, and Ce near 1.00. D) Eu near 1.40, and Gd near 1.15.

3.4.3   Interpretations

The alternating ankerite grainstones and silty carbonate layers below the S.I.L. probably represent tempestites alternating with fair-weather conditions. There was probably also a time when the land was subaerially exposed due to the silicification. The shattering of the chert layers was most probably caused by the seismic waves from the earthquake produced by the Sudbury meteorite. Soft sediment deformations in the layers overlying the S.I.L. could represent earthquakes caused by readjustment of the craton after the impact event. The ankerite grainstone and siltstones that overly the S.I.L. represent reflooding of the area and the crystals that dominate the silty parallel layers are thought to have precipitated in this shallow environment. The ocean probably regressed, leading to a facies of flat pebble conglomerate, which indicates a near shore environment. Later during burial stylolites formed due to the pressure.

3.5   LWD-99-1 Drill Core

3.5.1   Lithofacies Description

Drill core LWD-99-1 is located in the Virginia Horn region in Minnesota. The only coordinates available for this drill core are NE-NE Sec 13, T.57N., R.18W, archived at the Hibbing, MN drill core warehouse. Addison et al. (2005) previously researched this drill core. Figure 223 is a stratigraphic representation of drill core LWD-99-1. At the bottom of the drill core 27cm of silicified fine-grained carbonate grainstone with stylolites present. Sample LWD-99-1-1 ▲ is taken from this layer. Next is 34cm of fine-grained black chert with layers and cross-cutting veins, blobs of coarse-grained crystals, and some features that resemble mud cracks (Figures 224-227). Following this secondary assemblage is a 30cm thick unit of silicified fine-grained dark carbonate, with sample LWD-99-1-2 ☐ taken from this layer. There is a sharp contact and overlying is 13cm of contorted layering, followed by 14cm of neatly layered, cross-stratified, fine-grained carbonate grainstone. Overlying this unit is 11cm of a silicified and brecciated version of the underlying fine-grained carbonate grainstone. Next is 59cm of the Sudbury Impact Layer, followed by 4cm of silicified coarse-grained grainstone that is cherty. Overlying this unit is 21cm of fine-grained silicified micrite, with a contorted top (Figure 228), and near the base what look to be pseudomorphs of possibly gypsum crystals (Figure 229). On top lies 8cm of large crystals in diffuse veins, followed by 13cm of ripped-up pieces, followed by 7cm of coarsening upwards crystals. Sample LWD-99-1-3 ☐ is taken from this unit. Succeeding this unit is 14cm of silt-sized carbonate material with occasional black micrite rip ups, followed by 30cm of siltstone layers with black micritic tops that coarsen upwards. There is an erosively cut lens with grainstone pieces cutting into the siltstone (Figure 230). This is followed by 20cm of crystals in parallel laminated sediment where crystals coarsen upwards, and there is an erosive

contact at top of this unit. This is succeeded by 8cm of ripped-up pieces with clasts at the bottom of the unit being full of crystals, and pieces at the top of the unit are micritic (Figure 231). There is a sharp contact followed by 10cm of a coarsening upwards sequence of crystals, with the bottom possibly being originally fine-grained grainstone. On top lies 3cm of black micrite rip-up pieces, followed by 18cm of crystals that become smaller upwards. Sample LWD-99-1-4 ◇ is taken from this unit. Next is a 6cm thick unit of parallel laminated sediment with crystals growing inside it, followed by 6cm of large crystals in lath-shaped blocks, succeeded by 10cm of black micrite rip-ups that are angular and embedded with cracks. Overlying is 3cm of crystals floating on top of rip-ups, followed by 4cm of green very silicified fine-grained material, succeeded by 1cm of very silicified black shale. This in turn is succeeded by 6cm of parallel laminated very silicified green, fine-grained grainstone, followed by 4cm of green, shale-like material with carbonate-filled vugs. This is overlain by 5cm of green silicified mudstone containing layers with an average thickness of 1cm then 4 layers of black silicified shale approximately 3mm thick, followed by 5cm of fine-grained green material that grades to black in the top few millimeters in the unit. Finally, overlying this unit is 5cm of poorly sorted siltstone with grainstone grains floating in it. There is one thin layer of lath-shaped grains approximately 2mm wide and 1mm long. Sample LWD-99-1-5 ◆ is taken from this unit.

Figure 223. Stratigraphic Representation of LWD-99-1 Drill Core.

2

LWD-99-1-3   ▢   Coarsening upwards carbonate crystals

1

LWD-99-1-2   ☐   Silicified fine-grained dark carbonate

LWD-99-1-1   △   Silicified fine-grained carbonate
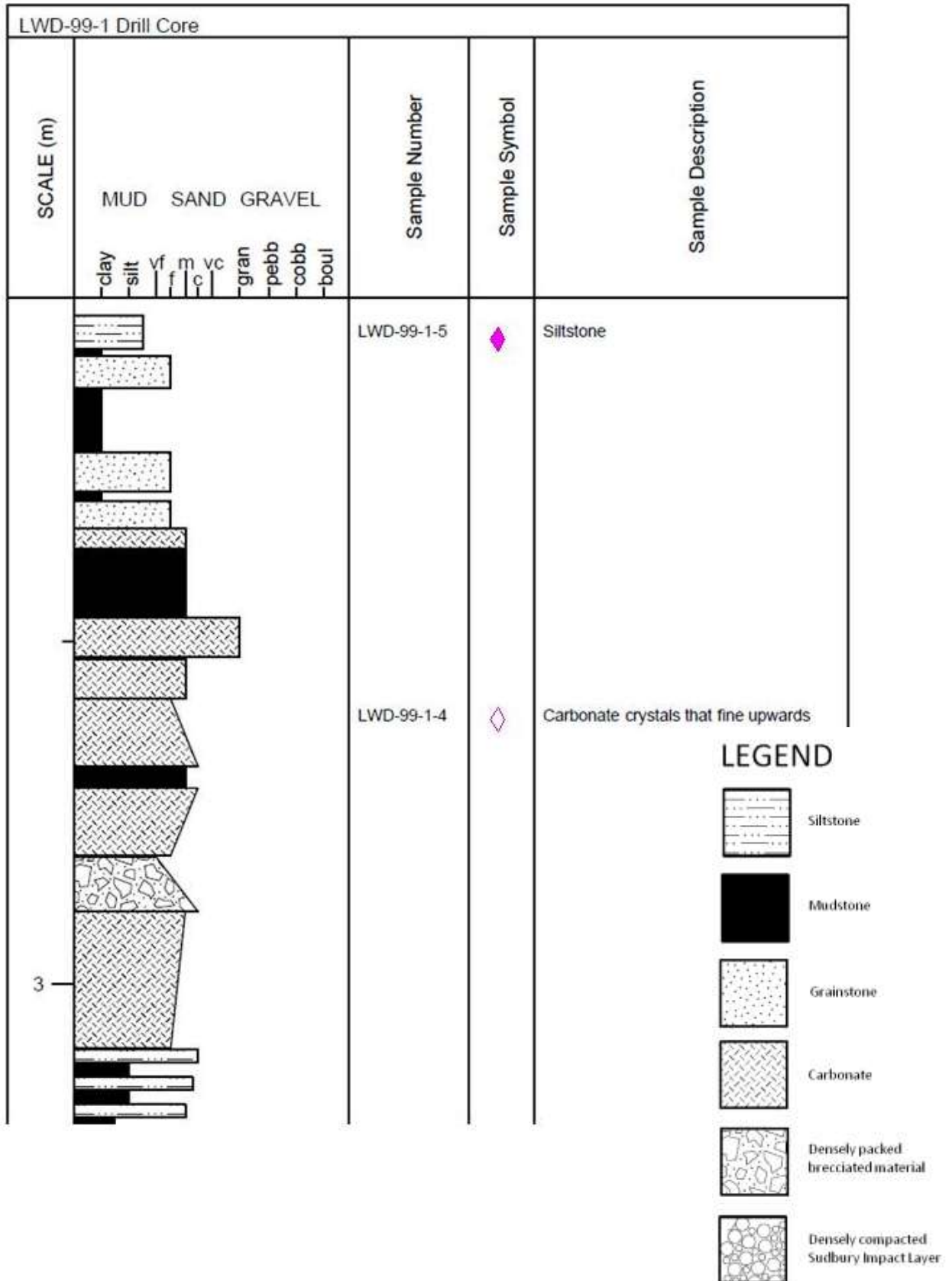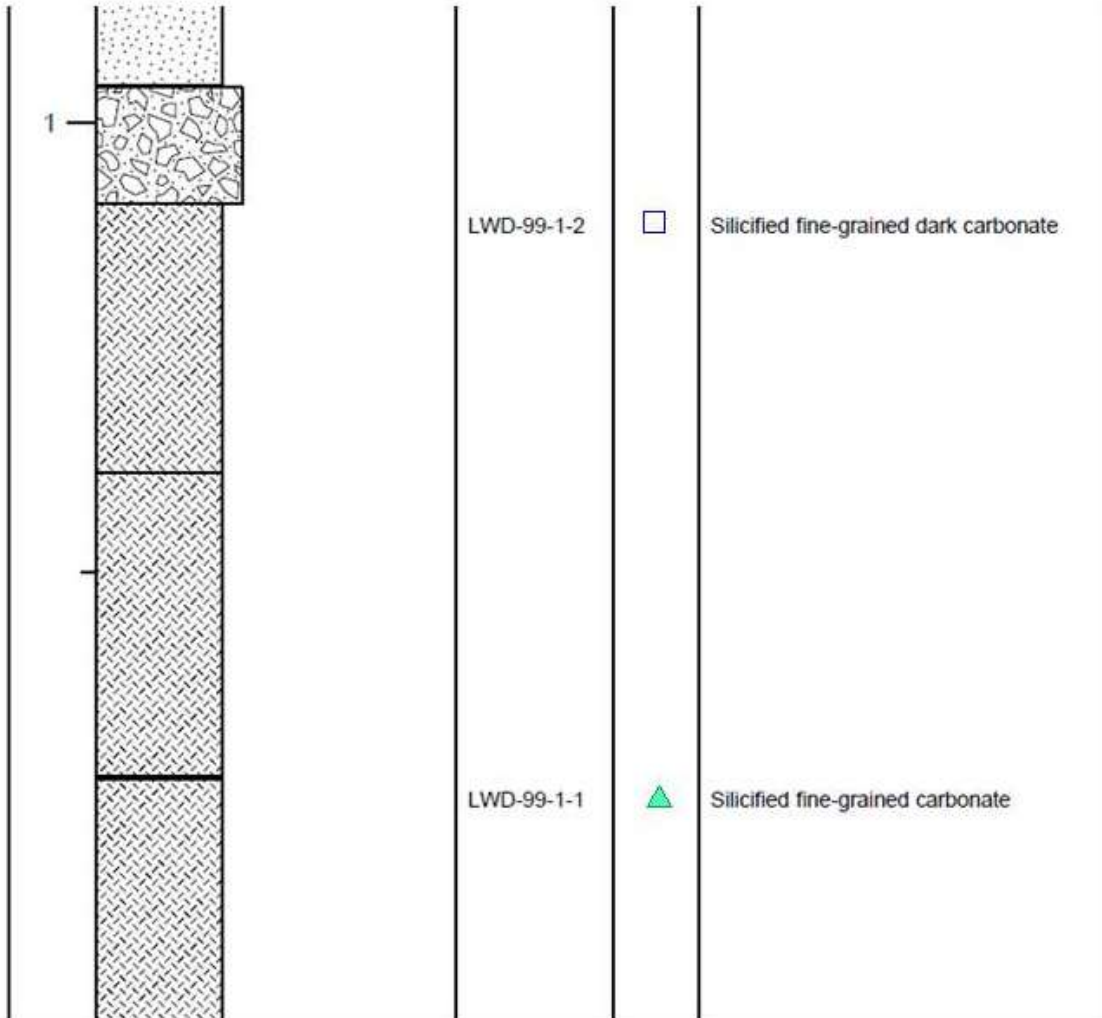
Figure 224. (Upper) Fine-grained black chert with layers and cross cutting veins with blobs of coarser crystals.
Figure 225. (Lower) Close up of individual crystals, some with rhomboid shape.

Figure 226. (Upper) Cracked crystals infilled with mud; it contains pieces of carbonate from surrounding area (top to right).
Figure 227. (Lower) Black rip-up with crystals growing around it.
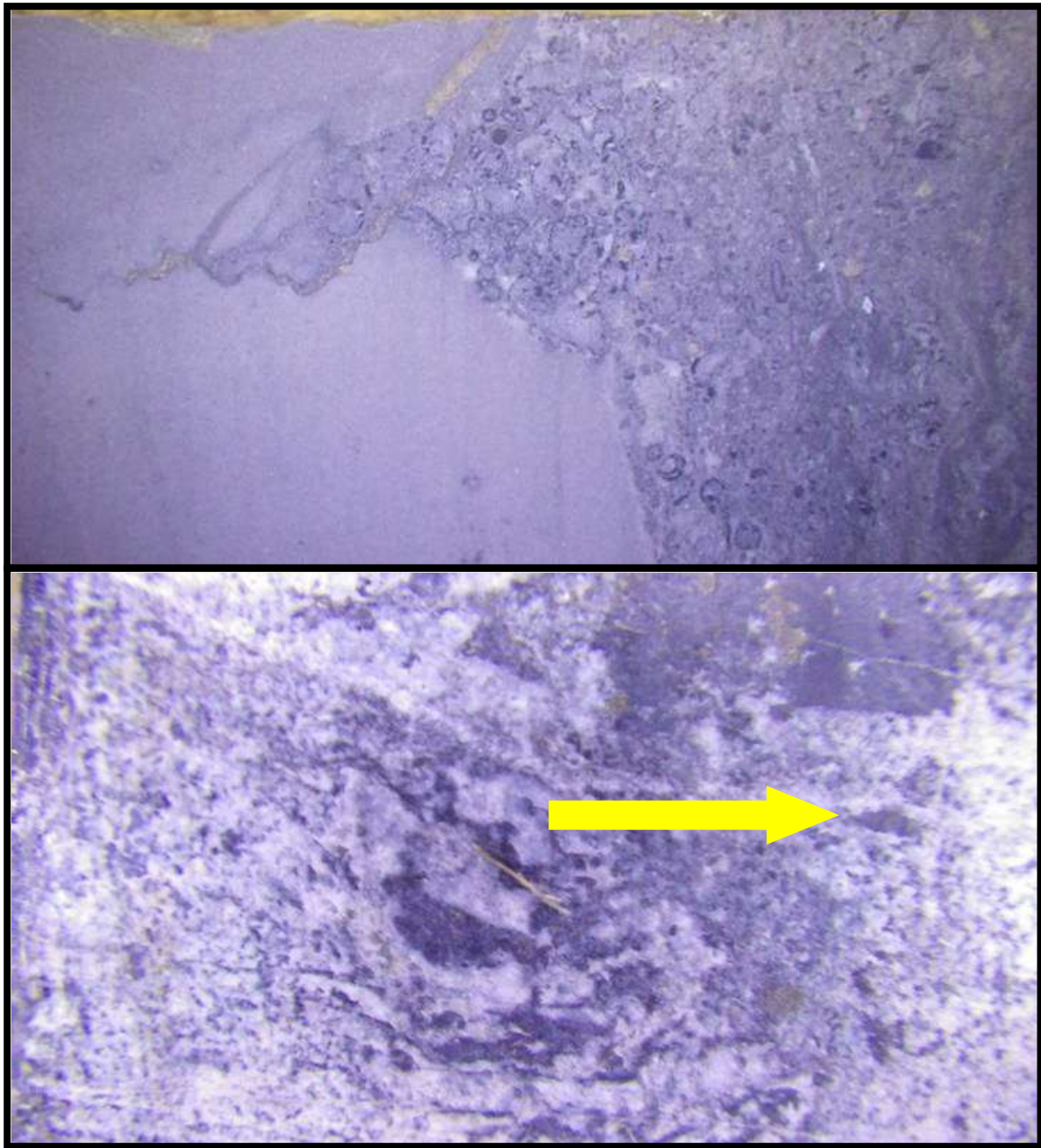
Figure 228. (Upper) Fine-grained silicified micrite with mudcrack filled with granules from overlying unit..
Figure 229. (Lower) Fine-grained silicified micrite layer, with pseudomorphed crystals (arrow).
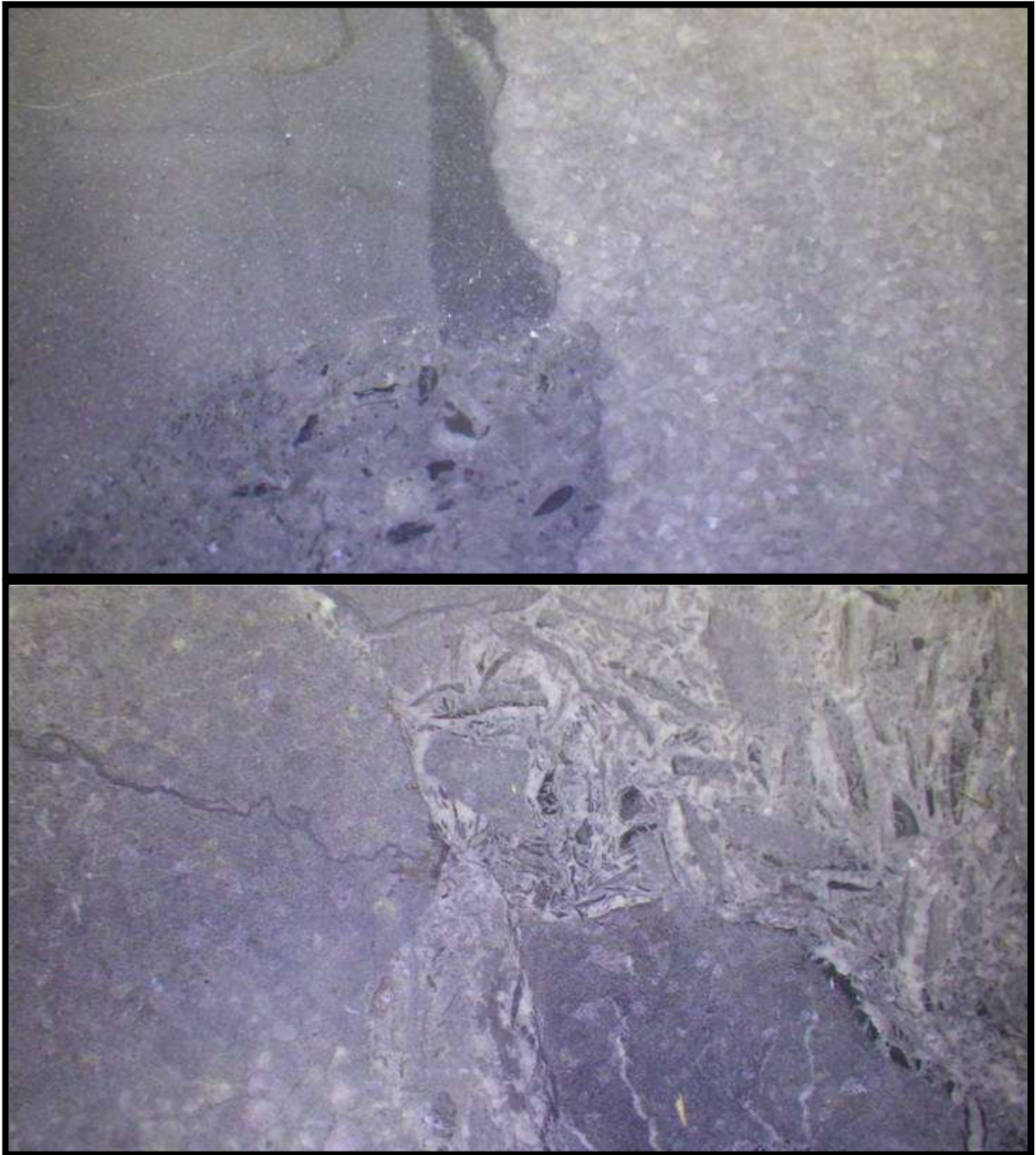
Figure 230. (Upper) Erosive cut lens with grainstone pieces cutting into the siltstone. Neomorphic spar to right.
Figure 231. (Lower) Micrite clasts at top of unit.

3.5.2   Geochemistry

View Table 13 for LWD-99-1 Drillcore geochemistry. There is a medium to high

amount of siliciclastic material that is mixed in with the chemical sediments in LWD-99-1.

Sample LWD-99-1-3, LWD-99-1-4, and LWD-99-1-5 exhibit REE enrichment in Figure 232B,

while in Figure 232C, LWD-99-1-1 and LWD-99-1-5 exhibit the highest V levels. These higher

concentrations are relates to larger amounts of siliciclastics. All samples in LWD-99-1 have

below detection Mo levels (Figure 232D). In Figure 233B, Y/Ho increases as samples go from a

positive to negative Ce anomaly. No correlation is found between Y/Ho and V in Figure 233C.

In Figure 233D, V levels decrease as samples go from negative to positive Ce anomaly.   In

Figure 234A, samples LWD-99-1-1, LWD-99-1-2, and LWD-99-1-3 have similar REE shaped

curves with slight pronounced positive Eu and Gd anomalies. Sample LWD-99-1-4 is enriched

in MREEs and HREEs with a slight positive Gd peak. Sample LWD-99-1-5 exhibits a negative

Eu anomaly, but a positive Gd anomaly. Figures 235B and 235C show no correlation. In Figure

235D, as samples increase in positive Gd anomaly they also increase in positive Eu anomaly.
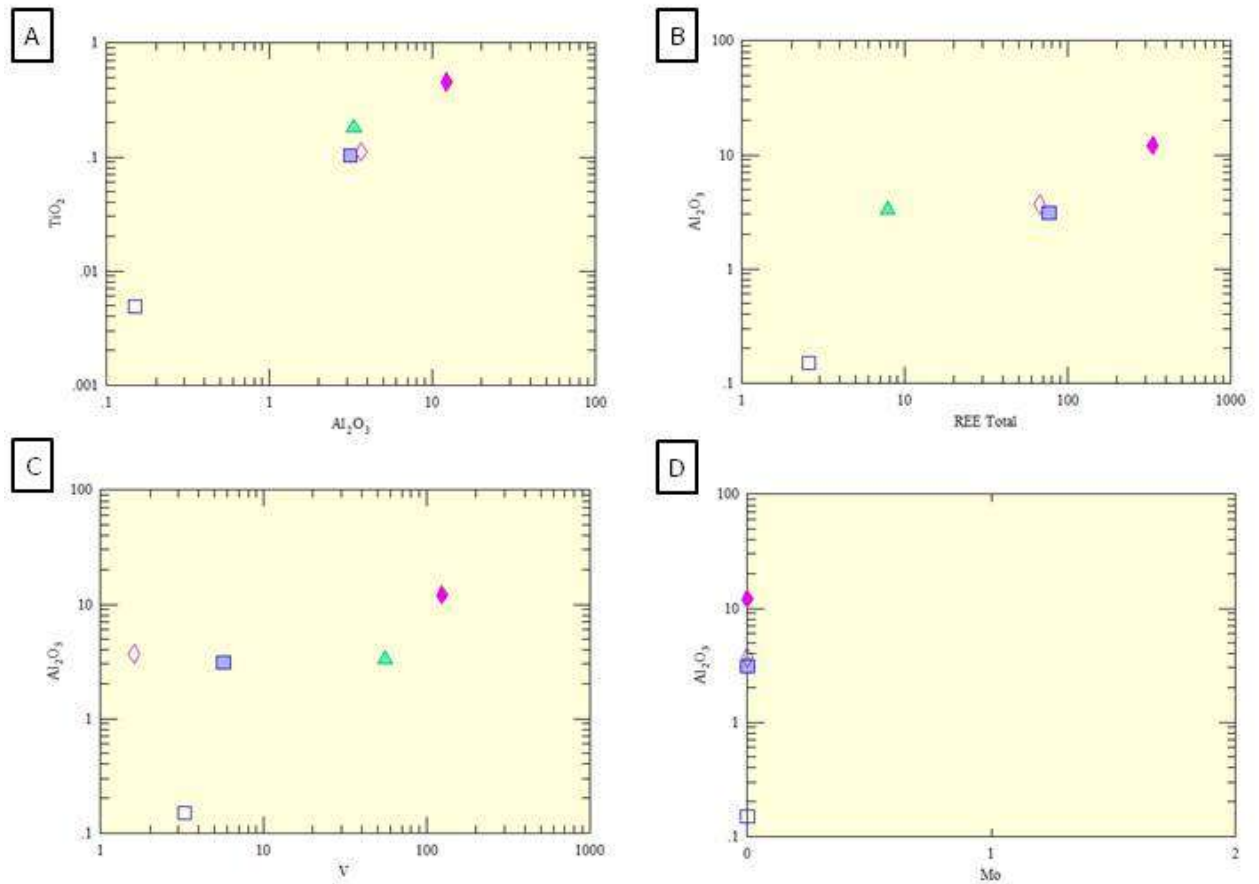
Figure 232. Bivariate plots of samples from LWD-99-1. A) Positive linear relationship exists between TiO_2 vs Al_2O_3. Moderate to large amounts of siliciclastics are present. B) Positive linear relationship exists between Al_2O_3 and REE Total, with sample LWD-99-1-5 exhibiting elevated Al_2O_3 levels and extreme REE enrichment. C) No correlation between Al_2O_3 and V. D) All samples have below detection amounts of Mo.
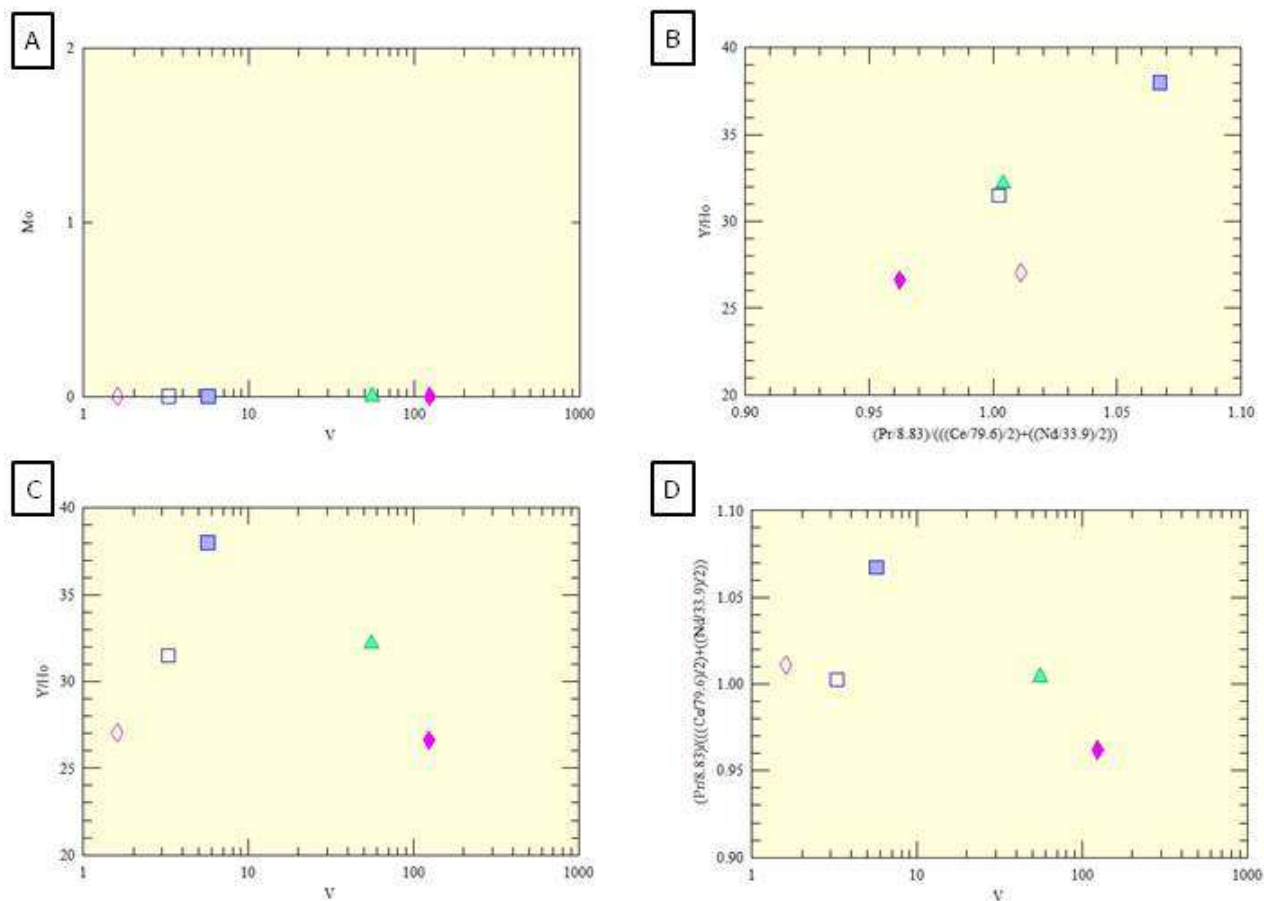
Figure 233. Bivariate plots of samples from LWD-99-1. A) No correlation between Mo and V. Sample values sit at below detection amounts of Mo, while samples LWD-99-1-1 and LWD-99-1-5 are the most enriched in V, though this is probably due to high levels of siliciclastics. B) Positive linear correlation between Y/Ho and Ce anomalies. As samples increase in Y/Ho ratio, they also go from slightly positive Ce anomalies to slightly negative anomalies. C) No correlation between Y/Ho ratio and V. D) No correlation between Ce anomaly and V.
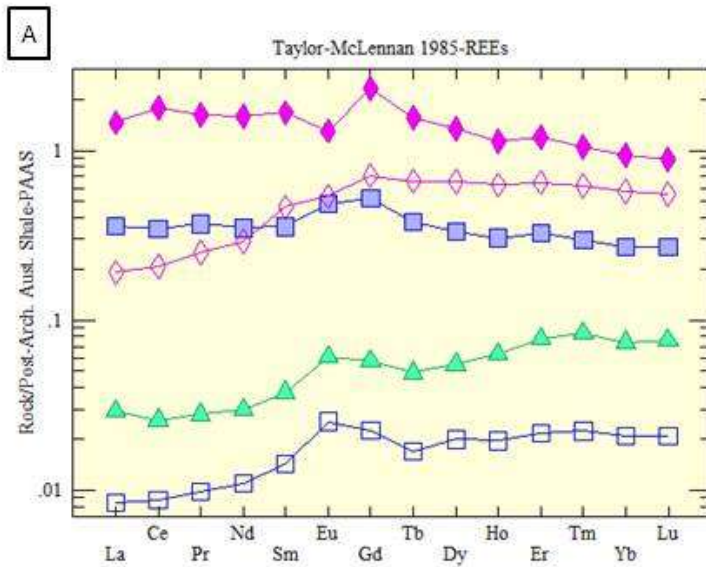
Figure 234. **Rare earth element spider plots standardized to Taylor and McLennan (1985) PAAS. A) Samples LWD-99-1-1, LWD-99-1-2 and LWD-99-1-3 display similar REE curves with elevated Eu and Gd positive anomalies. LWD-99-1-4 shows low LREEs with a peak of Gd anomaly. LWD-99-1-5 exhibits a negative Eu anomaly and a positive Gd anomaly. The large amount of siliciclastics in the latter two samples is probably effecting their curve shapes.**

272
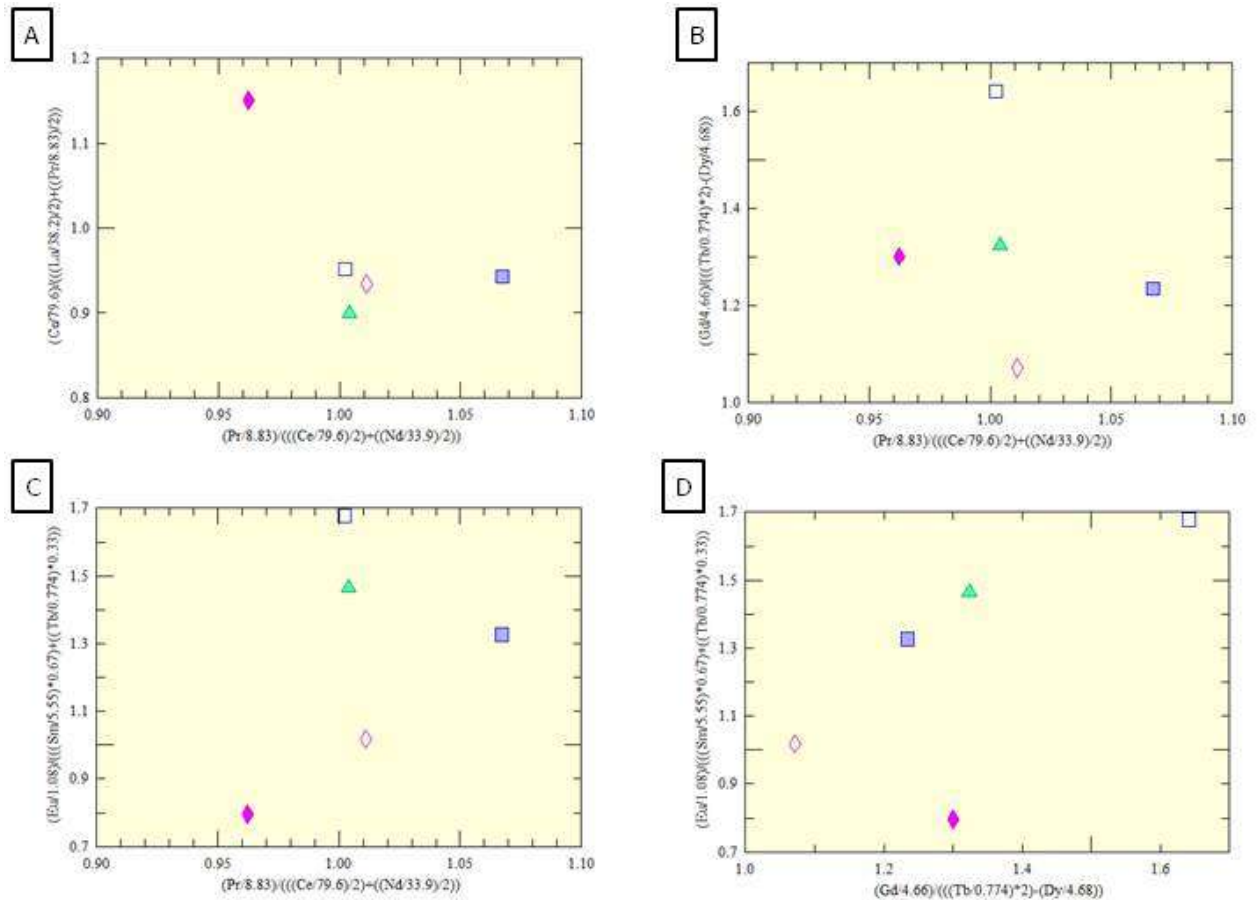
Figure 235. Bivariate plots exhibiting rare earth element anomalies of samples from LWD-99-1. All values were normalized to PAAS before anomaly calculations. A) Slight linear correlation exhibited between La and Ce anomalies. This relationship is probably due to Ce being present in both equations. B) No correlation between Gd and Ce. C) Samples with larger amounts of siliciclastics tend to have increased positive Eu anomalies. D) Samples LWD-99-1-1, LWD-99-1-2, LWD-99-1-3, and LWD-99-1-4 exhibit increasing levels of Eu as Gd increases. LWD-99-1-5 exhibits a negative Eu anomaly while showing a medium positive Gd anomaly as compared to the rest of the sample set.

3.5.3   Interpretations

The ankerite grainstones present near the base of drillcore LWD-99-1 indicate open marine conditions that were transformed to subaerial exposure denoted by the development of the silicification of layers. The fine-grained ejecta material in this core has the characteristics of deposition from a pyroclastic flow (for a description see Addison et al., 2003). The highly altered sediment that overlies the S.I.L. contains sporadic mudcracks suggesting possible deposition in the high intertidal with abundant crystal growth. When we move up the stratigraphic column there is a switch to layers with dominantly coarsening upwards increases in crystal size. This could indicate an edge-of-ocean scenario where water is drying out but a small amount of water is still supplying the crystals. The Rove Formation transgressed over this landscape.

4   Conclusions

4.1   The Gunflint Formation Greater than 3 Meters Below the Ejecta Layer

The upper portion of the Gunflint Formation greater than 3 meters below the Sudbury Impact Layer was examined to give a baseline for the rocks further removed from the exposure surfaces associated with the top of the formation. Grainstone facies alternating with fine-grained chemical sediments and, more rarely, mudstone is very common in this interval. These lenticular bedded units in the Gunflint Formation, best expressed by those present in the cliff face at Harbour Expressway and the Mapleward Railway Cut, have previously been assigned to the foreshore and upper shoreface environment (Pufahl, 1996; Pufahl and Fralick, 2000). Sections composed of thicker grainstone lenses with only minor fine-grained sediment were probably deposited in a more shore proximal location (Pufahl and Fralick, 2000), with the thicker lenses representing dunes and hummocky cross-stratified mounds (Fralick, 1988). Samples from these rocks contain moderate to large positive Eu anomalies (1.3 to 2.0) indicating that deposition was from seawater and not meteoric waters, though one sample from the TFBH2 drillcore has a lower Eu anomaly and a higher Y/Ho ratio (Figure 236) indicating there may have been a nearshore continental runoff influence during it's precipitation. The high levels of iron in the lenticular bedded facies of ankerite and hematite indicate iron-bearing seawater upwelling from the deep ocean (Cloud, 1972; Pufahl and Fralick, 2004) was able to cross the shelf and enter the shallow, near-shore environment.

Figure 236A and 236B shows that the sites with samples taken from the Gunflint Formation greater than 3 meters below the Sudbury Impact Layer have positive cerium anomalies, increasing positive europium values, and Y/Ho ratios of samples ranging from 29 to 40. These Y/Ho values are intermediate between common values for crustal rocks of

approximately 28 and of today's ocean, about 50 (Bau and Dulski, 1994). The values from the Gunflint are similar to those from other iron formations (Bau and Dulski, 1996; Bau et al., 1998) and are possibly lower than the modern ocean due to less preferential removal of Ho by scavenging on iron hydroxides in the Paleoproterozoic deep ocean. Figure 237A and 237B shows the samples analyzed from more than 3 meters below the ejecta layer all have V concentrations between 5 and 12ppm, below detection to 2ppm Mo, positive Eu anomalies between 1.3 and 2, and positive Ce anomalies between 0.82 and 0.91. The exceptions to this are the two lowest samples from the Gunflint Trail outcrop, which have no Ce anomaly and V contents between 40 and 50ppm. This indicates that these two samples have experienced some alteration raising their V contents and modifying their REE abundances. The positive Ce anomalies in the other samples can be attributed to preferential oxidative precipitation of Ce in waters of the nearshore environment. Other than this there is no evidence of these samples being modified by oxygen-bearing fluids.

4.1.1   Geochemistry
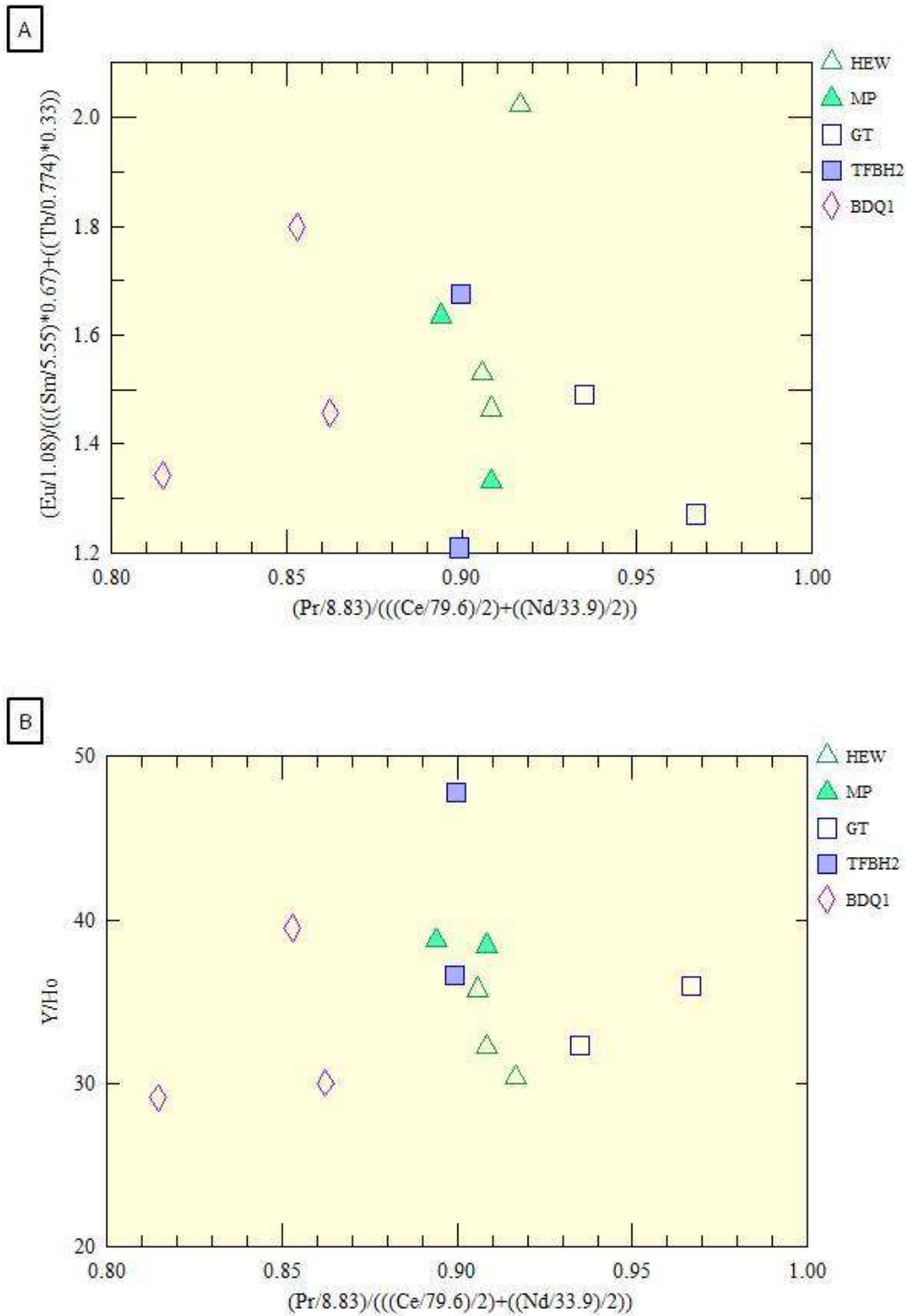
Figure 236. Bivariate plots of samples taken from the Gunflint Formation greater than 3 meters below the Sudbury Impact Layer. A) Samples displaying europium vs cerium anomalies. B) Samples displaying Y/Ho vs cerium anomaly.
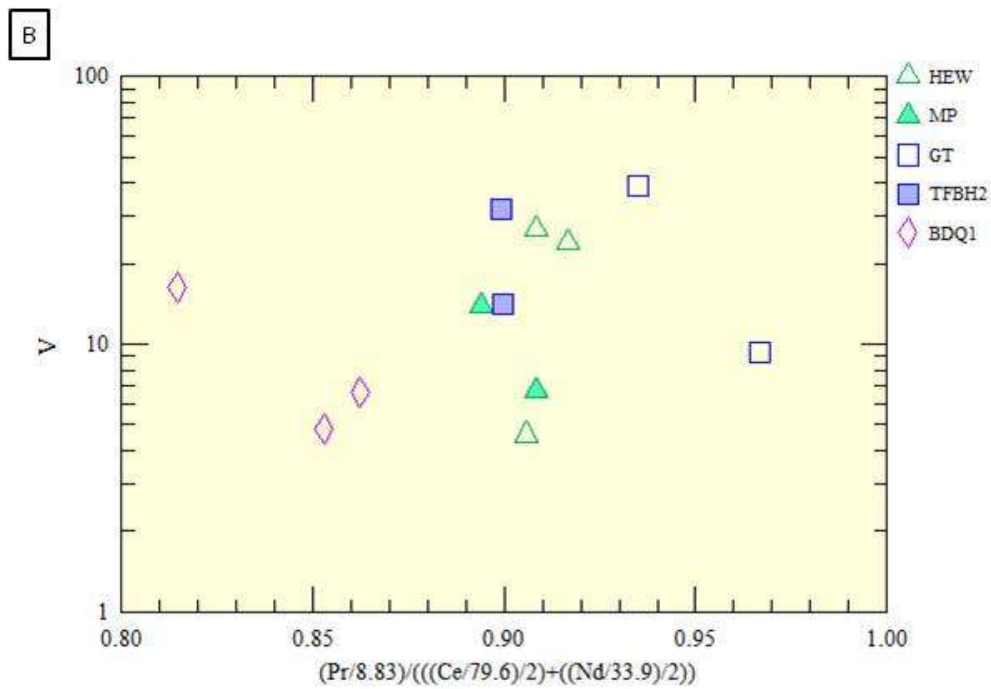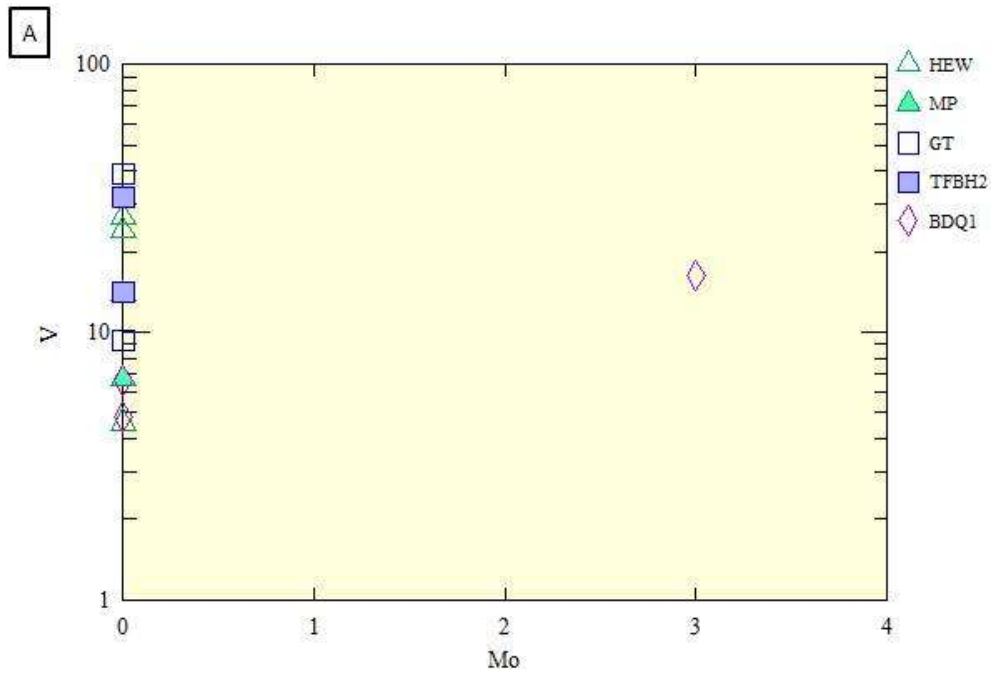
Figure 237. Bivariate plots of samples taken from the Gunflint Formation greater than 3 meters below the Sudbury Impact Layer. A) V vs Mo concentrations. B) V vs cerium anomaly.

4.2   Gunflint Formation Directly Underneath the Ejecta Layer

It is evident that the Gunflint Formation directly underneath the Sudbury Impact Layer was silicified prior to deposition of the S.I.L. Many of the grainstone facies present here have silicified portions, which is probably due to the regression of the ocean which led to the subaerial exposure interpreted at most sites (Poulton et al., 2004, Addison et al., 2010). In many outcrops and drill core, it is evident that the grainstones were silicified prior to impact because of their shattered nature, whether shattered from pre-impact stress or from the seismic waves the impact generated at the time. Pre-impact silicification is also indicated by silicified large boulders, cobbles and pebbles from the Gunflint Formation present in the impact layer itself. The stalactite formations found at Terry Fox lookout are located directly underneath the Sudbury Impact Layer, further evidence pointing to subaerial exposure. Figures 238A and 238B and Figures 239A and 239B show that some of the many Gunflint Formation samples taken from under the Sudbury Impact Layer have extreme negative cerium anomalies, with elevated positive europium anomalies, along with low Mo levels and moderate-to-extreme vanadium enrichments present. It is interesting to note that in BDQ-1 drillcore sample BDQ-1-7 has a V value of 1508ppm, the highest V value in the sample set. This siltstone that is situated directly underneath the ejecta layer was infiltrated by oxygenated water that percolated from the oxygenated S.I.L., with V coming out of solution and precipitating in the cement of the layers underneath the S.I.L. This sample also has a large negative Ce anomaly indicating oxygenated waters weathered REE bearing minerals, leaving Ce behind as the insoluble oxide, then precipitated the cement in the layer directly below the S.I.L. at the drillcore BDQ-1-7 site. The variation in the samples from those with very elevated V and/or Mo (Figure 239A), negative Ce anomalies and small Eu anomalies (Figure 238A) to those with no V or Mo anomalies, no or positive Ce anomalies and

moderate to high Eu anomalies, indicates that diagenetic alteration by oxic fluids was not

uniform and was probably concentrated along permeability pathways.

4.2.1   Geochemistry
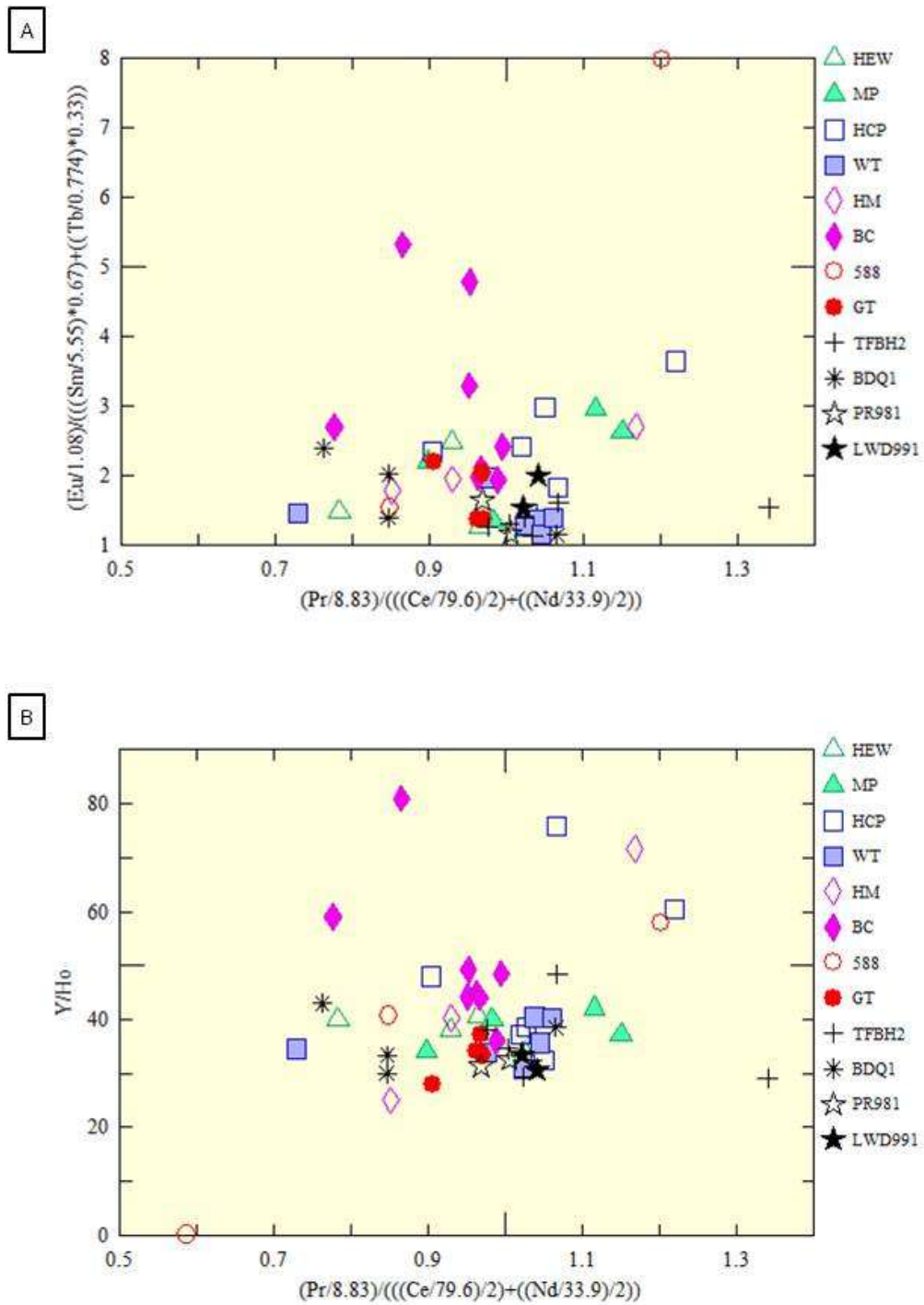
Figure 238. Bivariate plots of samples taken from the Gunflint Formation directly under the ejecta layer. A) Europium vs cerium anomalies. B) Y/Ho vs cerium anomaly.
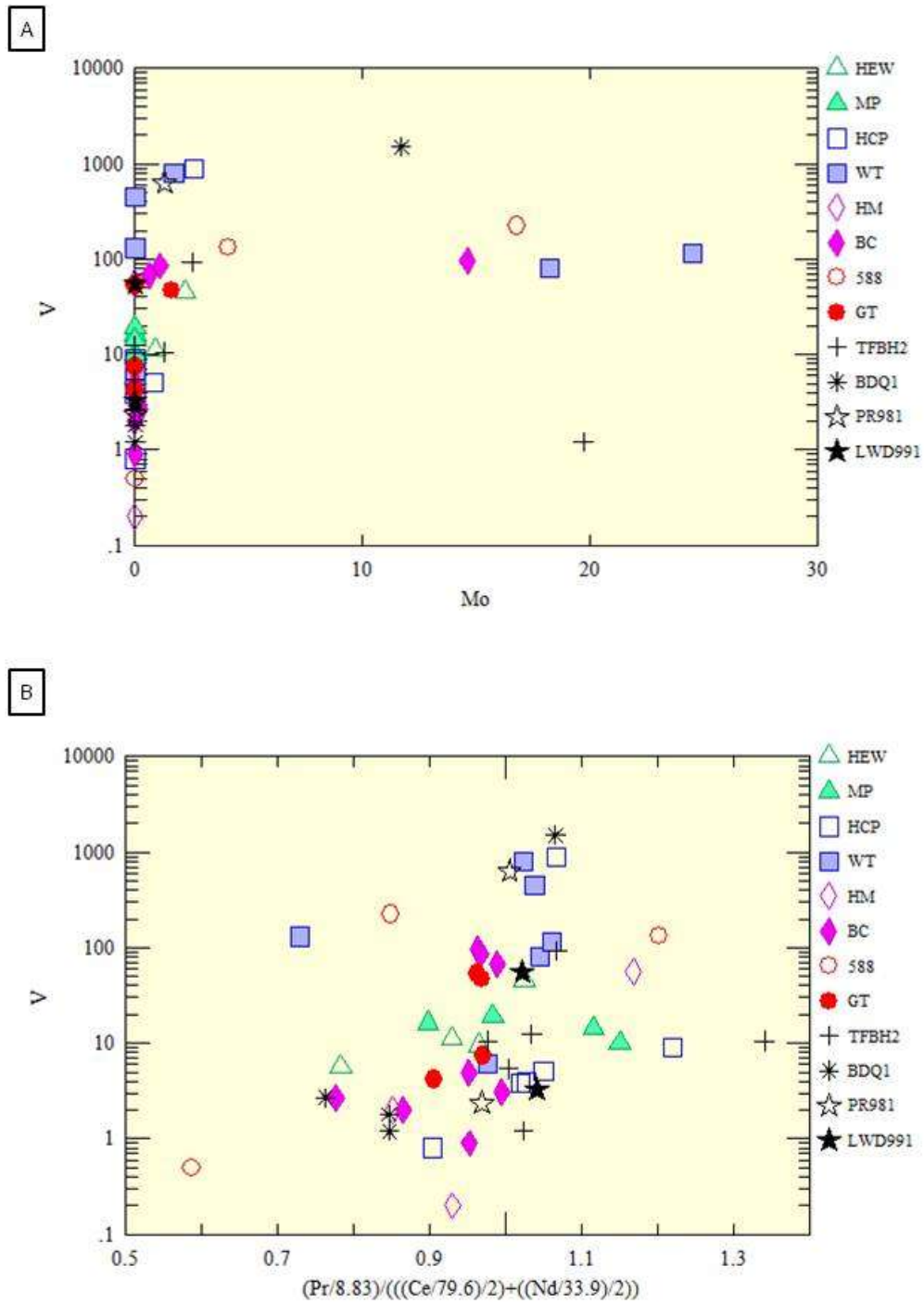
Figure 239. Bivariate plots of samples taken from the Gunflint Formation directly under the ejecta layer. A) V vs Mo concentrations. B) V vs cerium anomaly.

282

4.3   Limestone Layer Underneath the Ejecta Layer

Many samples taken from stromatolitic limestone fragments had both some of the largest V enrichments and the largest negative Ce anomalies. These both indicate precipitation of the abundant blocky calcite cements in the limestone from oxygenated water capable of transporting V in solution, and that these fluids went through a previous period of Ce oxidation and precipitation. This is similar to other Gunflint limestone occurrences where the cements were precipitated by oxygenated meteoric waters (Burton and Fralick, 2007; Fralick and Burton, 2008). Also, many limestone samples had no Eu anomaly, a characteristic that indicates formation of cements from Paleoproterozoic meteoric water, not seawater. Some stromatolitic fragments also have a large amount of Mo. Likewise, this can be related to other work on this limestone unit which put forward that these characteristics were produced by calcite cement formation in the meteoric phreatic zone by oxidized fluids (Burton and Fralick, 2007; Fralick and Burton 2008). In Figure 240A and 240B, the limestone has distinctive Y/Ho anomalies, with most values ranging from 44 to 50 (50 being similar to modern fresh water and seawater). Figure 241A and 241B indicates that all samples from the sites have negative cerium anomalies and elevated vanadium levels. Mapleward Roadcut outcrop indicates that the stromatolitic limestone had a V concentration of 711ppm, the highest in the sample set from this location. Hillcrest Park limestone sample HCP1B had one of the highest levels in this location with V being at 1335ppm, followed by HCP2B with V at 1007ppm, and highest Mo levels at 21.4ppm. The significance of the high V levels is that vanadium came out of solution at this location, and for V to be in solution it needs to go through an area of oxygenation where it can be leached. The limestone stromatolites at Highway 588 have a V level at 1464ppm, the highest in that sample set. Areas such as the Hill and Markland outcrop indicate that the limestone was in a

shallow-water environment due to the fine to medium-grained grainstone that surrounds the stromatolites, with eroded channels between them filled by coarse-grained sand, and the same sand banked up against rows of stromatolites, similar to what is seen behind logs on modern beaches.

4.3.1   Geochemistry
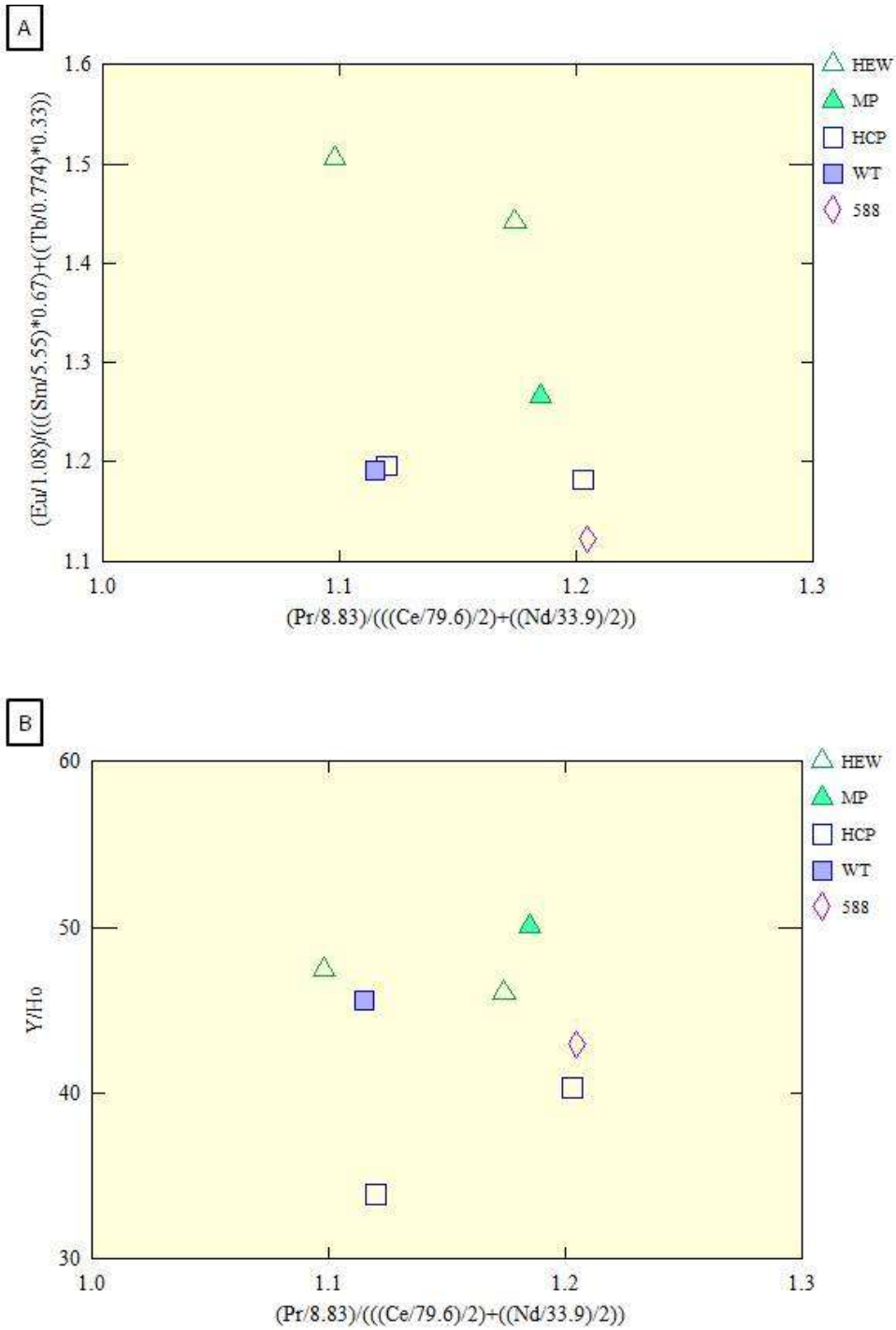
Figure 240. Bivariate plots of samples taken from the Limestone layer underneath the Sudbury Impact Layer. A) Europium vs cerium anomalies. B) Y/Ho vs cerium anomaly.
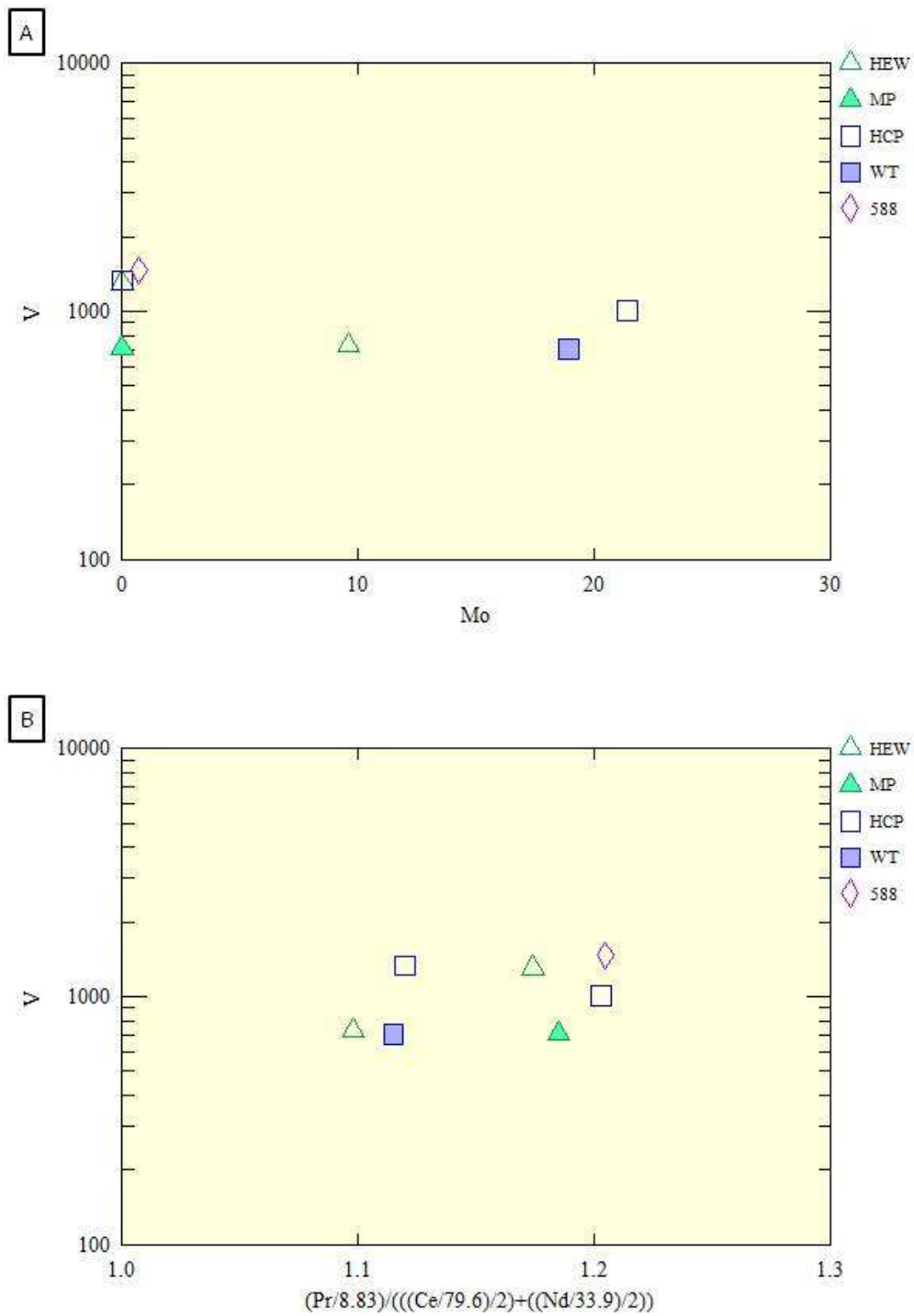
Figure 241. Bivariate plots of samples taken from the limestone layer underneath the Sudbury Impact Layer. A) V vs Mo concentrations. B) V vs cerium anomaly.

4.4   Sudbury Impact Layer

During the time of the deposition of the Sudbury Impact Layer, the area was undergoing a period of tectonic activity along the southern edge of the Superior craton (Addison et al., 2010). Rocks of the S.I.L. near Gunflint Lake indicate that brecciation and folding were the result of liquefaction produced by seismic waves that were generated by the Sudbury Impact, thus indicating that the impact occurred during a time when the Gunflint Lake area was at or slightly below sea level (Jirsa et al., 2011). The Thunder Bay area, on the other hand, contains a calcite-bearing unit that separates the silicified regression surface from the overlying Sudbury Impact Layer. This layer also contains meteoric water infiltrated cements formed prior to the deposition of the S.I.L. (Fralick and Burton, 2008). It can be concluded that the area was above sea level and silicified at the time of the deposition of the Sudbury Impact Layer.   It can be logically deduced that in the north, a regression surface was present, while the sea was present to the south. The length of the time span of this period of subaerial exposure, weathering, erosion and cementation modifying the deposits is not known, though it may have been extensive as 18 My exists between deposition of the S.I.L. and Rove Formation (Addison et al., 2010).

The Sudbury Impact Layer contains white blocky calcite cement which, by analogy with similar blocky calcite cements described and interpreted in the underlying limestone and other S.I.L. outcrops (Burton and Fralick, 2007; Fralick and Burton, 2008), indicates that meteoric water infiltrated the S.I.L. rather than oceanic water. Also, the mini-stalactite formations found in vugs at Hillcrest Park at the top of the Sudbury Impact Layer formed in the vadose zone, denoting subaerial exposure at some point in time. Almost all of the samples taken from the Sudbury Impact Layer have negative Ce anomalies (Figure 242A and 242B) and are enriched in V (Figure 243A and 243B), probably indicating deposition of their blocky calcite cements from

oxygenated water. The negative Ce anomalies indicate that the meteoric water that deposited the calcite cements was deficient in Ce compared to the other REEs. This was most likely caused by the water attaining its REE load during weathering in a somewhat oxic environment or encountering an oxic environment and having the Ce (III) oxidize to Ce (IV) and leave solution as a precipitate. The correlation between the negative Ce anomalies and enrichment of V and Mo in the samples also indicates that the meteoric waters the calcite cements formed from were somewhat oxic. Representative samples were taken from the ejecta layer from white blocky calcite cement at the Mapleward Roadcut that perfectly signify an oxygenated environment. Samples MP12, MP13, and MP14 have V levels from 73-709ppm but with low Mo levels (0-0.73ppm) (Figure 243A) and Cr levels from 44-62ppm. All calcite cement samples have negative Ce anomalies (Figure 242A and 242B) indicating oxygenated water was circulating during the time that the cements were precipitated. Many samples from the ejecta layer exhibit small to medium positive Eu anomalies (Figure 242A), presumably inherited from dissolution of ankerite. The Y/Ho ratios vary between the 30's and 40's (Figure 242B).

4.4.1   Geochemistry
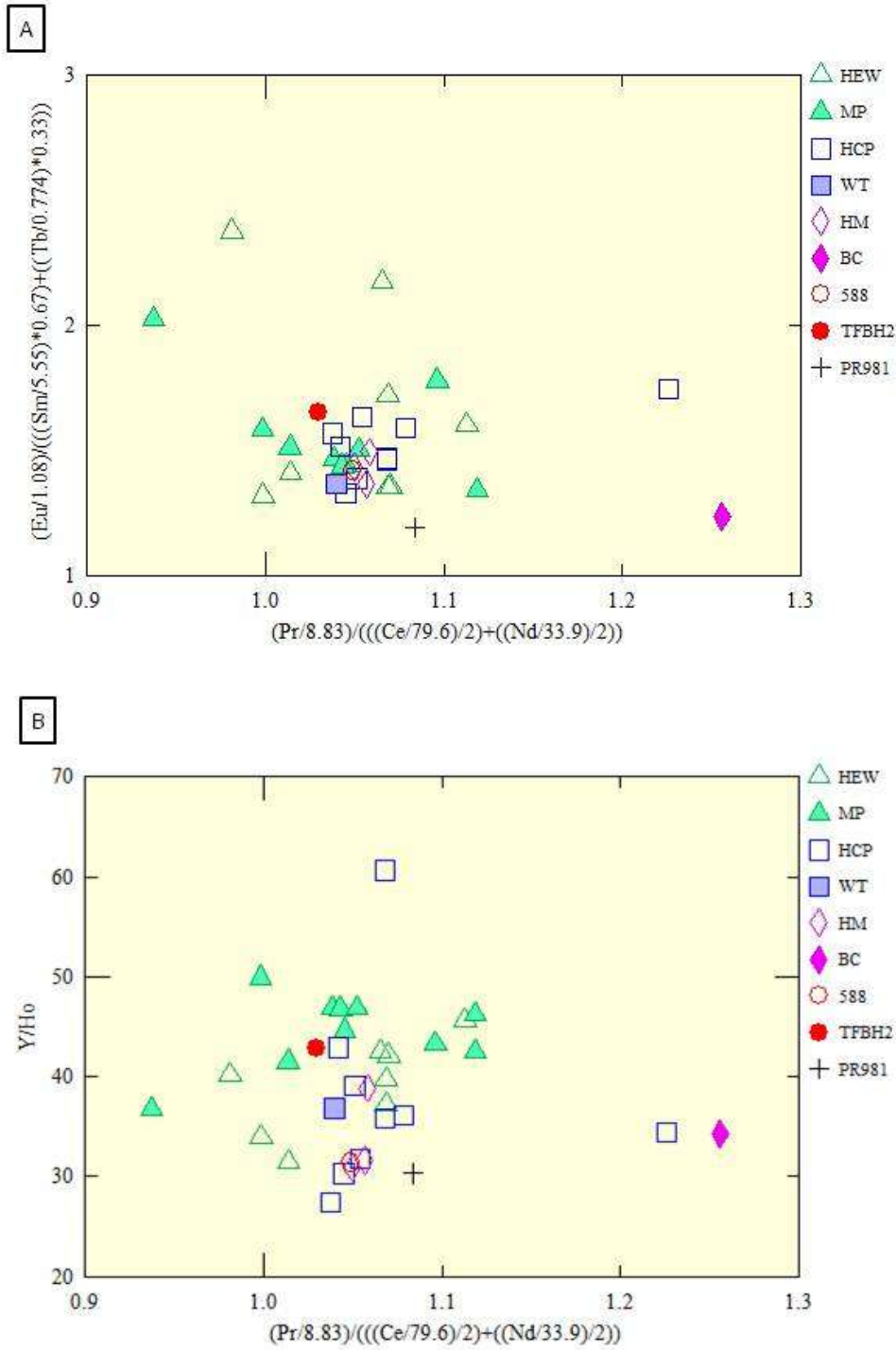
Figure 242. Bivariate plots of samples taken from the Sudbury Impact Layer. A) Europium vs cerium anomalies. B) Y/Ho vs cerium anomaly.
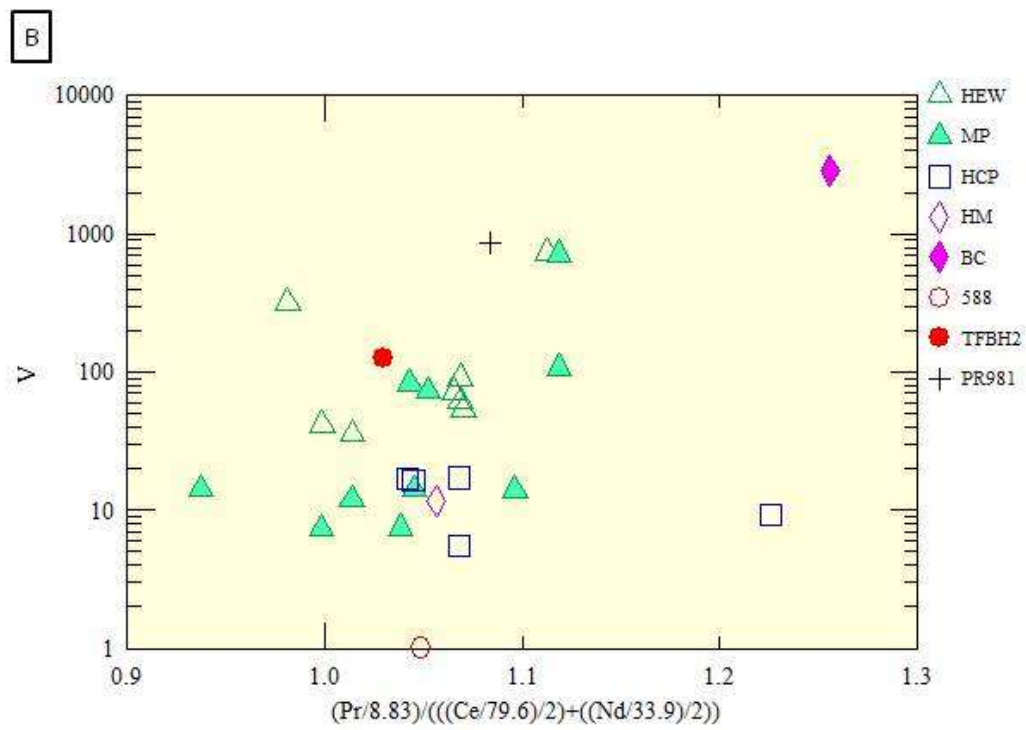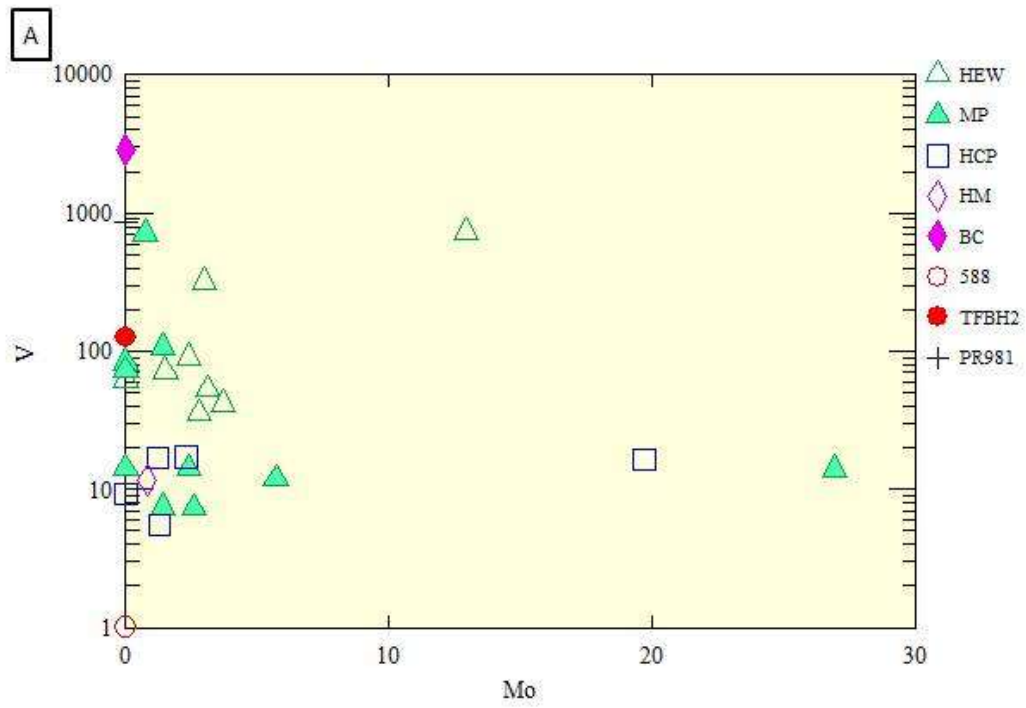
Figure 243. Bivariate plots of samples taken from the Sudbury Impact Layer. A) V vs Mo concentrations. B) V vs cerium anomaly.

4.5 Rocks Above Ejecta Layer

The area overlying the Sudbury Impact Layer consists of 2-3 meters of carbonate facies iron formation. In places, particularly immediately below the Rove Formation, there are large calcite crystals surrounded by thin coatings of dark mud forming chicken-wire structure. The crystals contain banded growth lines (refer back to thin section picture from drill core BDQ-1: Figure 189) interpreted to be caused by fluctuation of dissolved constituents in the water from which the crystals precipitated. It is assumed that the waters that precipitated the crystals were of meteoric origin due to the frequent banding colour changes (refer back to SEM images from drill core BDQ-1showing crystal banding: Figures 190, 191). The blue bands (dark bands) represent magnesium-rich growth bands, while green banding (light bands) represents iron-rich growth bands. The frequent changes can occur more readily in fresh water than in seawater due to the long and slow process of chemical change in the oceans.   The chicken-wire structure, which has been replaced by carbonate, is very similar in appearance to the chicken-wire anhydrite textures preserved in dolostone in Paleoproterozoic rocks of the Baltic Shield that were deposited on a coastal sabkha (Brasier et al., 2011) and mosaic chicken-wire anhydrite present in Devonian supratidal sabkhas of Bulgaria (Andreeva, 2015). The gypsum desert roses that are found in the Harbour Expressway area are very similar to those described by Whitlock (1930) as: "groups of overlapping platelike crystals deposited by groundwater in desert sand that resemble the petals of a rose." Most modern examples of desert roses have grown in loose sediment near the surface of sabkhas (ie., Almohandis, 2002) and are a strong indicator of an arid climate (Keyser, 1968). It is interesting to note that the rocks above the impact layer were subaerially exposed due to the fact that voids were formed in the sediment which contain stalactite features, such as in the upper Gunflint Trail boulder at the cliff site. The Harbour Expressway plaque is

above the Sudbury Impact Layer as well. Figure 244A and 244B, and Figure 245A and 245B

shows that all of the samples taken from above the Sudbury Impact Layer from the Gunflint Trail

and Harbour Expressway display negative cerium anomalies, low molybdenum levels, and

increasing vanadium levels. Drillcore BDQ-1 exhibits high V levels from the rhomb-shaped

crystals that are situated above the ejecta layer which have 463ppm V, 52ppm Mo, and 56ppm

Cr. The sample taken from BDQ-1 of the upper chicken-wire structure above the ejecta layer

exhibits near zero values of V and Cr, approximately 23ppm of Mo, and a slight negative Ce

anomaly, with only a slight positive Eu anomaly. Thus, in the drillcore from BDQ-1, evidence

of transport of V and Cr by oxidized fluids and precipitation in a sabkha environment is lacking,

whereas the REEs and Mo do indicate some oxidized fresh water influence. This is not unusual

as modern sabkhas, such as the south shore of the Persian Gulf, where areas are subjected to the

mixed influence of hypersaline seawater and freshwater (Purser and Loreau, 1973).

4.5.1 Geochemistry
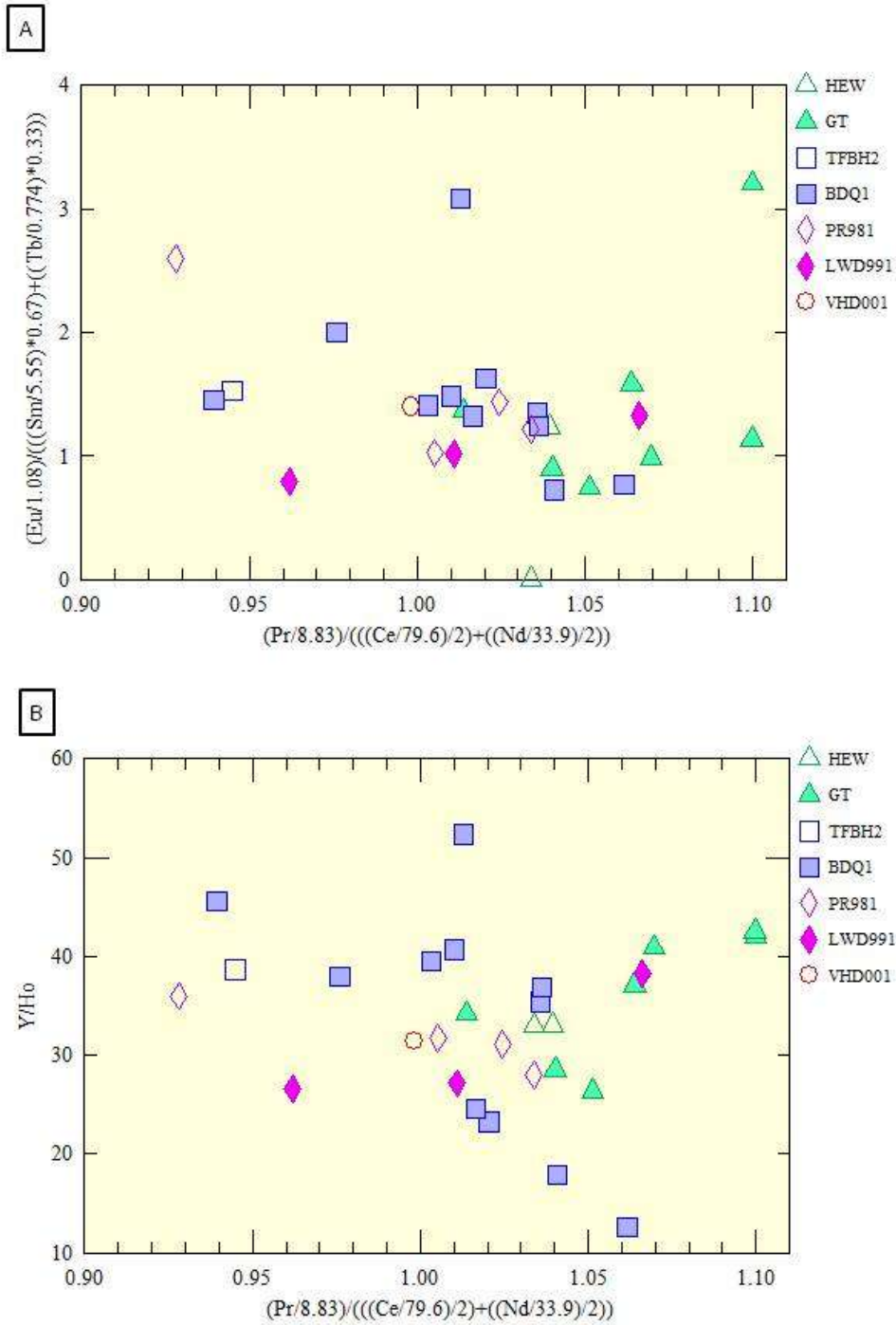
Figure 244. Bivariate plots of samples taken from the rocks above the Sudbury Impact Layer. A) Europium vs cerium anomalies. B) Y/Ho vs cerium anomaly.
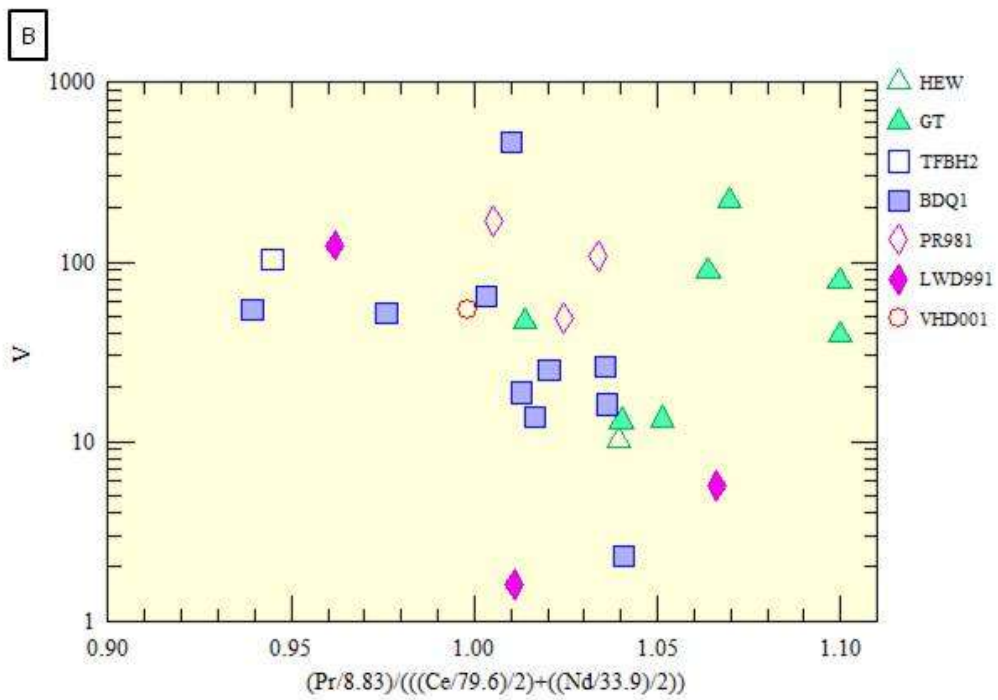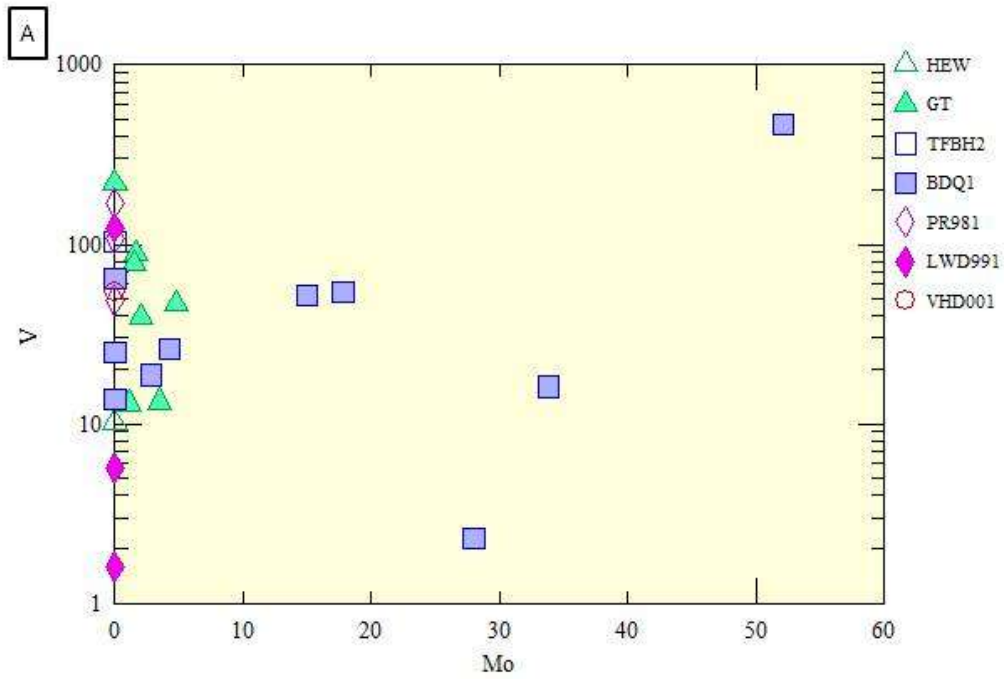
Figure 245. Bivariate plots of samples taken from the rocks above the Sudbury Impact Layer. A) V vs Mo levels. B) V vs cerium anomaly.

4.6 Generalized Paleogeographic Interpretations

Refer to Table 14 for generalized lithologies and sedimentary structures present in each of the five general units. At approximately 1878 Ma (Fralick et al., 1998; Fralick et al., 2002), the Gunflint Formation was deposited on a storm dominated, broad continental shelf (Pufalh and Fralick, 2004), comprising part of the Animikie basin. The lower member of the Gunflint Formation denotes a transgressive-regressive cycle consisting of slatey and cherty members with a capping subaerial exposure unit formed in the north (Fralick and Barrett, 1995) when the sea regressed, extending into the bottom part of the upper member of the Gunflint Formation. At the bottom of the upper unit, there is a stromatolitic occurrence.

The rest of the upper member of the Gunflint Formation records another transgression event with shoaling-upwards cycles (Pufahl and Fralick, 2004), until the uppermost layers are reached where a regression of the sea occurred and land was subaerially exposed. This was determined from evidence of lithification and silicification of the units near the top of the Gunflint Formation. Eventually, the area was either reflooded by a shallow sea or enveloped by the formation of a lake and the limestone unit at the top of the Gunflint Formation was deposited. The latter is more likely as the geochemistry of the stromatolites indicates a fresh water or meteoric water dominated environment.

It is important to notice that there are marked differences in the characteristics of the upper Gunflint Formation in the Thunder Bay area and the Gunflint Trail area. Burton and Fralick (2007) and Fralick and Burton (2008) noticed that the upper unit of the Gunflint Formation is a regressive surface with intense silicification, and is then overlain by local and distal brecciated material of the Sudbury Impact Layer. A white, blocky, calcite cement

developed here (Fralick and Burton; 2008). Conversely, the Gunflint Lake area has in the uppermost meters of the iron formation a brecciated and extremely folded unit that is then covered by the Sudbury Impact Layer. The brittle deformation of chert layers and folding of the other topmost layers in the Gunflint Lake area strongly indicates that the sediments were saturated and/or covered by water, shocked by the earthquake from the impact, and liquefied (Jirsa et al., 2011).

At approximately 1850 Ma (Krogh, 1984) the Sudbury Impact Layer was deposited overlying the Gunflint Formation. The S.I.L. varies in thickness over the area as the blast cloud carrying the debris in a base surge (Addison et al., 2008) deposited debris non-uniformly due to topographic differences. Sometime after the deposition of the ejecta layer, phreatic, blocky calcite cement formed in the Sudbury Impact Layer, whereas in some of the upper portions of the layer, freshwater vadose silica mini-stalactites formed in cavities. At some later time the area was reflooded by the sea and more carbonate facies iron formation was deposited in the very shallow setting. Extensive sabkhas developed at the time of the slight trangression of the sea. Eventually, the sea retreated and chicken-wire structure developed at the top of this succession.

At approximately 1832 Ma (Addison et al, 2005), the sea transgressed and eroded the top of the iron formation immediately prior to infilling the basin with Rove Formation shales and siltstones. The Rove Formation dominates the stratigraphic column above the Gunflint Formation for about 1000 meters, with carbonaceous shales gradationally transitioning upwards into outbuilding prodelataic, turbidite lobes (Meric and Fralick, 2005).

References

Addison, W.D. and Brumpton, G.R., 2012. Field trips 1 & 13 – Sudbury impactoclastic debrisites at Thunder Bay: Institute on Lake Superior Geology, Proceedings, v. 56, Part 2, p. 2-26.

Addison, W.D., Brumpton, G.R., Vallini, D.A., McNaughton, N.J., Davis, D.W., Kissin, S.A., Fralick, P.W., and Hammond, A.L., 2005. Discovery of distal ejecta from the 1850 Ma Sudbury impact event. Geology, v. 33, p. 193-196.

Addison, W.D., Brumpton, G.R., Fralick, P.W., and Kissin, S.A., 2009. The complex Gunflint-Rove Formations boundary at Thunder Bay, Ontario: two disconformities and a base surge debrisite. Institute on Lake Superior Geology Procedings, 55, p. 1-2.

Addison, W.D., Brumpton, G.R., Davis, D.W., Fralick, P.W., and Kissin, S.A., 2010. Debrisites from the Sudbury impact event in Ontario, north of Lake Superior, and a new age constraint: Are they base-surge deposits or tsunami deposits. In, R.L. Gibson and W.U. Reimold eds., Large Meteorite Impacts and Planetary Evolution IV. Geological Society of America, Special Paper 465, p. 245-268.

Algeo, T., 2004. Can marine anoxic events draw down the trace element inventory of seawater? Geology 32, p. 1057-1060.

Alibert, C., and McCulloch, M.T., 1993. Rare earth element and neodymium isotopic composition of the banded iron formations and associated shales from Hammersley, western Australia. Geochimica et Cosmochimica Acta, 57, p. 187-204.

Almohandis, A.A., 2002. Mineralogy and chemistry of desert roses, Ayn Dar area, Abqaiq, Eastern Province, Saudi Arabia. Qatar University Science Journal, 22, p. 191-204.

Anbar, A., 2004. Molybdenum Stable Isotopes: Observations, Interpretations, and Directions, p. 55. Mineralogical Society of America, p. 429-454.

Anbar, A., Knoll, A., 2002. Proterozoic ocean chemistry and evolution: a bioinorganic bridge? Science 297, p. 1137-1142.

Anbar, A., Duan, Y., Lyons, T., Arnold, G., Kendal, B., Creaser, R., Kaufman, A., Gordon, G., Scott, C., Garvin, J., Buick, R., 2007. A whiff of oxygen before the great oxidation event? Science 317, p. 1903-1906.

Andreeva, P.V., 2015. Middle Devonian (Giventian) supratidal anhydrites from the Moesian Platform (Northeastern Bulgaria). Carbonates and Evaporites, 30, p. 439-449.

Bau, M., 1999. Scavenging of dissolved yttrium and rare earth s by precipitating iron hydroxides: experimental evidence for Ce oxidation, Y-Ho fractionation, and lanthanide tetrad effect: Geochimica et Cosmochimica Acta, 63, p. 67-77.

Bau, M., and Dulski, P., 1994. Evolution of the yttrium-holmium systematics of seawter through time. Mineralogical Magazine, 58A, p. 61-62.

Bau, M., Dulski, P., Moller, P., 1995. Yttrium and holmium in South Pacific seawater: vertical distribution and possible fractionation mechanisms, Chem. Erde 55, p. 1-15.

Bau M., and Dulski, P., 1996. Distribution of yttrium and rare-earth elements in the Penge and Kuruman iron-formations, Transvaal Supergroup, South Africa: Precambrian Research, 79, p. 37-55.

Bau M., and Dulski, P., 1998. Comparing yttrium and rare earths in hydrothermal fluids from the Mid-Atlantic Ridge: implications for Y and REE behaviour during near-vent mixing and for the Y/Ho ratio of Proterozoic seawater. Chemical Geology 155, p. 77-90.

Bau, M, Hohndorf, A., Dulski, P., Beukes, N.J., 1997b. Sources of rare-earth elements and iron in Palaeoproterozoic iron-formations from the Transvaal Supergroup, South Africa: evidence from neodymium isotopes. Journal of Geology, 105, p. 121-129.

Bau, M., Beukes, N.J., and Romer, R.L., 1998. Increase of oxygen in the Earth's atmosphere and hydrosphere between ~2.5 and ~2.4 GA B.P: Mineralogical Magazine, 62A, p. 127-128.

Bilal, B.A., 1992. Thermodynamic study of Eu^{3+}/Eu^{2+} redox reaction in aqueous solutions at elevated temperature and pressures by means of cyclic voltammetry. Lanthanide Actinide Res. Z, Naturforsch., 46a: p. 1108-1116.

Bolhar, R. and Kranendonk, M.J., 2007. A non-marine depositional setting for the northern Fortesque Group, Pilbera craton, inferred from trace element geochemistry of stromatolitic carbonates. Precambrian Research 155, p. 229-250.

Bondesen, E., Raunsgaard, P.K., and Jorgensen, O., 1967. Precambrian Organisms and the Isotopic Composition of Organic Remains in the Ketilidian of South-West Greenland, Gronlands Geologiske Undersogelse Bulletin, 67, p.1-41, (Meddeleiser om Gronland 164, 4).

Brasier, A.T., Fallick, A.E., Prove, A.R., Melezhik, V.A., Lepland, A., and FAR-DEEP Scientists, 2011. Coastal sabkha dolomites and calcitised sulphates preserving the Lomagundi-Jutuli carbon isotope signal. Precambrian Research, 189, p. 193-211.

Braun, J.J., Viers, J., Dupre, B., Polve, M., Ndam, J., and Muller, J.P., 1998. Solid/liquid REE fractionation in the lateritic system of Goyoum, East Cameroon: the implications for the present dynamics of the soil covers of the humid tropical regions: Geochimica et Cosmochimica Acta, 62, p. 273-299.

Burton, J., and Fralick, P.W., 2007. Deposition and cementation of Paleoproterozoic Gunflint Formation carbonate: Implications for early hydrosphere chemistry. Institute on Lake Superior Geology, Proceedings and Abstracts, 57, Part 1, p. 18-19.

Byrne, R.H., Lee, J.H., 1993. Comparative yttrium and rare earth elements chemistries in seawater, Mar. Chem. 44, p. 121-130.

Chadwick, B., Claeys, P., and Simonson, B., 2001. New evidence for a large Paleoproterozoic impact: spherules in a dolomite layer in the Ketilidian orogen, South Greenland. Journal of the Geological Society, London, 158, p. 331-340.

Cherniak, D.L., 1998. REE diffusion in calcite: Earth and Planetary Science Letters, 160, p. 273-287.

Cloud, Jr.P.E., 1972. A working model of the primitive Earth. American Journal of Science 272, p. 537-548.

Collins, G.S., Melosh, H.J., and Marcus, R.A., 2005. Earth impact effects program: A web-based computer program for calculating the regional environmental consequences of a meteoroid impact on Earth: Meteorites & Planetary Science, 40, p. 817-840.

Colodner, D., Edmond, J., Boyle, E., 1995. Rhenium in the Black Sea: comparison with molybdenum and uranium. Earth and Planetary Science Letters 131 (1-2), p. 1-15.

Compton, J.S., White, R.A., and Smith, M., 2003. Rare earth element behaviour in soils and salt pan sediments of a semi-arid granitic terrain in Western Cape, South Africa: Chemical Geology, 201, p. 239-255.

Danielson, A., Moller, P., and Dulski, P., 1992. The europium anomaly in banded iron formation and the thermal history of the ocean-crust. Chemical Geology 97, p. 89-100.

Derry, L.A., and Jacobsen, S.B., 1990. The chemical evolution of Precambrian seawater: Evidence from REEs in banded iron formation: Geochimica et Cosmochimica Acta, 54, p. 2965-2977.

Dossing, L., Dideriksen, K., Stipp, S., Frei, R., 2011. Reduction of hexavalent chromium by ferrous iron: a process of chromium isotope fractionation and its relevance to natural environments. Chemical Geology 285 (1-4), p. 157-166.

Dia, A., Gruau, G., Olivie-Lauquet, G., Riou, C., Molenat, J., and Curmi, P., 2000. The distribution of rare-earths in groundwater: assessing the role of source-rock composition, redox changes and colloidal particles: Geochimica et Cosmochimica Acta, 64, p. 4131-4151.

Duan, Y., Anbar, A., Arnold, G., Lyons, T., Gordon, G., Kendall, B., 2010. Molybdenum isotope evidence for mild environmental oxygenation before the Great Oxidation Event. Geochimica et Cosmochimica Acta 74 (23), p. 6655-6668.

Dunham, R.J., 1962. Classification of carbonate rocks according to depositional texture. In, W.E. Hamm (Ed.), Classification of Carbonate Rocks, A Symposium. American Association of Petroleum Geologists, p. 108-121.

Dymek, R.F., Klein, C., 1988. Chemistry, petrology, and origin of banded iron-formation lithologies from the 3800 Ma Isua Supracrustal Belt, West Greenland. Precambrian Res. 39, p. 247-302.

Earth Impact Database, 2004. Earth Impact Database: www.unb.ca/passe/ImpactDatabase (accessed 2015).

Eary, L., Rai, D., 1989. Kinetics of chromate reduction by ferrous ions derived from hematite and biotite at 25 degrees C. American Journal of Science 289, p. 180-213.

El Khorily, E.M., 2005. Origin of the gypsum-rich silica nodules, Moghra Formation, Northwest Qattara depression, Western Desert, Egypt. Sedimentary Geology, 177, p. 41-55.

Emerson, S., Cranston, R., Liss, P., 1979. Redox species in a reducing fjord: equilibrium and kinetic considerations. Deep Sea Research Part A Oceanographic Research Papers 26 (8), p. 859-878.

Erickson, B., Helz, G., 2000. Molybdenum (VI) speciation in sulfidic waters: stability and lability of thiomolybdenates. Geochimica et Cosmochimica Acta 64 (7), p. 1149-1158.

Floran, R.J., Papike, J.J., 1978. Mineralogy and petrology of the Gunflint Iron Formation, Minnesota-Ontario: Journal of Petrology, 19, p. 215-288.

Fralick, P.W., 1988. Microbial bioherms, Lower Proterozoic Gunflint Formation, Thunder Bay, Ontario, in Geldsetzer, H.H.J., James N.P., and Tebbutt, G.E., eds., Reefs in Canada and Adjacent Areas: Canadian Society of Petroleum Geologists, Memoir 13, p. 24-29.

Fralick, P.W. and Barrett, T.J., 1995. Depositional controls on iron formation associations in Canada. In, ed. A.G. Plint, Sedimentary Facies Analysis. International Association of Sedimentologists Special Publication 22, p. 137-156.

Fralick, P.W., Davis, D.W., and Kissin, S.A., 2002. The age of the Gunflint Formation, Ontario, Canada: single zircon U-Pb age determination from reworked volcanic ash. Canadian Journal of Earth Sciences, 39, p. 1085-1091.

Fralick, P.W., and Burton, J., 2008. Geochemistry of the Paleoproterozoic Gunflint Formation carbonate: Implications for early hydrosphere-atmosphere evolution. Geochimica et Cosmochimica Acta, Special Supplement, 72, no. 125, p. A280.

Fralick, P.W., Grotzinger, J., and Edgar, L., 2012. Potential recognition of accretionary lapilli in distal impact deposits on Mars: a facies analog provided by the 1.85 Ga Sudbury impact deposit. In, J. Grotzinger and R. Milliken eds., The Sedimentary Geology of Mars. Journal of Sedimentary Research, Special Publication 102, p. 211-228.

Frei, R., Gaucher, C., Poulton, S., Canfield D., 2009. Fluctuations in Precambrian atmospheric oxygenation recorded by chromium isotopes. Nature 461, p. 250-253.

French, B.M., 1998. Traces of Catastrophe. Lunar and Planetary Institute, Contribution 954, p. 120.

Gault, D.E., Quaide, W.L., Oberbeck, V.R., 1968. Impact Cratering Mechanisms and Structures: Shock Metamorphism of Natural Materials, p. 87-99.

Gill, J.E., 1926. Gunflint iron-bearing formation, Ontario: Canada Department of Mines, Geological Survey, Summary Report, 1924, Part C, p. 28c-88c.

Goodwin, A.M., 1956. Facies relations in the Gunflint iron-formation: Economic Geology, 51, p. 565-595.

Grieve, R.A.F., 1998. Extraterrestrial impacts on earth: the evidence and the consequences. In: Grady, M.M., Hutchinson, R., McCall, G.J.H. & Rothery, D.A. (eds) Meteorites: Flux with Time and Impact Effects. Geological Society, London. Special Publications, 140, p. 105-131.

Gruau, G., Dia, A., Olivie-Lauquet, G., Davranche, M., and Pinay, G., 2004. Controls on the distribution of rare earth elements in shallow groundwaters: Water Research, 38, p. 3576-3586.

Helz, G., Miller, C., Charnock, J., Mosselmans, J., Pattrick, R., Garner, C., Vaughan, D., 1996. Mechanism of molybdenum removal from the sea and its concentration in black shales: EXAFS evidence. Geochemica et Cosmochimica Acta 60 (19), p. 3631-3642.

Helz, G., Bura-Nakic, E., Mikac, N., Ciglenecki, I., 2011. New model for molybdenum behaviour in euxinic waters. Chemical Geology 284 (3-4), p. 323-332.

Hemming, S.R., McLennan, S.M., Hanson, G.M., 1995. Geochemical and Nd/Pb isotopic evidence for the provenance of the early Proterozoic Virginia Formation, Minnesota: Implications for tectonic setting of the Animikie Basin: The Journal of Geology, 103, p.147-168.

Henderson, P., 1984. General geochemical properties and abundances of rare earth elements. In: P. Henderson (Editor), Rare Earth Element Geochemistry. Development in Geochemistry, 2. Elsevier, Amsterdam, p. 1-32.

Holland, H.D., 2006. The oxygenation of the atmosphere and ocean. Philosophical Transactions of the Royal Society B 361, p. 903-915.

Holser, W.T., 1997. Evaluation of the application of rare-earth elements to paleoceanography: Palaeogeography, Palaeoclimatology, Paleoecology, 132, p. 309-323.

Holstetler, P.B., and Garrels, R.M., 1962. Transportation and precipitation of uranium and vanadium at low temperatures, with special reference to sandstone-type uranium deposits: Economic Geology, 57, p. 137-152.

Jacobsen, S.B., and Pimentel-Klose, M.R., 1988a. A Nd isotopic study of the Hamersley and Michipicoten banded iron formations: the source of REE and Fe in Archean oceans. Earth Planet, Sci. Lett., 87: p. 29-44.

Jacobsen, S.B., and Pimentel-Klose, M.R., 1988b. Neodymium isotopic variations in Precambrian banded iron formations: Geophysical Research Letters, 15, p. 393-396.

Ji, H., Wang, S., Ouyang, Z., Zhang, S., Sun, C., Liu, X., and Zhou, D., 2004. Geochemistry of red residual underlying dolomites in karst terrains of Yunnan-Guizhou Plateau II: the mobility of rare earth elements during weathering: Chemical Geology, 203, p. 29-50.

Jirsa, M.A., Weiblen, P.A., Vislova, T. and McSwiggen, P.L., 2008. Sudbury impact layer near Gunflint Lake, NE Minnesota: Institute on Lake Superior Geology, Proceedings, v. 54, Part 1, p. 42-43.

Jirsa, M., Fralick, P, Weiblen, P., Anderson, J., 2011. Sudbury Impact Layer in the western Lake Superior Region: GSA Field Guides, 24, p. 147-169.

Johnston, D.T., Poulton, S.W., Fralick, P.W., P.W., Wing, B.A., Canfield, D.E., Farquhar, J., 2006. Evolution of the oceanic sulfur cycle at the end of the Paleoproterozoic: Geochimica et Cosmochimica Acta, 70, p. 5723-5739.

Kamber, B.S., Bolhar, R., and Webb, G.E., 2004. Geochemistry of late Archean stromatolites from Zimbabwe: evidence for microbial life in restricted epicontinental seas: Precambrian Research, 132, p.379-399.

Kawabe, I., Kitahara, Y., Naito, K., 1991. Non-chondritic yttrium/holmium ratio and lanthanide tetrad effect observed in pre-Cenozoic limestones, Geochem. J. 25, p. 31-44.

Kendall, B., Reinhard, C., Lyons, T., Kaufman, A., Poulton, S., Anbar, A., 2010. Pervasive oxygenation along late Archaean ocean margins. Nature Geoscience 3 (9), p. 647-652.

Keyser, A.W., 1968. Some indications of arid climate during deposition of the Beaufort series. Annuals of the Geological Survey, Republic of South Africa, 5, p. 77-78.

Kim, C., Zhou, Q., Deng, B., Thornton, E., Xu, H., 2001. Chromium (VI) reduction by hydrogen sulfide in aqueous media: stoichiometry and kinetics. Environmental Science & Technology 35 (11), p. 2219-2225.

Kim, C., Lan, Y., Deng, B., 2007. Kinetic study of hexavalent Cr(VI) reduction by hydrogen sulfide through goethite surface catalytic reaction. Geochemical Journal 41 (6), p. 397-405.

Kissin, S.A. and Fralick, P.W., 1994. Early Proterozoic volcanics of the Animikie Group, Ontario and Michigan, and their tectonic significance. Institute on Lake Superior Geology Proceedings, 40, p. 18-19.

Kissin, S.A., Vallini, D.A., Addison, W.D. and Brumpton, G.R., 2003. New zircon ages from the Gunflint and Rove Formations, northwestern Ontario. Institute on Lake Superior Geology Preceedings, 49, p. 43-44.

Koppi, A.J., Edis, R., Field, D.J., Geerin, H.R., Klessa, D.A., and Cockayne, J.H., 1996. Rare earth element trends and cerium-uranium-manganese associations in weathered rock from Koongarra, Northern Territory, Australia: Geochimica et Cosmochimica Acta, 60, p.1695-1707.

Krogh, T.E., Davis, D.W. and Corfu, F., 1984. Precise U-Pb zircon and baddeleyite ages for the Sudbury area. In, E.G. Pye ed., The Geology and Ore Deposits of the Sudbury Structure. Ontario Geological Survey, 1, p. 431-446.

Lei, W., Linsalata, P., Franca, E.P., and Eisenbud, M., 1986. Distribution and mobilization of cerium, lanthanum and neodymium in the Morro do Ferro basin, Brazil: Chemical Geology, 55, p. 313-322.

Lewan, M.D., and Maynard, J.B., 1982. Factors controlling enrichment of vanadium and nickel in the bitumen of oranic sedimentary rocks: Geochimica et Cosmochimica Acta, 46, p. 2547-2560.

Liu , X., Byrne, R.H., 1995. Comparative carbonate complexation of yttrium and gadolinium at 25ºC and 0.7 mol/cm^{-3} ionic strength, Mar. Chem. 51, p. 213-221.

Liu, Y.G., Miah, M.R.U., and Schmitt, R.A., 1988. Cerium: a chemical tracer for paleo-oceanic redox conditions: Geochimica et Cosmochimica Acta, 52, p. 1361-1371.

Machel, H.G., 1985. Fibrous gypsum and fibrous anhydrite in veins. Sedimentology, 32, p. 443-454.

Maric, M. and Fralick, P., 2005. Sedimentology of the Rove and Virginia Formations and their tectonic significance. Institute on Lake Superior Geology Proceedings, 51, p. 41-42.

Marsh, J.S., 1991. REE fractionation and Ce anomalies in weathered Karoo dolerite: Chemical Geology, 90, p. 189-184.

Morford, J., Emerson, S., 1999. The geochemistry of redox sensitive trace metals in sediments. Geochimica et Cosmochimica Acta 63 (11-12), p. 1735-1750.

Moorhouse, W.W., and Goodwin, A.M., 1960. Gunflint iron range in the vicinity of Port Author and Gunflint Iron Formation of the Whitefish Lake area. Ontario Department of Mines, 69, Part 7, p. 67.

Murray, R.W., Buchholtz ten Brink, M.R., Jones, D.L., Gerlach, D.C., and Russ, G.P., 1990. Rare earth elements as indicators of different marine depositional environments in chert and shale: Geology, 18, p. 268-271.

Northrop, H.R., and Goldhaber, M.B., 1990. Genesis of the tabular-type vanadium-uranium deposits of the Henry Basin, Utah: Economic Geology, 85, p. 215-269.

Nozaki, Y, Zhang, J., 1995. The rare earth elements and yttrium in the coastal/offshore mixing zone of Tokyo Bay waters and the Kuroshio, in : H. Sakai, Y. Nozaki (Eds.), Biogeochemical Processes and Ocean Flux in the Western Pacific, Terra, Tokyo, p. 171-184.

Nozaki, Y., Zhang, J., and Amakawa, H., 1997. The fractionation between Y and Ho in the marine environment. Earth and Planetary Science Letters 148 (1997) p. 329-340.

Ohta, A., and Kawabe, I., 2001. REE (III) adsorption onto Mn dioxide and Fe oxyhydroxide: Ce (III) oxidation by Mn dioxide: Geochimica et Cosmochimica Acta, 65, p. 695-703.

Ojakangas, R.W., 1983. Tidal deposits in the early Proterozoic basin of the Lake Superior reion - the Palms and Pokegama Formations: evidence for subtidal-shelf deposition of Superior type banded iron foramtion, in Medaris, L.G., ed., Early Proterozoic Geology of the Great Lakes Region: Geological Society of America, Memoir 160, p. 49-66.

Olivarez, A.M., Owen, R.M., 1989. Rare earth element/iron variations in hydrothermal sediments: Implications for the REE content of seawater. Geochimica et Cosmochimica Acta, 53: p. 757-762.

Pettenati, M., Mercury, L., and Azaroual, M., 2008. Capillary geochemistry in non-saturated zone of soils. Water content and geochemical signatures. Applied Geochemistry, 23, p. 3799-3818.

Pettine, M., Millero, F., Passino, R., 1994. Reduction of chromium (VI) with hydrogen sulfide in NaCl media. Marine Chemistry 46 (4), p. 335-344.

Philipp. S., 2008. Geometry and formation of gypsum veins in mudstones at Watchet, Somerset, SW England. Geological Magazine, 145, p. 831-844.

Poulton, S.W., Fralick, P.W., and Canfield, D.E., 2004. The transition to a sulphidic ocean ~1.84 billion years ago. Nature, 451, p. 173-177.

Premovic, P.I., Premovic, M.S., and Pavlovic, N.Z., 1986. Vanadium in ancient sedimentary rocks of marine origin: Geochimica et Cosmochimica Acta, 50, p.1923-1931.

Pufahl, P.K., 1996. Stratigraphic architecture of a Paleoproterozoic iron formation depositional system: the Gunflint, Mesabi and Cuyuna iron ranges. Unpublished M.Sc. thesis, Lakehead University, p. 167.

Pufahl, P.K. and Fralick, P.W., 1995. Paleogeographic reconstruction of the Gunflint-Mesabi-Cuyuna depositional system: a basin analysis approach. Institute on Lake Superior Geology Proceedings, 41, p. 59-60.

Pufahl, P.K., and Fralick, P.W., 2000. Fieldtrip 4, Depositional Environments of the Paleoproterozoic Gunflint Formation. Institute on Lake Superior Geology, Field Trip Guidebook, 46. Blue Section, p. 44.

Pufahl, P.K., and Fralick, P.W., 2004. Depositional controls on Paleoproterozoic shallow water iron formation accumulation, Gogebic Range, Wisconsin, U.S.A.: Sedimentology, 54, p. 791-808.

Purser, B.H. and Loreau, 1973. Aragonitic supratidal encrustations on the Trucial Coast of the Persian Gulf. In, ed. B.H. Purser, The Persian Gulf. Springer, Berlin, p. 343-376.

Rankin, P.C., and Chils, C.W., 1976. Rare-earth elements in iron-manganese concretions from some New Zealand soils: Chemical Geology, 18, p. 55-64.

Ruhlin, D.E., Owen, R.M., 1986. The rare earth element geochemistry of hydrothermal sediments from the East Pacific Rise: Examination of a seawater scavenging mechanism. Geochimica et Cosmochimica Acta, 50: p. 393-400.

Schneider, D.A., Bickford, M.E., Cannon, W.F., Schulz, K.J., and Hamilton, M.A., 2002. Age of volcanic rocks and syndepositional iron formation, Marquette Range Supergroup; implications for the tectonic setting of Paleoproterozoic iron formations of the Lake Superior region: Canadian Journal of Earth Sciences, 39, p. 999-1012.

Schulz, K.J., and Cannon, W.F., 2007. The Penokean Orogeny in the Lake Superior region: Precambrian Research, 157, p. 4-25.

Scott, C., Lyons, T., Bekker, A., Shen, Y., Poulton, S., Chu., X., Anbar, A., 2008. Tracing the stepwise oxygenation of the Proterozoic ocean. Nature 452, p. 456-459.

Siebert, C., Nagler, T., von Blanckenburg, F., Kramers, J., 2003. Molybdenum isotope record as a potential new proxy for paleoceanography. Earth and Planetary Science Letters 211, p. 159-171.

Shegelski, R.J., 1982. The Gunflint Formation in the Thunder Bay area, *in* Franklin, J.M., ed., Field Trip Guidebook 4: Winnipeg, Manitoba, Canada, Geological Association of Canada, p.14-31.

Shiller, A.M., and Mao, L., 1999. Dissolved vanadium o the Louisianna shelf: effects of oxygen depletion: Continental Shelf Research, 19, p. 1007-1020.

Shiller, A.M., and Mao, L., 2000. Dissolved vanadium in rivers: effects of silicate weathering: Chemical Geology, 165, p. 13-22.

Sholkovitz, E.R., 1995. The aquatic chemistry of rare earth elements in rivers and estuaries: Aquatic Geochemistry, 1, p. 13-22.

Slack, J.F. and Cannon, W.F., 2009. Exterrestrial demise of banded iron formation 1.85 billion years ago. Geology, v. 37, p. 1011-1014.

Smedley, P.L., 1991. The geochemistry of rare earth elements in groundwater from the Carnmennellis area, southwest England: Gechimica et Cosmochimica Acta, 55, p. 2767-2779.

Spencer, D., Berwer, P., Sachs, P., 1972. Aspects of the distribution and trace element composition of suspended matter in the Black Sea. Geochemica et Cosmochimica Acta 36 (1), p. 71-86.

Spray, J.G., Butler, H.R., and Thompson, L.M., 2004. Tectonic influeces on the morphology of the Sudbury impact structure: Implications for terrestrial cratering and modeling: Meteoritics and Planetary Science, 39, p. 287-301.

Sugiyama, M., 1989. Seasonal variation of vanadium concentration in Lake Biwa, Japan: Geochemistry Journal, 23, p. 111-116.

Sverjensky, D.A., 1984. Europium redox equilibria in aqueous solution: Earth and Planetary Science Letters, 67, p. 70-78.

Tanton, T.L., 1931. Fort William and Port Arthur, and Thunder Cape Map Areas, Thunder Bay District, Ontario: Canada Department of Mines, Geology Survey, Memoir 167 p. 222, 3 maps.

Taylor, S., McLennan, S., 1995. The geochemical evolution of the continental crust. Reviews of Geophysics 33 (2), p. 241-265.

Turkmen, I., and Ozkul, M., 1999. Sedimentology and evaporate genesis of Neogene continental sabkha playa complex, Karakecili Basin, central Anatolia, Turkey. Carbonates and Evaporites, 14, p. 21-31.

Van Wyck, N., Johnson, C.M., 1997. Common lead, Sm-Nd, and U-Pb constraints on petrogenesis, crustal architecture, and tectonic setting of the Penokean orogeny (Paleoproterozoic) in Wisconsin: Geological Society of America Bulletin, 109, p. 799-808.

Voegelin, A., Nagler, T., Beukes, N., and Lacassie, J., 2010. Molybdenum isotopes in late Archaean carbonate rocks: Implications for early Earth oxygenation. Precambrian Research 182 (1-2), p. 70-82.

Wanty, R.B., and Goldhaber, M.B., 1992. Thermodynamics and kinematics of reactions involving vanadium in natural systems: accumulation of vanadium in sedimentary rocks: Geochimica et Cosmochimica Acta, 56, p. 1471-1483.

Webb, G.E., Northdurft, L.K., Kamber, B.S., Kloprogge, J.T., and Zhaos, J.Z., 2009. Rare earth element geochemistry of scleractinian coral skeleton during meteoric diagenesis: a sequence through neomorphism of aragonite to calcite: Sedimentology, 53, p. 1433-1463.

Wehrli, B., and Stumm, W., 1989, Vanadyl in natural waters: adsorpotion and hydrolysis promote oxygenation: Geochimica et Cosmochimica Acta, 53, p. 69-77.

Whitlock, H.P., 1930. Desert roses. Natural History, 30, p. 421-425.

Wille, M., Kramers, J., Nagler, T., Beukes, N., Schroder, S., Meisel., T., Lacassie, J., Voegelin, A., 2007. Evidence for a gradual rise of oxygen between 2.6 and 2.5 Ga from Mo isotopes and Re-PGE signatures in shales. Geochimica et Cosmochimica Acta 2007, p. 2417-2435.

Wright, J., Schrader, H., and Holser, W.T., 1987. Paleoredox variations in ancient oceans recorded by rare earth elements in fossil apatite: Geochimica et Cosmochimica Acta, 51, p. 631-644.

Yang, J., Sun, W., Wang, Z., Xue, Y., and Tao, X., 1999. C=Variations in Sr and Cr isotopes and Ce anomalies in successions from China: evidence for the oxygenation of Neoproterozoic seawater: Precambrian Research, 93, p. 215-233.

Zhang, J., Amakawa, H, Nozaki, Y., 1994. The comparitive behaviours of yttrium and lanthanides in the seawater of the North Pacific, Geophys. Res. Lett. 2, p. 2677-2680.

Zhong, S., and Mucci, A., 1995. Partitioning of rare earth elements (REEs) between calcite and seawater solutions at 25ºC and 1atm and high dissolved REE concentrations: Geochimica et Cosmochimica Acta, 58, p. 443-453.

Tables

	Al2O3	CaO	Fe2O3	K2O	MgO	MnO	Na2O	P2O5	TiO2	Cr	Mn	Mo	V	Y	Ho
HEW2	0.35	49.85	0.22	0.02	0.55	0.03	0.48	0.01	0.01	3.00	218.07	0.00	10.10	0.65	0.02
HEW3A	0.00	0.05	0.06	0.00	0.02	0.00	0.01	0.00	0.00	1.80	4.00	2.00	0.00	0.15	0.00
HEW4	5.98	0.20	2.15	3.32	1.08	0.00	0.34	0.06	0.22	66.50	25.30	3.00	318.80	9.24	0.23
HEW5	4.84	35.64	1.08	1.67	1.33	0.15	0.78	0.07	0.16	4.70	1142.20	2.80	10.40	17.07	0.48
HEW6	2.00	41.78	0.55	0.66	1.01	0.07	0.58	0.05	0.08	16.10	558.50	0.00	73.90	9.70	0.23
HEW7	2.11	46.21	1.12	0.64	1.11	0.10	0.68	0.04	0.08	8.80	783.00	2.20	45.10	6.05	0.18
HEW8	1.52	1.09	3.23	0.05	0.80	0.01	0.06	0.35	0.07	19.50	92.30	0.00	9.50	5.28	0.13
HEW9	3.30	32.51	7.58	0.00	2.75	0.19	0.34	0.05	0.11	37.70	1435.20	3.70	41.70	6.45	0.19
HEW10	3.59	37.71	5.41	0.07	3.56	0.16	0.61	0.16	0.15	39.90	1235.20	2.80	35.60	8.80	0.28
HEW11	2.19	39.75	3.81	0.00	2.48	0.14	0.61	0.09	0.05	101.90	1050.20	0.00	1302.00	27.60	0.60
HEW12	2.38	24.91	6.04	0.03	10.28	0.19	0.73	0.08	0.09	36.40	1494.20	0.00	61.40	10.72	0.27
HEW13	6.46	24.79	11.41	0.11	5.55	0.08	0.62	0.19	0.27	83.40	604.80	2.40	90.00	13.02	0.35
HEW14	4.47	34.33	8.73	0.00	3.92	0.10	0.69	0.04	0.15	53.40	755.20	3.10	52.90	13.06	0.31
HEW15	1.72	37.04	4.61	0.00	3.50	0.20	0.71	0.16	0.04	80.00	1539.20	9.60	731.00	26.08	0.55
HEW16	1.43	35.16	4.28	0.00	3.63	0.21	0.53	0.12	0.04	78.10	1631.20	12.90	731.40	21.90	0.48
HEW17	2.94	27.14	4.83	0.08	9.92	0.21	0.70	0.09	0.12	35.00	1623.20	1.50	71.80	10.62	0.25
HEW18	3.75	0.64	18.45	0.11	2.00	0.03	0.31	0.05	0.14	23.17	219.87	0.00	23.97	3.64	0.12
HEW19	0.83	14.46	11.63	0.07	1.34	0.35	0.89	0.04	0.01	2.07	2736.27	0.00	4.57	4.64	0.13
HEW20	3.64	0.24	12.82	0.03	1.70	0.01	0.14	0.04	0.18	33.07	102.07	0.00	26.87	3.22	0.10
HEW21	1.22	25.96	13.09	0.00	0.73	0.60	0.58	6.91	0.06	13.67	4610.27	0.00	5.67	52.23	1.31
HEW22	1.61	0.20	3.75	0.05	0.61	0.00	0.04	0.01	0.08	22.70	33.50	0.90	11.20	1.52	0.04

	REEs Total	Ce	Dy	Eu	Gd	La	Nd	Pr	Sm	Tb	Er	Lu	Tm	Yb
HEW2	2.70	0.72	0.08	0.02	0.10	0.43	0.32	0.09	0.06	0.01	0.07	0.01	0.01	0.09
HEW3A	0.85	0.30	0.03	0.00	0.03	0.14	0.11	0.03	0.01	0.00	0.01	0.00	0.00	0.01
HEW4	54.43	19.01	1.09	0.64	1.73	8.96	8.34	2.10	1.36	0.20	0.76	0.09	0.10	0.60
HEW5	102.47	34.25	2.59	0.75	3.74	15.99	16.74	4.26	3.18	0.46	1.44	0.18	0.19	1.16
HEW6	41.91	12.52	1.15	0.29	1.57	6.29	5.85	1.49	1.15	0.20	0.72	0.09	0.09	0.57
HEW7	45.73	16.75	1.01	0.32	1.76	7.56	7.56	1.96	1.34	0.19	0.52	0.06	0.06	0.41
HEW8	39.11	15.00	0.73	0.24	1.29	6.98	6.03	1.56	0.98	0.14	0.39	0.04	0.05	0.26
HEW9	52.76	19.97	1.00	0.32	1.67	10.93	7.49	2.08	1.19	0.19	0.62	0.07	0.09	0.51
HEW10	68.23	24.17	1.56	0.55	2.55	12.87	10.91	2.80	1.94	0.30	0.79	0.08	0.09	0.55
HEW11	97.32	19.27	2.76	0.78	3.67	19.47	13.31	3.29	2.49	0.47	1.86	0.19	0.23	1.34
HEW12	65.72	22.19	1.42	0.58	2.29	12.22	9.81	2.68	1.67	0.26	0.82	0.10	0.10	0.61
HEW13	71.94	22.64	1.81	0.55	2.58	12.69	10.84	2.85	1.99	0.32	1.11	0.14	0.14	0.91
HEW14	63.80	19.73	1.48	0.40	1.91	12.86	8.10	2.30	1.38	0.25	1.01	0.11	0.13	0.78
HEW15	111.24	28.94	2.79	0.90	4.06	21.48	15.86	4.03	2.82	0.50	1.68	0.17	0.20	1.18
HEW16	92.45	24.30	2.38	0.77	3.34	18.03	12.49	3.31	2.24	0.41	1.45	0.16	0.18	1.07
HEW17	60.61	19.71	1.28	0.63	1.99	12.27	8.40	2.33	1.41	0.23	0.76	0.08	0.09	0.56
HEW18	31.70	13.07	0.64	0.32	1.03	5.39	4.57	1.21	0.79	0.12	0.38	0.05	0.05	0.32
HEW19	61.16	27.21	0.77	0.37	1.79	13.26	8.42	2.36	1.29	0.16	0.40	0.04	0.05	0.28
HEW20	20.83	7.84	0.52	0.18	0.79	3.03	3.00	0.75	0.59	0.10	0.32	0.04	0.05	0.29
HEW21	718.58	350.32	8.62	4.45	22.40	123.85	105.18	25.93	16.45	1.94	3.74	0.21	0.32	1.63
HEW22	9.19	3.41	0.22	0.10	0.28	1.65	1.11	0.31	0.17	0.04	0.15	0.02	0.02	0.14

Table 1. Harbour Expressway Geochemistry.

	Al2O3	CaO	Fe2O3	K2O	MgO	MnO	NaO2	P2O5	TiO2	Cr	Mn	Mo	V	Y	Ho
MP1	2.07	2.40	47.93	0.16	4.34	1.00	0.80	0.23	0.07	15.27	7769.27	0.00	13.87	5.42	0.14
MP2	1.13	10.07	29.74	0.03	5.89	0.62	0.84	0.04	0.06	10.87	4790.27	0.00	6.67	5.76	0.15
MP3	2.24	0.31	7.65	0.04	1.05	0.02	0.21	0.01	0.06	13.37	155.27	0.00	16.27	1.70	0.05
MP4B	2.43	0.01	6.17	0.01	1.29	0.01	0.10	0.03	0.05	12.47	70.57	0.00	19.07	2.79	0.07
MP5	1.00	7.33	5.57	0.04	3.30	0.19	0.35	0.00	0.03	9.67	1457.27	5.70	11.97	5.39	0.13
MP6	0.12	1.61	0.84	0.00	0.05	0.01	0.00	0.00	0.00	0.47	68.47	1.40	7.47	3.75	0.08
MP7	1.11	22.09	2.41	0.00	0.75	0.06	0.62	0.10	0.04	10.97	451.77	2.60	7.37	6.98	0.14
MP8A	0.88	15.27	5.17	0.01	7.15	0.25	0.58	0.01	0.06	12.27	1963.27	2.40	14.27	13.82	0.31
MP8B	0.87	5.69	3.27	0.00	1.92	0.08	0.15	0.00	0.06	8.98	639.23	26.93	14.00	12.55	0.29
MP9	1.25	9.78	6.39	0.00	4.49	0.16	0.50	0.07	0.03	8.97	1203.73	1.40	107.50	13.60	0.32
MP10	1.76	39.16	3.67	0.00	1.56	0.56	0.66	0.40	0.02	35.68	4333.33	0.00	711.10	76.53	1.53
MP11A	0.65	0.71	0.97	0.02	0.19	0.00	0.04	0.00	0.03	1.78	36.53	0.00	10.10	2.97	0.08
MP11B	0.77	0.37	1.49	0.01	0.30	0.00	0.04	0.00	0.03	2.38	17.63	0.00	14.20	3.36	0.08
MP12	6.64	35.74	12.04	0.00	4.08	0.16	0.69	0.12	0.10	44.28	1236.33	0.00	82.90	23.85	0.51
MP13	5.89	31.19	12.01	0.00	3.54	0.10	0.54	0.07	0.04	62.68	769.43	0.00	73.10	19.69	0.42
MP14	3.07	38.89	7.05	0.00	1.95	0.16	0.50	0.39	0.03	57.88	1251.33	0.73	709.30	52.68	1.14
MP15	0.95	0.21	1.91	0.00	0.38	0.00	0.03	0.01	0.04	4.48	9.03	0.00	14.10	1.47	0.04

	REE Total	Ce	Dy	Eu	Gd	La	Nd	Pr	Sm	Tb	Er	Lu	Tm	Yb
MP1	43.18	17.07	0.78	0.36	1.50	7.67	6.47	1.60	1.16	0.15	0.42	0.05	0.05	0.35
MP2	36.61	14.02	0.74	0.24	1.20	6.31	4.85	1.28	0.89	0.14	0.47	0.07	0.07	0.43
MP3	11.26	4.41	0.23	0.12	0.38	1.89	1.46	0.39	0.28	0.04	0.14	0.02	0.03	0.14
MP4B	19.70	7.53	0.36	0.11	0.58	3.82	2.73	0.76	0.42	0.06	0.24	0.03	0.03	0.17
MP5	26.60	8.45	0.59	0.17	0.76	5.51	3.22	0.90	0.51	0.10	0.42	0.05	0.06	0.34
MP6	8.68	1.36	0.33	0.07	0.31	0.91	0.90	0.20	0.19	0.05	0.25	0.03	0.04	0.21
MP7	22.82	5.78	0.63	0.18	0.78	3.49	2.77	0.68	0.52	0.10	0.42	0.04	0.05	0.26
MP8A	50.00	13.73	1.35	0.34	1.49	7.95	5.98	1.61	1.07	0.21	1.02	0.12	0.14	0.84
MP8B	34.16	7.03	1.13	0.27	1.09	4.80	3.31	0.90	0.60	0.16	1.00	0.11	0.14	0.78
MP9	52.70	13.11	1.45	0.38	1.78	9.36	7.25	1.87	1.33	0.24	0.99	0.11	0.13	0.77
MP10	225.45	37.20	7.57	1.93	10.45	32.20	33.80	7.66	6.96	1.34	4.52	0.39	0.52	2.84
MP11A	8.20	1.47	0.30	0.11	0.29	1.00	0.91	0.23	0.18	0.04	0.29	0.04	0.04	0.25
MP11B	7.79	1.17	0.31	0.12	0.27	0.70	0.81	0.19	0.17	0.04	0.29	0.03	0.04	0.21
MP12	107.96	33.13	2.65	0.86	4.38	17.42	14.75	3.92	2.86	0.49	1.58	0.18	0.19	1.20
MP13	86.04	26.16	2.17	0.69	3.37	14.00	11.33	3.08	2.15	0.39	1.31	0.14	0.16	0.98
MP14	214.28	51.88	6.18	1.99	10.31	32.20	35.21	8.35	7.26	1.17	3.26	0.28	0.35	2.00
MP15	8.76	3.19	0.20	0.09	0.35	1.52	1.10	0.30	0.20	0.04	0.13	0.02	0.02	0.10

Table 2. Mapleward Railway Cut Geochemistry.

	Al2O3	CaO	Fe2O3	K2O	MgO	MnO	Na2O	P2O5	TiO2	Cr	Mn	Mo	V	Y	Ho
HCP1A	0.16	9.69	0.81	0.04	0.18	0.06	0.05	0.03	0.01	1.60	461.07	0.00	3.90	2.70	0.07
HCP1B	2.62	24.92	4.82	0.90	6.23	0.40	0.63	0.30	0.05	94.20	3120.47	0.00	1335.00	42.32	1.25
HCP1C	0.73	7.19	1.47	0.25	0.33	0.03	0.11	0.68	0.03	61.80	253.57	2.60	887.70	21.24	0.28
HCP1D	5.97	3.79	4.47	1.31	3.38	0.05	0.34	0.46	0.19	49.80	354.17	1.30	5.50	16.98	0.28
HCP2A	0.12	1.56	3.94	0.02	0.61	0.02	0.03	0.01	0.01	1.80	188.47	0.00	9.10	1.21	0.02
HCP2B	2.24	25.29	4.39	0.95	10.11	0.21	0.48	0.85	0.03	45.00	1640.47	21.40	1007.00	105.18	2.61
HCP2C	0.06	0.51	0.48	0.02	0.10	0.01	0.02	0.00	0.00	0.80	46.97	0.00	0.80	0.48	0.01
HCP4A	1.67	7.35	1.79	0.27	0.65	0.04	0.22	0.03	0.04	13.20	317.17	1.20	16.90	4.29	0.10
HCP4B	4.98	18.92	5.79	1.10	9.61	0.14	0.48	0.17	0.19	43.90	1061.47	19.70	16.40	10.00	0.33
HCP4C	5.80	30.96	6.16	1.03	4.65	0.11	0.39	0.03	0.21	49.80	825.57	3.00	0.00	7.58	0.21
HCP5A	1.27	2.71	1.18	0.31	0.59	0.02	0.09	0.01	0.04	10.40	142.47	0.00	3.80	2.23	0.06
HCP5B	1.92	32.80	1.14	0.47	1.03	0.12	0.32	0.02	0.07	15.70	933.57	1.80	0.00	2.54	0.08
HCP5C	2.47	16.38	4.62	0.47	3.02	0.14	0.35	0.03	0.07	19.70	309.27	0.00	0.00	7.67	0.28
HCP5D	2.85	14.98	3.43	0.56	4.69	0.10	0.43	0.01	0.09	24.10	751.66	0.00	0.00	6.65	0.17
HCP5E	10.14	5.40	6.43	2.65	4.36	0.04	0.39	0.12	0.32	81.70	309.27	2.30	17.20	10.02	0.28
HCP5F	1.71	1.37	1.40	0.37	0.73	0.01	0.07	0.01	0.07	16.70	93.96	0.80	5.10	2.59	0.08
HCP STALACS	0.16	0.57	1.10	0.00	0.05	0.04	0.03	0.01	0.01	3.76	284.23	0.00	9.20	1.72	0.05

	REE Total	Ce	Dy	Eu	Gd	La	Nd	Pr	Sm	Tb	Er	Lu	Tm	Yb
HCP1A	21.48	7.61	0.41	0.17	0.80	4.69	3.19	0.86	0.58	0.09	0.18	0.01	0.02	0.10
HCP1B	181.46	43.89	5.76	1.36	7.51	31.17	27.25	6.70	5.30	0.97	3.85	0.46	0.51	3.15
HCP1C	51.66	9.59	1.26	0.44	1.64	7.27	5.78	1.37	1.11	0.21	0.81	0.07	0.09	0.50
HCP1D	66.84	18.70	1.49	0.58	2.46	9.35	10.59	2.58	2.04	0.28	0.80	0.08	0.09	0.54
HCP2A	3.26	0.68	0.07	0.05	0.09	0.53	0.34	0.10	0.07	0.01	0.05	0.00	0.01	0.04
HCP2B	387.19	65.73	13.31	3.72	19.38	57.95	73.18	15.85	15.46	2.46	7.13	0.53	0.76	3.95
HCP2C	1.25	0.27	0.04	0.02	0.04	0.13	0.14	0.03	0.03	0.01	0.03	0.00	0.00	0.02
HCP4A	21.26	6.60	0.52	0.20	0.80	3.22	3.38	0.84	0.66	0.10	0.29	0.03	0.03	0.20
HCP4B	94.24	35.09	1.94	0.78	3.49	16.01	16.88	4.33	3.10	0.40	0.98	0.10	0.12	0.69
HCP4C	41.29	13.80	1.01	0.36	1.33	6.76	6.01	1.67	1.10	0.18	0.66	0.07	0.08	0.48
HCP5A	11.15	3.46	0.31	0.15	0.38	1.89	1.54	0.40	0.30	0.05	0.19	0.02	0.02	0.15
HCP5B	24.62	9.23	0.41	0.19	0.76	5.41	3.79	1.06	0.61	0.08	0.24	0.02	0.03	0.17
HCP5C	50.95	17.33	1.35	0.44	1.83	9.26	7.13	1.96	1.34	0.23	0.90	0.15	0.13	0.93
HCP5D	47.94	17.43	1.01	0.37	1.59	8.96	7.19	2.00	1.34	0.20	0.51	0.06	0.06	0.40
HCP5E	47.53	14.25	1.47	0.48	1.88	6.21	7.52	1.89	1.60	0.26	0.83	0.09	0.11	0.64
HCP5F	8.66	2.07	0.32	0.15	0.30	1.09	1.02	0.26	0.21	0.05	0.26	0.03	0.04	0.21
HCP STALACS	8.40	2.16	0.24	0.08	0.27	1.79	1.21	0.34	0.21	0.04	0.16	0.02	0.02	0.10

Table 3. Hillcrest Park Geochemistry.

	Al2O3	CaO	Fe2O3	K2O	MgO	MnO	Na2O	P2O5	TiO2	Cr	Mn	Mo	V	Y	Ho
WT1	0.18	3.52	2.25	0.04	1.44	0.10	0.02	0.01	0.01	4.50	749.37	0.00	6.10	1.35	0.04
WT2	0.19	13.48	5.05	0.02	6.91	0.31	0.04	0.02	0.01	2.10	2367.47	0.00	129.90	3.45	0.10
WT3	6.44	15.48	15.18	0.11	11.79	0.51	0.50	0.15	0.21	51.60	3940.47	25.60	0.00	18.41	0.50
WT4	1.66	18.59	8.02	0.09	9.87	1.03	0.60	0.99	0.02	39.10	7982.47	18.90	705.20	64.25	1.41
WT5	10.18	0.33	7.83	2.30	2.81	0.01	0.16	0.12	0.29	93.80	109.77	0.00	451.90	14.93	0.37
WT6	12.59	0.60	20.38	1.19	4.94	0.06	0.26	0.18	0.44	193.50	462.97	1.70	795.30	18.41	0.60
WT7	2.31	25.17	7.14	0.05	16.08	0.73	0.73	0.02	0.05	2.50	5688.47	18.20	79.60	21.04	0.59
WT8	1.55	24.44	6.20	0.19	14.65	0.89	0.87	0.05	0.05	7.60	6899.47	24.50	115.30	9.64	0.24

	REE Total	Ce	Dy	Eu	Gd	La	Nd	Pr	Sm	Tb	Er	Lu	Tm	Yb
WT1	7.36	2.43	0.21	0.09	0.33	1.16	1.01	0.26	0.21	0.04	0.12	0.01	0.01	0.09
WT2	13.15	4.51	0.43	0.10	0.54	1.54	1.24	0.30	0.28	0.07	0.29	0.03	0.04	0.23
WT3	89.02	26.81	2.48	0.72	3.28	14.44	13.10	3.32	2.53	0.43	1.49	0.17	0.19	1.16
WT4	270.49	61.41	7.90	2.57	13.20	35.80	53.20	11.52	11.03	1.56	3.82	0.29	0.39	2.14
WT5	40.91	7.95	1.69	0.42	1.83	2.98	5.42	1.19	1.42	0.27	1.16	0.14	0.16	0.98
WT6	58.35	11.75	2.69	0.62	3.02	4.52	8.36	1.78	2.17	0.44	1.89	0.24	0.26	1.60
WT7	104.22	32.14	2.80	0.69	3.72	16.67	15.40	3.96	2.88	0.49	1.81	0.24	0.24	1.56
WT8	49.56	15.42	1.23	0.39	1.86	8.74	7.20	1.90	1.34	0.23	0.71	0.08	0.09	0.52

Table 4. Waverly Towers Geochemistry.

	Al2O3	CaO	Fe2O3	K2O	MgO	MnO	Na2O	P2O5	TiO2	Cr	Mn	Mo	V	Y	Ho
HM1	0.13	0.73	9.54	0.03	0.26	0.04	0.02	0.04	0.01	0.00	318.97	0.00	2.00	1.00	0.04
HM2	0.17	14.39	2.52	0.02	0.91	0.16	0.11	0.02	0.00	47.20	1259.47	0.00	0.20	1.61	0.04
HM3	0.25	14.63	2.21	0.03	0.42	0.07	0.22	0.05	0.01	4.10	528.17	0.00	56.50	8.60	0.12
HM4	3.72	21.64	4.47	0.76	1.87	0.16	0.09	0.17	0.13	29.30	1229.47	0.80	11.60	17.68	0.56
HM5	5.12	23.91	7.29	0.52	2.69	0.13	0.23	0.17	0.22	48.30	1026.47	0.00	0.00	12.67	0.41
HM6	6.46	30.11	8.53	0.66	3.31	0.31	0.56	0.08	0.23	51.80	2397.47	0.00	0.00	17.09	0.44

	REE Total	Ce	Dy	Eu	Gd	La	Nd	Pr	Sm	Tb	Er	Lu	Tm	Yb
HM1	5.41	1.77	0.22	0.07	0.25	0.75	0.69	0.16	0.16	0.04	0.13	0.01	0.04	0.11
HM2	8.25	2.67	0.19	0.07	0.27	1.68	1.01	0.26	0.17	0.03	0.12	0.01	0.03	0.09
HM3	19.61	3.01	0.50	0.23	0.57	2.94	1.94	0.49	0.37	0.08	0.37	0.04	0.08	0.30
HM4	83.26	23.97	2.68	0.73	3.53	12.13	12.32	3.10	2.48	0.46	1.69	0.22	0.46	1.47
HM5	64.04	19.27	1.93	0.54	2.62	10.78	8.84	2.33	1.72	0.33	1.25	0.15	0.33	1.05
HM6	80.97	24.77	2.06	0.60	2.49	15.00	10.42	2.89	1.88	0.34	1.41	0.19	0.34	1.21

Table 5. Hill and Markland Geochemistry.

	Al2O3	CaO	Fe2O3	K2O	MgO	MnO	Na2O	P2O5	TiO2	Cr	Mn	Mo	V	Y	Ho
BC6	0.25	10.52	1.08	0.03	0.11	0.07	0.11	0.00	0.01	0.50	526.07	0.00	0.90	1.97	0.04
BC7	0.62	34.17	1.66	0.03	0.34	0.11	0.53	0.05	0.02	4.10	824.07	0.00	4.90	4.41	0.10
BC8	0.17	15.12	0.75	0.02	0.14	0.06	0.21	0.02	0.00	1.10	456.57	0.20	2.70	1.18	0.02
BC9	0.25	29.38	0.69	0.03	0.41	0.07	0.29	0.01	0.01	0.90	547.77	0.00	3.10	0.97	0.02
BC10	0.65	29.52	8.00	0.03	8.21	0.43	0.65	0.02	0.02	2.70	3363.47	0.60	67.10	2.52	0.07
BC11	0.77	27.32	9.57	0.02	10.91	0.48	0.71	0.04	0.02	2.90	3696.47	14.60	97.30	2.69	0.06
BC12	0.09	6.21	0.61	0.03	0.21	0.06	0.02	0.01	0.00	0.20	451.77	0.00	2.00	0.81	0.01
BC13	0.54	24.16	9.98	0.01	8.73	0.62	0.59	0.01	0.01	2.60	4794.47	1.10	85.30	1.32	0.03
BC14	2.52	32.87	5.30	0.07	1.95	0.10	0.39	1.44	0.05	87.30	802.97	0.00	2848.00	110.47	3.22

	REE Total	Ce	Dy	Eu	Gd	La	Nd	Pr	Sm	Tb	Er	Lu	Tm	Yb
BC6	12.21	4.46	0.20	0.25	0.36	2.53	1.49	0.42	0.26	0.04	0.11	0.01	0.01	0.07
BC7	22.92	7.10	0.47	0.31	0.67	5.25	2.71	0.71	0.44	0.08	0.33	0.04	0.04	0.25
BC8	4.99	1.80	0.10	0.06	0.15	0.78	0.52	0.13	0.10	0.02	0.06	0.01	0.01	0.05
BC9	3.20	0.74	0.08	0.03	0.10	0.60	0.38	0.09	0.06	0.01	0.05	0.01	0.01	0.04
BC10	11.16	3.28	0.29	0.11	0.41	2.00	1.40	0.36	0.26	0.05	0.20	0.02	0.03	0.17
BC11	12.42	3.85	0.27	0.12	0.40	2.29	1.63	0.41	0.29	0.05	0.18	0.02	0.02	0.14
BC12	4.09	1.35	0.08	0.08	0.14	0.85	0.49	0.12	0.08	0.01	0.04	0.00	0.00	0.02
BC13	6.46	1.99	0.13	0.07	0.20	1.34	0.82	0.21	0.15	0.03	0.09	0.01	0.01	0.07
BC14	464.57	80.00	16.14	4.46	25.17	82.03	87.05	19.81	17.03	3.03	9.00	0.72	1.00	5.44

Table 6. Baseball Central Geochemistry.

	Al2O3	CaO	Fe2O3	K2O	MgO	MnO	Na2O	P2O5	TiO2	Cr	Mn	Mo	V	Y	Ho
588A1	0.05	0.53	0.12	0.02	0.12	0.00	0.01	0.00	0.00	0.80	27.37	0.00	0.50	0.15	0.00
588A2	0.35	29.65	15.18	0.01	11.70	0.45	0.17	0.03	0.02	0.35	5.30	16.80	223.60	3.66	0.09
588A3	6.12	28.61	8.70	0.62	3.23	0.16	0.28	0.20	0.26	6.12	59.20	0.00	1.00	18.22	0.58
588B1	0.14	8.64	1.61	0.00	0.75	0.08	0.06	0.10	0.00	7.90	606.60	4.10	134.00	21.39	0.37
588B2	2.56	31.84	10.82	0.00	6.95	0.50	0.98	0.13	0.03	5.97	2101.73	0.70	1464.00	56.23	1.31

	REE Total	Ce	Dy	Eu	Gd	La	Nd	Pr	Sm	Tb	Er	Lu	Tm	Yb
588A1	0.58	0.19	0.02	0.01	0.02	0.07	0.05	0.01	0.01	0.00	0.02	0.00	0.00	0.02
588A2	12.56	3.60	0.39	0.09	0.47	1.79	1.27	0.31	0.24	0.06	0.29	0.03	0.04	0.21
588A3	90.26	26.90	2.74	0.76	3.73	15.17	12.27	3.24	2.45	0.47	1.74	0.23	0.23	1.52
588B1	62.00	10.22	1.67	2.49	2.14	10.43	7.72	1.89	1.40	0.28	1.08	0.10	0.13	0.70
588B2	195.08	37.69	5.86	1.26	6.93	36.41	28.25	6.95	5.22	0.96	4.07	0.42	0.53	3.00

Table 7. Highway 588 Geochemistry.

	Al2O3	CaO	Fe2O3	K2O	MgO	MnO	NaO2	P2O5	TiO2	Cr	Mn	Mo	V	Y	Ho
GT1	4.32	2.76	4.64	0.61	1.83	0.04	0.66	0.06	0.17	41.80	285.70	1.60	88.90	12.61	0.34
GT2	2.08	38.24	4.74	0.05	4.39	0.19	0.80	1.03	0.12	35.30	1502.20	0.00	219.40	100.26	2.45
GT3	8.13	14.65	10.64	1.06	6.58	0.16	1.06	0.11	0.40	28.90	1246.20	2.00	39.10	39.54	0.94
GT4	15.89	5.81	7.30	3.50	4.72	0.05	2.32	0.53	0.69	21.30	372.90	4.80	46.60	171.27	5.01
GT5	2.89	36.72	2.44	0.71	2.04	0.15	1.17	0.04	0.06	5.26	1130.73	1.10	12.90	47.64	1.67
GT6	13.84	0.18	2.47	6.28	2.58	0.02	0.47	0.05	0.27	17.00	137.80	3.50	13.20	61.13	2.32
GT7	2.08	36.60	1.95	0.19	1.38	0.09	1.42	0.22	0.04	11.20	726.60	1.50	77.80	43.81	1.03
GT8	1.09	3.13	42.83	0.04	4.33	0.58	0.59	0.39	0.07	105.90	4508.20	0.00	9.30	10.42	0.29
GT9	2.92	5.83	44.07	0.10	5.52	0.50	0.95	0.21	0.12	94.00	3897.20	0.00	39.10	14.21	0.44
GT10	3.19	11.50	65.44	0.10	9.31	0.97	1.46	0.32	0.15	181.50	7521.20	0.00	53.40	22.52	0.66
GT11	2.03	9.16	26.01	0.08	4.26	0.30	0.71	0.17	0.09	56.10	2332.20	1.60	46.50	15.22	0.41
GT13	1.18	12.27	22.11	0.02	8.42	0.31	0.73	0.02	0.03	51.10	2439.20	0.00	7.40	12.69	0.38
GT14	0.05	1.43	0.62	0.00	0.12	0.03	0.02	0.03	0.00	1.77	207.63	0.00	4.20	0.56	0.02

	REE Total	Ce	Dy	Eu	Gd	La	Nd	Pr	Sm	Tb	Er	Lu	Tm	Yb
GT1	39.54	9.08	1.68	0.44	1.59	4.05	5.01	1.23	1.18	0.27	0.98	0.12	0.13	0.81
GT2	378.35	89.47	12.49	2.62	17.28	51.93	59.09	13.54	12.58	2.22	7.13	0.86	0.89	5.55
GT3	121.72	27.94	4.39	2.45	4.72	13.70	14.21	3.74	3.32	0.72	2.90	0.37	0.40	2.39
GT4	420.15	63.13	22.38	4.32	20.09	28.68	44.53	9.43	12.50	3.35	15.77	2.34	2.27	15.09
GT5	161.11	34.53	8.11	1.16	7.49	18.62	19.84	4.68	5.31	1.31	4.95	0.68	0.69	4.43
GT6	327.66	102.58	11.30	1.68	12.46	43.43	51.61	13.05	10.87	1.82	7.37	0.88	1.01	6.15
GT7	139.37	27.21	5.19	1.19	6.59	16.70	20.88	4.65	4.87	0.90	3.07	0.38	0.40	2.48
GT8	52.14	17.05	1.39	0.36	2.01	8.24	7.27	1.83	1.29	0.25	0.88	0.09	0.12	0.66
GT9	60.75	18.12	2.02	0.56	2.51	8.00	8.13	1.93	1.68	0.34	1.35	0.16	0.19	1.13
GT10	115.03	38.33	3.16	0.84	4.28	18.00	15.60	4.00	2.83	0.53	2.04	0.25	0.27	1.72
GT11	44.41	9.25	1.86	0.65	2.10	3.82	5.50	1.19	1.40	0.30	1.28	0.16	0.18	1.08
GT13	30.06	4.06	1.76	0.37	1.63	1.06	3.57	0.67	1.13	0.27	1.16	0.15	0.16	1.01
GT14	2.36	0.69	0.08	0.03	0.11	0.33	0.30	0.07	0.07	0.01	0.05	0.01	0.01	0.03

Table 8. Gunflint Trail Geochemistry.

	Al2O3	CaO	Fe2O3	K2O	MgO	MnO	NaO2	P2O5	TiO2	Cr	Mn	Mo	V	Y	Ho
TFBH2-1	2.64	1.40	25.14	0.00	3.14	0.33	0.35	0.07	0.11	70.30	2576.20	0.00	31.80	4.39	0.12
TFBH2-2	2.84	18.77	10.35	0.00	2.21	0.40	0.73	0.04	0.09	19.17	3108.73	0.00	14.10	4.78	0.10
TFBH2-3	1.87	8.33	0.81	0.45	0.51	0.08	0.18	0.02	0.09	17.47	641.03	0.00	12.60	14.93	0.46
TFBH2-4	2.31	6.79	4.97	0.01	3.90	0.18	0.22	0.15	0.09	22.30	1361.20	1.30	10.60	6.86	0.18
TFBH2-5	0.31	0.39	2.28	0.01	0.22	0.02	0.02	0.01	0.02	3.87	161.83	0.00	10.60	0.58	0.02
TFBH2-6	0.56	26.69	6.76	0.00	16.77	0.76	1.04	0.05	0.01	1.77	5904.73	19.70	1.20	7.31	0.25
TFBH2-7	0.35	6.35	3.09	0.00	8.61	0.27	0.53	0.00	0.00	1.17	2086.73	0.00	5.40	3.11	0.09
TFBH2-8	0.41	12.48	4.63	0.00	0.79	0.15	0.24	5.41	0.01	15.67	1175.73	2.50	93.80	69.79	1.44
TFBH2-9	3.85	27.50	7.30	0.09	6.82	0.52	0.53	0.16	0.16	53.60	4054.20	0.00	126.50	20.12	0.47
THBH2-10	2.92	17.94	20.38	0.00	4.92	0.45	0.43	0.05	0.09	18.87	3488.73	0.00	103.50	16.63	0.43

	REE Total	Ce	Dy	Eu	Gd	La	Nd	Pr	Sm	Tb	Er	Lu	Tm	Yb
TFBH2-1	34.38	13.94	0.60	0.17	1.01	6.78	4.48	1.22	0.69	0.11	0.41	0.05	0.06	0.35
TFBH2-2	44.57	16.52	0.59	0.31	1.44	11.94	5.68	1.49	0.96	0.13	0.31	0.04	0.04	0.24
TFBH2-3	46.60	9.66	2.11	0.39	2.04	4.56	5.69	1.32	1.47	0.34	1.51	0.26	0.23	1.65
TFBH2-4	23.58	5.98	0.91	0.23	1.10	2.17	3.35	0.75	0.84	0.16	0.52	0.06	0.07	0.40
TFBH2-5	5.74	1.60	0.10	0.04	0.16	1.69	0.98	0.29	0.13	0.02	0.06	0.01	0.01	0.05
TFBH2-6	46.99	15.33	1.41	0.55	2.35	5.91	8.48	2.00	2.01	0.29	0.63	0.05	0.07	0.35
TFBH2-7	12.52	3.35	0.48	0.13	0.61	1.54	1.71	0.41	0.45	0.09	0.28	0.03	0.04	0.22
TFBH2-8	250.75	56.59	7.47	2.87	12.02	34.15	40.30	8.95	8.72	1.43	3.93	0.33	0.43	2.34
TFBH2-9	88.73	25.75	2.43	0.95	3.71	12.49	13.42	3.27	2.79	0.46	1.41	0.17	0.18	1.12
THBH2-10	86.68	30.50	2.11	0.70	2.96	13.62	11.39	3.00	2.18	0.38	1.31	0.17	0.18	1.13

Table 9. TFBH2 Drill Core Geochemistry.

	Al2O3	CaO	Fe2O3	K2O	MgO	MnO	Na2O	P2O5	TiO2	Cr	Mn	Mo	V	Y	Ho
BDQ-1-1	0.44	2.72	11.45	0.03	1.18	0.13	0.01	0.06	0.02	15.63	979.83	0.00	6.60	0.90	0.03
BDQ-1-2	1.07	21.60	25.15	0.03	8.31	0.59	0.56	0.04	0.04	49.23	4580.63	3.00	16.30	3.20	0.11
BDQ-1-3	0.25	13.41	6.49	0.01	4.35	0.16	0.00	0.02	0.01	8.23	1270.63	0.00	4.80	0.79	0.02
BDQ-1-4	0.14	2.36	2.39	0.01	0.74	0.04	0.00	0.02	0.00	0.00	287.83	0.00	2.70	0.86	0.02
BDQ-1-5	0.24	29.17	12.34	0.01	9.96	0.20	0.10	0.01	0.00	14.33	1548.63	0.00	1.20	1.00	0.03
BDQ-1-6	0.07	1.84	1.73	0.01	0.47	0.03	0.00	0.00	0.00	0.00	261.93	0.00	1.80	0.30	0.01
BDQ-1-7	1.84	31.93	7.64	0.25	5.85	0.33	0.26	0.94	0.05	68.83	2546.63	11.70	1508.00	72.07	1.87
BDQ-1-8	2.43	32.62	7.92	0.04	9.45	0.31	0.57	0.06	0.07	10.33	2419.63	15.00	52.20	3.42	0.09
BDQ-1-9	6.05	25.45	11.88	0.88	6.10	0.18	0.80	0.22	0.22	56.23	1378.63	52.10	463.70	22.38	0.55
BDQgyp1	1.10	28.27	7.09	0.11	8.92	0.35	0.54	0.04	0.03	19.50	2723.20	4.30	26.10	8.14	0.23
BDQgyp2	1.11	14.69	2.13	0.05	1.01	0.08	0.24	0.02	0.03	9.10	623.50	2.80	18.70	8.38	0.16
BDQgyp3	0.75	30.15	4.91	0.00	11.84	0.29	0.78	0.04	0.02	16.60	2213.20	17.80	54.50	7.29	0.16
BDQgyp4	0.99	26.93	7.74	0.00	7.57	0.27	0.91	0.02	0.02	5.97	2101.73	0.00	64.80	9.09	0.23
BDQ-1-10	4.15	57.94	0.92	1.03	1.64	0.13	1.02	0.02	0.05	0.00	991.33	33.80	16.10	11.06	0.30
BDQ-1-11	3.65	49.35	1.39	0.72	1.60	0.08	0.76	0.02	0.05	0.00	618.03	28.00	2.30	12.70	0.71
BDQ-1-13	3.45	70.61	0.81	0.76	1.31	0.27	1.16	0.03	0.04	0.00	2119.63	23.40	0.00	15.69	1.25
BDQ-1-14	2.51	45.87	0.88	0.62	0.68	0.09	1.07	0.03	0.10	63.63	708.40	0.00	25.13	5.12	0.22
BDQ-1-15	2.25	48.05	0.71	0.50	0.81	0.10	1.38	0.05	0.07	13.93	806.50	0.00	13.63	10.07	0.41

	REE Total	Ce	Dy	Eu	Gd	La	Nd	Pr	Sm	Tb	Er	Lu	Tm	Yb
BDQ-1-1	5.39	2.05	0.13	0.04	0.19	0.80	0.73	0.18	0.14	0.02	0.08	0.01	0.01	0.07
BDQ-1-2	19.31	7.55	0.49	0.13	0.66	2.88	2.44	0.60	0.46	0.08	0.34	0.04	0.05	0.29
BDQ-1-3	5.01	1.95	0.11	0.04	0.16	0.91	0.61	0.16	0.10	0.02	0.07	0.01	0.01	0.05
BDQ-1-4	3.69	1.38	0.10	0.05	0.13	0.39	0.42	0.10	0.09	0.02	0.07	0.01	0.01	0.05
BDQ-1-5	6.05	2.19	0.13	0.05	0.18	1.24	0.70	0.18	0.12	0.02	0.10	0.01	0.01	0.08
BDQ-1-6	1.39	0.50	0.03	0.01	0.04	0.24	0.15	0.04	0.02	0.01	0.02	0.00	0.00	0.02
BDQ-1-7	326.90	77.28	9.30	2.42	13.35	64.95	52.22	11.81	10.37	1.69	5.28	0.44	0.60	3.25
BDQ-1-8	21.90	7.59	0.45	0.22	0.72	4.16	3.14	0.81	0.56	0.08	0.29	0.05	0.04	0.28
BDQ-1-9	79.58	20.48	2.55	0.73	2.99	10.06	10.66	2.55	2.29	0.42	1.76	0.26	0.25	1.63
BDQgyp1	47.36	15.49	1.13	0.35	1.61	8.66	6.82	1.81	1.25	0.21	0.73	0.12	0.10	0.73
BDQgyp2	33.33	9.79	0.80	0.45	0.99	5.93	3.79	1.05	0.66	0.13	0.53	0.08	0.08	0.52
BDQgyp3	27.60	7.84	0.70	0.18	0.91	4.64	3.20	0.80	0.56	0.11	0.51	0.09	0.08	0.52
BDQgyp4	37.21	10.81	1.01	0.27	1.15	6.17	4.58	1.20	0.87	0.17	0.76	0.11	0.11	0.69
BDQ-1-10	54.27	17.23	1.36	0.32	1.63	10.06	6.74	1.90	1.20	0.22	1.01	0.15	0.14	0.93
BDQ-1-11	91.08	29.14	3.38	0.50	3.91	13.11	15.18	3.74	3.24	0.58	2.21	0.31	0.32	2.06
BDQ-1-13	200.61	68.86	6.71	1.20	9.06	35.67	36.78	9.14	7.67	1.23	3.61	0.42	0.46	2.85
BDQ-1-14	44.09	15.29	1.13	0.41	1.54	9.03	6.58	1.74	1.23	0.20	0.71	0.11	0.10	0.69
BDQ-1-15	80.26	28.02	2.07	0.61	2.84	15.14	12.31	3.21	2.27	0.36	1.31	0.20	0.19	1.26

Table 10. BDQ-1 Drill Core Geochemistry.

	Al2O3	CaO	Fe2O3	K2O	MgO	MnO	NaO2	P2O5	TiO2	Cr	Mn	Mo	V	Y	Ho
PR-98-1-1	0.61	28.75	5.66	0.00	10.72	1.24	1.03	0.02	0.01	1.60	9608.20	0.00	2.35	4.07	0.13
PR-98-1-2	2.06	30.81	5.13	0.00	9.70	1.74	1.03	0.83	0.01	34.10	13445.20	1.30	627.55	65.31	2.01
PR-98-1-3	16.87	1.95	3.34	6.06	3.71	0.05	0.71	0.50	0.71	201.90	423.70	0.00	869.15	34.87	1.15
PR-98-1-4	2.68	24.25	5.72	0.14	10.44	0.72	0.86	0.06	0.07	12.90	5591.20	0.00	48.85	10.57	0.34
PR-98-1-5	5.52	25.12	4.67	0.94	11.07	0.43	0.95	0.17	0.39	24.50	3369.20	0.00	107.65	18.48	0.66
PR-98-1-6	0.08	9.05	1.06	0.00	1.81	0.12	0.10	0.00	0.00	3.10	957.00	0.70	0.00	1.08	0.03
PR-98-1-7	7.23	20.26	6.48	0.74	9.22	0.27	0.68	0.05	0.15	27.60	2065.20	0.00	168.60	36.50	1.15

	REE Total	Ce	Dy	Eu	Gd	La	Nd	Pr	Sm	Tb	Er	Lu	Tm	Yb
PR-98-1-1	23.94	7.87	0.57	0.18	0.75	5.15	2.99	0.80	0.49	0.10	0.40	0.05	0.06	0.35
PR-98-1-2	365.17	111.80	10.74	3.11	16.53	50.18	66.11	14.88	13.44	2.04	5.42	0.35	0.55	2.73
PR-98-1-3	230.76	73.65	6.16	1.95	9.60	34.56	42.53	10.43	8.38	1.18	3.29	0.32	0.40	2.31
PR-98-1-4	74.45	26.02	1.74	0.57	2.45	14.64	10.58	2.89	1.95	0.31	1.05	0.16	0.15	1.04
PR-98-1-5	116.80	36.05	3.29	0.98	4.70	19.35	19.85	4.74	4.02	0.61	1.98	0.25	0.26	1.60
PR-98-1-6	7.08	2.65	0.17	0.09	0.25	1.27	0.94	0.25	0.16	0.03	0.09	0.01	0.01	0.07
PR-98-1-7	153.25	43.04	5.51	0.98	6.00	22.12	19.48	4.95	4.20	0.89	3.59	0.58	0.54	3.71

Table 11. PR-98-1 Drill Core Geochemistry.

	Al2O3	CaO	Fe2O3	K2O	MgO	MnO	Na2O	P2O5	TiO2	Cr	Mn	Mo	V	Y	Ho
VHD-00-1-1	2.86	18.04	4.57	0.69	10.55	0.63	0.70	0.04	0.11	25.27	4856.73	0.00	54.60	13.22	0.42

	REE Total	Ce	Dy	Eu	Gd	La	Nd	Pr	Sm	Tb	Er	Lu	Tm	Yb
VHD-00-1-1	82.55	27.63	2.12	0.65	2.71	15.08	12.00	3.09	2.26	0.37	1.33	0.20	0.19	1.27

Table 12. VHD-00-1 Drill Core Geochemistry.

	Al2O3	CaO	Fe2O3	K2O	MgO	MnO	Na2O	P2O5	TiO2	Cr	Mn	Mo	V	Y	Ho
LWD-99-1-1	3.29	0.14	8.02	0.00	1.31	0.01	0.13	0.02	0.18	20.70	88.70	0.00	55.25	2.01	0.06
LWD-99-1-2	0.15	0.40	0.32	0.00	0.18	0.00	0.00	0.00	0.00	1.30	33.20	0.00	3.25	0.61	0.02
LWD-99-1-3	3.12	40.90	0.49	0.94	0.92	0.07	0.93	0.04	0.10	2.70	542.30	0.00	5.65	11.49	0.30
LWD-99-1-4	3.66	26.06	0.78	1.21	0.69	0.08	0.38	0.05	0.11	1.96	582.23	0.00	1.60	16.83	0.62
LWD-99-1-5	12.14	0.31	3.39	4.50	1.77	0.03	0.87	0.12	0.46	106.20	195.30	0.00	123.85	29.77	1.12

	REE Total	Ce	Dy	Eu	Gd	La	Nd	Pr	Sm	Tb	Er	Lu	Tm	Yb
LWD-99-1-1	7.81	2.04	0.26	0.07	0.27	1.12	1.01	0.25	0.21	0.04	0.22	0.03	0.03	0.21
LWD-99-1-2	2.55	0.69	0.09	0.03	0.11	0.32	0.37	0.09	0.08	0.01	0.06	0.01	0.01	0.06
LWD-99-1-3	76.65	27.33	1.56	0.52	2.45	13.70	11.84	3.26	1.98	0.29	0.92	0.12	0.12	0.76
LWD-99-1-4	67.31	16.46	3.07	0.58	3.32	7.31	9.85	2.22	2.58	0.51	1.85	0.24	0.25	1.62
LWD-99-1-5	332.21	141.16	6.28	1.41	10.89	55.85	54.03	14.30	9.28	1.22	3.43	0.39	0.43	2.65

Table 13. LWD-99-1 Drill Core Geochemistry.

UNIT	LITHOLOGIES AND STRUCTURES
Gunflint Formation Greater than 3 Meters Below the Ejecta Layer	-Grainstone facies alternating with fine-grained chemical sediments -Mudstone very common -Lenticular bedded units -Thick lenses of grainstones -Hummocky, cross-stratification present
Gunflint Formation Directly Underneath the Ejecta Layer	-Silicified grainstone facies -Stalactite formation
Limestone Layer Underneath the Ejecta Layer	-Fine-grained grainstone -Coarse-grained grainstone -Stromatolites -Chlorite grains -Blocky calcite cement
Sudbury Impact Layer	-Gunflint Lake S.I.L.: Contains brecciation and folding -Thunder Bay area: Contains impact conglomerate overlain by lapilli or devitrified glass -Blocky, white calcite cement -Stalactite formation
Rocks Above the Ejecta Layer	-2-5 meters of carbonate facies iron formation -Below the Rove contact, chicken-wire structure present -Carbonate replaced gypsum desert roses and lath-like crystals -Stalactite formation

Table 14. Lithologies and Sedimentary Structures Present.